

HIGH RESOLUTION IMAGING AND ANALYSIS OF ENDOTHELIAL TUBULOGENESIS AND BLOOD VESSEL FORMATION

VICTORIA ALICE SALISBURY



**UNIVERSITY OF
BIRMINGHAM**

A thesis submitted to the University of Birmingham for the degree of
DOCTOR OF PHILOSOPHY

Physical Sciences of Imaging in the Biomedical Sciences

School of Chemistry

College of Engineering and Physical Sciences

University of Birmingham

August 2016

UNIVERSITY OF
BIRMINGHAM

University of Birmingham Research Archive

e-theses repository

This unpublished thesis/dissertation is copyright of the author and/or third parties. The intellectual property rights of the author or third parties in respect of this work are as defined by The Copyright Designs and Patents Act 1988 or as modified by any successor legislation.

Any use made of information contained in this thesis/dissertation must be in accordance with that legislation and must be properly acknowledged. Further distribution or reproduction in any format is prohibited without the permission of the copyright holder.

Abstract

The process of angiogenesis in which new blood vessels form from pre-existing vessels, can be intensively studied through the use of *in vitro* and *in vivo* models. The *in vitro* co-culture tube formation assay is used to assess the ability of endothelial cells to develop into three dimensional tubular structures which mimics the growth of capillaries. Different fluorescent labelling techniques were developed and utilised alongside confocal microscopy to visualise endothelial tubulogenesis and investigate the mechanisms of lumenogenesis. Imaging the actin cytoskeletal organisation by expressing the lifeact peptide conjugated to fluorescent proteins revealed that F-actin fibres outline lumens within endothelial tubules and enabled clear visualisation of filopodia formation.

Further studies presented in this thesis aimed to develop, test and evaluate computational tools for analysing endothelial sprouting from fluorescently labelled spheroids generated using the *in vitro* hanging drop spheroid assay and quantify blood vessel formation in the *in vivo* zebrafish model. The results confirmed that both analysis tools were able to rapidly quantify a wide range of angiogenic images and generated comparable results to frequently used manual methods. The developed computational analysis tools are user friendly and can be used to assess the effects of inhibitor compounds and silencing vascular related genes.

Dedication

I dedicate this thesis to my wonderful parents - for your endless love and support

Acknowledgements

Firstly, I wish to thank my supervisor Dr. Victoria Heath, it has been an honour and a pleasure to have been your student, your advice and support throughout the past four years has been invaluable. I also greatly appreciate the help that has been given to me from Prof. Roy Bicknell and Dr. Iain Styles. I would like to thank all the members of the PSIBS Doctoral Training Centre and to the EPSRC for funding this research.

Thank you to Rob Shaw for answering all of my microscopy questions, Prof. Steve Watson for allowing me to use the IMARIS software and to Yavor Hadzhiev and Nan Li for their advice on the zebrafish work.

To all of the members of the Bicknell group, both past and present thank you for making the lab and office such an enjoyable place to work. A special thank you goes to the 2011 PSIBS cohort, to Lois, Ashleigh, Rachel, Chris, Dave and Ting for your friendship and laughter during these past five years.

Finally, I wish to thank my wonderful family. To my mum and dad, I cannot express how grateful I am for the lifetime of support and continued encouragement that you have given me. Thank you also goes to Becky and Tom for being there for me. To my grandad, who inspired me to follow a career in science and for always keeping a keen interest in how my research was progressing. Heartfelt thanks goes to my husband Alexis, for your endless support and encouragement, for always being there for me and listening to all of my worries. Thank you for sharing this journey with me.

Table of Contents

Chapter One

Introduction	1
1.1 Project aims.....	2
1.2 Endothelial cells and their role in vascular development	4
1.2.1 Introduction	4
1.2.2 The formation of blood vessels	4
1.2.3 Angiogenic mechanisms	6
1.2.3.1 Sprouting angiogenesis	6
1.2.3.2 Intussusception angiogenesis.....	8
1.2.4 Mechanisms of lumen formation	9
1.2.4.1 Endothelial cell rearrangement mechanism	10
1.2.4.2 Vacuole fusion mechanism	12
1.2.5 Importance of kinases in angiogenesis	15
1.3 Actin cytoskeleton organisation.....	17
1.3.1 Cytoskeleton overview	17
1.3.2 Actin dynamics.....	18
1.3.3 Visualising the actin cytoskeleton	22
1.4 Models of angiogenesis.....	23
1.4.1 Overview.....	23

1.4.2 <i>In vitro</i> assays.....	23
1.4.2.1 Cellular viability assays.....	23
1.4.2.2 Cellular migration.....	24
1.4.2.3 Endothelial sprouting	25
1.4.2.4 Matrigel tube formation assay.....	26
1.4.2.5 Co-culture tube formation assay	26
1.4.3 <i>In vivo</i> models of angiogenesis.....	29
1.4.3.1 Zebrafish overview.....	29
1.4.3.2 The development of the vasculature in zebrafish.....	30
1.4.3.3 Analysis of the zebrafish vasculature.....	35
1.4.3.4 Genes studied using the zebrafish model.....	37
1.4.3.4.1 Vascular endothelial growth factor A (VEGF).....	37
1.4.3.4.2 C-type lectin domain family 14, membrane A (CLEC14A)	37
1.4.3.4.3 Endothelial cell-specific chemotactic regulator (ECSCR).....	38
1.4.3.4.4 Epidermal growth factor, lactophilin and seven transmembrane domain containing protein 1 on chromosome 1(ELTD1)	38
1.4.3.4.5 Roundabout 4 (ROBO4).....	38
1.4.3.4.6 Regulator of calcineurin 1 (RCAN)	39
1.4.3.4.7 Ets-1 related protein (ETSRP) and ets related gene (ERG) ..	39
1.5 Imaging and analysing assays modelling angiogenesis	40

1.5.1 Overview.....	40
1.5.2 Microscopy techniques	40
1.5.2.1 Optical light microscopy	40
1.5.2.2 Fluorescence microscopy	41
Chapter Two	
Materials and Methods.....	45
2.1 Reagents and equipment	46
2.2 Antibodies.....	47
2.2.1 Primary antibodies	47
2.2.2 Secondary antibodies	47
2.3 Plasmids.....	48
2.4 Inhibitor compounds	48
2.4.1 Kinase inhibitor compounds.....	48
2.4.2 Other inhibitor compounds.....	51
2.5 Morpholino oligonucleotides	51
2.6 Cell biology	52
2.6.1 Mammalian cell culture	52
2.6.2 Passaging and counting cells	53
2.6.3 Storing cells	54

2.6.4 Fluorescently labelling mammalian cells.....	54
2.6.4.1 Fluorescently labelling cells with cytoplasmic dyes	54
2.6.4.2 Lentiviral transduction of HUVECs.....	55
2.6.5 Fluorescence activated cell scanning (FACS)	55
2.6.6 Immunofluorescence	56
2.6.6.1 Co-culture staining of podocalyxin and collagen IV.....	57
2.7 Endothelial assays	58
2.7.1 Co-culture tube formation assay	58
2.7.1.1 Histological staining of endothelial cells	60
2.7.2 Matrigel tube formation assay.....	61
2.7.3 Scratch wound assay.....	61
2.7.4 Hanging drop spheroid angiogenesis assay	62
2.7.4.1 Fixing and mounting endothelial spheroids	64
2.7.5 Cell viability assay	64
2.8 Microbiology and cloning.....	65
2.8.1 Cloning procedure	65
2.8.2 Bacterial culture.....	67
2.8.3 Purification and sequencing of DNA	67

2.8.4 Amplifying the lifeact-GFP insert using polymerase chain reaction	68
2.8.5 DNA separation and purification	68
2.8.6 Restriction digestion reactions of DNA	69
2.8.7 DNA ligation reaction to create the pWPXL-lifeact-GFP plasmid.....	69
2.8.8 Heat shock transformation.....	69
2.9 Zebrafish methods.....	70
2.9.1 Strains and maintenance of zebrafish.....	70
2.9.2 Breeding of transgenic zebrafish and maintenance of embryos	70
2.9.3 Morpholino oligonucleotide injections	71
2.10 Imaging and image analysis	71
2.10.1 Imaging the zebrafish vasculature	71
2.10.2 Image analysis software	72
2.10.3 Statistical analysis	72

Chapter Three

Investigating lumen formation within endothelial tubules	74
3.1 Chapter summary.....	75
3.2 Chapter introduction	76
3.3 Establishing optimal conditions for the co-culture tube formation assay	77

3.4 Using fluorescent cytoplasmic dyes to study lumen formation	80
3.5 Visualising the uptake of fluorescent media into luminal spaces of tubules	89
3.6 Staining of tubular apical and basolateral cell surface markers	91
3.7 Expressing the lifeact peptide to outline developing lumens and visualise filopodia formation	94
3.8 Visualising cellular interactions and lumen formation by using a mixture of lifeact-GFP and lifeact-RFP expressing cells	102
3.9 Chapter discussion	107

Chapter Four

Designing, testing and evaluating a computer based method to analyse endothelial sprouting for screening purposes	113
4.1 Chapter summary	114
4.2 Chapter introduction	115
4.3 Computer based analysis tool designed to analyse endothelial sprouting	116
4.4 Testing and evaluating the computer based analysis tool	123
4.5 Screening kinases to identify those with roles in sprouting angiogenesis	134
4.6 Applying the computer based analysis tool to spheroids treated with p-21 activated kinase (PAK) inhibitors	143
4.7 Applying the computer based analysis tool to spheroids treated with Bruton's tyrosine kinase (BTK) inhibitors	145

4.8 Screening kinases to identify those with roles in endothelial migration and tube formation	148
--	-----

4.9 Chapter discussion	159
------------------------------	-----

Chapter Five

Developing, testing and evaluating computer based analysis methods for quantifying the zebrafish vasculature	167
---	------------

5.1 Chapter summary	168
---------------------------	-----

5.2 Chapter introduction	169
--------------------------------	-----

5.3 Computer based analysis methods for analysing the zebrafish vasculature	170
---	-----

5.4 Imaging the effects of silencing vascular related genes	183
---	-----

5.5 Analysing and evaluating the effects of silencing vascular related genes	189
--	-----

5.6 Analysing the effects of inhibitor treatment on vascular development	198
--	-----

5.7 Evaluating the computer based analysis method	202
---	-----

5.8 Chapter discussion	208
------------------------------	-----

Chapter Six

General discussion	215
---------------------------------	------------

6.1 Overall project findings	216
------------------------------------	-----

6.1.1 Summary of findings from investigating lumen formation within endothelial tubules	216
---	-----

6.1.2 Summary of findings from designing, testing and evaluating a computer based method to analyse endothelial sprouting for screening purposes	217
6.1.3 Summary of findings from developing, testing and evaluating computer based analysis methods for quantifying the zebrafish vasculature	218
6.2 Use of fluorescently labelled endothelial cells	218
6.3 Comparing the computer based analysis methods.....	220
6.4 Future work	222
6.4.1 Future work investigating lumen formation within endothelial tubules .	222
6.1.2 Future work for designing, testing and evaluating a computer based method to analyse endothelial sprouting for screening purposes.....	223
6.1.3 Future work for developing, testing and evaluating computer based analysis methods for quantifying the zebrafish vasculature	224
References	226
Appendices	240
7.1 Identification of the different parameters measured by the ImageJ Spheroid Analysis plugin for spheroid quantification	241
7.2 Screening kinases to identify those with roles in endothelial sprouting	243
7.3 Identification of the different parameters measured by the computer analysis tools for quantifying intersegmental blood vessel growth and connectivity	249
7.4 ImageJ zebrafish vasculature analysis macro	251

Table of Figures

Figure 1.1 Sprouting and intussusception angiogenesis	7
Figure 1.2 Endothelial cell rearrangement mechanism of lumen formation	11
Figure 1.3 Vacuole fusion mechanism of lumen formation	13
Figure 1.4 Filamentous actin polymerisation	19
Figure 1.5 The formation of the intersegmental blood vessels in zebrafish	34
Figure 1.6 Imaging set-up of a confocal fluorescence microscope	42
Figure 2.1 Procedure for the co-culture tube formation assay	59
Figure 2.2 Schematic diagram of the hanging drop spheroid angiogenesis assay	63
Figure 2.3 Cloning procedure to insert the lifeact-GFP sequence into the pWPXL plasmid to replace the original GFP gene	66
Figure 3.1 Both basic fibroblast growth factor and bovine brain extract promoted tubule formation and was not enhanced by the addition of VEGF	79
Figure 3.2 CFSE labelled endothelial cells produced high fluorescence emission allowing the structure of endothelial tubules to be imaged with confocal microscopy	81
Figure 3.3 CFSE labelled endothelial cells continued to produce high fluorescence emission from cells days after labelling	82
Figure 3.4 Labelling endothelial cells with CFSE did not significantly affect tubule formation	85
Figure 3.5 Lumen formation was visualised in CFSE labelled endothelial tubules using the co-culture tube formation assay	86
Figure 3.6 Evidence of the endothelial cell rearrangement mechanism was observed within endothelial tubules formed using cells labelled with CFSE and CellTracker orange	88
Figure 3.7 Tubular lumens take up fluorescent dextran tracer from surrounding culture media	90
Figure 3.8 Lumen formation was confirmed within endothelial tubules by staining for apical and basolateral cell surface markers	92
Figure 3.9 Expression of the lifeact peptide conjugated to fluorescent proteins within endothelial cells enabled the organisation of the actin cytoskeleton to be visualised	95

Figure 3.10 Expressing lifeact in endothelial tubules allowed developing lumens and vacuoles to be visualised	97
Figure 3.11 Use of lifeact in endothelial tubules allowed visualisation of lumens and filopodia extensions	98
Figure 3.12 Lumen formation was confirmed by analysing the image pixel intensities and visualising 3D projections of endothelial tubules	99
Figure 3.13 Filopodia were clearly observed on endothelial tubules by staining for the endothelial specific glycoprotein CD31	101
Figure 3.14 Filopodia and developing lumens formed within endothelial tubules expressing lifeact-GFP and lifeact-RFP	103
Figure 3.15 Example images of endothelial lumenogenesis mechanisms observed in tubules which expressed the lifeact peptide conjugated to fluorescent proteins	105
Figure 4.1 A time lapse experiment demonstrating that endothelial sprouting is a dynamic process	117
Figure 4.2 A stable endothelial sprouting network was observed sixteen hours after embedding the spheroids in collagen	119
Figure 4.3 The ImageJ Spheroid Analysis plugin can be used to analyse endothelial sprouting from fluorescent spheroid images	122
Figure 4.4 The Spheroid Analysis ImageJ plugin was capable of analysing a range of sprouting morphologies	125
Figure 4.5 A linear relationship was calculated upon measuring the total sprouting length using the ImageJ plugin and manual analysis of spheroids	127
Figure 4.6 The highest correlation was calculated between the number of endothelial segments and end points	132
Figure 4.7 The smallest correlation was determined between the number of segments and the average sprout length	133
Figure 4.8 The hanging drop spheroid angiogenesis assay can be used to screen different inhibitors and determine their effects on sprouting angiogenesis	136
Figure 4.9 ImageJ Spheroid Analysis results for inhibiting kinases in the hanging drop spheroid angiogenesis assay	137
Figure 4.10 P-21 activated kinase (PAK) inhibitor PF-3758309 significantly reduced endothelial sprouting	144
Figure 4.11 Bruton's tyrosine kinase (BTK) inhibitors significantly reduced endothelial sprouting	147

Figure 4.12 Bar charts showing the effect of the inhibitor concentrations on cell viability	149
Figure 4.13 The scratch wound angiogenesis assay was used to screen kinases for those with roles in cell migration	151
Figure 4.14 Analysis of the scratch wound angiogenesis assay identified that eighteen inhibitors significantly affected cell migration	152
Figure 4.15 The matrigel tube formation assay was used to screen kinases with roles in endothelial tubulogenesis	154
Figure 4.16 Analysis of the matrigel tubular images confirmed that 28 inhibitors significantly affected endothelial tubulogenesis	155
Figure 5.1 Steps of the ImageJ based approach to analyse vascular images of <i>fli1</i> -GFP zebrafish	172
Figure 5.2 Steps of the IMARIS approach to analyse <i>fli1</i> -GFP zebrafish vascular images	174
Figure 5.3 Developmental time course images of the zebrafish vasculature	176
Figure 5.4 Line graphs of vascular analysis comparing the data generated by the ImageJ and IMARIS methods of analysis	178
Figure 5.5 Studying linear relationships between the outputs generated from the ImageJ and IMARIS analysis methods	182
Figure 5.6 Silencing CLEC14A and ECSCR caused defective ISV development at 30 hpf in <i>fli1</i> -GFP zebrafish	185
Figure 5.7 Knocking down ELTD1, ROBO4, VEGFA and RCAN disrupted ISV and DLAV growth in <i>fli1</i> -GFP zebrafish	187
Figure 5.8 Silencing the ETS transcription factor family member ETSRP caused defective and absent ISV growth in <i>fli1</i> -GFP zebrafish	188
Figure 5.9 Quantitative ImageJ analysis of vascular images studying the knock down of CLEC14A and ECSCR in <i>fli1</i> -GFP zebrafish at 30 hpf	190
Figure 5.10 Quantitative ImageJ analysis of vascular images studying the effect of silencing vascular related genes on the number of vessel segments, junctions and end points at 48 hpf	191
Figure 5.11 Quantitative ImageJ analysis of vascular images studying the effect of silencing vascular related genes on the average and total vessel length at 48 hpf	192
Figure 5.12 Bar charts showing the severity of vascular disruption caused by silencing vascular related genes	194

Figure 5.13 Similar patterns of results were obtained using the ImageJ and manual analysis methods	195
Figure 5.14 Sunitinib treatment disrupted ISV growth and DLAV connectivity	199
Figure 5.15 Ibrutinib inhibited ISV formation in <i>fli1</i> -GFP zebrafish	200
Figure 5.16 Ibrutinib treatment significantly reduced vessel growth and connectivity in <i>fli1</i> -GFP zebrafish embryos	201
Figure 5.17 The strongest correlation was identified between the parameters of total vessel length and the number of junctions	205
Figure 5.18 Measuring the number of end points revealed a high degree of variation in the vascular images	206
Figure 7.1 Identification of the parameters measured by the Spheroid Analysis plugin for the quantification of endothelial sprouting	242
Figure 7.2 The effect on the total sprouting length when kinase inhibitors were added to the hanging drop spheroid assay	244
Figure 7.3 The effect on the average sprouting length when kinase inhibitors were added to the hanging drop spheroid assay	245
Figure 7.4 The effect on the number of segments when kinase inhibitors were added to the hanging drop spheroid assay	246
Figure 7.5 The effect on the number of junctions when kinase inhibitors were added to the hanging drop spheroid assay	247
Figure 7.6 The effect on the number of end points when kinase inhibitors were added to the hanging drop spheroid assay	248
Figure 7.7 Identification of the parameters measured by the computer analysis methods for the quantification of intersegmental blood vessel growth and connectivity	250
Figure 7.8 ImageJ zebrafish vasculature analysis macro code	251

List of Tables

Table 1.1 Stages of embryonic zebrafish development	32
Table 2.1 Primary antibodies	47
Table 2.2 Secondary antibodies	47
Table 2.3 Plasmids	48
Table 2.4 Kinase inhibitor compounds	49
Table 2.5 Other inhibitor compounds	51
Table 2.6 Zebrafish morpholino oligonucleotide sequences	52
Table 3.1 Quantification of the lumenogenesis mechanisms that were observed during endothelial tubular formation	106
Table 4.1 Significant correlations were identified between the different parameters measured using the Spheroid Analysis plugin	130
Table 4.2 Heat map table showing the effect of kinase inhibitors on the process of sprouting angiogenesis	140
Table 4.3 Heat map table to show the screening results of the kinase inhibitors on endothelial migration, tube formation and sprouting	157
Table 5.1 Significant correlations were identified between the different parameters measured using the ImageJ analysis method	203

List of Abbreviations

ABP(s)	Actin binding protein(s)
ADP	Adenosine diphosphate
ANG	Angiopoietin
Arp2/3	Actin related protein 2/3
ATP	Adenosine triphosphate
AVRG	Attributed vessel development graphs
BCIP	5-bromo-4-chloro-3-indolyl phosphate
bFGF	basic fibroblast growth factor
BMX	Bone marrow kinase in chromosome X
BSA	Bovine serum albumin
BTk	Bruton's tyrosine kinase
CaMK II	Calmodulin-dependent protein kinase II
CCD	Charged couple device
CDK	Cyclin-dependent kinase
cDMEM	Complete Dulbecco's modified Eagle's medium
CFSE	Carboxyfluorescein diacetate succinimidyl ester
CK1/2	Casein kinase 1/2
CLEC14A	C-type lectin domain family 14, member A
CLSM	Confocal laser scanning microscopy
cM199	Complete M199 medium
CSDM	Confocal spinning disk microscopy
DA	Dorsal aorta
DAG	Diacylglycerol
DAPI	4'6-diamidino-2-phenylindole
ddH ₂ O	Double distilled water
dH ₂ O	Distilled water

DLAV	Dorsal longitudinal anastomotic vessel
Dll4	Delta-like-4
DMEM	Dulbecco's modified Eagle's medium
DMSO	Dimethyl sulfoxide
DNA	Deoxyribonucleic acid
dNTP	Deoxyribonucleotide
DOCK4	Dedicator of cytokinesis 4
dpf	Days post-fertilisation
E. coli	Escherichia coli
ECM	Extracellular matrix
ECSCR	Endothelial cell-specific chemotaxis regulator
EDTA	Ethylenediaminetetraacetic acid
EfnB2/4	Ephrin B2/4
EGF	Epidermal growth factor
EGFP	Enhanced green fluorescence protein
EGFR	Epidermal growth factor receptor
EHS	Engelbreth-Holm Swarm
ELTD1	Epidermal growth factor, latrophilin and seven transmembrane domain containing 1
ERG	ETS related gene
ERK	Extracellular-signal regulated kinase
ERSRP	ETS-1 related protein
FACS	Fluorescence activated cell scanning
F-actin	Filamentous actin
FAK	Focal adhesion kinase
FCS	Foetal calf serum
FDA	Food and Drug Administration
Fli1	Friend leukemia integration 1
Flk1	Fetal liver kinase 1

Flt1	Fms-like tyrosine kinase 1
G-actin	Globular actin
GAP	GTPase activating protein
Gata2	GATA binding protein 2
GEF	Guanine nucleotide exchange factor
GFP	Green fluorescence protein
GSK-3	Glycogen synthase kinase 3
HDF(s)	Human dermal fibroblast(s)
HEK 293T(s)	Human embryonic kidney 293T cell(s)
HER	Human epidermal growth factor receptor
hpf	Hours post-fertilisation
HUVEC(s)	Human umbilical vein endothelial cell(s)
IC ₅₀ value	Half the maximum inhibitory concentration
ICM	Intermediate cell mass
IF	Immunofluorescence
IFN	Interferon
IHC	Immunohistochemistry
IKK2	Inhibitor of kappa light polypeptide gene enhancer in B-cells, kinase beta
IRAK1	Interleukin 1 receptor associated kinase 1
IRK	Insulin receptor kinase
ISV(s)	Intersegmental blood vessel(s)
JAK-2/3	Janus kinase 2/3
JNK	c-Jun N-terminal kinase
LB	Luria Bertani
MAPK	Mitogen activated protein kinase
MEK1/2	Mitogen activated protein kinase kinase 1/2
MLC	Myosin light chain
MLCK	Myosin light chain kinase

MMP(s)	Matrix metalloproteinases
MO(s)	Morpholino oligonucleotide(s)
mRNA	Messenger RNA
MS-222	Tricaine methanesulfonate
MT1-MMPs	Membrane type I matrix metalloproteinases
mTOR	Mammalian target of rapamycin
MTS	3-(4,5-dimethylthiazol-2-yl)-5-(3-carboxymethoxyphenyl)-2-(4-sulfophenyl)-2H-tetrazolium
MTT	3-(4,5-dimethylthiazol-2-yl)-2,5-diphenyltetrazolium bromide
NBT	Nitro blue tetrazolium
NF- κ B	Nuclear factor kappa B
NGFR	Nerve growth factor receptor
NIS	Nikon Imaging Software
ns	No statistical significant difference
p value	Probability value
PAK	P-21 activated kinase
PAR3	Partitioning defect 3
PBS	(Dulbecco's) Phosphate buffered saline
PCR	Polymerase chain reaction
PCV	Posterior cardinal vein
PDGF	Platelet derived growth factor
PDGFR	Platelet derived growth factor receptor
PEI	Polyethylenimine
PFA	Paraformaldehyde
PI3-K	Phosphoinositide 3-kinase
PKA/C/G	Protein kinase A/C/G
PLC/D	Phospholipase C/D
PTU	1-phenyl 2-thiourea
R value	Pearson product moment correlation coefficient

r ² value	Coefficient of determination
RASIP1	RAS interacting protein 1
RCAN	Regulator of calcineurin
RFP	Red fluorescence protein
RNA	Ribonucleic acid
Robo	Roundabout
ROBO4	Roundabout4
ROCK	Rho associated kinase
ROS	Reactive oxygen species
RTKs	Receptor tyrosine kinases
SEM	Standard error of the mean
SH2	Src homology 2 domain
Syk	Spleen tyrosine kinase
TAE	Tris acetate EDTA
TEM	Tumour endothelial marker
TKI	Tyrosine kinase inhibitors
UTR	Untranslated region
UV	Ultraviolet
v/v	Volume per volume
VEGF	Vascular endothelial growth factor A
VEGFR1/2	Vascular endothelial growth factor receptor 1/2
w/v	Weight per volume
WASP	Wilsott-Aldrich syndrome protein
WST-1	4-[3-(4-iodophenyl)-2-(4-nitrophenyl)-2H-5-tetrazolio]-1,3-benzene disulfonate
XTT	3'-[1-[(phenylamino)-carbonyl]-3,4-tetrazolium]-bis(4-methoxy-6-nitro) benzene-sulfonic acid hydrate

Chapter One

Introduction

1.1. Project aims

The main focus of this PhD project was to monitor, manipulate and analyse in detail the process of angiogenesis through the development of high resolution fluorescence imaging techniques and the generation of useful analysis tools to quantify angiogenic images.

The following aims are presented in the three results chapters in this thesis:

To utilise and develop fluorescent imaging techniques to study the process of endothelial lumen formation within tubules formed in the *in vitro* co-culture tube formation assay

Confocal imaging was used alongside various fluorescent labelling techniques to study and monitor the extension of endothelial cells into three dimensional tubules using the co-culture tube formation assay. The intracellular process of lumen formation within endothelial tubules was imaged by fluorescently labelling the cytoplasm of endothelial cells, staining for apical and basal cell surface markers as well as visualising the organisation of the actin cytoskeleton. The endothelial lumenogenesis mechanisms were visualised, assessed and quantified in endothelial tubules formed using this tube formation assay.

To design, test and evaluate a computer based analysis tool for quantifying endothelial sprouting from fluorescently labelled spheroids produced using the *in vitro* hanging drop spheroid angiogenesis assay

A computer based analysis tool was specifically designed to permit rapid and automated analysis of endothelial sprouting from spheroids generated from the

hanging drop spheroid angiogenesis assay. The Spheroid Analysis ImageJ plugin was tested and evaluated by applying the analysis method to a wide range of endothelial sprouting images generated through a kinase screen using a library of 80 small molecule kinase inhibitors in the assay. Alongside the hanging drop spheroid angiogenesis assay, the scratch wound *in vitro* angiogenesis assay and the matrigel tube formation assay were used to screen and identify important kinases with roles in endothelial sprouting, migration and tube formation. The data generated from the kinase screen has been represented in analysis heat map tables which enabled easy and rapid identification of kinase inhibitors that affected these endothelial processes.

To generate a computer based analysis method to assess and quantify the development of the intersegmental blood vessels in embryonic zebrafish

Two computer assisted analysis methods using IMARIS and ImageJ software were generated which permitted quantification of numerous vascular parameters from fluorescent zebrafish images. Normal vascular development was studied by monitoring and imaging the formation of the intersegmental blood vessels in *fli1-GFP* zebrafish embryos with time-course confocal imaging. Abnormal vascular development was studied by knocking down vascular related genes and the effects of inhibitor compounds on vessel development were observed. Both normal and abnormal vascular development was assessed and quantified using the computer based analysis methods and comparative studies were performed by performing manual analysis on the vascular images.

1.2. Endothelial cells and their role in vascular development

1.2.1. Introduction

The endothelium consists of a single layer of endothelial cells which line the internal walls of blood and lymphatic vessels¹. Blood vessels transport oxygen, nutrients and hormones to tissues and the lymphatic vessels return interstitial fluid consisting of blood plasma and leukocytes from the interstitial space back to the blood vessels². The vascular network contributes to the important physiological processes of tissue growth and repair, cell delivery and immunity³. Endothelial cells are highly metabolically active cells and dysregulation of these cells can cause malignant, ischemic, immune and inflammatory disorders³⁻⁵.

1.2.2. The formation of blood vessels

The *de novo* formation of blood vessels is initiated from blood islands in the developing organism, these are formed from mesodermal derived hemangioblasts which either undergo differentiation to produce angioblasts, which are the endothelial precursor cells or hematopoietic stem cells⁶. Upon stimulation from vascular endothelial growth factor A (VEGF) signalling through the transmembrane receptor tyrosine kinase VEGFR2, the blood islands fuse together to form the first primitive plexus of blood vessels in the embryonic organism^{6,7}. The process which generates this primitive vascular network is known as vasculogenesis⁸.

The primary capillary plexus then undergoes remodelling and stabilisation by the attachment of mural cells to the abluminal endothelial surface, for smaller blood vessels such as capillaries this involves the attachment of pericytes and for larger vessels it involves the attachment of vascular smooth muscle cells. Once the vessel

has been stabilised, the vascular network is expanded through endothelial sprouting, intussusception and collateral growth^{4,9}. The process in which new blood vessels form from the pre-existing vascular network is known as angiogenesis, a process which is predominantly driven by endothelial proliferation^{8,10}.

The process of angiogenesis is not only critical for supporting embryonic development; it also has crucial roles within adult organisms such as aiding the multistep process of wound repair. During the proliferative phase of wound healing, the normally quiescent endothelial cells are recruited to the site of vascular damage and angiogenesis is initiated to sustain the growth of newly formed replacement tissue¹¹. Angiogenesis is also a highly active process in female adult organisms, since there is a requirement for rapid vessel growth in uterine and placental tissues during pregnancy as well as during the female menstrual cycle^{5,12}.

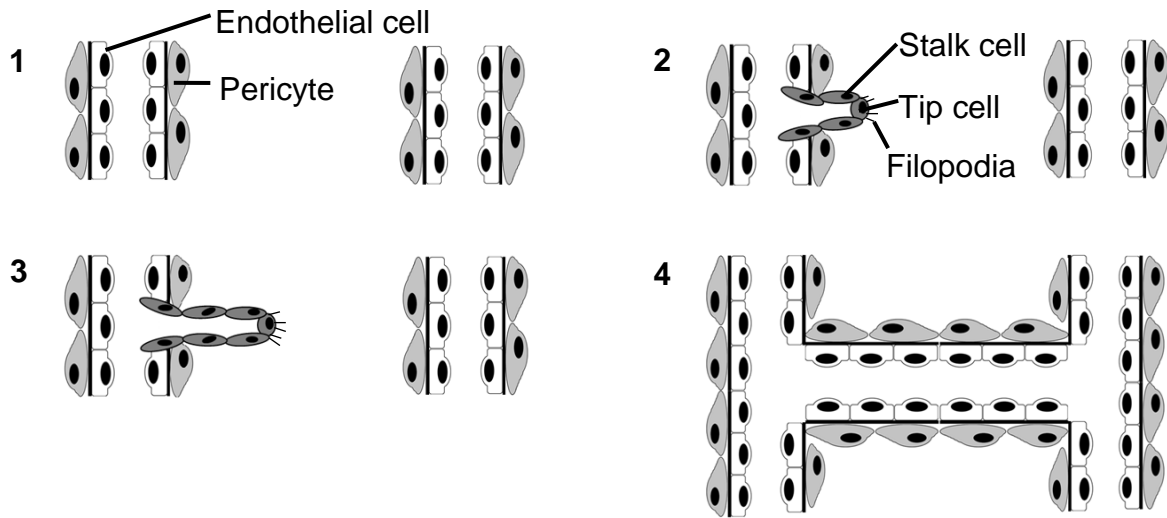
However, dysregulation of endothelial cells can support the progression of pathological diseases. Pathological conditions associated with vessel regression or reduced vessel growth include ischemia, hypertension and neurodegeneration⁴. Enhanced activation of the angiogenic pathway is associated with atherosclerosis, obesity, asthma and inflammatory associated diseases such as arthritis⁴. Angiogenesis also supports tumour growth and metastasis, as tumours are limited to 1-2 mm in diameter which is equivalent to approximately 1 million cells without the infiltration of blood vessels into the hypoxic tumour environment to supply oxygen to the tumour cells¹³.

1.2.3. Angiogenic mechanisms

1.2.3.1. Sprouting angiogenesis

The process of sprouting angiogenesis is controlled through signalling pathways from critical regulatory factors, the pathway can be stimulated by an enhancement of pro-angiogenic signalling molecules such as VEGF, angiopoietin-2 (ANG-2) and chemokines which are released by tumour or inflammatory cells^{1,14}. In response to angiogenic stimulation, pericytes detach from the basement membrane and the vessel is destabilised through the action of matrix metalloproteinases (MMPs)¹⁴. There are strong intercellular adhesions between endothelial cells to ensure vessel integrity, the cells are connected by junctional proteins of VE-cadherin and claudins, however MMP degradation weakens the endothelial contacts causing increased vascular permeability and enables endothelial migration¹⁴. Particular endothelial cells within the vessel become activated and initiate endothelial sprouting which expands the vascular network, these endothelial cells are known as tip cells and they direct the growth of the newly formed blood vessel¹. These dynamic and motile tip cells function by extending cytoplasmic projections known as filopodia into the local micro-environment and respond to chemotropic signals from ephrins and semaphorins through receptors on their cell surface thereby sensing gradients of angiogenic factors¹⁵. The cells located behind the endothelial tip cell in the developing sprout are known as endothelial stalk cells and these cells are responsible for elongating the sprout via cellular proliferation¹. The process of sprouting angiogenesis is outlined in figure 1.1.

Sprouting Angiogenesis



Intussusception Angiogenesis

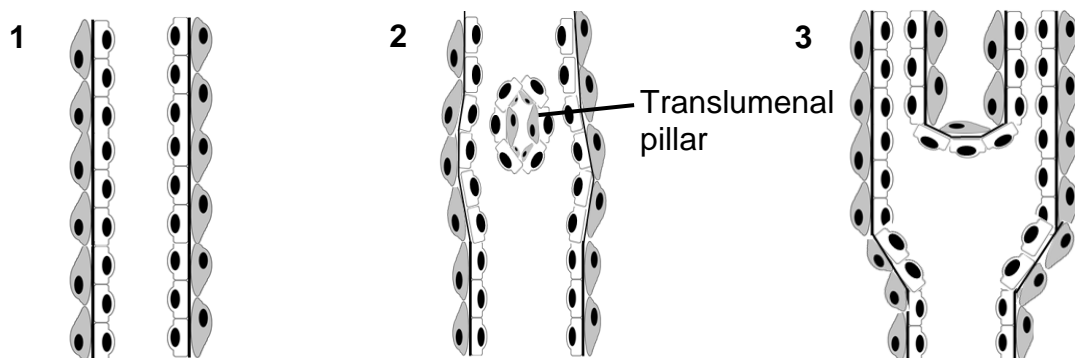


Figure 1.1 Sprouting and intussusception angiogenesis

In sprouting angiogenesis, 1) two neighbouring blood vessels exist as quiescent vessels, 2) a tip cell emerges upon activation of an endothelial cell in one vessel and destabilisation of the basement membrane, 3) stalk cells located behind the tip cell proliferate to elongate the endothelial sprout, 4) the endothelial sprout forms a junction with the neighbouring vessel, forming a complex and interconnecting vascular network.

In intussusception angiogenesis, 1) a blood vessel exists, 2) protrusion of opposing sides of the vessel wall come into contact, which is stabilised by basement membrane components, collagen and pericytes, 3) the formation of a mature translumenal pillar within the vessel, increases the complexity of the vasculature.

Signalling from the delta-like-4 (Dll4) and notch pathway determines tip and stalk cell fate and determines endothelial behaviour. Dll4 is a membrane bound endothelial specific notch ligand which is upregulated on tip cells and binds to the heterodimeric notch receptor on adjacent endothelial cells to promote the stalk cell phenotype^{1,16}. The stalk cells continue to proliferate and elongate the sprout until the tip cell connects with a nearby vessel generating vascular junctions, contributing to vascular complexity. Endothelial stalk cells then establish a lumen via the process of lumenogenesis, a critical step in angiogenesis which creates a continuous open channel encapsulated by endothelial cells which enables blood flow¹⁵.

Tubular lumens are generated either through the rearrangement and morphological changes of endothelial cells in which an extracellular space develops into a lumen or by the process of pinocytosis and vacuole fusion, in which intracellular vacuoles of adjacent cells fuse together to form a continuous lumen^{17,18}. Lumenogenesis allows establishment of blood flow which increases the amount of oxygen to the tissue thereby causing a reduction in pro-angiogenic signalling and subsequently results in quiescent behaviour of the vessel¹. Additionally, the integration of the newly formed vessel as well as the release of platelet derived growth factor B (PDGFB) from endothelial tip cells during this process triggers the attachment of mural cells to the endothelial cells thereby stabilising the new vessel¹.

1.2.3.2. Intussusception angiogenesis

Another angiogenic mechanism which functions to expand the vascular network in organisms is intussusception or splitting angiogenesis. This angiogenic mechanism involves the generation of transluminal tissue pillars within mature vessels leading to vessel separation, as shown in figure 1.1¹⁹. The process of intussusception is

initiated by protruding endothelial cell walls on opposing sides of the vessel. The vascular protrusion leads to intercellular contact within the vessel which is stabilised by the formation of basement membrane and the diameter of the vascular pillar increases due to the formation of collagen and attachment of pericytes²⁰. The establishment of a transluminal vascular pillar increases the complexity of the vascular network and occurs comparatively faster than sprouting angiogenesis which depends on endothelial proliferation¹⁹.

Both angiogenic mechanisms of sprouting and intussusception are essential post vasculogenesis to enhance the complexity and connectivity of the primary vascular network to provide an efficient circulatory system. Sprouting angiogenesis is the dominant mechanism required to establish newly formed vessels, whereas intussusception angiogenesis is crucial for remodelling the vasculature²⁰. Once blood flow in the vessels has been established, vascular remodelling is achieved through vessel regression and pruning to ensure there is efficient blood transport. Vessels which participate in limited blood transport regress through the retraction of endothelial cells, in which the endothelial cells either relocate to another vessel or undergo apoptosis²¹.

1.2.4. Mechanisms of lumen formation

All developing vessels must undergo the process of lumenogenesis to establish a lumen to transport blood and prior to lumen formation the endothelial cells exist as a cord of cells tightly connected by cellular junctions. The cellular and molecular mechanisms of endothelial lumenogenesis have been widely debated, due to the complex morphology of the tubules, the lack of specific apical and basolateral cell surface markers as well as the difficulty posed by imaging intracellular structures,

many researchers have had difficulty identifying the exact mechanisms behind the formation of tubular lumens¹⁷. However, there is evidence to support two models of endothelial lumen formation; the endothelial cell rearrangement mechanism and the vacuole fusion mechanism, these mechanisms may occur under different environmental conditions *in vivo* and *in vitro*²².

1.2.4.1. Endothelial cell rearrangement mechanism

In the first stage of the endothelial cell rearrangement or cord hollowing lumenogenesis mechanism, the apical and basolateral endothelial cell surfaces are established by cellular polarisation^{17,23}. The apical cell surface is that which interacts with the lumen, whereas the basal cell surface is on the abluminal side²⁴. Following the establishment of the apicobasal polarity, junctional proteins are redistributed along the endothelial cell surfaces with negatively charged CD34-sialomucins, dextran sulphate and glycoprotein podocalyxin redirected to the apical cell membrane, a process regulated by VE-cadherin and $\beta 1$ integrin²³. Electrostatic repulsion between two apical endothelial surfaces of adjacent cells from the negatively charged proteins on these cell membranes drives the initial formation of a small extracellular space at the cell-cell contact region²⁵, as shown in figure 1.2. Successive expansion of the extracellular space is achieved through repositioning of podocalyxin, which recruits F-actin and moesin to the apical cell membrane where actomyosin contractility causes cytoskeletal reorganisation and morphological rearrangement of the endothelial cells²³. Signalling by the Rac1 guanine nucleotide exchange factor (GEF) dedicator of cytokinesis 4 (DOCK4) has been identified to be necessary for lumen formation through the rearrangement of the endothelial cytoskeleton in the cell rearrangement mechanism²⁶.

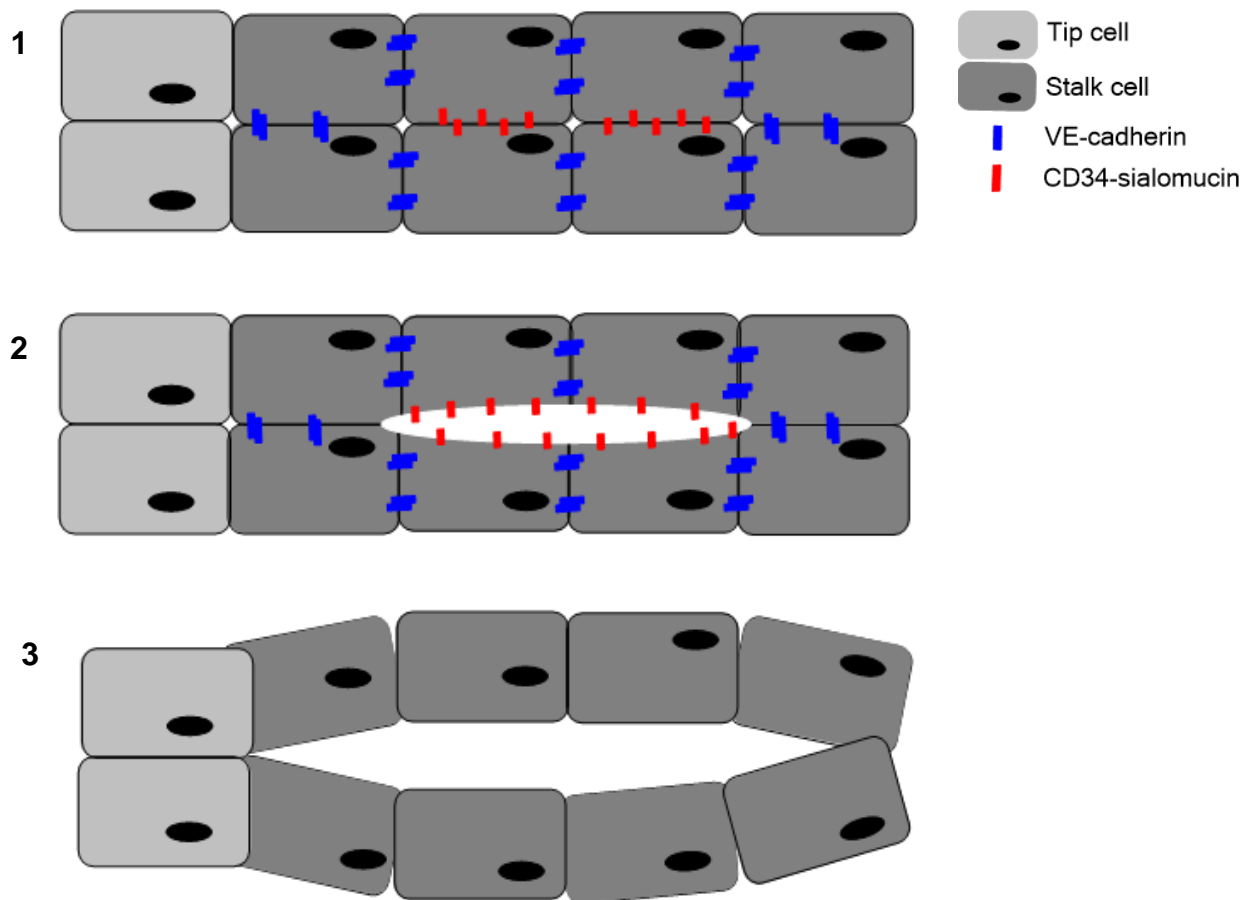


Figure 1.2 Endothelial cell rearrangement mechanism of lumen formation

In the endothelial cell rearrangement mechanism of endothelial tubular lumen formation, 1) VE-cadherin establishes apical and basolateral polarity and there is expression of the negatively charged CD34-sialomucins on the cell surfaces of neighbouring endothelial cells, 2) the negatively charged apical cell surfaces repel each other through electrostatic repulsion and an extracellular space forms between the cells, 3) morphological changes driven by cytoskeletal rearrangement between the endothelial cells forms the lumen in the extracellular space.

The endothelial cell rearrangement mechanism of lumenogenesis has been observed in the formation of aortic lumens in mouse embryos, with the diffusion of interstitial fluid into the extracellular space causing luminal expansion²⁵. Similarly Xu *et al.* found evidence which supported this model in murine aortic endothelial cells and identified that RAS interacting protein 1 (RASIP1) plays a critical regulatory role during this process. Upon silencing of this protein endothelial lumens failed to form²⁷. Jin *et al.* also identified that angioblasts undergo morphological changes from a cuboidal shape into an elongated shape to aid lumengogenesis in the dorsal aorta (DA) in zebrafish embryos at 18 hours post- fertilisation (hpf)²⁸. Additionally, Blum *et al.* imaged the presence and organisation of endothelial junctional proteins within the intersegmental blood vessels (ISVs) in developing zebrafish embryos and observed that lumens within ISV develop via the endothelial cell rearrangement mechanism²⁹.

1.2.4.2. Vacuole fusion mechanism

The alternative endothelial tubular lumen formation mechanism is known as the vacuole fusion or cell hollowing mechanism. This process is initiated by integrin mediated pinocytosis, in which invaginations of the cell membrane containing surrounding fluid enters the endothelial tubule³⁰. Subsequent fusion of small intracellular pinocytosed vesicles forms large intracellular vacuoles, these adjacent cell vacuoles fuse together causing luminal expansion³⁰, as shown in figure 1.3. The extracellular space is further enlarged by the proteolysis action of membrane type I matrix metalloproteinases (MT1-MMP) and there is removal of endothelial junctions which causes the extracellular space to become an established tubular lumen encapsulated by several endothelial cells³¹.

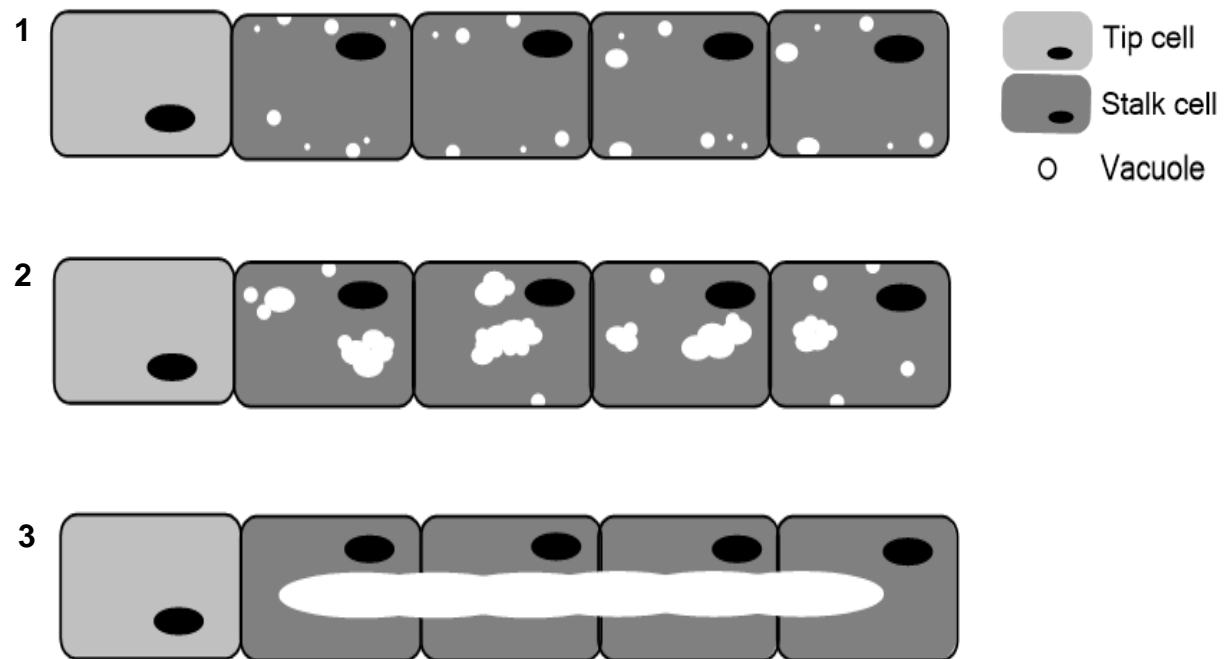


Figure 1.3 Vacuole fusion mechanism of lumen formation

In the vacuole fusion mechanism of endothelial tubular lumen formation, 1) pinocytotic vesicles bringing in surrounding media into the endothelial cells, 2) vesicles fuse to create vacuoles, 3) adjacent cell vacuoles fuse creating a lumen as a channel throughout the cells.

The vacuole fusion mechanism of lumen formation has been the predominant mechanism observed within endothelial tubules developed *in vitro*, particularly within tubules formed on extracellular matrices of collagen and fibrin^{30,32-36}. Yang *et al.* identified that the vacuole fusion mechanism was responsible for lumen formation within tubules formed in collagen gels by visualising the uptake of the fluorescent dye 6-carboxyfluorescein into luminal spaces of tubules³⁵. These reports have identified the importance of the Rho family GTPases particularly RhoA, Cdc42 and Rac1 in regulating pinocytosis and vacuole fusion, as well as outlining the importance of integrin $\alpha_2\beta_1$ for endothelial cell binding to collagen which leads to successive lumen formation. Specifically, this lumenogenesis mechanism has been found to be dependent on Rac1 and Cdc42 recruitment to the intracellular vacuole surfaces within endothelial cells^{30,34}.

The vacuole fusion mechanism has also been identified to occur *in vivo* by Kamei *et al.* as high resolution time-lapse two-photon imaging was used to visualise intracellular as well as intercellular fusion of vacuoles during the development of the ISVs in zebrafish¹⁸. ISV development and lumen formation has also been studied by Blum *et al.* as single cell imaging was used to visualise the localisation of junctional proteins within developing ISVs²⁹. In this way, Blum *et al.* observed lateral adhesions within these blood vessels which corresponded to overlapping endothelial cells and lumen formation via the endothelial cell rearrangement mechanism²⁹. Recent work by Gebala *et al.* also supports the endothelial cell rearrangement mechanism as the prevailing mechanism of lumen formation within the ISVs and identified the importance of blood flow to drive luminal expansion through both unicellular and multicellular regions of these vessels³⁷. Gebala *et al.* visualised the formation of

inverse blebs at the apical membrane of endothelial cells during the process of luminal expansion within the ISVs and concluded that blood flow is required to form these spherical deformations, this mechanism of lumen expansion has been termed inverse membrane blebbing³⁷.

1.2.5. Importance of kinases in angiogenesis

Protein phosphorylation mediates important eukaryotic signal transduction pathways and regulates essential cellular processes including proliferation, differentiation, motility and apoptosis³⁸⁻⁴¹. Phosphorylation is a reversible, covalent modification which involves the transfer of the γ -phosphate from a purine nucleotide triphosphate such as adenosine triphosphate (ATP) to a hydroxyl group on a target protein by the action of a kinase; and the removal of the phosphate group from the protein is catalysed by a phosphatase⁴¹.

Eukaryotic protein kinases are classified into tyrosine-specific protein kinases, serine/threonine-specific protein kinases and dual specificity protein kinases based on which specific amino acid residue is targeted for the addition of the γ -phosphate group⁴². Phosphorylation events cause a conformational change in the target protein which subsequently results in altered function or localisation of the protein. Disregulation or disfunctional kinases contribute to pathological diseases such as cancer, cardiovascular disease, diabetes and inflammation and as a result, protein kinases have been widely studied as potential targets for therapeutic drugs⁴²⁻⁴⁶. Currently, the Food and Drug Administration (FDA) has approved thirty inhibitors for clinical usage which target and inhibit the action of protein kinases^{45,47}. Most protein kinase inhibitors are ATP-competitors therefore they prevent action of the kinase by targeting the ATP binding site and blocking the conversion of ATP to adenosine

diphosphate (ADP), preventing the release of the γ -phosphate group for the phosphorylation reaction. Once bound the inhibitor is surrounded by a hydrophobic pocket which inactivates the kinase molecule^{46,48,49}.

Kinases play important mediatory roles within signalling pathways including regulating the angiogenic pathway. Binding of VEGF to the extracellular domain of the tyrosine kinase receptors VEGFR1 and VEGFR2 causes auto-phosphorylation of the intracellular portion of the receptor⁵⁰. Auto-phosphorylation of VEGFR2 activates the phospholipase C (PLC)- protein kinase C (PKC)- mitogen activated protein kinase (MAPK) pathway as well as stimulating other tyrosine and serine/threonine kinases which leads to an enhancement of endothelial migration and proliferation and promotes new blood vessel growth^{50,51}. Since VEGF signalling is a mediator for the 'angiogenic switch', the receptor tyrosine kinases have been targeted by therapeutic inhibitors to prevent tumour angiogenesis, for example sunitinib, sorafenib and pazopanib have all been approved as anti-angiogenic therapeutic agents for the treatment of kidney cancer⁵¹⁻⁵⁴. Bevacizumab is a monoclonal antibody that targets VEGF to prevent VEGFR2 activation⁵⁵.

Another family of receptor tyrosine kinases are the platelet derived growth factor receptors α and β (PDGFR). PDGFR is activated through binding of the PDGF ligand causing an auto-phosphorylation event of the receptor, enhancing endothelial proliferation through binding to SH2 domain containing proteins from 10 different protein families^{50,56}. Signalling via PDGFR β induces VEGF transcription leading to activation of the angiogenic pathway, this response is stimulated in sarcomas⁵⁷. Many therapeutic agents which target VEGFR are also known to target PDGFR; these include sorafenib, sunitinib, PKC412, SU6668⁵⁷⁻⁵⁹. Additionally, PDGFR is

highly expressed by pericytes, therapies which block this receptor tyrosine kinase have been found to cause detachment of pericytes in tumour vasculature leading to vessel destabilisation and prevention of tumour growth^{45,60-62}. Combined therapeutic strategies inhibiting both VEGF and PDGF signalling has been identified to further disrupt tumour angiogenesis compared with inhibition of VEGF alone^{62,63}.

Other important kinases which mediate and regulate the angiogenic pathway through the control of cellular migration, proliferation and differentiation, include the tyrosine kinase epidermal growth factor receptor (EGFR) and serine/threonine kinases including mitogen activated protein kinases (MAPK), myosin light chain kinase (MLCK), protein kinase A (PKA), protein kinase G (PKG) and protein kinase C (PKC)⁶⁴⁻⁶⁶. The different isoforms of PKC become activated through signalling of intracellular calcium ions, diacylglycerol (DAG) and phospholipids such as phosphatidylserine, this activation event causes PKC to modulate nuclear transcriptional events⁶⁷. Furthermore, PKC α activation has been shown to induce VEGF signalling and promote angiogenic activity in endothelial cells⁶⁸.

1.3. Actin cytoskeleton organisation

1.3.1. Cytoskeleton overview

The eukaryotic cytoskeleton is a highly dynamic complex network of proteins consisting of interconnecting filaments and molecular motors. The three primary polymeric filaments of the cytoskeleton are the microtubules, intermediate filaments and actin microfilaments, which act to maintain and support cellular integrity and organise the positioning of intracellular components^{69,70}.

The microfilaments are the smallest of the three cytoskeletal components consisting of filamentous actin (F-actin) fibres with diameters approximately 5-7 nm, the actin cytoskeleton is highly organised within the endothelium and each fibre is structured as an asymmetrical double helix⁷¹. Vimentin and keratin are the predominant intermediate filaments expressed in endothelial cells, these filaments have diameters approximately 10 nm and act to support the structure and shape of the endothelial cells⁷²⁻⁷⁴. Microtubules are the largest cytoskeletal component with diameters approximately 25 nm, these filaments exist as hollow tubes generated from 13 protofilaments assembled from heterodimers of α and β globular tubulin peptides⁷³. The three primary cytoskeletal components self-assemble into an interconnected filamentous network associated with motor proteins in the endothelial cytoplasm, generating and distributing tensional forces which co-ordinate essential cellular processes of motility, trafficking organelles and vesicles and cell division^{73,75,76}.

1.3.2. Actin dynamics

Polymerisation of F-actin fibres from globular actin (G-actin) monomers occurs in three stages, the polymerisation process begins from nucleation in which a stable trimer of G-actin monomers is produced, as shown in figure 1.4. The second stage is the elongation phase which causes rapid assembly of the actin filaments through the addition of G-actin monomers at the barbed or plus end of the fibre⁷⁶. ATP bound in the centre of the G-actin monomers is hydrolysed to ADP upon attachment to the F-actin fibre⁷¹. The third stage is known as the steady state phase in which actin filament treadmilling stably maintains the length of the F-actin fibres. In this stage, G-actin monomers are added to the barbed end of the actin fibres at the same rate as

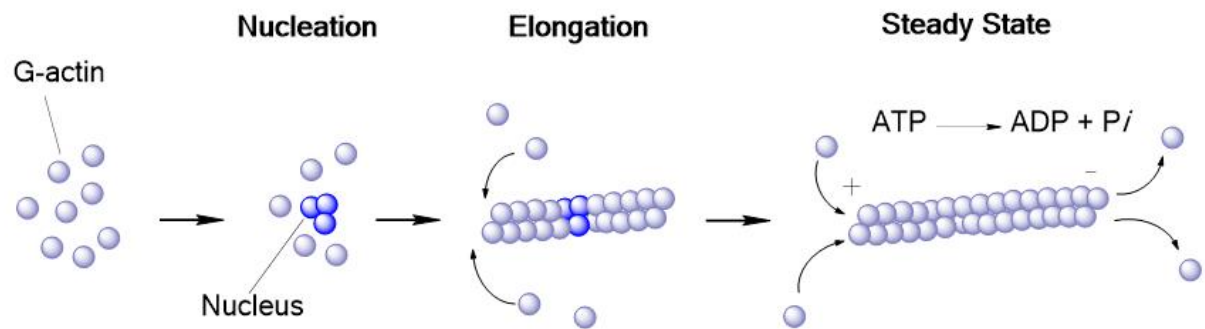


Figure 1.4 Filamentous actin polymerisation

Three globular actin (G-actin) monomers combine to form a nucleus in nucleation, which activates the elongation process in which G-actin monomers bind together to form long fibres known as filamentous actin (F-actin), the elongation process extends the length of the fibre. Actin treadmilling maintains the lengths of the F-actin fibres, as G-actin assembles at the + end and G-actin monomers disassemble at the – end. Upon binding of the monomers, ATP is hydrolysed causing an increase in energy and G-monomer dissociate with ADP bound.

the release of the monomers at the pointed or negative end, generating a polarised actin fibre⁷⁷.

The rate of F-actin polymerisation and remodelling of the actin organisation is regulated through associations with actin binding proteins (ABPs). The ABP profilin promotes actin polymerisation by binding to monomeric actin and driving the exchange of ADP to ATP⁷⁸. Conversely, the ABP cofilin promotes disassembly of G-actin monomers at the pointed end of the fibre and remains bound to the monomers preventing further polymerisation reactions^{73,78}. ABPs that promote F-actin assembly are known as nucleating proteins, of which actin related protein 2/3 complex (Arp2/3) is responsible for crosslinking F-actin fibres and branching fibres by 70°, whereas formin nucleates unbranched filaments^{76,79}.

In quiescent endothelial cells, the actin network is organised as a web of polymeric semi-flexible fibres crosslinked by Arp2/3^{76,80}. A cortical actin rim is situated below the plasma membrane with the ends of the F-actin fibres bound to vinculin, which is a member of large dynamic protein assemblies known as focal adhesion complexes at the cell periphery^{71,81,82}. The focal adhesion complexes consist of transmembrane integrin receptors, which connect actin cytoskeleton with the surrounding extracellular matrix enabling the cell to adhere to a substrate⁸¹. Additionally, the actin cytoskeleton can be organised into actin bundles or stress fibres. These stress fibres exist as tightly packed polarised filaments which are activated by MLCK and generate contractile forces by associating with myosin II and α -actinin, to direct cell migration and proliferation^{71,82}.

In response to a stimulant such as VEGF or basic fibroblast growth factor (bFGF), endothelial cells undergo directed cell migration which is reliant on remodelling the actin cytoskeleton. The Rho family of small GTPases including Rac1, RhoA and Cdc42 are critical regulators of facilitating actin rearrangement for motility⁸³. Cdc42 regulates filopodia formation through association with Wiskott–Aldrich syndrome protein (WASP) and Arp2/3¹⁵. Filopodia are long cytoplasmic projections on the leading edge of the cell which contain tight bundles of parallel F-actin fibres and many receptors to sense the local microenvironment for guidance cues¹⁵. Through activation by p-21 activated kinase (PAK), Rac1 co-ordinates lamellipodia formation which involves rapid polymerisation of actin and actin crosslinking by Arp 2/3¹⁵. RhoA mediates the formation of actin stress fibres, whereby 10-30 F-actin fibres are linked by α -actinin, fascin, espin and filamin; via activation of Rho associated kinase (ROCK) to create thick bundles of actin^{81,84-86}.

Actomyosin contractility regulates cellular morphology and motility, therefore the efficient function of the actin cytoskeleton with continual turnover of signalling molecules and focal adhesion proteins is critical for endothelial cells to extend into tubular structures^{6,87}. An increase in actomyosin contractility has been detected upon endothelial tubule formation *in vitro*⁸⁸. This enhancement of actomyosin contractility is driven by an increase in myosin light chain (MLC) phosphorylation mediated by ROCK⁸⁹. The increase in contractility is likely to ensure endothelial junctional integrity and reduce vascular permeability⁷¹. Vascular endothelial cells constantly experience shear stress *in vivo* which induces mechanosignal transduction pathways which in turn organises the cytoskeleton and ensures that actin stress fibres are arranged parallel to the direction of blood flow in areas of high shear stress^{90,91}.

1.3.3. Visualising the actin cytoskeleton

The organisation and function of the actin cytoskeleton can be studied in fixed or live endothelial cells using a variety of different approaches. Visualising the actin cytoskeleton often involves the use of fluorescently labelled phalloidin or actin specific antibodies, since these techniques can disrupt actin function by preventing depolymerisation of the F-actin fibres they are better suited and used to image the actin cytoskeleton in fixed cells^{73,92}. Fluorescent conjugates of the toxin phalloidin are able to bind with high affinity to single F-actin fibres, enabling visualisation and quantitation of the amount of F-actin fibres present in the cells⁹³.

Visualising the actin organisation in live cells can be achieved by performing microinjection of fluorescently labelled actin or carrying out cellular transfections to introduce and express fluorescently labelled actin within cells. Using this approach of binding large globular fusion proteins directly to actin can adversely affect actin function through the interference and attachment of such large proteins to the fibres⁹⁴. Alternatively, the lifeact peptide is able to bind to individual F-actin fibres without compromising the function of the actin cytoskeleton, the lifeact peptide is currently the smallest known peptide consisting of 17 amino acids that is able to bind to F-actin⁹⁵. When the lifeact peptide is conjugated to fluorescent proteins and expressed in eukaryotic cells, the actin cytoskeleton can be visualised using fluorescent live cell microscopy techniques⁹⁵.

1.4. Models of angiogenesis

1.4.1. Overview

During angiogenesis, endothelial cells must undergo invasion, migration, proliferation and differentiation to form three dimensional tubular structures which undergo lumenogenesis, whilst interacting with surrounding cells and extracellular matrix (ECM) components⁶. There are many *in vitro*, *ex vivo* and *in vivo* assays which model the different aspects of the angiogenic process, a combination of multiple assays are typically used to identify compounds that modulate angiogenesis.

1.4.2. *In vitro* assays

1.4.2.1. Cellular viability assays

Cellular viability assays are used to evaluate the cytotoxic effects of compounds at selected concentrations. The assay assesses mitochondrial activity and although it produces a readout which should correlate with the number of viable cells, this assay can give erroneous results if cellular treatments being examined perturbs mitochondrial function. Cell viability assays often use tetrazolium salt reduction, resazurin reduction, protease markers, ATP detection or flow cytometry for identification purposes⁹⁶.

The 3-(4,5-dimethylthiazol-2-yl)-2,5-diphenyltetrazolium bromide (MTT) assay uses a metabolic tetrazolium salt reduction reaction to assess cell viability. The tetrazolium salt is cleaved by lactate dehydrogenase enzymes in mitochondria of viable cells and the formation of the formazan salt can be detected at 540 nm using spectrophotometry techniques⁹⁷. Other tetrazolium salts can also be used in the MTT assay such as 3'-[1-[(phenylamino)-carbonyl]-3,4-tetrazolium]-bis(4-methoxy-6-

nitro)benzene-sulfonic acid hydrate (XTT), 3-(4,5-dimethylthiazol-2-yl)-5-(3-carboxymethoxyphenyl)-2-(4-sulfophenyl)-2H-tetrazolium (MTS) or 4-[3-(4-iodophenyl)-2-(4-nitrophenyl)-2H-5-tetrazolio]-1,3-benzene disulfonate (WST-1)⁹⁸⁻¹⁰⁰.

1.4.2.2. Cellular migration

Upon angiogenic stimulation, endothelial cells undergo a migratory response by firstly degrading the surrounding ECM to allow for endothelial invasion into the perivascular region⁶. Several *in vitro* angiogenesis assays can be utilised to evaluate the migratory response induced by angiogenic factors, these include the Boyden chamber or transfilter assay, the teflon fence assay, phagokinetic track assay and the scratch wound assay¹⁰¹.

In the scratch wound assay, a selected area of adhered endothelial cells is removed using a scraping tool from a confluent monolayer of cells. The cells at the edge of the scratch initiate directed migration to reform the monolayer due to stimulation from the release of cellular content from the damaged cells and the loss of cellular contact¹⁰². The rate of endothelial migration into the scratch area can be monitored using time lapse microscopy and imaging is usually performed using optical microscopy techniques such as phase contrast microscopy¹⁰³. The rate of endothelial migration is determined by taking successive images of the same field of view usually over a 12 hr time period and measuring the distance of cell migration into the scratch area using image analysis packages such as ImagePro Premier, Metamorph or ImageJ^{104,105}. As well as determining the effect of compounds on the migratory response, this assay has been used to study the rearrangement of the cytoskeleton during migration as well as the role of specific genes and proteins including the Rho family GTPases^{103,106-109}.

1.4.2.3. Endothelial sprouting

The hanging drop spheroid angiogenesis assay is an *in vitro* angiogenesis assay that can be used to study endothelial invasion, migration and proliferation and is also commonly used to mimic tumour angiogenesis¹¹⁰⁻¹¹³. In this three dimensional assay, endothelial sprouts are rapidly produced as outgrowths from a multicellular endothelial mass known as a spheroid, once the spheroid has been embedded into an ECM component such as collagen. The end-point of the assay can be captured using optical light microscopy, which produces two dimensional images of a three dimensional spherical object. However, imaging the assay in this way can produce low contrast images of the endothelial sprouts due to light transmittance through the thin endothelial cells, contrasted by the densely packed multicellular spheroid which has greater light absorbance. Upon firstly reporting the protocol for this assay, Korff and Augustin recommended two approaches for analysing the spheroids; the first approach suggested was to measure the three longest endothelial sprouts for ten spheroids per experimental condition¹¹⁴. The second approach was to calculate a cumulative sprouting length by measuring the lengths of all sprouts per spheroid¹¹⁴. This particular analysis approach is currently widely used alongside the use of microscopy and image analysis software such as the DP-Soft Olympus imaging system to aid quantification of the endothelial sprouts¹¹⁵⁻¹¹⁸. An alternative approach for analysing the endothelial sprouting images includes determining the area occupied by the endothelial outgrowth¹¹⁹.

Similar to *ex vivo* assays which require quantification of vessel outgrowths from the implanted or embedded tissue, endothelial sprouts can develop as tight clusters with multiple branching points connected to other sprouts, which can be challenging to

quantify manually. To overcome this problem, fluorescence labelling of cellular components such as the nuclei using Hoechst dye enable computer assisted quantification of the number of cells forming outgrowths¹²⁰. To further enhance image contrast in the spheroid assay, fluorescent labelling of the endothelial cells can be performed to enable imaging using higher resolution fluorescence microscopy, Chung *et al.* used Calcein AM dye to specifically label viable cells green¹²¹.

1.4.2.4. Matrigel tube formation assay

Tubulogenesis assays represent the final stages of the angiogenic pathway involving cellular differentiation, morphological extension into tubular structures and lumenogenesis mimics the growth of smaller blood vessels such as the capillaries¹²²⁻¹²⁴. Tube formation assays are dependent on the presence of ECM components surrounding the endothelial cells which promotes endothelial extension into three dimensional tubular structures^{125,126}.

Two dimensional tube formation assays involve plating endothelial cells directly on top of ECM components such as fibrin, collagen or onto matrigel which is the naturally derived basement membrane extract which is a protein rich mixture secreted by Engelbreth–Holm–Swarm (EHS) tumour cells¹²⁷. Endothelial cells undergo attachment and rapidly differentiate to produce tubular networks within 3 hrs of being plated, the formation of tubules can be easily assessed for the lengths, number, junctions and end points using computerised software¹²⁷⁻¹²⁹.

1.4.2.5. Co-culture tube formation assay

The co-culture tube formation assay is another tube formation assay, first outlined by Bishop *et al.* in 1999 it involves culturing endothelial cells with connective stromal

cells of fibroblasts or smooth muscle cells for a period of 6 -14 days to stimulate the formation of three dimensional endothelial tubules that mimic capillary growth¹³⁰. The endothelial cells are plated directly on top of the stromal cells which closely mimics the environment of *in vivo* endothelial cells, whereby the endothelial cells would be in contact with the blood or media and are able to interact with different cell types¹³¹. In the co-culture tube formation assay using fibroblasts, the fibroblasts secrete ECM components which act as a physical scaffold for the endothelial cells thereby influencing the development of tubular morphology¹³². Key ECM components secreted by fibroblasts include collagen I, IV, VI, fibronectin, tenascin-C and decorin, and endothelial cells use integrin mediated signalling to ensure stable adhesion and subsequent elongation into tubules, such as $\alpha_1\beta_3$ integrin signalling to bind to collagen IV^{22,133}. Importantly, the fibroblasts must also secrete pro-angiogenic factors such as VEGF to promote endothelial migration, fibroblasts secrete VEGF in response to being stimulated by bFGF which is supplied in the co-culture media^{134,135}.

Tubulogenesis assays have been used to study factors which influence and regulate the process of lumenogenesis. Lumen formation was firstly imaged in the co-culture tube formation assay in 1999 using transmission electron microscopy¹³⁰. Since this time, *in vitro* endothelial lumenogenesis has been frequently studied using fluorescence microscopy, lumen formation can be identified within endothelial tubules formed via the co-culture tube formation assay by staining for the glycoprotein podocalyxin, a member of the CD34-sialomucins which localises to the apical cell surface within endothelial tubules undergoing lumenogenesis^{25,26}. Signalling by the Rac1 guanine nucleotide exchange factor (GEF) dedicator of cytokinesis 4 (DOCK4)

has been proven to be necessary for lumen formation through rearrangement of the endothelial cytoskeleton in tubules developed in the co-culture tube formation assay²⁶.

To visualise the formation of endothelial tubular networks, endothelial cells can be fluorescently labelled prior to use in the tube formation assay or visualised using immunofluorescence with specific antibodies which target endothelial cells¹³⁶. Immunostaining can also be used to image tubular networks, the endothelial specific glycoprotein CD31 can be targeted with a primary antibody, followed by a secondary antibody conjugated to alkaline phosphatase. The addition of the alkaline phosphatase substrate 5-bromo-4-chloro-3-indolyl phosphate/nitro blue tetrazolium (BCIP/NBT) enables visualisation of the endothelial tubules, which can be imaged with optical microscopy¹³⁰. Specifically designed computer software packages such as AngioSys and Wimasis WimTube, which are both commercially available, can be used to analyse tubular network images. These analysis tools require high contrast images therefore post-processing image operations may be required to enhance visualisation of the tubular network against the image background. Post-processing operations can be performed using tools in the Image Processing Tool Kit in Adobe Photoshop CS2¹³⁷. These image processing operations include binarisation to clearly identify the tubules in the image, removing image artefacts and noise pixels using Gaussian blurring, filling holes and enhancing the contrast and brightness of the image¹³⁷.

To analyse the tubular networks, AngioSys and Wimasis perform a series of processing operations on the tubular image to identify the numbers, lengths, tubular junctions and end-points. The main image processing operations include

thresholding which identifies the tubules within the image based on the pixel intensity values and skeletonisation which reduces all of the tubules to one pixel in diameter which can be rapidly analysed for the desired measurements. The analysis data generated by these two analysis tools can be saved as a CSV file which can be exported to Microsoft Excel for further quantification.

Another tubular analysis tool is Leica QWin software, this software has been designed to process biological images and provide quantification. Guidolin *et al.* published a series of steps that could be performed using this software to analyse phase contrast tubular images, which included using an edge detection filter to identify the tubules, prior to thresholding and skeletonisation¹³⁸. Another approach to analyse vascular images is to use plugins downloaded to the public domain Java-based NIH ImageJ image processing program. The Angiogenesis Analyzer plugin can be used to analyse meshed cellular networks and can be applied to phase contrast tubular images as well as fluorescently labelled tubular images¹⁴⁰. The plugin analyses the tubular network by skeletonising the network and the user can define the outputs for loops, nodes, branches and extremities, producing quantification on a wide number of image parameters¹³⁹.

1.4.3. *In vivo* models of angiogenesis

1.4.3.1. Zebrafish overview

Danio rerio, known as zebrafish are tropical freshwater teleost fish which during embryogenesis serve as an *in vivo* vertebrate model for studying angiogenesis. Zebrafish reproduce by external fertilisation, producing 100-200 transparent embryos per breeding pair¹⁴⁰. At two days post-fertilisation (dpf) all internal organs of the

zebrafish have formed and at five dpf the larvae hatch and are able to swim to locate food, this rapid development and optical properties of the embryos lends itself to cardiovascular imaging, silencing genes and testing compounds that affect vasculogenesis and angiogenesis¹⁴¹⁻¹⁴³. The zebrafish genome has been well characterised through the use of forward and reverse genetics which has identified vascular related genes with functional orthologues in humans; however, a whole genome duplication event occurred in the teleost lineage upon divergence from the telepod lineage, this caused gene redundancy which can be a limitation when studying this organism¹⁴⁴.

During embryogenesis oxygen diffuses into the developing zebrafish which allows the embryo to develop externally¹⁴⁵. Passive diffusion of compounds from the surrounding embryonic media into the organism can be utilised to investigate the effects on vascular and embryonic development. Furthermore, embryonic gene expression can be easily modified through injection of phosphorodiamidate oligonucleotide morpholino oligomers (MOs) into the centre of the yolk at the one cell stage of development¹⁴⁶. The MOs consist of around 25 nucleobases connected via a non-ionic phosphorodiamidate backbone with 6-membered methylenemorpholine rings¹⁴⁷. Complementary base pairing of the morpholino bases to the targeted ribonucleic acid (RNA) prevents expression of the gene of interest¹⁴⁷. There are two types of oligonucleotide morpholino that can be used to silence genes in zebrafish: those that target and block the process of protein translation by targeting the 5' untranslated region (UTR) of messenger RNA (mRNA) which is situated upstream of the start codon thus preventing the ribosome from binding and producing the target protein¹⁴⁸. The second type of oligonucleotide morpholino interferes with the splicing

process and prevents the spliceosome from binding to the target region; therefore MO injection causes steric blocking of the ribosome or spliceosome¹⁴⁹. To determine the localisation of gene expression within zebrafish, *in situ* hybridisation can be performed on the organism as a whole¹⁵⁰.

1.4.3.2. The development of the vasculature in zebrafish

The rapid embryonic development of zebrafish occurs in seven stages: zygote, cleavage, blastula, gastrula, segmentation, pharyngula and hatching¹⁵¹, the developmental processes that occur at each stage are outlined in table 1.1. The differentiation of blood cells occurs within the segmentation stage of development and the flow of blood is established in the later pharyngula stage¹⁵¹. During development, the multipotent haematopoietic stem cells migrate medially from the lateral mesoderm to form the intermediate cell mass (ICM), these cells differentiate into haematopoietic or endothelial cells during the formation of the yolk sac blood islands^{152,153}. *In situ* hybridisation has shown that the expression of the ETS domain transcription factor *friend leukemia integration 1 (fli1)* initially overlaps *GATA binding protein 2 (gata2)* expression in the lateral mesoderm of zebrafish embryos, prior to divergence of the expression patterns, leading to *fli1* specifically expressed in the developing vasculature and *gata2* in regions of blood formation¹⁵⁴. Investigation into the *cloche* zebrafish mutant revealed that the expression pattern of *fli1* is one of the earliest genetic markers for angioblast production¹⁵⁴. *Fli1* gene expression is utilised in the transgenic *Fli1:eGFP^{y1}* (*fli1*-GFP) line of zebrafish generated by Lawson and Weinstein; these fish express EGFP throughout the vasculature endothelium enabling the development and growth of new blood vessels throughout embryogenesis to be easily visualised¹⁵⁵. Other approaches to image the zebrafish

Table 1.1 Stages of embryonic zebrafish development

Description of the embryonic developmental changes of zebrafish through each of the seven stages of development to adult fish, the table was adapted from Kimmel *et al.* (1995)¹⁵¹.

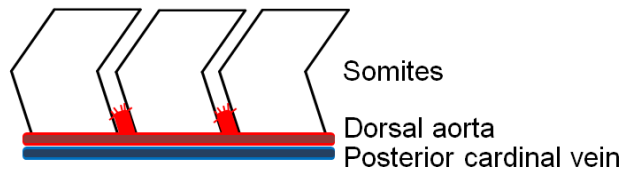
Stage of embryonic development	Time in hours post fertilisation (hpf)	Description of development
Zygote	0 - 0.75	The fertilised egg completes the first zygotic cell cycle
Cleavage	0.75 – 2.15	2 – 7 cell divisions occur synchronously
Blastula	2.15 – 5.15	2 more metasynchronous rounds of cell division, midblastula transition, epiboly begins
Gastrula	5.15 – 10	Morphogenetic movements of involution, convergence and extension form the epiblast, hypoblast and embryonic axis
Segmentation	10 – 24	Development of somites, blood cells differentiate, pharyngeal arch primordia and neuromeres, organogenesis starts, tail forms
Pharyngula	24 – 48	Body axis straightens from its early curvature around the yolk sac, pigmentation, blood flow initiated, fins form
Hatching	48 - 72	Completion of primary organ systems, cartilage development in head, pectoral fin develops, hatching occurs
Early larvae	72	Inflation of swim bladder, food-seeking and active avoidance behaviour

vasculature include dye injection or alkaline phosphatase staining; however these techniques require fixation of the tissue therefore only a particular time point or end-point of vascular development can be imaged¹³³.

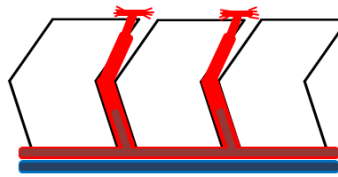
The development of the zebrafish vasculature is initiated by angioblast migration to the embryonic midline from the lateral plate mesoderm, this gives rise to the first axial blood vessels of the zebrafish, the dorsal aorta (DA) and posterior cardinal vein (PCV)^{28,156}. Angioblast differentiation into endothelial cells is co-ordinated initially by sonic hedgehog signalling, which induces VEGF signalling; this co-ordinated signalling promotes delta-like-4 (Dll4) expression in endothelial tip cells causing an initiation in endothelial spouting from the DA and promotes notch signalling in adjacent endothelial cells which decreases their sprouting behaviour¹⁵⁵.

VEGF and notch signalling tightly regulates the expression of ephrin B2 (EfnB2) in arterial angioblasts, whilst venous angioblasts express ephrin B4 (EfnB4) promoting ventral migration of these cells¹⁵⁶. Repulsive signalling between EfnB2 and EfnB4 controls the directional endothelial sprouting of these cells during the establishment of arterial and ventral vessels¹⁵⁶. At approximately 17 hpf, the arterial and venous angioblasts differentiate into endothelial cells of arteries and veins and cellular junctions between the cells of these blood vessels are established, along with the presence of adherens junctions²⁸. The first angiogenic vessels to form in the zebrafish are the ISVs at 24 hpf¹⁴⁵. The formation of ISVs is stimulated by VEGFA signalling as activated endothelial cells sprout bilaterally from the DA; each tip cell extends filopodia to direct the vessel growth along the somite boundary and the stalk cells located behind the tip cell proliferate to extend the vessel length to 4-6 endothelial cells per ISV²⁹. As the ISVs approach the neural tube they separate into

24 hpf



30-40 hpf



48 hpf

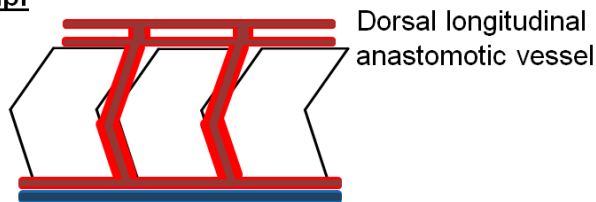


Figure 1.5 The formation of the intersegmental blood vessels in zebrafish

At 24 hpf, the endothelial cells begin to sprout from the dorsal aorta and the tip cells extend filopodia to undergo pathfinding to direct the growth of the intersegmental blood vessels (ISVs). At 30-40 hpf, the ISVs branch to form T junctions and VE-cadherin becomes expressed at the cellular junctions and lumen formation also begins at the ISVs. At 48 hpf, filopodia formation is inhibited and the dorsal longitudinal anastomatic vessel forms to connect the ISVs. There is continuous blood flow formation through complete lumenalisation in the ISVs. Figure was adapted from Leslie *et al.* (2007)¹⁶⁰.

rostral and caudal branches and connect to form the dorsal longitudinal anastomotic vessel (DLAV), establishing the primary vessel network within the organism¹⁵⁷, shown in figure 1.5. The mechanism of lumen formation in the ISVs has been widely debated^{18,29}. At around 32 hpf, further angiogenic sprouting occurs from the PCV to produce the intersegmental veins and incorporate the lymphatic system, at 48 hpf a fully connected and elaborate vascular network is formed¹⁵⁷⁻¹⁵⁹.

The relatively transparent nature of the zebrafish embryo offers great benefits from an imaging perspective when studying the zebrafish vascular system¹⁴¹. High image contrast can be achieved using the *fli1*-GFP zebrafish between the fluorescent endothelium and the surrounding tissues of the organism by treatment with 1-phenyl 2-thiourea (PTU), which can be added into media surrounding the embryos to prevent tyrosinase activity which would cause pigment formation from melanophores during melanogenesis¹⁶¹.

1.4.3.3. Analysis of the zebrafish vasculature

Fluorescence microscopy can be used to image the developing vascular system of *fli1*-GFP zebrafish and to assess vascular development the ISVs are frequently specifically targeted for analysis as these are the first angiogenic vessels to form¹⁴⁵. Other real-time imaging methods used to study the vascular system include the use of laser polarised gases, which dissolve into the blood for magnetic resonance imaging and confocal microangiography, which are used in particular to study small vessels less than 100 μm in diameter^{162,163}.

A frequently used approach to analyse the ISVs is to manually classify the ISV growth into categories based on the appearance of vascular disruption, such as

'mild', 'intermediate' or 'severe' disruption¹⁶⁴⁻¹⁶⁷ or this assessment is alternatively represented by the number of ISVs that have connected or remain disconnected to the DLAV in the trunk and tail regions of the zebrafish¹⁶⁸⁻¹⁷⁷. As with other vascular images, semi-automated analysis methods using ImageJ or microscopy software such as the Nikon Imaging Software (NIS) Elements can be employed to aid the measurement calculations for the lengths of the ISVs¹⁷⁸.

As stated by Vogt *et al.* there is a lack of computer assisted analysis tools that can be applied directly to zebrafish vascular images and this often prevents this vertebrate model being used in high throughput screening studies¹⁷⁹. This group created an automated image-based phenotypic analysis tool, whereby the ISVs of zebrafish can be quantified using Cognitive Network Technology when imaged using a high content reader¹⁷⁹. A considerable advantage of this analysis method is its capability of analysing embryos in various orientations. Another computer based method reported by Tran *et al.* which analyses the ISVs involves implementing a quantitative screening approach using an interactive algorithm created using Discovery-1/MetaMorph software and the MetaMorph Neurite Outgrowth application drop in; this method requires manual identification of the vessels of interest¹⁸⁰. An alternative method to analyse endothelial cell sprouting from the DA includes the use of image registration methods to measure the incremental increase in the vessel lengths with time, this method focuses on the ability of the endothelial cells to initiate angiogenesis and therefore analysis of vessel connectivity is not required^{181,182}. In addition to providing quantitation, many of the analysis frameworks often give excellent visual representations of the vasculature such as representing the connecting vasculature as attributed vessel represent graphs (AVRG)¹⁸³.

1.4.3.4. Genes studied using the zebrafish model

In this project, a computational method was developed as an analysis tool to enable rapid quantification of the developed vasculature within zebrafish embryos. To test and evaluate the computational method, the analysis approach was applied to fluorescent zebrafish images which exhibited both normal and abnormal ISV formation. To achieve a range of vascular abnormalities the following genes were silenced at the one-cell stage during zebrafish embryogenesis by MO injection: C-type lectin domain family 14, member A (CLEC14A), endothelial cell-specific chemotaxis regulator (ECSCR), epidermal growth factor, latrophilin and seven transmembrane domain-containing protein 1 on chromosome 1 (ELTD1), roundabout4 (ROBO4), vascular endothelial growth factor A (VEGF), regulator of calcineurin 1 (RCAN), ets-1 related protein (ETSRP) and ets related gene (ERG).

1.4.3.4.1 Vascular endothelial growth factor A (VEGF)

VEGF has been identified to be one of the most potent angiogenic factors and is fundamental throughout embryogenesis to generate a functional vascular system; the different VEGF isoforms generated by alternative splicing regulates blood vessel development through binding to the tyrosine kinase receptor VEGFR2 present on endothelial cell surfaces to induce migration and proliferation^{1,184-188}. In mice, disruption of a single VEGF allele causes embryonic lethality between days 11-12¹⁸⁸.

1.4.3.4.2 C-type lectin domain family 14, member A (CLEC14A)

CLEC14A is a tumour endothelial marker (TEM) that has been found to be expressed highly on tumour vasculature compared with normal tissue¹⁸⁹; this C-type lectin was first identified as a TEM by Mura *et al.* in 2012. CLEC14A promotes and regulates angiogenesis by stimulating filopodia formation, endothelial migration and tube

formation¹⁸⁹. Mura *et al.* showed that CLEC14A is initially expressed in the zebrafish at 12 hpf and it is specifically expressed within the DA, PCV and ISVs¹⁸⁹.

1.4.3.4.3 Endothelial cell-specific chemotaxis regulator (ECSCR)

Vascular endothelial cells specifically express ECSCR as a cell surface glycosylated type I transmembrane protein, which regulates endothelial cell survival and chemotaxis¹⁹⁰. Verma *et al.* showed by real-time polymerase chain reaction (PCR) that *ecscr* expression in zebrafish rapidly increases between 10 and 24 hpf, this correlates with the formation of the axial blood vessels and angioblast migration within the embryo¹⁶⁶.

1.4.3.4.4 Epidermal growth factor, latrophilin and seven transmembrane domain-containing protein 1 on chromosome 1 (ELTD1)

ELTD1 is an orphan adhesion G-protein coupled receptor¹⁹¹. It has been reported by that ELTD1 is a regulator of angiogenesis which is upregulated within tumour endothelial cells and silencing the receptor in zebrafish embryos causes impaired vessel formation and sprouting¹⁹¹.

1.4.3.4.5 Roundabout 4 (ROBO4)

Roundabout (*robo*) receptors were initially identified as co-ordinators of axon guidance in neurons and repulsive signalling is mediated by the binding of slit protein ligands to the receptors¹⁹². De Smet *et al.* reported that ROBO4 expression is a requirement for the stabilisation of stalk cells during the angiogenic process¹⁵. ROBO4 is the predominant roundabout receptor that is expressed in the vasculature of zebrafish and it is expressed within angioblasts, in the DA, PCV and ISVs¹⁹³. Bedell *et al.* showed that the injection of the ROBO4 targeted morpholino caused

misdirected and truncated ISVs and therefore concluded that ROBO4 was essential for directed sprouting of the ISVs¹⁹³.

1.4.3.4.6 Regulator of calcineurin 1 (RCAN)

RCAN was identified by Fuentes *et al.* in 2000 using the yeast and mammalian two-hybrid assays to be a binding protein of calcineurin 1, which is a calmodulin binding protein and a serine/threonine protein phosphatase^{194,195}. Two RCAN isoforms exist; one has the inclusion of exon 1 (RCAN1.1) and the other exon 4 (RCAN1.4), the expression of RCAN1.4 is regulated by VEGF and has been shown to be important in regulating endothelial migration and upon knock down of RCAN1.4 endothelial cells become defective in undergoing tubular morphologies¹⁹⁵⁻¹⁹⁷.

1.4.3.4.7 Ets-1 related protein (ETSRP) and ets related gene (ERG)

Members of the ets transcription factor family play vital roles in embryonic development including vasculogenesis and angiogenesis, two of these transcription family members are ETSRP and ERG. ETSRP is firstly expressed at the two somite stage in zebrafish embryos correlating with the expression in angioblasts¹⁹⁸. *Erg* is closely related and highly homologous to *fli1* and zebrafish have only one gene responsible for the expression of ERG in the mesoderm during embryonic development^{168,199}. Knocking down ETSRP has shown to cause defects in vascular development, whereas apparent normal vasculature was observed upon ERG silencing^{168,198}. Interestingly, Ellett *et al.* reported a synergic functional interaction between ERG and ETSRP and therefore a double knock down to silence both ERG and ETSRP in zebrafish should reduce ISV development compared with silencing ETSRP alone¹⁶⁸.

1.5. Imaging and analysing assays modelling angiogenesis

1.5.1. Overview

Imaging and analysis techniques are essential to our understanding of the molecular, cellular and functional processes within the angiogenic pathway. Being able to identify and assess factors such as the location, quantity, morphology and permeability of the vasculature, along with identifying the presence of specific vascular markers and determining the effect of compounds on angiogenesis, can only be evaluated upon the correct use of high resolution imaging modalities and appropriate analysis techniques. To analyse endothelial processes and vascularisation from *in vitro*, *ex vivo* and *in vivo* angiogenic images, quantification of endothelial migration, proliferation, sprouting or the global tubular network is usually assessed.

1.5.2. Microscopy techniques

1.5.2.1. Optical light microscopy

An imaging modality widely used to study biological specimens is the transmitted or bright-field light microscope, which is able to image different types of samples due to the focussing ability of the long working distance objective lens²⁰⁰. In the brightfield imaging system, transillumination light is passed through a condenser lens to focus the light rays onto the specimen, light passes through the specimen to the objective lens and a magnified image is observed through an eye-piece or as a digital image via a charged couple device (CCD)²⁰¹. This imaging set-up allows for fast image acquisition and different biological components within the specimen absorb varying amounts of light; this generates image contrast allowing visualisation of different

components within the specimen. A similar imaging system is used for phase contrast microscopy which produces an image dependent on the proportion of light interference from the biological specimen.

Optical light microscopy techniques can allow for endothelial or vascular morphologies to be investigated however, thin biological specimens such as endothelial cells absorb only small amounts of light which generates low contrast images; this can produce undefined object boundaries within the image which can be problematic for analysis procedures. For accurate analysis, clear distinctions between the object of interest, background and other biological components are required; this is of particular importance for computer assisted analysis methods. In optical light microscopy this problem is coupled with low optical imaging resolution. Low resolution arises because there is overall illumination of the three dimensional specimen, therefore out of focus light contributes to image blurring. To reduce this problem, cells or proteins within the specimen can be labelled or stained to enhance the signal.

1.5.2.2. Fluorescence microscopy

Fluorescence microscopy is an optical microscopy technique and therefore the principle set up of image acquisition is similar to that of the brightfield imaging system, however the light source is selected at a specific wavelength to excite fluorophores from within the specimen known as the excitation wavelength. Fluorophores are chemical compounds that emit light upon excitation to higher energy states. Electrons from within the fluorophores are excited to higher energy states and upon their return to their original energy state release photons of light. The emitted light is distinguished from the original excitation light using a spectral

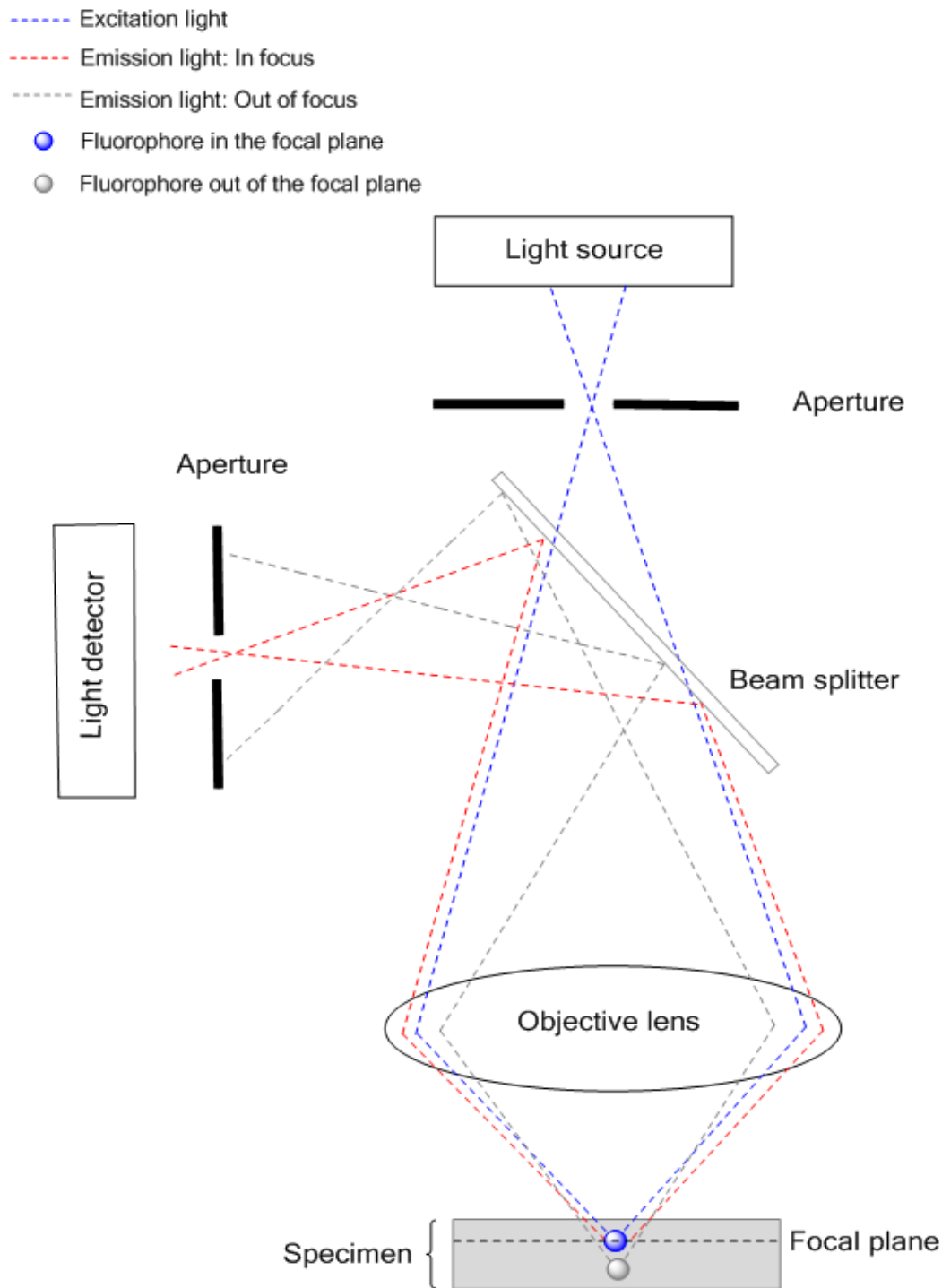


Figure 1.6 Imaging set-up of a confocal fluorescence microscope

The light paths and imaging set-up of a confocal fluorescence microscope are shown, whereby the fluorophores from within the specimen are activated by the excitation light (blue) from the light source. Light emitted from the fluorophore from within the focal plane is refracted by the objective lens (red) and with use of the beam splitter is directed to the light detector. Whereas, light emitted from fluorophores outside of the focal plane (grey) do not contribute to the image as they are excluded by the aperture.

emission filter, which along with the dichroic mirror is specifically selected dependent on the fluorophore being imaged. To generate images of specimens containing multiple fluorophores, successive images for each fluorophore must be acquired and combined after image acquisition^{202,203}. Fluorescence microscopy can be applied to fixed or live biological specimens and offers a higher signal-to-background ratio in comparison to brightfield microscopy²⁰⁴. Confocal fluorescence microscopy such as confocal laser scanning microscopy (CLSM) or confocal spinning disk microscopy (CSDM) offer significant imaging advantages over conventional epifluorescence microscopy, as the presence of an aperture excludes out-of-focus light which is emitted from fluorophores which are not present in the imaging focal plane, as shown in the confocal microscopy diagram in figure 1.6. Out-of-focus light can contribute to high background fluorescence resulting in a low image resolution; only light emitted from fluorophores from within the focal plane of the specimen is detected in confocal microscopy^{205,206}. To further enhance imaging resolution, a series of single images from sequential focal planes can be captured at regular intervals along the z axis using confocal microscopy, known as optically sectioning the specimen. The images can be combined by compression to give a higher resolution maximum projection image of the specimen by improving the signal-to-noise ratio^{207,208}.

Fluorescence microscopy has proved to be a useful imaging tool for studying and understanding the molecular and functional aspects of angiogenesis. Using fluorescence microscopy techniques has enabled dynamic tracking of proteins and identification of protein and cellular interactions; use of fluorescent proteins has been widely used to study tumour angiogenesis and tumour progression by performing techniques such as expressing GFP in tumour vessels and RFP in tumour cells

permitting non-invasive whole body imaging in mice²⁰⁷⁻²⁰⁹. Fixing and staining angiogenic tissue samples using fluorescently tagged antibodies which target specific proteins is currently widely used in angiogenic research, as well as fluorescence vascular imaging making use of fluorescent imaging agents and carriers *in vivo*²¹⁰⁻²¹².

However, the limitations of using fluorescence microscopy to image the localisation of fluorophores include photobleaching which prevents the fluorophores producing a fluorescent signal as the electrons become permanently unable to be excited, this results in reduced spatial resolution in the acquired image^{213,214}. Fluorophores can also exhibit spectral cross-talk between excitation and emission spectra²¹⁵. Another limitation is specimen phototoxicity, when the electrons from within the fluorophores are excited they can participate in reactions involving molecular oxygen which produces reactive oxygen species (ROS); ROS adversely affects cell viability by damaging cellular proteins, lipids and nucleic acids^{216,217}.

Chapter Two

Materials and Methods

2.1 Reagents and equipment

All reagents that were used in this PhD project were of analytical or molecular biology grade standard and if not stated otherwise the reagents were purchased from Sigma-Aldrich.

For general tissue culture, a CO₂ humidified incubator (Sanyo) was used to maintain cell lines; it supplied a constant atmosphere of 5% CO₂ at 37 °C. For storing and growing zebrafish embryos, a 100 l laboratory incubator was used at 28.5 °C (Genlab).

The centrifuges that were commonly used were: for 1.5 ml eppendorf tubes: Heraeus Pico 17 Microcentrifuge (Thermo Scientific), maximum speed 17000 x g. For 15 ml – 50 ml volumes: Heraeus Biofuge Primo (Thermo Scientific), maximum speed 2576 x g.

The contents of solutions that were used are mentioned within the relevant methods sections.

2.2 Antibodies

2.2.1 Primary antibodies

Primary antibodies were used for either immunofluorescence (IF) or immunohistochemistry (IHC), the concentrations used are outlined in table 2.1.

Table 2.1 Primary antibodies

Antibody	Code	Company	Concentration
Mouse monoclonal anti-human CD31	JC70A	Dako Cytomation	1.29 µg/ml (IHC)
Goat polyclonal anti-human Podocalyxin	AF1658	R & D Systems	0.4 µg/ml (IF)
Rabbit polyclonal anti-human Collagen IV	Ab6586	Abcam	0.4 µg/ml (IF)

2.2.2 Secondary antibodies

Secondary antibodies were used for either immunofluorescence (IF) or immunohistochemistry (IHC) and the concentrations used are outlined in table 2.2.

Table 2.2 Secondary antibodies

Antibody	Code	Company	Concentration
Alexafluor 488 polyclonal donkey anti-rabbit IgG	A21206	Invitrogen	4 µg/ml (IF)
Alexafluor 488 polyclonal goat anti-mouse IgG	A11001	Invitrogen	4 µg/ml (IF)
Alexafluor 594 polyclonal goat anti-rabbit IgG	A11067	Invitrogen	4 µg/ml (IF)
Alexafluor 594 polyclonal goat anti-mouse IgG	A11020	Invitrogen	4 µg/ml (IF)
Goat polyclonal Anti-mouse IgG conjugated to Alkaline Phosphatase	A4656	Sigma	Used at 1:500 (IHC)
Rhodamine Ulex Europaeus Agglutinin I (UEA I)	RL-1062	Vector Laboratories	0.02 mg/ml (IF)

2.3 Plasmids

To enable visualisation of endothelial cells or tagged proteins using confocal microscopy, human umbilical vein endothelial cells (HUVECs) were transduced with plasmids to express the fluorescent proteins GFP or RFP. The plasmids that were used are described in table 2.3.

Table 2.3 Plasmids

Plasmid	Company	Use
psPAX2	Addgene	Lentiviral packaging plasmid
pMD2G	Addgene	Lentiviral envelope plasmid
pWPI	Addgene	Lentiviral plasmid used to express EGFP to facilitate tracking of cells
pWPXL	Addgene	Lentiviral plasmid used to express EGFP to facilitate tracking of cells
pEGFP-N1-lifeact	A gift from Dr. Steve Thomas, University of Birmingham, UK.	Contained the lifeact sequence between the EcoR1 and Age1 restriction sites in the multiple cloning site (MCS)
pWPXL-lifeact-RFP	A gift from Prof. Maddy Parsons, Kings College London, UK.	Transduced cells expressed lifeact-RFP for F-actin visualisation
pWPXL-lifeact-GFP	Produced by Victoria Salisbury, University of Birmingham, UK.	Transduced cells expressed lifeact-GFP for F-actin visualisation

2.4 Inhibitor compounds

2.4.1 Kinase inhibitor compounds

The screen-well kinase inhibitor library was supplied by Enzo Life Sciences, code: BML-2832, the library contained 80 different small molecule kinase inhibitor compounds described in table 2.4. The IC₅₀ values for the compounds were

determined from a combination of supplier's information and scientific literature, the concentration of inhibitors used in the angiogenesis assays were ten times the IC₅₀ values.

Table 2.4 Kinase inhibitor compounds

Compound	Target	IC₅₀ value
PD-98059	MEK	55 µM
U-0126	MEK	70 nM
SB-203580	P38 MAPK	500 nM
H-7·2HCl	PKA, PKG, MLCK, PKC	6 µM
H-9·HCl	PKA, PKG, MLCK, PKC	70 µM
Staurosporine	Pan-specific	0.88 nM
AG-494	EGFR, PDGFR	700 nM
AG-825	HER1-2	350 nM
Lavendustin A	EGFR	11 nM
RG-1462	EGFR	3 µM
TYRPHOSTIN 23	EGFR	35 µM
TYRPHOSTIN 25	EGFR	3 µM
TYRPHOSTIN 46	EGFR	10 µM
TYRPHOSTIN 47	EGFR	2.4 µM
TYRPHOSTIN 51	EGFR	800 nM
TYRPHOSTIN 1	Negative control	35 µM
TYRPHOSTIN AG 1288	Tyrosine kinases	21 µM
TYRPHOSTIN AG 1478	EGFR	3 nM
TYRPHOSTIN AG 1295	Tyrosine kinases	2.5 µM
TYRPHOSTIN 9	PDGFR	500 nM
Hydroxy-2-naphthalenylmethylphosphonic acid (Methylphosphonic acid)	IRK	100 µM
PKC-412	PKC	50 nM
Piceatannol	Syk	10 µM
PP1	Src family	170 nM
AG-490	JAK-2	5 µM
AG-126	IRAK	50 µM
AG-370	PDGFR	20 µM
AG-879	NGFR	40 µM
LY 294002	PI3-K	1.4 µM
Wortmannin	PI3-K	40 nM
GF 109203X	PKC	20 nM
Hypericin	PKC	3.3 µM
Ro 31-8220 mesylate	PKC	27 nM
D-erythro-Sphingosine	PKC	3 µM
H-89·2HCl	PKA	135 nM
H-8	PKA, PKG	1.2 µM

HA-1004·2HCl	PKA, PKG	170 µM
HA-1077·2HCl	PKA, PKG	10.7 µM
2-Hydroxy-5-(2,5-dihydroxybenzylamino)benzoic acid (Benzoic acid)	EGFR, CaMK II	200 nM
KN-62	caMK II	900 nM
KN-93	caMK II	370 nM
ML-7·HCl	MLCK	700 nM
ML-9·HCl	MLCK	10 µM
2-Aminopurine	P58 PITSRE β1	341.6 µM
N9-isopropyl-olomoucine	CDK	3 µM
Olomoucine	CDK	3 µM
Iso-olomoucine	Negative control	3 µM
Roscovitine	CDK	700 nM
5-Iodotubericidin	ERK2, CK1, CK2 Adenosine kinase	10.9 µM
LFM-A13	BTK	2.5 µM
SB-202190	P38 MAPK	30 nM
PP2	Src family	100 nM
ZM 336372	cRAF	70 nM
SU 4312	Flk1	800 nM
AG-1296	PDGFR	400 nM
GW 5074	cRAF	9 nM
Palmitoyl-DL-carnitine	PKC	12.59 µM
Rottlerin	PKC delta	100 µM
Genistein	Tyrosine kinases	12 µM
Daidzein	Negative control	12 µM
Erbstatin analog	EGFR	770 nM
Quercetin·2H₂O	PI3-K	3.8 µM
SU1498	Flk1	700 nM
ZM 449829	JAK-3	20 µM
BAY 11-7082	IKK pathway	10 µM
5,6-dichloro-1-β-D-ribofuranosylbenzimidazole (Ribofuranosylbenzimidazole)	CK 2	10 µM
2,2',3,3',4,4'-Hexahydroxy-1,1'-biphenyl-6,6'-dimethanol dimethyl ether (Dimethyl ether)	PKC alpha, gamma	50 µM
SP 600125	JNK	90 nM
Indirubin	GSK-3 beta, CDK5	5 µM
Indirubin-3'-monooxime	GSK-3 beta	190 nM
Y-27632·2HCl	ROCK	3.55 µM
Kenpaullone	GSK-3 beta	230 nM
Terreic acid	BTK	10 µM
Triciribine	Akt pathway	130 nM
BML-257	Akt	27 µM
SC-514	IKK2	12 µM

BML-259	Cdk5	64 nM
Apigenin	CK-II	30 μ M
BML-265	EGFR	28.8 nM
Rapamycin	mTOR	0.1 nM

2.4.2 Other inhibitor compounds

All other inhibitor compounds that were used in the assays that model angiogenesis are described in table 2.5, along with the inhibitor concentrations that were used.

Table 2.5 Other inhibitor compounds

Compound	Target	Concentration	Company
PF-3758309	P-21 activated kinase (PAK)	1.25 - 5 μ M	Bioquote Ltd
IPA-3	P-21 activated kinase (PAK)	2.5 - 10 μ M	Tocris Bioscience
Ibrutinib	Bruton's tyrosine kinase (BTK)	5.0 nM - 15 μ M	Stratech Scientific Ltd
AVL-292	Bruton's tyrosine kinase (BTK)	50 nM	Stratech Scientific Ltd
Sunitinib	Receptor tyrosine kinases	0.1 – 1.0 μ M	Supplied by Dr. Mike Cross at the University of Liverpool, UK.

2.5 Morpholino oligonucleotides

All morpholino oligonucleotides (MOs) were purchased from Gene Tools. The RNA antisense morpholino oligonucleotide sequences were designed to block sites either involved in splicing pre-mRNA or by sterically preventing the binding of the translation initiation complex. All morpholino oligonucleotide sequences are listed in table 2.6.

Table 2.6 Zebrafish morpholino oligonucleotide sequences

Morpholino Oligonucleotide	Morpholino Oligonucleotide Sequence from 5' – 3'
VEGFA Morpholino	GTATCAAATAAACAACCAAGTTCAT
VEGFA Mismatch	GTAACAATTAAACAACCATGTTGAT
ROBO4 Morpholino	TTTTTTAGCGTACCTATGAGCAGTT
ROBO4 Mismatch	TTTTTTACCCTACGTATGACCACTT
ECSCR UTR Morpholino	GCGTAAGTCCAAATGACGTTCAATC
ECSCR UTR Mismatch	GGCAAACCTCGAAATCACCTTCAATC
ECSCR Splice Morpholino	CATCAGTAGAAAACCTACCAAAGGC
ECSCR Splice Mismatch	CATGACTACAAAACCTACGAAACGC
CLEC14 Morpholino	ACCATCAGAAATCCATGTCTGCTC
CLEC14 Mismatch	CCTCTTACCTCAGTTACAATTTATA
ELTD1 Morpholino	CATTGGAGAACTGTGTAAAACTCC
ELTD1 Mismatch	CATTGCACAACTGTCTAAATAGTCC
ERG Morpholino	CAGACGCCGTCATCTGCACGCTCAG
ETSRP Morpholino	TTGGTACATTTCCATATCTTAAAGT
ETSRP Mismatch	CAGTGAGACCTTAATTCAAGTATAAC
RCAN Morpholino	ACTTCATTGTTTTCAGGTGCATGAC
RCAN Mismatch	ACATGATTCTTTTGAGCTGCATGAC

2.6 Cell biology

2.6.1 Mammalian cell culture

HUVECs were isolated from umbilical veins of umbilical cords supplied by the tissue bank of the Human Biomaterials Resource Centre at the University of Birmingham. HUVECs were cultured in complete M199 (cM199) medium which was M199 media supplemented with 10% (v/v) foetal calf serum (FCS) (PAA Cell Culture Co.), bovine brain extract, 90 µg/ml heparin, 4 mM L-Glutamine, 100 units/ml penicillin and streptomycin (Invitrogen). HUVECs were cultured in cM199 media with the addition of antibiotics unless HUVECs were used for siRNA-mediated knock down of genes in which case HUVECs were cultured in cM199 media without antibiotics.

Human embryonic kidney 293T cells (HEK293Ts) and human dermal fibroblasts (HDFs) (PromoCell) were cultured in complete Dulbecco's Modified Eagle's Medium (cDMEM) which was DMEM supplemented with 10% (v/v) FCS (PAA Cell Culture Co.), 4 mM L-Glutamine and 100 units/ml penicillin and streptomycin (Invitrogen). All mammalian cell media was filtered using 0.22 μ m pore filter units (Millipore) and stored at 4 °C. Prior to use all mammalian cell media was pre-warmed to 37 °C for 20 mins in a water bath.

Mammalian cells were cultured using plastic plates (Falcon) and incubated at 37 °C in a humidified 5% (v/v) CO₂ atmosphere to allow cell proliferation. For plating and growing HUVECs, plates were pre-coated with 0.1% (w/v) gelatin in phosphate buffered solution (PBS) for 20 mins at 37 °C. For washing mammalian cells, 1x PBS solution was made from diluting 10x Dulbecco's PBS (Life Technologies) with distilled water (dH₂O), which was autoclaved and stored at room temperature. PBS was made up to contain 140 mM NaCl, 10 mM Na₂PO₄, 2.7 mM KCl, 1.76 mM KH₂PO₄ at pH 7.4.

2.6.2 Passaging and counting cells

For cell detachment, cultured cells were washed 3 times with PBS before being trypsinised with 0.1% (w/v) trypsin-EDTA (Life Technologies) in PBS solution. 6 ml media was added to a 10 cm plate for cell collection as the presence of FCS in the culture media inhibited trypsin activity. The cell solution was centrifuged at 195 x g for 5 mins and the cell pellet was re-suspended in media. HUVECs and HDFs were passaged 1:3 once a week and HEK293Ts 1:10 twice a week onto 10 cm plates. To

count cells, 10 μ l cell suspensions were added to a haemocytometer counting chamber (Neubauer).

2.6.3 Storing cells

For storing cells, cell pellets were resuspended in 10% (v/v) dimethyl sulfoxide (DMSO) and 90% (v/v) FCS and the cell solution was gradually frozen to -80 °C. Cells were then transferred to liquid nitrogen storage.

2.6.4 Fluorescently labelling mammalian cells

2.6.4.1 Fluorescently labelling cells with cytoplasmic dyes

To provide high resolution images of endothelial tubulogenesis and sprouting, endothelial cells were fluorescently labelled with cytoplasmic dyes such as CellTracker dyes (Invitrogen) or carboxyfluorescein succinimidyl ester (CFSE) (Life Technologies). Alternatively HUVECs were transduced to express a fluorescent protein such as GFP or RFP.

CFSE was stored as a 10 mM stock solution in DMSO, dilutions were made in PBS and cells were labelled at a final concentration of 5 μ M. Harvested HUVECs were incubated for 10 mins at 37 °C with the CFSE labelling solution. Two washing steps were performed using 5 ml of cM199 and centrifugation at 195 x g for 5 mins. Finally the labelled cells were re-suspended in 1 ml cM199. Similarly, HUVECs were labelled with CellTracker dyes using a final concentration of 10 μ M in PBS and incubated for 30 mins at 37 °C.

2.6.4.2 Lentiviral transduction of HUVECs

HEK293Ts were used as lentiviral producer cells to produce HUVECs that expressed GFP. Lentivirus was produced as follows, 3×10^6 HEK293T cells were plated onto a 10 cm plate 24 hrs prior to polyethylenimine (PEI) transfection using lentiviral plasmids: 3.3 μg psPAX2 (packaging vector), 1.3 μg pMD2G (envelope vector) and 4.4 μg pWPI or pWPXL (transfer vector) carrying the GFP gene of interest (Addgene). The 9 μg plasmid DNA and 36 μl 1 mg/ml PEI was added into 1 ml OptiMEM and mixed by low speed vortexing. The transfection media was incubated for 10 mins at room temperature before addition drop-wise into the culture media of a confluent 10 cm plate of HUVECs. The transfected HEK293T plate was incubated at 37 °C for 48 hrs then the lentiviral media was collected.

To transduce HUVECs to generate GFP expressing cells, the collected lentiviral media was centrifuged at 195 x g for 5 mins and filtered with a 0.45 μm^2 pore syringe filter (Corning). 90 $\mu\text{g}/\text{ml}$ heparin, bovine brain extract and 8 $\mu\text{g}/\text{ml}$ polybrene was added to the lentiviral media before being added to 1×10^6 seeded HUVECs. The lentiviral media remained on the HUVECs for 24 hrs at 37 °C before the media was replaced with fresh cM199.

2.6.5 Fluorescence activated cell scanning (FACS)

To determine whether cells were fluorescently labelled, a Becton Dickinson FACSCalibration and Becton Dickinson CellQuest Pro software was used to measure and analyse the intensity of the fluorescence emission from cells. Approximately 3×10^5 cells were placed in 1 ml cell culture media and kept on ice prior to analysis.

2.6.6 Immunofluorescence

To study the localisation of endothelial proteins in adhered HUVECs compared with the localisation in endothelial tubules, HUVECs were either plated directly onto sterile coverslips to form a confluent monolayer or were co-cultured on the coverslips with HDFs in the co-culture tube formation assay, as described in section 2.7.1.

To prepare the coverslips, each coverslip was placed into 1 M HCl for 10 mins on a rotating falcon tube holder, rinsed 5 times with ddH₂O before being stored in 70% (v/v) ethanol. The coverslips were washed 10 times with PBS before seeding cells onto them. Pre-coated gelatin coverslips were used for the culture and immunofluorescence of HUVECs.

To fix and stain proteins within endothelial cells, the media from the cultured cells was removed using an aspirator, washed 3 times with PBS and fixed for 10 mins using 4% (w/v) paraformaldehyde (PFA) in PBS at room temperature. The cells were washed 3 times using PBS, neutralised for 10 mins with 50 mM ammonium chloride. The cells were washed 3 times with PBS then permeabilised with 0.1% (v/v) triton x100 in PBS for 4 mins, then washed again 3 times with PBS. Blocking buffer containing 10% (v/v) foetal calf serum (FCS), 3% (w/v) bovine serum albumin (BSA), 0.1% (v/v) Tween-20, 0.01% (w/v) NaN₃ was added to the cells for 1 hr at room temperature. The cells were incubated with 50 µl primary antibody in blocking buffer for 30-60 mins by manually removing the coverslips from the plates using tweezers. The droplets of primary antibody-blocking buffer were pipetted onto parafilm before the coverslip was placed onto the droplet. The coverslips were washed 3 times with PBS before the cells were incubated with 50 µl secondary antibody in blocking buffer solution for 30-60 mins at room temperature. As a marker for endothelial cells,

rhodamine labelled Ulex (Vector Laboratories) was added in addition to the secondary antibody in blocking buffer.

The cells were then washed 3 times with PBS and once with dH₂O before being mounted onto glass slides using 5.5 µl ProLong Gold Antifade reagent with DAPI (Invitrogen) or Vectashield mounting medium with or without DAPI (Vector Laboratories). The glass slides were placed in darkness overnight and the coverslip was secured in place the following morning with clear nail varnish. Mounted coverslips were stored at -20 °C. To study the localisation of endothelial proteins, a Zeiss 780 Zen confocal microscope was used.

2.6.6.1 Co-culture staining of podocalyxin and collagen IV

Apical and basal cell surface markers podocalyxin and collagen IV were stained to investigate lumen formation in endothelial tubules formed using the co-culture tube formation assay. Cells were plated and cultured on coverslips in wells of a 24 well plate. The co-culture media was removed from the wells and washed 3 times with PBS, the cells were then fixed using 4% (w/v) PFA in PBS at room temperature for 20 mins. The cells were permeabilised with 0.1% (v/v) triton x100 in PBS for 20 mins. The cells were then blocked with 0.5% (w/v) BSA in PBS for 20 mins at room temperature. 200 µl of primary antibody solution of podocalyxin and/or collagen IV in blocking buffer was added to the cells and incubated at 4 °C overnight. The following morning, the wells were washed 3 times with PBS, each wash lasted 5 mins. The secondary antibodies in blocking buffer were added to the cells and incubated for 1 hr at room temperature. Any unbound antibody was removed by 3 washing steps using PBS, before the cells were mounted onto glass slides as described in section

2.6.6. The stained endothelial tubules were imaged using a Zeiss 780 Zen confocal microscope.

2.7 Endothelial assays

2.7.1 Co-culture tube formation assay

The tube formation assay is an organotypic assay that enables visualisation of the endothelial morphological differentiation stages in angiogenesis. The tube formation assay can provide information on the stages of cell migration and proliferation and allows for assessment of the ability of endothelial cells to develop into three dimensional tubules which mimic the appearance of small blood vessels. The development of tubules in the co-culture tube formation assay relies on the secretion of extracellular matrix (ECM) components by fibroblasts; endothelial cells use the matrix as a scaffold to support cellular extension and expansion into tubules^{125,126}.

To image endothelial tubule growth using confocal microscopy, 6.9×10^4 HDFs were plated onto matTek dishes (MatTek Corporation) in cDMEM and incubated at 37 °C for 5 days to allow secretion of ECM from the HDFs. Fresh cDMEM media was replaced on the fourth day of culture. 6.9×10^4 fluorescently labelled HUVECs in cM199 were plated directly on top of HDFs and the media was replaced every other day, as outlined in figure 2.1. To perform live-cell imaging of endothelial tubules, the co-culture media was removed immediately before imaging and replaced with imaging media which contained DMEM that lacked phenol red, supplemented with 10% (v/v) FCS, 90 µg/ml heparin, 4 mM L-Glutamine, 100 units/ml penicillin and streptomycin and bovine brain extract. Endothelial tubules were imaged on a Nikon A1R inverted confocal microscope and a Zeiss 780 Zen confocal microscope.

A Co-culture tube formation assay procedure:

Day 1: Plate and culture human dermal fibroblasts (HDFs)

Day 3: Grow endothelial cells (HUVECs)

Day 4: Feed HDFs by refreshing cDMEM media

Day 5: Plate HUVECs directly on top of HDFs

Day 7: Feed co-culture by refreshing cM199 media

Day 9: Feed co-culture by refreshing cM199 media

Day 11: Feed co-culture by refreshing cM199 media

End point: Fix and stain endothelial tubules or perform live-cellular imaging

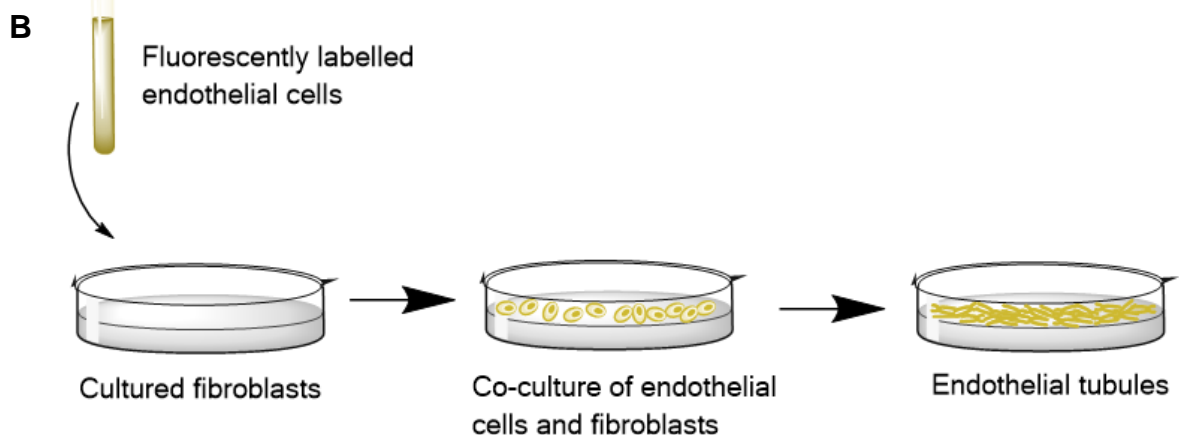


Figure 2.1 Procedure for the co-culture tube formation assay

A) Step-by-step procedure of the co-culture tube formation assay involving the co-culture of endothelial cells (HUVECs) on top of human dermal fibroblasts (HDFs) to form endothelial tubules, **B)** Schematic diagram of the co-culture tube formation assay. Fluorescently labelled endothelial cells are plated directly on top of cultured fibroblasts, co-culture stimulates the extension of the endothelial cells into three dimensional tubules. Confocal microscopy can be used to visualise the fluorescent endothelial tubular network.

The cells were kept on a heated stage at 37 °C throughout imaging and the cell media was replaced with cM199 after imaging to continue to culture the cells.

2.7.1.1 Histological staining of endothelial cells

Histologically staining endothelial cells was performed to image the extensive network of tubules formed in the co-culture tube formation assay and to analyse tubule growth and branching. The protocol for co-culturing HUVEC and HDFs to develop tubules was performed as described in section 2.7.1 using a 12-well plate and 3×10^4 cell densities. After 6 days of co-culture with replacement of media every other day, the cells were washed once with 1 ml PBS and fixed for 30 mins with 70% (v/v) ethanol cooled to -20 °C. The wells were then washed twice with 1 ml PBS and incubated with 400 µl 1.29 µg/ml mouse monoclonal Anti-human CD31 primary antibody (Dako) in 1% (w/v) BSA-PBS for 1 hr at 37 °C. Unbound primary antibody was removed by washing 3 times with 1 ml PBS. The cells were then incubated for 1 hr at 37 °C with 400 µl secondary antibody goat polyclonal Anti-mouse IgG conjugated to alkaline phosphatase diluted 1:500 in 1% (w/v) BSA in PBS. Cells were washed twice with 1 ml PBS and 3 times with 1 ml dH₂O before adding 500 µl alkaline phosphatase substrate SigmaFAST 5-bromo-4-chloro-3-indolyl phosphate/ nitro blue tetrazolium (BCIP/NBT). The SigmaFAST BCIP/NBT had been dissolved in 10 ml dH₂O, the substrate remained on cells for 25 mins at room temperature. The phosphatase reaction was stopped by washing with dH₂O and the wells were left to dry in darkness overnight at room temperature. A Leica MZ16 optical microscope was used to image the histological stained endothelial cells.

2.7.2 Matrigel tube formation assay

Natural basement membrane extract matrigel (VWR International) was thawed on ice and used immediately once thawed. Prior to the addition of 70 μ l of 10 mg/ml matrigel to each well of a 12-well plate (Falcon), each well was rinsed with PBS; the plate was then incubated at 37 °C for 30 mins to allow the matrigel to solidify. 1.4×10^5 HUVECs in cM199 medium containing inhibitors if required were plated into each well, on top of the solidified matrigel. The plate was incubated at 37 °C, 5% CO₂ atmosphere for 12 hrs to allow endothelial tubular networks to form.

Images of the tubules were captured using the IncuCyte Imaging system (Essen BioScience) 12 hrs after the cells were plated. Four images per condition were captured and analysed. The ImageJ plugin Angiogenesis Analyzer was used to analyse the tubular images and the mean number of meshes was measured.

2.7.3 Scratch wound assay

6×10^3 HUVECs were plated in wells of a 96-well plate, which had been pre-coated with gelatin two days prior to scratching. The cells were maintained at 37 °C in a 5% CO₂ atmosphere. A scratch in the monolayer of cells was made using the IncuCyte scratcher, to remove debris the cells were washed once with PBS. To screen the effect of different kinase inhibitors on cell migration, the kinase inhibitors were added to the cells in a total volume of 100 μ l in cM199. To monitor cell migration, images were captured by the IncuCyte Imaging system (Essen BioScience) immediately, 6 hrs and 12 hrs after the scratch was made. Analysis of scratch wound closure was calculated by the IncuCyte software and checked manually.

2.7.4 Hanging drop spheroid angiogenesis assay

Cultured HUVECs were trypsinised and counted as described in section 2.6.2, if required the HUVECs were also fluorescently labelled with CFSE as described in section 2.6.4.1. Spheroids were formed from 1000 cells and 60 spheroids were generated per condition. HUVECs were resuspended in 20% (w/v) methylcellulose stock solution in cM199 at 5×10^4 cells/ml. 20 μ l of cell solution was pipetted into wells of a Nunc 60-well microplate and inverted overnight at 37 °C, 5% CO₂ atmosphere to generate spheroid masses via the hanging drop method, the schematic diagram for the assay is shown in figure 2.2. After 24 hrs the spheroids were embedded in a collagen matrix, by firstly making a solution of 3.35 mg/ml type I collagen from rat tail diluted in 10x DMEM in dH₂O. 10 μ l 5 N sodium hydroxide was added to the solution before mixing with a second solution containing 1.2% (w/v) methylcellulose solution in cM199.

The spheroids were collected from the microplate and centrifuged at 195 x g for 5 mins. The spheroid pellet containing 60 spheroids was resuspended in 200 μ l collagen solution, which was transferred into a well of a 24-well plate. The cells were incubated at 37 °C, 5% CO₂ atmosphere for 10 mins before 100 μ l cM199 was added on top of each well of embedded spheroids. If required, inhibitors were added into the 100 μ l culture media. The plate was placed at 37 °C, 5% CO₂ atmosphere for 16 hrs before fixing and imaging on a Zeiss 780 Zen confocal microscope or a Leica MZ16 optical microscope.

For studying endothelial sprouting, time-course imaging of the spheroids was performed using the CellIQ System which captured fluorescence and phase contrast images every hour for the duration of 27 hrs.

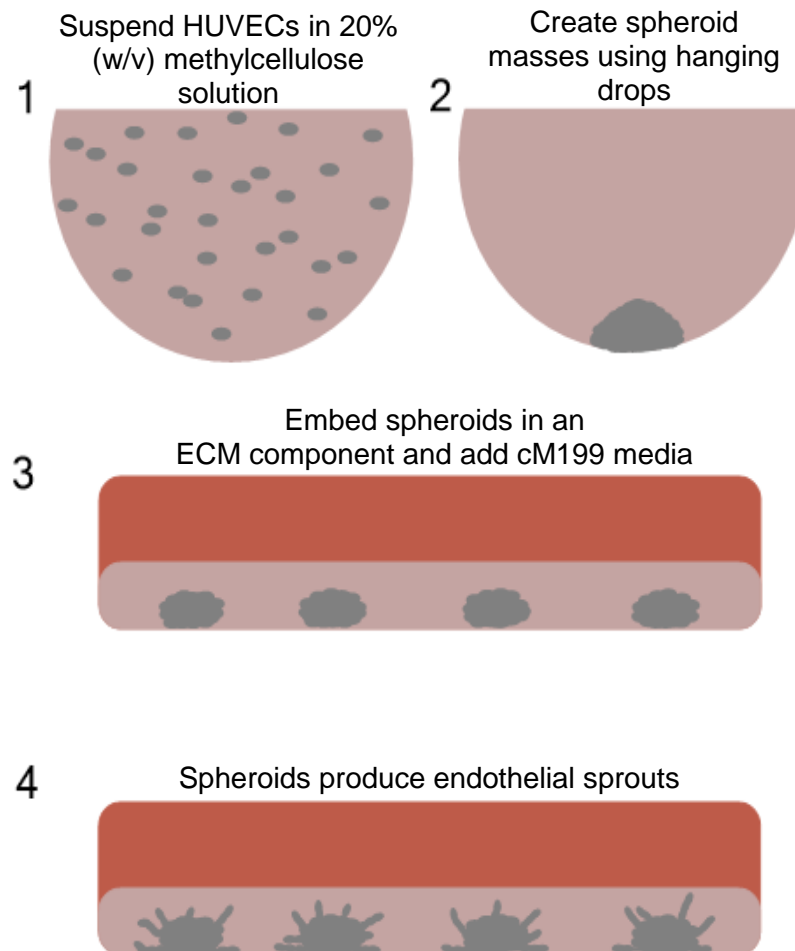


Figure 2.2 Schematic diagram of the hanging drop spheroid angiogenesis assay

1) Suspend HUVECs in cM199 media containing 20% (w/v) methylcellulose and pipette 20 μ l droplets into a 60-well microplate and invert overnight, 2) at the base of the droplet a multicellular spheroid mass forms over the course of 24 hrs, 3) embed multiple spheroids in an extracellular matrix of collagen and add cM199 media to the embedded spheroids, 4) the spheroids rapidly undergo endothelial sprouting.

2.7.4.1 Fixing and mounting endothelial spheroids

Culture media was removed from the wells of embedded spheroids and the spheroids were washed 3 times with PBS before 4% (w/v) PFA was added for 30 mins at room temperature for fixation. The PFA was removed and the embedded spheroids were washed 3 times with PBS before curved forceps were used to remove the embedded spheroids from the well and were mounted onto a glass slide. 8-10 μ l vectashield mounting medium with DAPI (Vector Laboratories) was added before a coverslip was placed over the spheroids and left to set. Imaging of the spheroids was carried out using a Zeiss 780 Zen confocal microscope.

2.7.5 Cell viability assay

The WST-1 cell proliferation kit (Cayman Chemical) was used to assess the cytotoxic effects of inhibitor concentrations on HUVECs. Mitochondrial dehydrogenases of viable cells were able to cleave the tetrazolium salt WST-1 to formazan, which was detected by measuring the absorbance of light at 450 nm.

6×10^3 HUVECs were plated in wells of a 96-well plate which had been pre-coated with gelatin, inhibitors in cM199 were added to cells in a total volume of 100 μ l. Two controls were used; control wells either contained 100 μ l cM199 without cells or 100 μ l DMSO in cM199 with cells. The 96-well plate was incubated at 37 °C, 5% CO₂ atmosphere for 24 hrs then 10 μ l WST-1 was added to each well, excluding the media only control wells. The plate was placed onto an orbital shaker for 1 min before incubation for 2 hrs at 37 °C. The light absorbance of each well was measured at 450 nm by a microcell reader. Four repeats were performed for each inhibitor compound and a mean absorbance value was calculated.

2.8 Microbiology and cloning

2.8.1 Cloning procedure

All cloning reagents of restriction enzymes and their corresponding buffers were purchased from New England Biolabs (NEB).

The lifeact-GFP sequence from the pEGFP-N1 plasmid was inserted into the lentiviral pWPXL plasmid; the cloning procedure which was performed is outlined in figure 2.3. The lifeact-GFP sequence was amplified from the pEGFP-N1-lifeact plasmid using the VS1 forward primer with the sequence 5'-TAGTAGGTTTAAAC ACCATGGGCGGTGTCGCAGATTTGATCAAG-3' and VS2 reverse primer with the sequence 5'-CTACTACCCGGGTTATGATCTAGAGTCGCGGCC-3' to add in the SmaI and PmeI restriction enzyme sites to enable both the pWPXL plasmid and the lifeact-GFP sequence to be cut using the same restriction enzymes. The amplified DNA was then cut with SmaI and PmeI (NEB) and the linearised plasmid and insert were purified from gel electrophoresis using the GeneJET Gel Extraction Kit (Fermentas). Ligations were set up with a 1:3 ratio of pWPXL:lifeact-GFP insert using T4 ligase (NEB). α -select gold chemically competent *E.coli* were transformed with the pWPXL-lifeact-GFP plasmid and the bacterial colonies were expanded in LB broth containing 0.1 mg/ml ampicillin. The plasmid was purified from bacterial culture using the GeneJET plasmid miniprep kit (Fermentas) and the Qiagen plasmid maxi kit (Qiagen). All DNA sequencing was carried out by the Functional Genomics & Proteomics Laboratory, School of Biosciences at the University of Birmingham, UK. The primers used for sequencing the pEGFP-N1 plasmid were the forward primer: MCS N1: PL_MCS_N1 with the sequence 5'-GTCGTAACAACCTCCGCCC-3' and

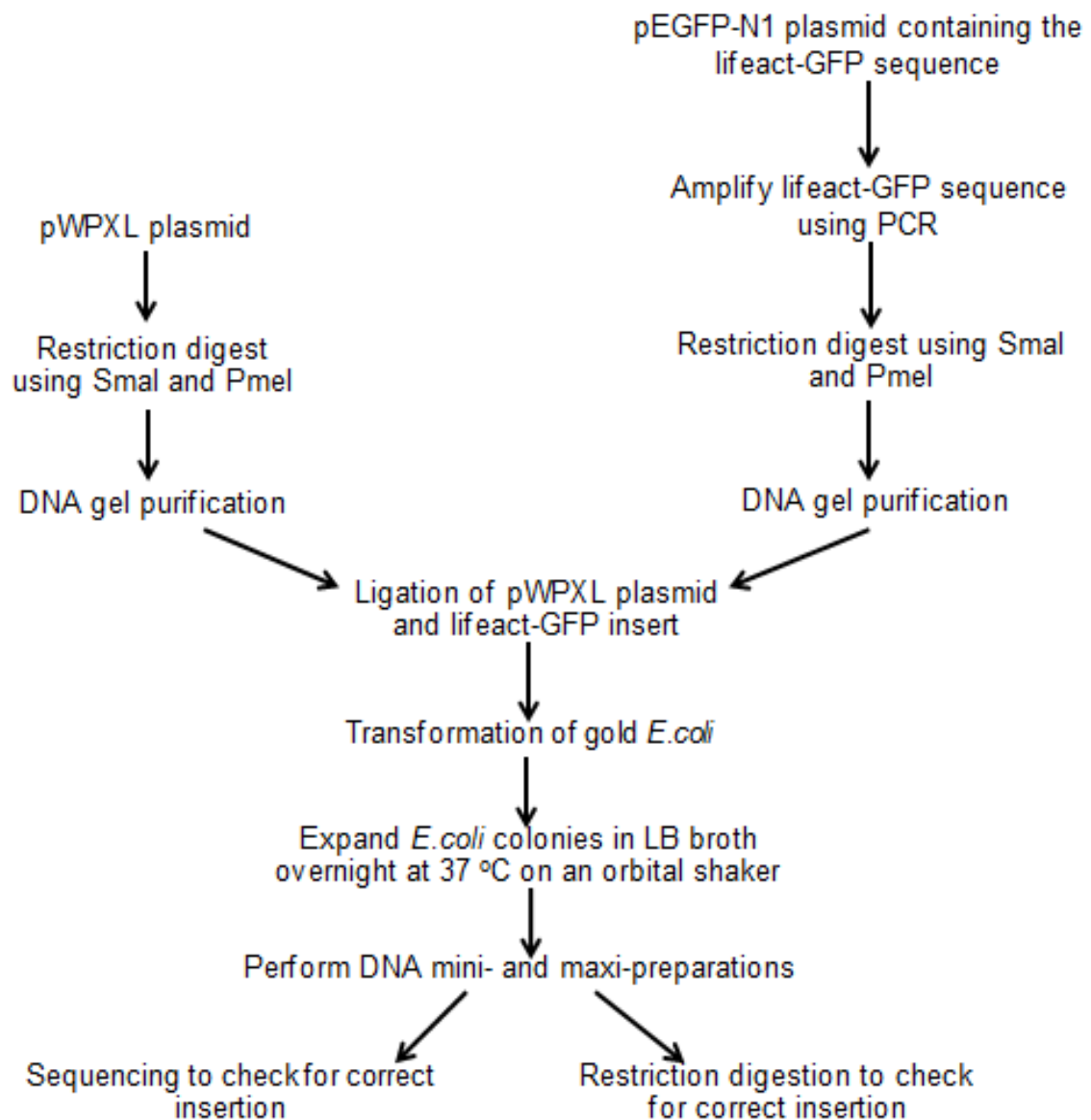


Figure 2.3 Cloning procedure to insert the lifeact-GFP sequence into the pWPXL plasmid to replace the original GFP gene

The lifeact-GFP sequence from pEGFP-N1 was amplified and SmaI and PmeI restriction sites were added to the sequence using PCR. The same restriction enzymes; SmaI and PmeI were used to digest pWPXL to allow for the insertion of the lifeact-GFP insert. The products of the digestion reactions were separated using agarose gel electrophoresis and purified to obtain the linearised plasmid and insert. A ligation reaction using ligase, the insert and the plasmid generated the new construct consisting of the pWPXL plasmid with the lifeact-GFP sequence inserted. The construct was introduced into gold *E.coli* by heat-shock transformation and the bacteria were grown on LB agar plates containing ampicillin antibiotic. Selected colonies were expanded in LB broth overnight at 37 °C on an orbital shaker. DNA mini- and maxi-preparations were performed to extract the plasmid from lysed bacteria. A series of restriction digestion reactions and sequencing were performed to verify the correct site of insertion and ensure no DNA mutations had taken place.

reverse primer: PL_BEFORE_EGFP2 with the sequence 5'-GCTTGCCGTAG GTGGCAT-3'.

To measure DNA concentrations 2 µl of plasmid DNA solution was loaded onto a NanoDrop ND-1000 Spectrophotometer (LabTech) for assessment and as a way of storing DNA and plasmid constructs, 30 % (v/v) glycerol was mixed in a 1:1 ratio with bacterial culture and stored at -80 °C.

2.8.2 Bacterial culture

E.coli containing the pEGFP-N1 plasmid was streaked onto Luria Bertani (LB) agar plates containing 0.03 mg/ml kanamycin. The bacterial plate was incubated at 37 °C overnight. The following day bacterial colonies were grown up in liquid LB broth with kanamycin.

E.coli containing the pWPXL-lifeact-GFP plasmid was streaked onto LB agar plates containing 0.1 mg/ml ampicillin antibiotics and *E.coli* colonies were expanded in LB broth containing ampicillin.

2.8.3 Purification and sequencing of DNA

The pEGFP-N1 plasmid and the pWPXL-lifeact-GFP plasmid were purified from bacterial cultures either by producing small quantities of plasmid using the GeneJET plasmid miniprep kit (Fermentas) or via larger size production using the Qiagen plasmid maxi kit (Qiagen). For both plasmid production procedures the manufacturer's instructions were followed for the production and purification of DNA.

2.8.4 Amplifying the lifeact-GFP insert using polymerase chain reaction (PCR)

To introduce the SmaI and PmeI restriction enzyme sites into the lifeact-GFP sequence for subsequent insertion into the pWPXL plasmid, PCR was performed to amplify the sequence using specifically designed primers VS1 and VS2 as mentioned in section 2.8.1.

100 µl PCR mix was made up containing: 5 µl pEGFP-N1 plasmid, 1 µl phusion enzyme, 1 µl forward primer VS1, 1 µl reverse primer VS2, 2 µl 10 nM deoxyribonucleotides (dNTPs), 20 µl 5x HF buffer and 70 µl PCR H₂O. The PCR program was performed as follows: 10 sec initial denaturation at 98 °C, followed by 30 cycles of denaturation at 98 °C for 10 secs, annealing at 55 °C for 30 secs and elongation at 72 °C for 1 minute.

After PCR, a 10 µl sample of the PCR mix was run in gel electrophoresis on a 1.5% (w/v) agarose gel alongside a 1 kb DNA ladder (GeneRuler) to ensure that the amplification process was successful.

2.8.5 DNA separation and purification

DNA was separated using DNA agarose gel electrophoresis; 1-2% (w/v) agarose gels were made from dissolving agarose powder (VWR International) in Tris acetate EDTA (TAE) buffer solution. The TAE solution was made up to contain 1 mM EDTA, 40 mM Tris-base, 18 mM glacial acetic acid. The gels were stained with SYBR Safe DNA stain (Invitrogen) to allow for DNA visualisation under ultraviolet (UV) light. Gels were suspended in TAE buffer solution to separate DNA strands which had been labelled with 6x loading dye. A 1 kb DNA ladder (Fermentas) was loaded alongside

DNA samples to check the sizes of DNA samples. DNA bands were visualised using the Gene Genius Bio Imaging System (Syngene).

DNA bands were manually cut out of the DNA agarose gels using a scalpel and extraction of the DNA from the agarose gel was performed following the instruction manual of the GeneJET Gel Extraction Kit (Fermentas).

2.8.6 Restriction digestion reactions of DNA

Restriction digests were performed to cut the GFP gene out from pWPXL to allow for the insertion of the lifeact-GFP sequence. The restriction digest reactions contained 5 µg plasmid DNA or purified PCR products, 2.5 µl restriction enzyme and 5 µl 10x restriction enzyme buffer with 5 µl 10x BSA if required for enzyme activity. The total volume of the restriction digestion reactions was scaled between 10–50 µl dependent on if the digestion reaction was for diagnostic purposes.

2.8.7 DNA ligation reaction to create the pWPXL-lifeact-GFP plasmid

DNA ligation was performed to ligate the lifeact-GFP DNA insert into the linearised pWPXL plasmid. The ligation reaction, alongside controls were performed at room temperature using 2 µl T4 Ligase (NEB), 2 µl 10x ligase buffer and 150 ng insert, 50 ng vector in a DNA volume of 16 µl. The total ligation reaction was in 20 µl volume solutions, kept at room temperature for 2 hrs.

2.8.8 Heat-shock transformation

Heat shock transformation was performed to introduce the pWPXL-lifeact-GFP plasmid into competent bacteria. 5 µl plasmid DNA generated by the ligation process in section 2.8.7 was added to 50 µl α-select gold chemically competent *E.coli*. The transformation mix containing the bacteria and plasmid DNA was incubated on ice for

30 mins before being heat shocked for 30 secs at 42 °C in a water bath. The transformation mix was then placed back on ice for 1 min. 100 µl LB was added to the transformation mix and was placed at 37 °C in a shaking incubator for 1 hr. The transformed bacteria were spread onto LB agar plates containing antibiotics and placed in an incubator at 37 °C overnight.

2.9 Zebrafish methods

2.9.1 Strains and maintenance of zebrafish

The *in vivo* model of angiogenesis that was used in this study was the *Danio rerio*, commonly known as the zebrafish, which is a widely used vertebrate model. The stable transgenic line of zebrafish Tg[fli1:EGFP] (*fli1*-GFP) generated by Weinstein and Lawson was used in this study¹⁵⁵. The *fli1*-GFP zebrafish expressed the EGFP protein in the vascular endothelium throughout embryogenesis driven by the *fli1* promoter which created the ideal model for studying and visualising the growth and development of the vascular system in this organism.

The fish were maintained at the

2.9.2 Breeding of transgenic zebrafish and maintenance of embryos

To achieve vascular imaging of the zebrafish, transgenic *fli1*-GFP zebrafish were bred to produce embryos. Adult female and male zebrafish were placed in a breeding tank separated by a divider overnight. The following morning the divider was removed and embryos were collected in 1x E3 media which contained 34.8 g NaCl, 1.6 g KCl, 5.8 g CaCl₂, 9.78 g MgCl₂, which was kept at 28.5 °C. The 1x E3 media was made by diluting a 60x E3 stock solution of E3 media into 1L with dH₂O, with the

addition of 100 µl 1% methylene blue (Sigma) to prevent fungal infections. A 60x E3 stock solution was made from dissolving 34.8 g NaCl, 1.6 g KCl, 5.8 g CaCl₂, 9.78 g MgCl₂ into a total volume of 2 l ddH₂O. At 24 hpf, the 1x E3 media surrounding the zebrafish embryos was changed with 1x E3 media containing 80 µM 1-phenyl 2-thiourea (PTU) to prevent embryonic pigment formation.

2.9.3 Morpholino oligonucleotide injections

Antisense morpholino oligonucleotides were ordered from Gene Tools (USA). The morpholino oligonucleotides were reconstituted into ddH₂O and were microinjected into transgenic *fli1*-GFP zebrafish embryos at the 1-cell stage of development. The concentrations of morpholino oligonucleotide solutions which were used ranged from 0.2-0.8 ng per embryo. Phenol red was co-injected alongside the morpholino oligonucleotide solution to act as a tracer for the injection procedure. Mismatched morpholino oligonucleotides were injected into 1-cell stage embryos as controls to the gene targeting morpholino oligonucleotide sequences.

2.10 Imaging and image analysis

2.10.1 Imaging the zebrafish vasculature

Prior to imaging the zebrafish embryos, each embryo was manually dechorionated using forceps and anaesthetised prior to imaging using 1-2 drops of MS-222 in E3 media to ensure the movement of embryos was minimised. The zebrafish were then placed onto MatTek dishes and imaged using a Zeiss 780 Zen microscope. Embryos were imaged at varying developmental time points including 24 hpf, 26 hpf, 28 hpf, 30 hpf, 36 hpf, 48 hpf and 72 hpf.

Confocal image sections of the embryonic zebrafish vascular system were compressed using Zen 2012 Zeiss microscopy software and the subsequent vasculature images were analysed using the developed ImageJ Zebrafish Vasculature Analysis Macro or IMARIS software to assess and quantify the numbers of vessel segments, junctions, end-points, the total and average vessel lengths.

2.10.2 Image analysis software

Optical images of histologically stained endothelial cells were analysed using AngioSys Image Analysis software (Cellworks). Fluorescent endothelial spheroid images were analysed using the designed Spheroid Analysis ImageJ plugin (National Institutes of Health). The matrigel tube formation images were analysed using the ImageJ Angiogenesis Analyzer plugin (National Institutes of Health). The scratch wound assay images were analysed using the IncuCyte software (Essen Bioscience). The Zen 2012 Zeiss microscopy software was used to process and generate compressed confocal z-stacks of endothelial tubular images and zebrafish vasculature images. The zebrafish vasculature analysis macro was generated using ImageJ (National Institutes of Health) to allow for quantification of the zebrafish vascular system. The alternative zebrafish vasculature analysis method was created using IMARIS x64 7.6.5 software (Bitplane).

2.10.3 Statistical analysis

Unless stated otherwise, all assays were performed at least three times with similar results.

GraphPad Prism 6 software was used to statistically analyse data, determine the Pearson product moment correlation coefficients (R values) and the coefficient of

determination values (r^2 values) and plot correlation graphs. The statistical tests which were used for the data sets are outlined in the results section, often the non-parametric Mann-Whitney test was performed on data sets which does not assume a normal distribution of the data. To compare two independent data sets an unpaired Student's t-test was performed. The p values were indicated in the results as follows: $p \leq 0.0001$ as ****, $p \leq 0.001$ as ***, $p \leq 0.01$ as **, $p \leq 0.05$ as *, $p > 0.05$ as ns for non-significant.

Chapter Three

Investigating lumen formation within endothelial tubules

3.1. Chapter summary

The aim of this chapter was to utilise and develop various fluorescent imaging techniques to study the process of lumenogenesis within endothelial tubules formed using the *in vitro* co-culture tube formation angiogenesis assay. In this chapter, different fluorescent imaging approaches are presented which involved labelling the endothelial cytoplasm or actin cytoskeleton prior to using the endothelial cells in the co-culture tube formation assay to enable tubular imaging using confocal microscopy.

The structure for this chapter is as follows: section 3.2 chapter introduction, section 3.3 establishing optimal conditions for the co-culture tube formation assay, section 3.4 using fluorescent cytoplasmic dyes to study lumen formation, section 3.5 visualising the uptake of fluorescence media into luminal spaces of tubules, section 3.6 staining of tubular apical and basolateral cell surface markers, section 3.7 expressing the lifeact peptide to outline developing lumens and visualise filopodia formation, section 3.8 visualising cellular interactions and lumen formation by using a mixture of lifeact-GFP and lifeact-RFP expressing cells, section 3.9 chapter discussion.

3.2. Chapter introduction

The development of vascular sprouts during angiogenesis involves endothelial invasion, migration and proliferation; the endothelial sprouts continue to elongate creating three dimensional tubules which fuse with existing blood vessels to form part of an elaborate cardiovascular network¹⁴. The newly formed vessels must produce an intracellular lumen encapsulated by endothelial cells to enable blood flow. Following lumenogenesis, there is re-establishment of the basement membrane and attachment of mural cells to stabilise and strengthen the vessel¹.

The co-culture tube formation assay assesses the ability of endothelial cells to undergo tubulogenesis¹²⁶. In this widely used *in vitro* assay modelling angiogenesis, endothelial cells are plated and cultured directly on top of fibroblasts to mimic the growth of small blood vessels such as the capillaries¹³⁰. In this chapter, the co-culture tube formation assay was used to establish endothelial tubules and investigate the process of lumenogenesis.

The cellular and molecular mechanisms involved within *in vivo* and *in vitro* lumen formation have been widely debated by the scientific community and at present there is evidence to support two models of endothelial lumenogenesis; the vacuole fusion mechanism and the endothelial cell rearrangement mechanism. In the vacuole fusion mechanism, small intracellular vesicles fuse together to form vacuoles within the endothelial tubules, these large intracellular vacuoles fuse with adjacent cell vacuoles creating a large open channel spanning through several endothelial cells^{32,218}. This mechanism of lumenogenesis has been supported by Kamei *et al.* which observed vacuole fusion within intersegmental blood vessels (ISVs) in zebrafish¹⁸. The second mechanism of lumen formation is the endothelial cell rearrangement mechanism,

where the lumen develops from an extracellular space between adjacent endothelial cells. This process is initiated by cell surface polarisation which establishes apical and basolateral surfaces due to interactions of RAS interacting protein 1 (RASIP1) and aided by the recruitment of negatively charged dextran sulphate and CD34-sialomucins which are repositioned to the apical cell surface²³. An extracellular space is created between the apical surfaces of the cells which is subsequently expanded by actomyosin contractility, causing rearrangement of endothelial morphology²³. The endothelial tubular lumen is further enlarged by the removal of cellular junctions by the action of proteolysis mediated by membrane type I matrix metalloproteinases (MT1-MMP) allowing an influx of surrounding fluid³¹. The aortic lumen in mouse embryos was found by Strilić *et al*, 2009 to develop extracellularly, supporting this mechanism of lumenogenesis²⁵.

3.3. Establishing optimal conditions for the co-culture tube formation assay

To study the structure of the endothelial tubules, it was important to establish the appropriate co-culture media constituents to achieve optimal growth of the endothelial tubules in the co-culture tube formation assay. Typically in our laboratory this assay is performed using bovine brain extract as a bFGF containing growth supplement, however to determine if the substitution of basic fibroblast growth factor (bFGF) with bovine brain extract lead to an enhancement of tubular development, endothelial tubular growth in the two conditions was compared. Additionally, VEGF was added to the media to determine if there was further enhancement of tubular growth when this pro-angiogenic factor was present.

In this study, endothelial cells were plated directly on top of fibroblasts and were co-cultured for six days in M199 media containing FCS, heparin, penicillin and streptomycin with either bovine brain extract or 10 ng/ml bFGF, with or without the presence of 10 ng/ml VEGF. The co-cultures were fixed and histologically stained on the sixth day of co-culture and representative images of the endothelial tubules are shown in figure 3.1A. The images of the tubular networks were analysed and tubules were quantified using AngioSys software. The number of endothelial tubule junctions and mean tubule length were calculated and are shown in figure 3.1B.

Endothelial tubular growth occurred in all co-culture media conditions tested, statistical analysis using an ANOVA test and a Dunnett post-test revealed that there were no statistical differences in the growth of the tubules formed in the different media constituents. Furthermore, the addition of VEGF to the co-cultures did not statistically enhance tubular formation further; this result revealed that the fibroblasts must have secreted a high concentration of VEGF into the surrounding media in response to being stimulated by bFGF, so the addition of the 10 ng/ml VEGF was not enough to cause a further increase in tubule growth. Since no significant statistical differences were calculated between the four co-culture media conditions, the standard approach of using cM199 with bovine brain extract was used for subsequent studies using the co-culture tube formation assay with endothelial cells and fibroblasts.

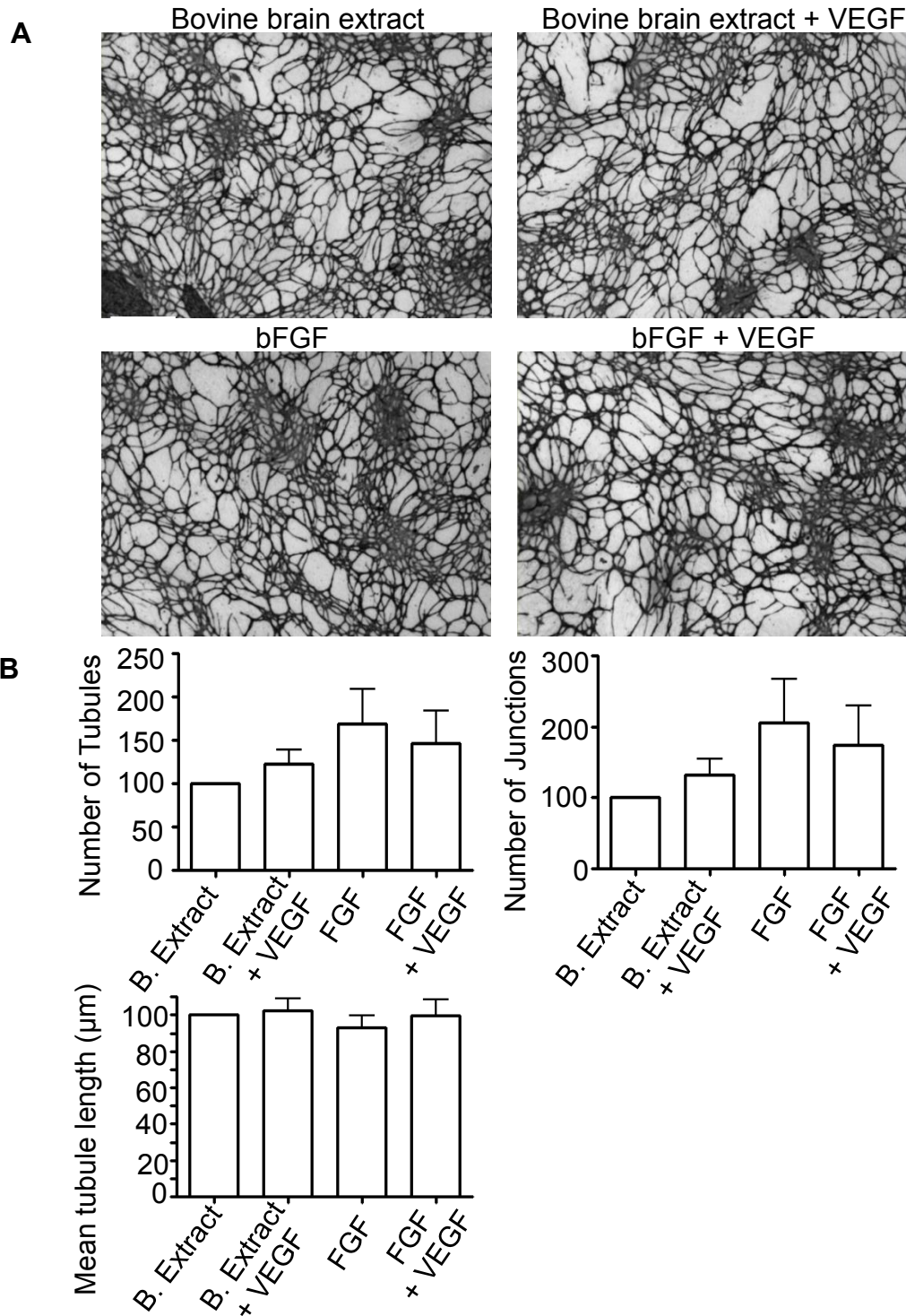


Figure 3.1 Both basic fibroblast growth factor and bovine brain extract promoted tubule formation and was not enhanced by the addition of VEGF

A) Histologically stained endothelial tubular images formed after six days in co-culture media containing either bovine brain extract or 10 ng/ml bFGF with or without 10 ng/ml VEGF, scale: 1 mm. **B)** Bar charts showed the AngioSys software analysis of the tubular images, an ANOVA and Dunnett post-test revealed the p values were non-significant between the different media constituents, n = 3 with different cords, error bars show the SEM.

3.4. Using fluorescent cytoplasmic dyes to study lumen formation

To visualise at high resolution the three dimensional structure of endothelial tubules, confocal microscopy was required to optically section the tubules to obtain image slices which can be compressed to enable detailed visualisation of the endothelial tubules. The optical image slices were examined individually for the formation of lumens within the endothelial tubule and were also used to create three dimensional reconstructions to interactively visualise the tubules from all different angles.

To generate fluorescent tubules, firstly endothelial cells were transduced to express cytoplasmic GFP using the lentiviral plasmids pWPI and pWPXL. The fluorescently labelled endothelial cells were used in the co-culture tube formation assay to produce fluorescent tubules which were imaged after two days of co-culture; images of these tubules are shown in figure 3.2A. Limitations of this study were that the GFP expressing tubules could only be imaged using epifluorescence microscopy due to the relatively low fluorescence emission from these tubules therefore only the overall morphology of the tubules was observed. Further structural details of the tubules such as filopodia formation or the development of lumens could not be visualised.

A second fluorescence labelling method involved labelling endothelial cells with 5 μ M CFSE produced endothelial tubules with higher fluorescence emission than GFP expressing tubules. When visualised with confocal microscopy the CFSE labelled tubules enabled higher resolution tubular images to be captured, as shown in figure 3.2C shows the appearance of an endothelial tip cell and a tubular lumen.

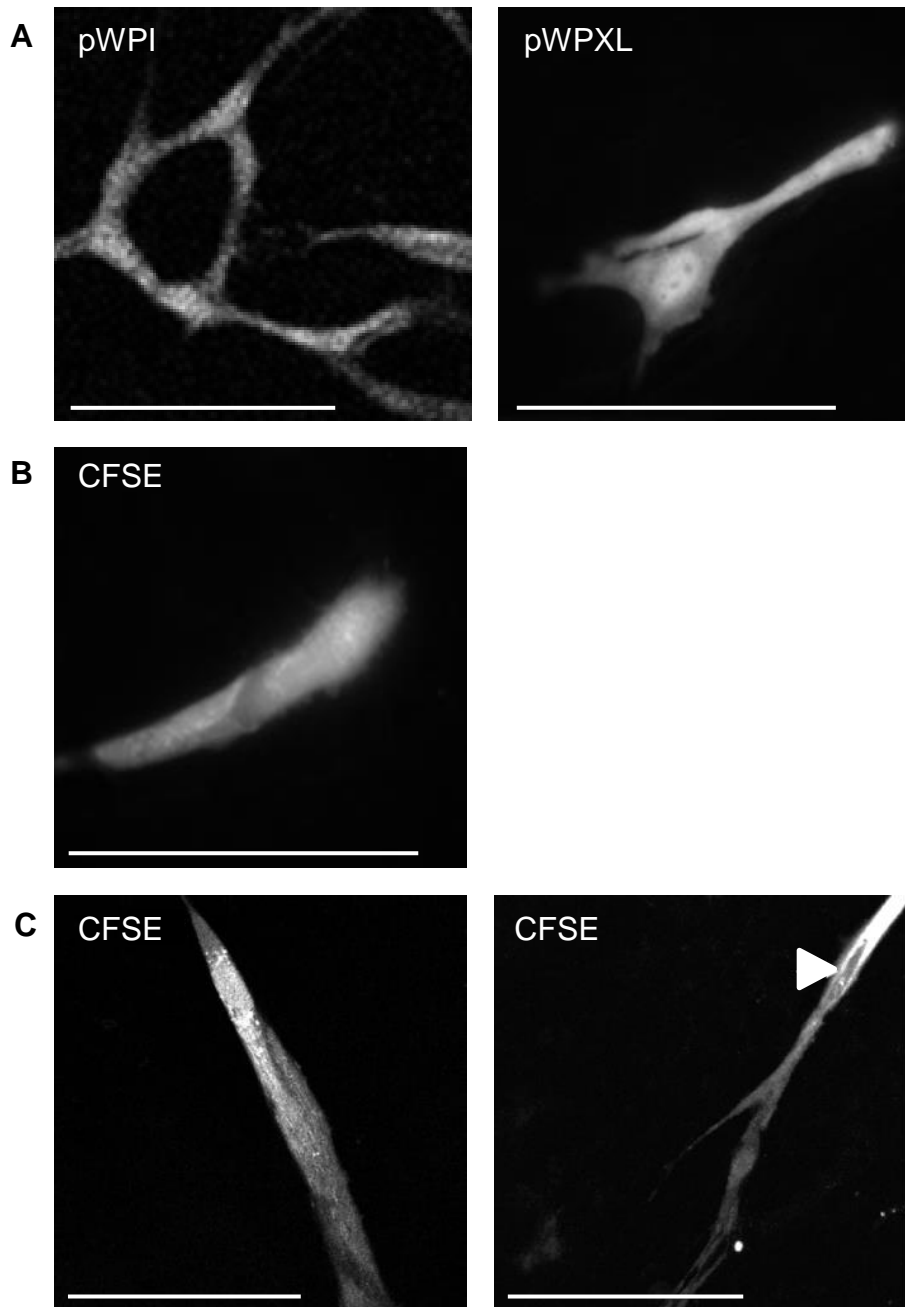


Figure 3.2 CFSE labelled endothelial cells produced high fluorescence emission allowing the structure of endothelial tubules to be imaged with confocal microscopy

A) Epifluorescence images revealed low intensity fluorescence emission from tubules expressing GFP via pWPI and pWPXL transduction. **B)** Epifluorescence image of a CFSE labelled tubule. **C)** Confocal microscopy images of a tip cell and lumen formation within CFSE labelled tubules. Endothelial tubules were imaged after 2 days of co-culture in the tube formation assay, scale: 100 μ m.

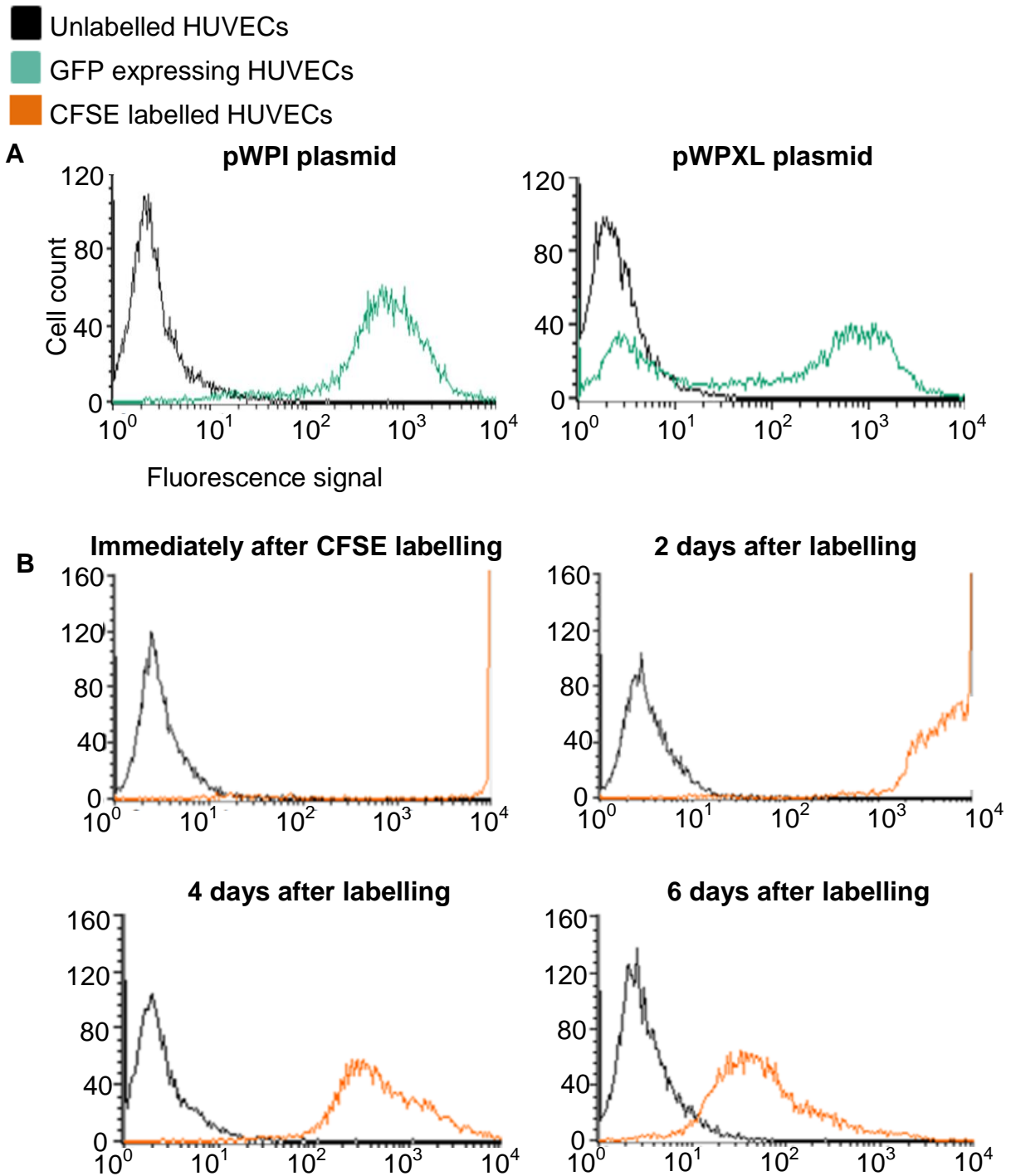


Figure 3.3 CFSE labelled endothelial cells continued to produce high fluorescence emission from cells days after labelling

Fluorescence Activated Cell Scanning (FACS) plots of the fluorescence emission from unlabelled HUVECs (black) and **A**) GFP expressing HUVECs from pWPI and pWPXL transduction (green), **B**) HUVECs labelled with 5 μ M CFSE (orange), FACS analysis was performed immediately after labelling and 2, 4 and 6 days after labelling.

Fluorescence activated cell scanning (FACS) analysis of endothelial cells expressing cytoplasmic GFP via pWPI and pWPXL transduction as well as labelling endothelial cells with CFSE revealed that the cells were successfully transduced and were fluorescently labelled. The FACS plots analysing the GFP expressing cells and the CFSE labelled cells compared with the unlabelled endothelial cell control sample are shown in figure 3.3, the shift in the fluorescence emission peak compared with the unlabelled endothelial control confirmed that the cells were successfully labelled.

CFSE passively diffuses into the cellular cytoplasm, where it becomes covalently coupled to amines inside the cell through cleavage of the acetate groups by intracellular esterases²¹⁹. Once modified the fluorescent carboxyfluorescein succinimidyl ester can stably exist in the cell without leaking out, which permits its usage as a cell proliferation dye²¹⁹. The FACS analysis showed that labelling endothelial cells with CFSE produced an intense fluorescence signal immediately after labelling compared with the unlabelled endothelial control and the GFP expressing endothelial cells. The FACS plot showed that the fluorescence emission in CFSE labelled cells remained high for around four days, which was sufficient for monitoring the development and growth of the endothelial tubules. Observation of tubules in culture showed that the fluorescence emission from the CFSE labelled tubules remained relatively high after six days and therefore CFSE proved to be a useful fluorescence dye for labelling endothelial cells prior to use in the co-culture tube formation assay to monitor tubule growth and development.

To determine whether CFSE labelling of endothelial cells caused any adverse effects on tubule formation, the co-culture tube formation assay was performed using endothelial cells that had been labelled with 5 μ M CFSE and tubular growth was

compared with that of unlabelled endothelial cells. The endothelial cells were co-cultured with fibroblasts for six days before being fixed and histologically stained; the histological tubular images are shown in figure 3.4A. The assay was repeated using endothelial cells from three different cords and the images were analysed using AngioSys software. Statistical analysis using a Student's t-test revealed that there were no significant differences in tubule formation when using unlabelled or CFSE labelled endothelial cells in the co-culture tube formation assay. The bar charts in figure 3.4B show quantification of the numbers of tubules, junctions and mean tubule length with unlabelled and CFSE labelled tubules.

Since labelling endothelial cells with CFSE did not significantly affect tubular formation, this fluorescence dye was used to determine if endothelial lumenogenesis occurred within tubules formed in this assay. CFSE labelled endothelial tubules were produced using the co-culture tube formation assay and were optically sectioned using confocal microscopy at 1 μm intervals to investigate the process of lumen formation. As shown in figures 3.5A and 3.5B, developing lumens within CFSE labelled endothelial tubules were visualised, the opening and closing of the luminal space can be observed in the sections which confirmed that this intracellular process occurs within tubules formed in this assay. This finding was also confirmed by the visualisation of an enclosed tubular lumen surrounded by plasma membrane in the xyz plane which was generated by the selection of a transverse section across the tubule which spanned across the developing lumen, shown in figure 3.5C.

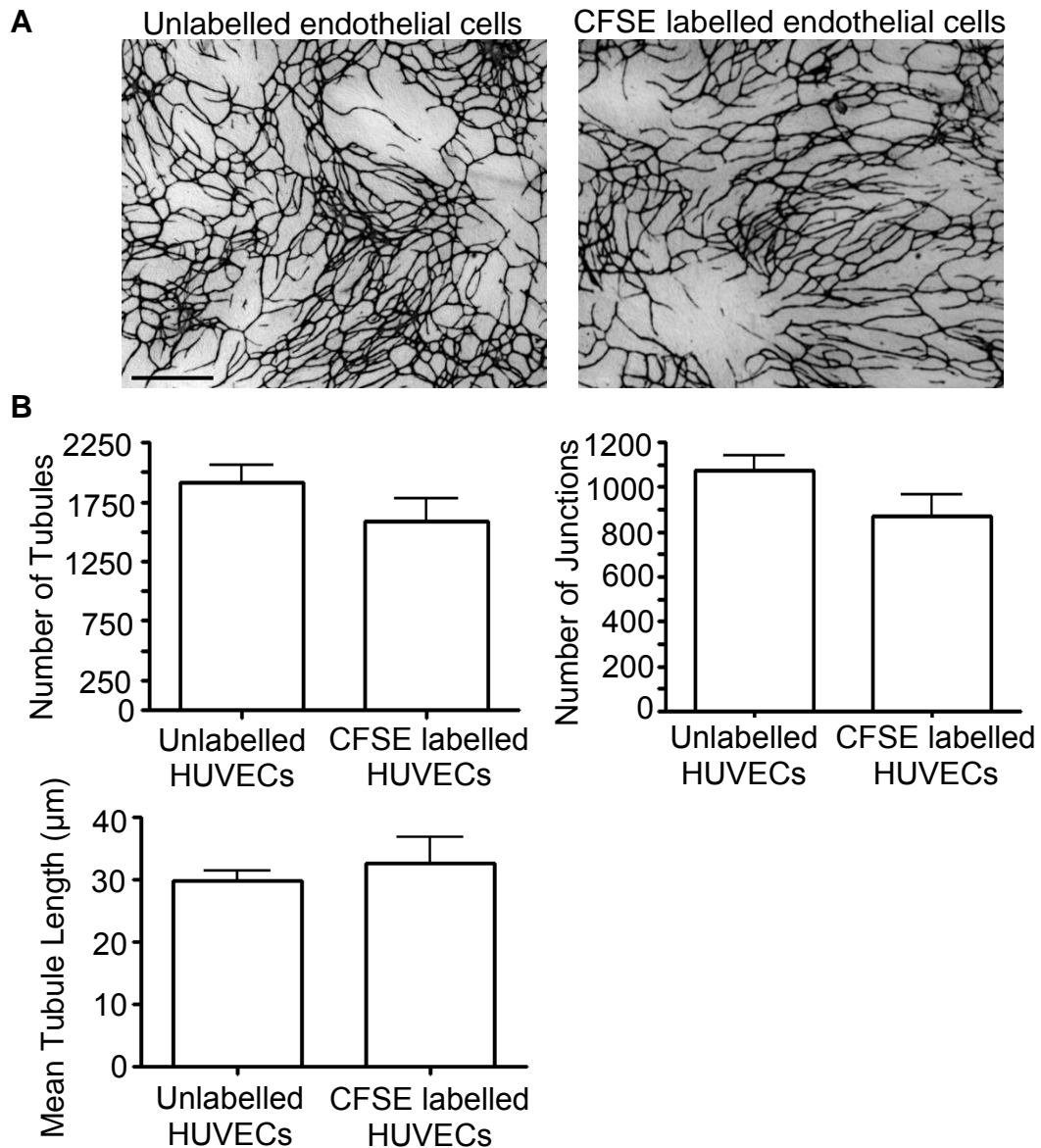


Figure 3.4 Labelling endothelial cells with CFSE did not significantly affect tubule formation

Unlabelled and 5 μM CFSE labelled endothelial cells were plated on top of fibroblasts and co-cultured for six days before being histologically stained. **A)** Histologically stained tubular images, scale bar: 1 mm. **B)** The histologically stained tubular images were analysed using AngioSys software, the bar charts showed the quantification of the number of tubules, junctions and mean tubule length formed when using unlabelled and CFSE labelled endothelial cells in the tube formation assay. Statistical analysis was performed using a Student's t-test, where the p values were non-significant for all parameters, $n = 3$, error bars show the SEM.

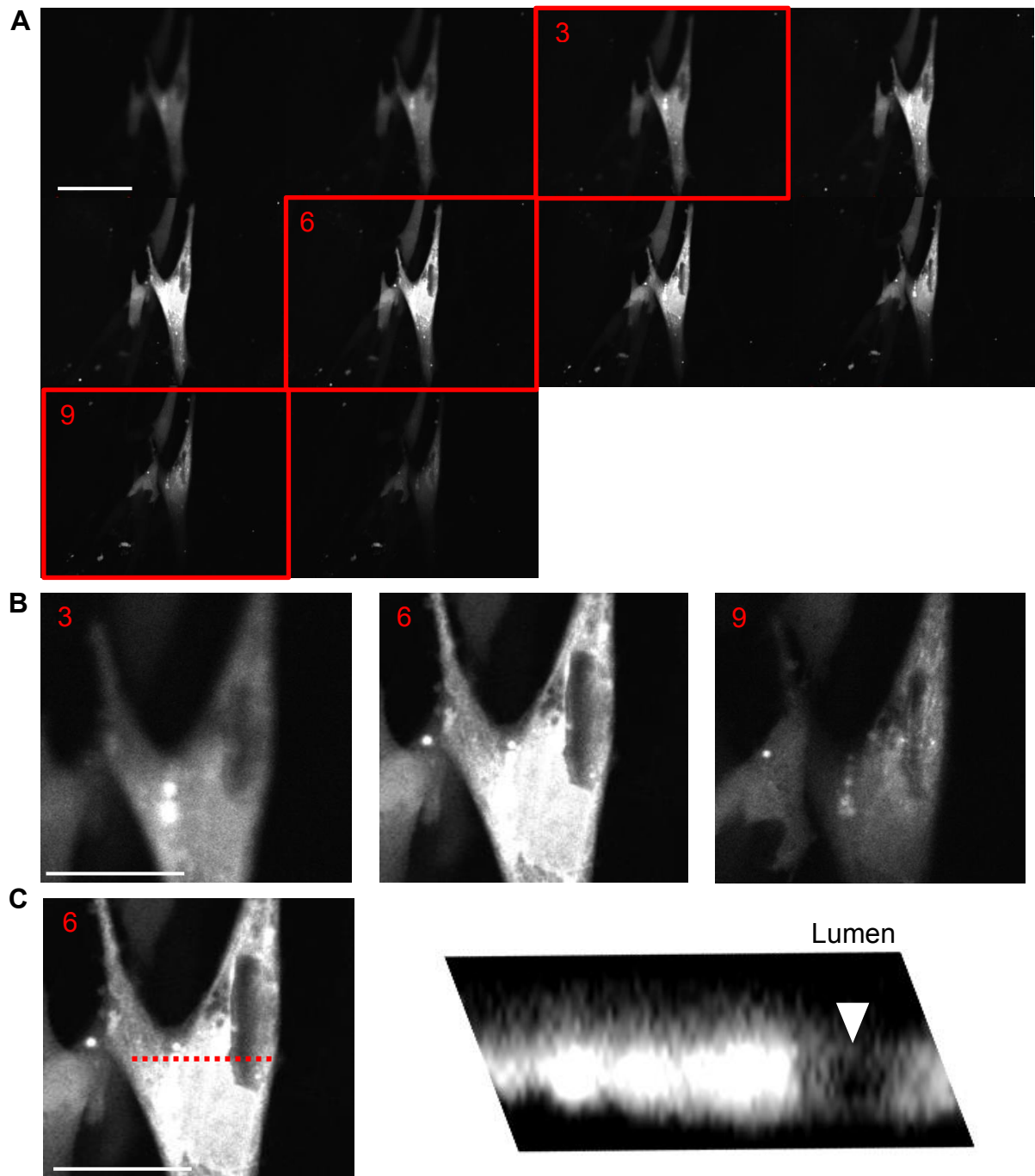


Figure 3.5 Lumen formation was visualised in CFSE labelled endothelial tubules using the co-culture tube formation assay

Endothelial cells were labelled with 5 μM CFSE and plated directly onto fibroblasts and co-cultured for six days prior to optical sectioning using confocal microscopy. **A)** A series of optical sections showed the formation of a lumen within an endothelial tubule, optical sections were taken every 1 μm , scale: 50 μm . **B)** Higher magnification images of the developing lumen within the CFSE labelled tubule, scale: 25 μm . **C)** At the position indicated by the red dotted line in the tubular image, a xyz plane was generated showing an enclosed tubular lumen surrounded by plasma membrane, scale: 25 μm .

To acquire mechanistic information about the process of lumen formation in tubules formed using the co-culture tube formation assay and determine whether lumens were formed via the vacuole fusion process or the endothelial cell rearrangement mechanism, a two colour fluorescence labelling approach was taken. CFSE labelling of endothelial cells was performed alongside labelling cells with 5 mM CellTracker orange, the two sets of fluorescently labelled endothelial cells were mixed prior to plating onto the fibroblasts. Two examples of lumen formation are shown in figure 3.6, the greyscale image revealed the difficulty in imaging and identifying the presence of lumens using a single fluorescence channel and the two coloured image allowed visualisation of lumens between cells that were labelled with different fluorescence dyes.

Endothelial tubules formed using CFSE labelled endothelial cells and CellTracker orange labelled endothelial cells were imaged on the seventh day of co-culture and the tubules were imaged using confocal microscopy and visually assessed for the presence of lumen formation. 137 endothelial tubules were imaged using two colour confocal microscopy, each tubular image was converted to greyscale for visual assessment and each tubule was studied for the presence of lumen formation. Upon the identification of lumenal formation within an endothelial tubule, the corresponding two coloured fluorescence image was examined to determine if the lumen had formed via the endothelial cell rearrangement mechanism or the vacuole fusion mechanism. There are clear morphological differences in the appearance of lumens developed via the two different lumenogenesis mechanisms; the presence of a curved and elongated lumen flanked by two endothelial cells was a visual indication of the endothelial cell rearrangement mechanism, as shown in the tubular images in

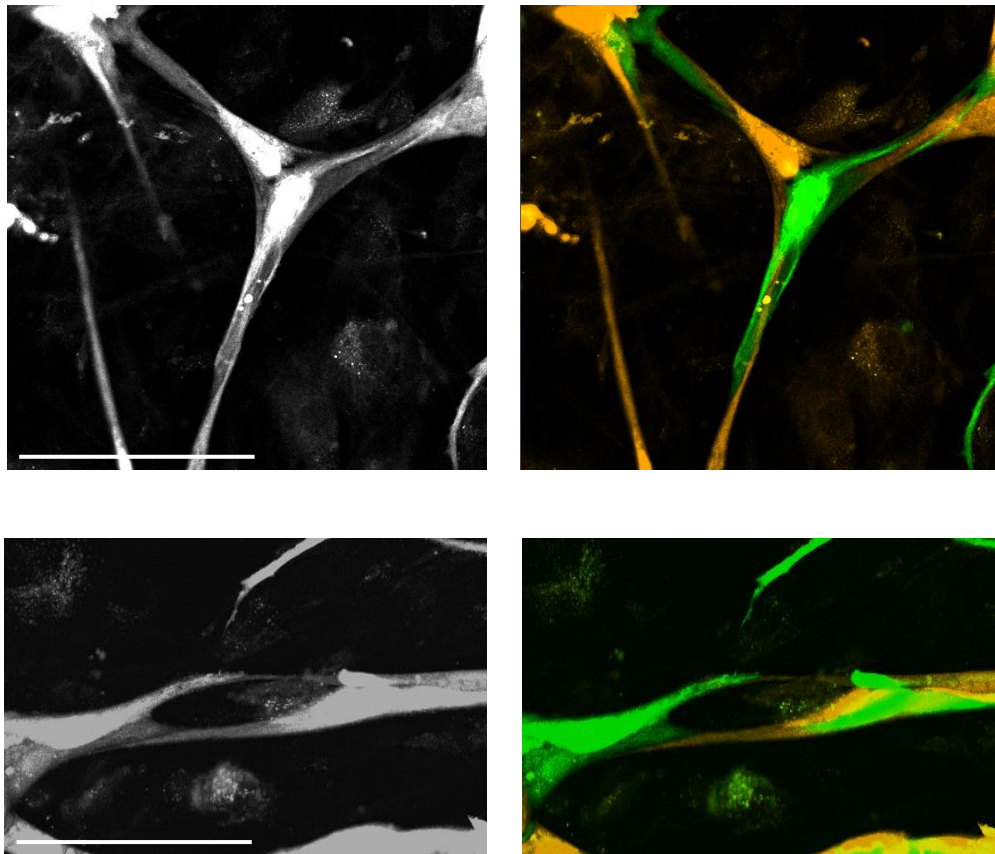


Figure 3.6 Evidence of the endothelial cell rearrangement mechanism was observed within endothelial tubules formed using cells labelled with CFSE and CellTracker orange

Endothelial cells were labelled with either 5 μ M CFSE (green) or 5 mM CellTracker orange (orange) and were mixed prior to plating on top of fibroblasts. Imaging was performed on the seventh day of co-culture. Greyscale and corresponding coloured images of endothelial tubules showed evidence of lumen formation, scale: 100 μ m.

figure 3.6, where an extracellular space developed into the lumen between adjacent endothelial cells, which were often labelled with different coloured fluorescent dyes. Whereas, endothelial lumens which form via the vacuole fusion mechanism often initially have several small circular luminal spaces within close proximity showing the presence of vacuoles. During luminal expansion there is vacuole fusion and larger irregular shaped lumens can be observed. Upon quantitation of the tubular images, 74.5% tubules contained lumens, all of these lumens were formed via the endothelial cell rearrangement mechanism. The high percentage of tubules containing lumens also provided evidence that the co-culture tube formation assay is a suitable assay to study the later processes of angiogenesis including endothelial extension into tubules and lumen formation.

3.5. Visualising the uptake of fluorescence media into luminal spaces of tubules

To provide further evidence that endothelial tubules developed lumens in the co-culture tube formation assay, red fluorescent dextran tracer was added into the co-culture media two days prior to imaging CFSE labelled endothelial tubules. The tubules were formed over a period of six days and upon imaging the dextran tracer was visualised within some stalk cells of the tubules, indicated by the arrows in figure 3.7.

The presence of dextran tracer inside the tubules revealed that the tubules were in the initial stages of lumen development as the luminal space was relatively small measuring approximately 8 μm . Visualising the endothelial tubules in this way was

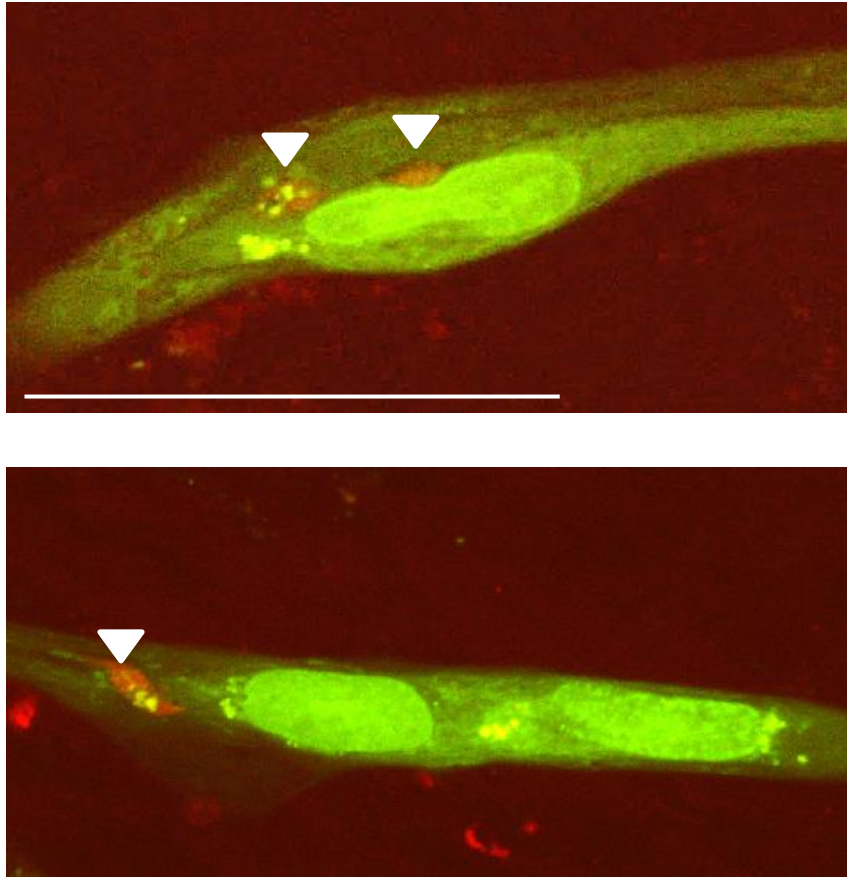


Figure 3.7 Tubular lumens take up fluorescent dextran tracer from surrounding culture media

Dextran Texas red fluorescent dye was added to the co-culture media two days prior to imaging endothelial tubules labelled with 5 μM CFSE. The red fluorescent tracer was taken up into luminal spaces within some stalk cells of endothelial tubules as indicated by the arrows, scale: 50 μm .

able to confirm that lumens developed within the tubules formed in the co-culture tube formation assay.

3.6. Staining of tubular apical and basolateral cell surface markers

Prior to lumen formation, the endothelial cells exist as a cord of cells connected by cellular junctions. As stated by Herbert and Stainier, the first stage of endothelial tubular lumenogenesis involves establishing the apical and basolateral cell surfaces via polarisation, this step is followed by the redistribution of junctional proteins and the glycoprotein podocalyxin is repositioned to the apical endothelial cell membrane²³. Podocalyxin is then responsible for the recruitment of F-actin and moesin to this surface which aids in expanding the lumen²³. Therefore, podocalyxin is an apical cell surface marker for the process of lumenogenesis.

The ECM secreted by the fibroblasts in the co-culture tube formation assay acts as a scaffold for the endothelial cells and therefore plays a critical role in influencing the tubular morphology. Collagen I, IV and VI are key components of the basal lamina along with other matrix proteins including fibronectin, tenascin-C and decorin²². Endothelial cells use $\alpha_1\beta_3$ integrin mediated signalling to adhere to collagen IV providing an anchoring mechanism to enable extension and elongation to form successful tubules. Collagen IV is a basolateral cell surface marker for the process of lumenogenesis.

In this study, lumen formation was further investigated by staining for the presence and localisation of podocalyxin and collagen IV in endothelial tubules on the seventh, fourteenth and twenty-first day of co-culture in the co-culture tube formation assay, the corresponding images are shown in figure 3.8.

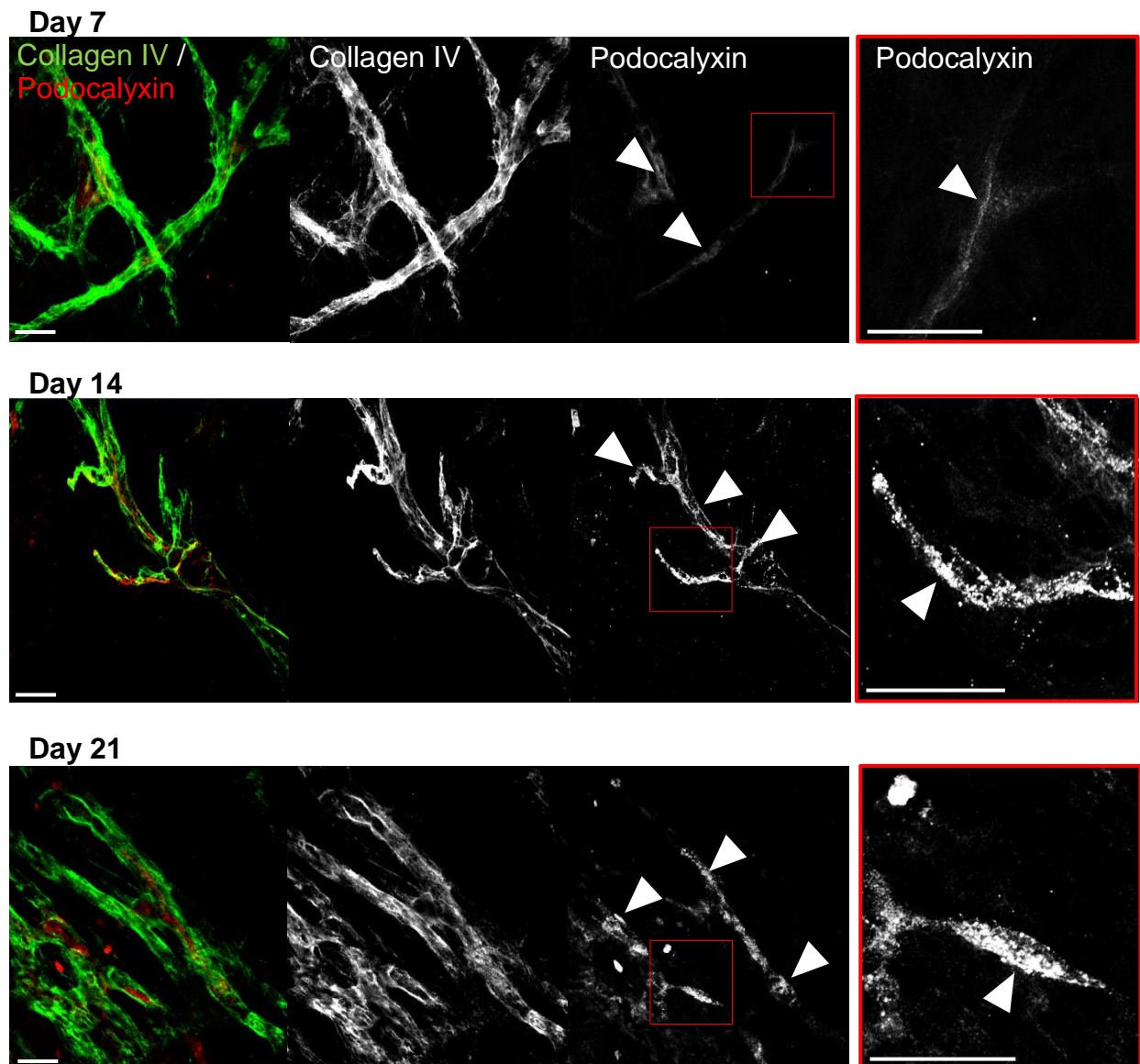


Figure 3.8 Lumen formation was confirmed within endothelial tubules by staining for apical and basolateral cell surface markers

Endothelial tubules formed using the co-culture tube formation assay were stained on the seventh, fourteenth and twenty-first day of co-culture for the cell surface markers podocalyxin and collagen IV. Tubule formation was identified with collagen IV staining and lumen formation was identified with podocalyxin staining. The arrows in the podocalyxin images indicate which regions of the tubules formed lumens; a tubular lumen region was also outlined with a red box and shown at higher magnification. The higher magnification podocalyxin stained images shows the accumulation of podocalyxin expression on the apical tubular surface during tubular formation in the co-culture tube formation assay, scale: 50 μ m.

Staining for podocalyxin and collagen IV in the investigation of lumen formation confirmed that both apical and basal cell surface markers were present on tubules from day seven through to twenty-one of co-culture. Collagen IV was imaged on the basal surface of the tubules, whereas podocalyxin was imaged on the apical surfaces. An advanced tubular network was observed on day twenty-one of co-culture, which was evident due to the strong staining of collagen IV on the tubules. The images of the stained endothelial tubules also revealed that there was an increase in the level of apical podocalyxin expression on the tubules from day seven to fourteen of co-culture, as shown in the high magnification podocalyxin images in figure 3.8. There was a large increase in podocalyxin expression between day seven to fourteen, however the level of podocalyxin on day twenty-one appeared to be comparable to that of day fourteen.

The confocal tubular images were quantified for tubule and lumen formation through the visualisation of collagen IV and podocalyxin, ten fields of view on days seven, fourteen and twenty one of co-culture were assessed. The quantification revealed that there was a 60.42% increase in tubule formation from day seven to twenty-one of co-culture, as the number of endothelial tubules on day seven was 29, on day fourteen was 26 and on day twenty-one was 48. The percentage of tubules containing lumens remained high for the duration of the assay with 75.86% tubular lumens present on day seven, 73.08% on day fourteen and 68.75% on day twenty-one.

3.7. Expressing the lifeact peptide to outline developing lumens and visualise filopodia formation

F-actin is recruited to the lumen by podocalyxin prior to lumen expansion in developing tubules²³. Therefore, to visualise the organisation of the actin cytoskeleton in endothelial tubules undergoing lumen formation, endothelial cells that had been transduced to express the lifeact peptide fused to fluorescent proteins were used in the co-culture tube formation assay.

Endothelial cells were transduced to express the pWPXL-lifeact-GFP or lifeact-RFP plasmids and were plated directly onto fibroblasts in the co-culture tube formation assay. Live-cell imaging to study the actin dynamics of the tubules was performed to visualise the organisation of the actin fibres within the endothelial tubules during co-culture.

The confocal image in figure 3.9A shows the actin organisation in an adhered endothelial cell; fibrous networks of F-actin fibres were distributed as a web throughout the cell and the presence of an actin rim was visualised at the plasma membrane which clearly outlined the cellular edges. Using endothelial cells which expressed the lifeact peptide conjugated to the fluorescent proteins GFP and RFP in the co-culture tube formation assay allowed excellent visualisation of the organisation of the actin fibres at the branching points of the tubules, shown in figure 3.9B and revealed the F-actin fibres present within the large numbers of filopodia on the surface of the tip and stalk cells, shown in figure 3.9C. The F-actin fibres were shown to be present in a structurally organised manner along the full length of the tubules with thicker actin fibres situated at the tubular edges.

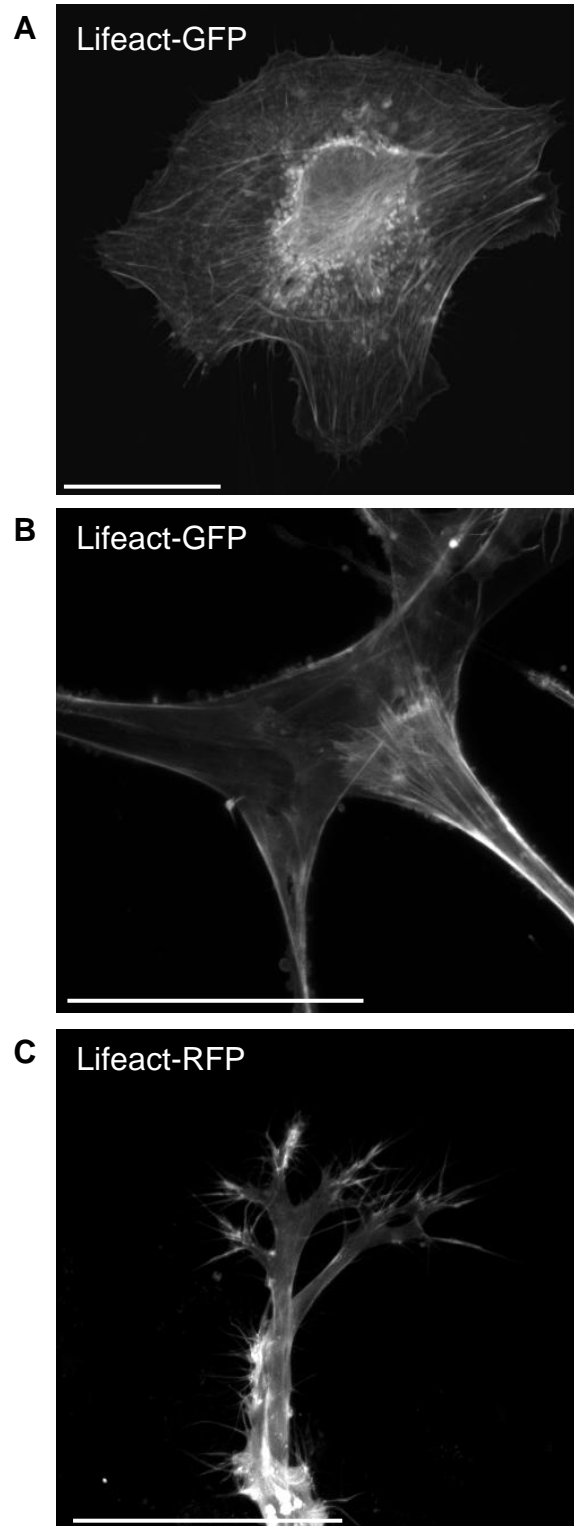


Figure 3.9 Expression of the lifeact peptide conjugated to fluorescent proteins within endothelial cells enabled the organisation of the actin cytoskeleton to be visualised

A) Confocal image of an endothelial cell which expressed the lifeact-GFP plasmid,
B) Confocal images of endothelial tubules expressing the lifeact-GFP plasmid,
C) lifeact-RFP plasmid. Imaging was performed on the sixth day of the co-culture tube formation assay, scale: 50 μm .

Visualising the lifeact expressing endothelial tubules revealed that the F-actin fibres were situated around the endothelial lumens, the lumens predominantly formed within stalk cells of the tubules; however as shown in the examples in figures 3.10 and 3.11, lumens were also observed within tip cells. Imaging the actin filaments within the tubule of figure 3.10 revealed that there was a large luminal space in the centre of the tip cell which was close to a vesicle. The optical sections of the tubule showed the lumen undergoing expansion by the fusion of vacuoles indicated by the irregular shape of the lumen. The xyz planes in figures 3.10B and 3.10C were generated from transverse tubular sections and showed that both the developing lumen and nearby vacuole were surrounded by plasma membrane. Similarly, the developing lumen and nearby vacuole within the tip cell of the tubule, shown in figure 3.11 were encapsulated by plasma membrane as shown by the xyz planes in figures 3.11B and 3.11C.

To further investigate tubular lumen formation, the image pixel intensity values were studied and provided further evidence and confirmation that lumens formed within the endothelial tubules. An optical slice of a lifeact-GFP expressing tubule shown in figure 3.11A was analysed using ImageJ for the greyscale pixel intensity values spanning across the tubule as indicated by the yellow line in figure 3.12A. A pixel intensity value of zero in the binary image indicated black in colour and signified the image background, whereas a value of 255 indicated a colour of white which signified the fluorescent tubular object in the image.

The corresponding pixel intensity plot in figure 3.12A revealed that the luminal space in the tubule correlated with a similar pixel intensity as the background. The luminal area had a measured pixel intensity value of approximately 15-20. The pixel value of

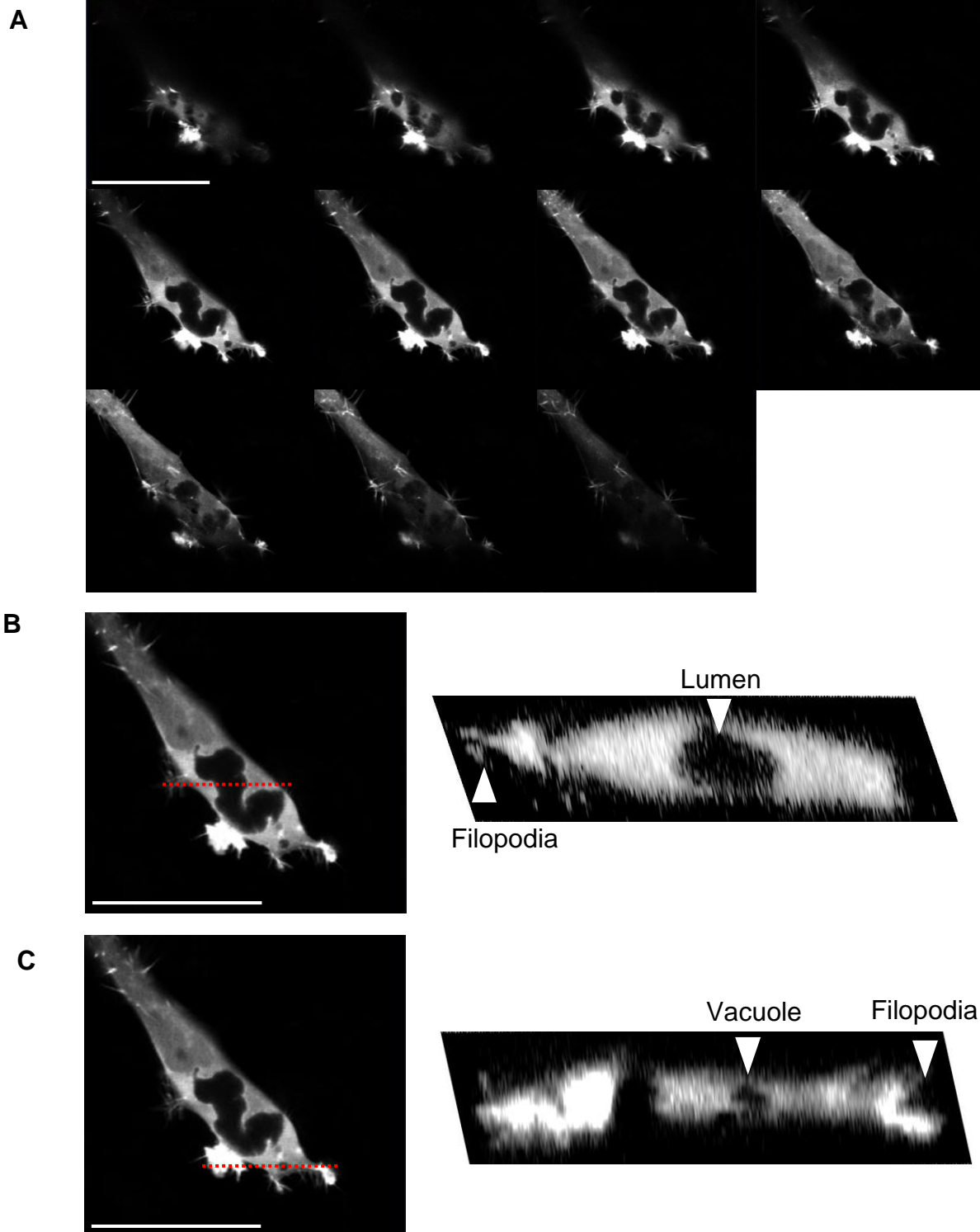


Figure 3.10 Expressing lifeact in endothelial tubules allowed developing lumens and vacuoles to be visualised

An endothelial tubule expressing lifeact-GFP was imaged on day six of co-culture. **A)** Optical sections of a lifeact-GFP expressing tubule were taken every 1 μm using confocal microscopy, **B)** at the position indicated from the red dotted line on the endothelial tubule image, xyz planes of the developing lumen and **C)** vacuole were generated showing that the lumen and vacuole were surrounded by plasma membrane, scale: 50 μm .

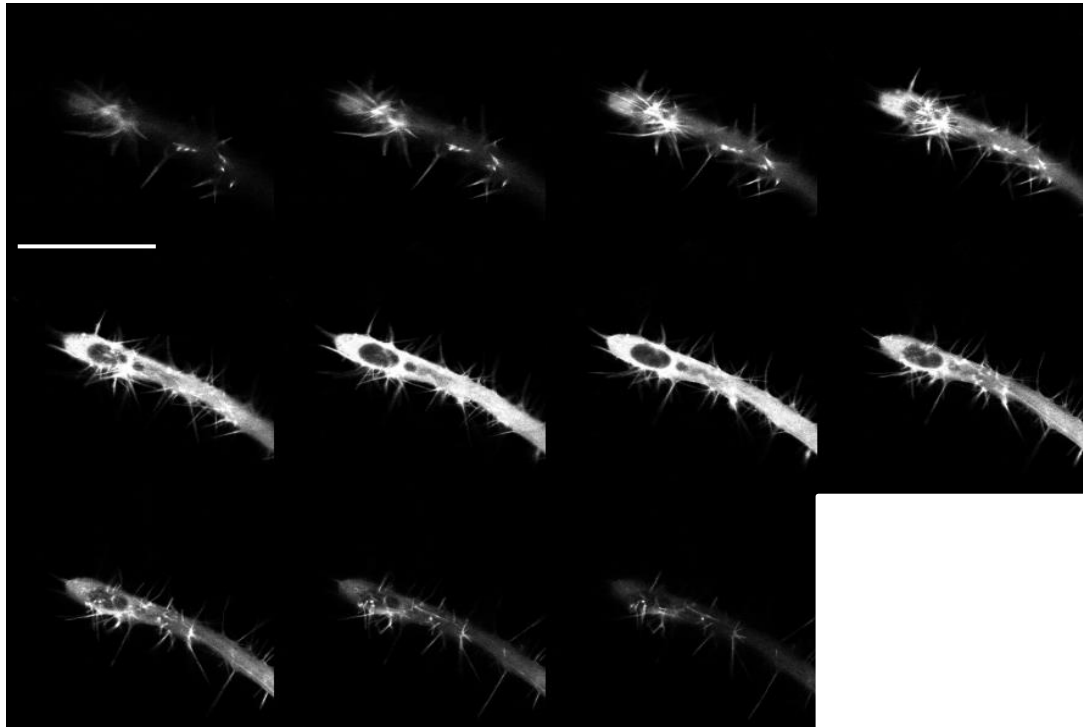
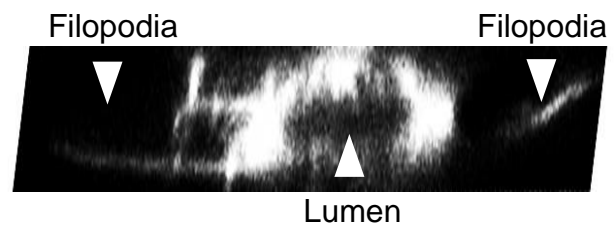
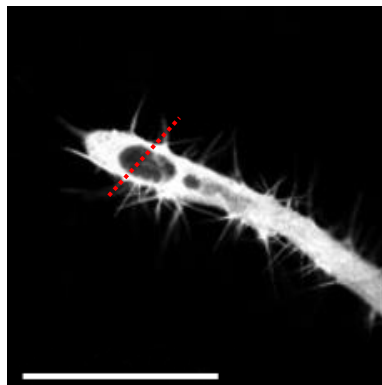
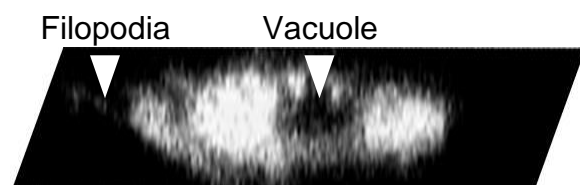
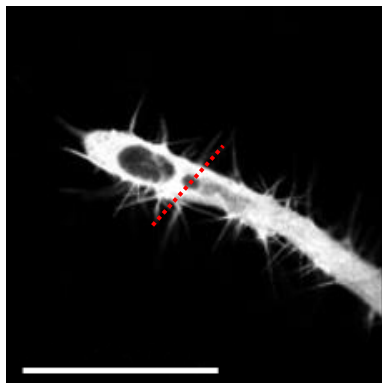
A**B****C**

Figure 3.11 Use of lifeact in endothelial tubules allowed visualisation of lumens and filopodia extensions

An endothelial tubule expressing lifeact-GFP was imaged on day six of co-culture. **A)** Optical sections of a lifeact-GFP expressing tubule were taken every 1 μm using confocal microscopy, **B)** at the position indicated from the red dotted line on the endothelial tubule image, xyz planes of the developing lumen and **C)** vacuole were generated showing that the lumen and vacuole were surrounded by plasma membrane, scale: 20 μm .

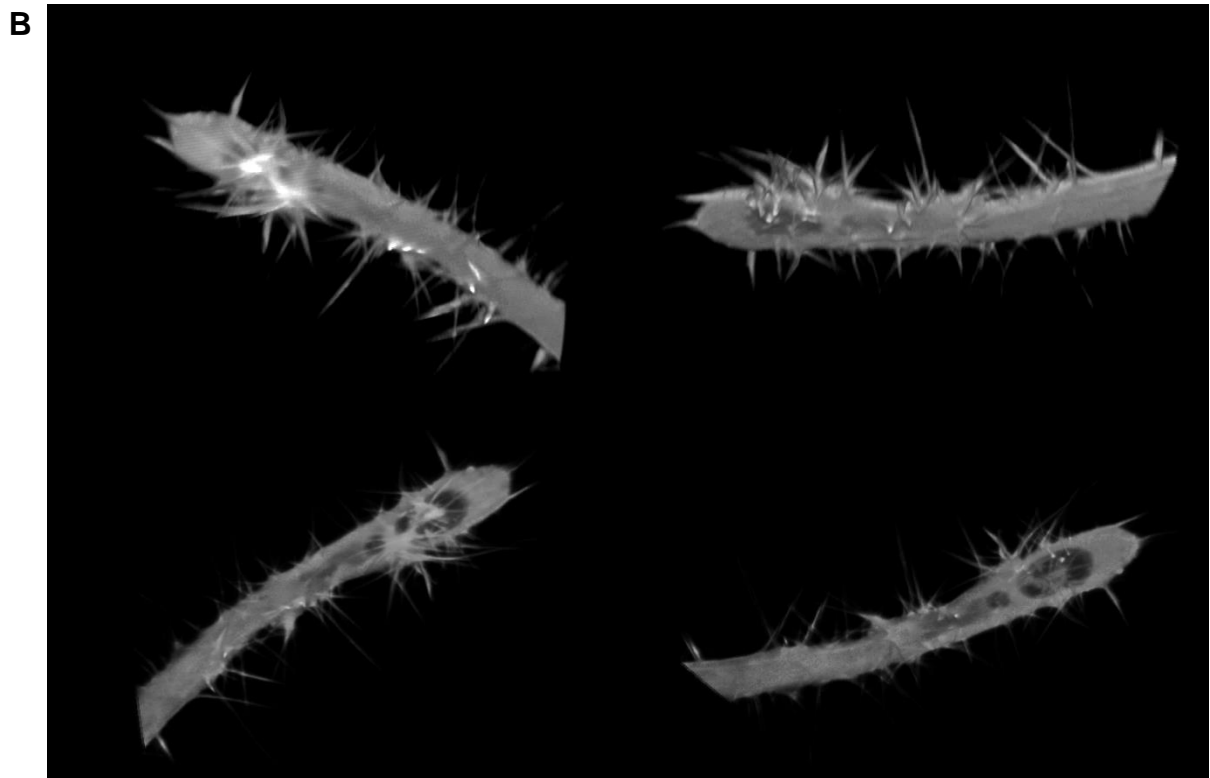
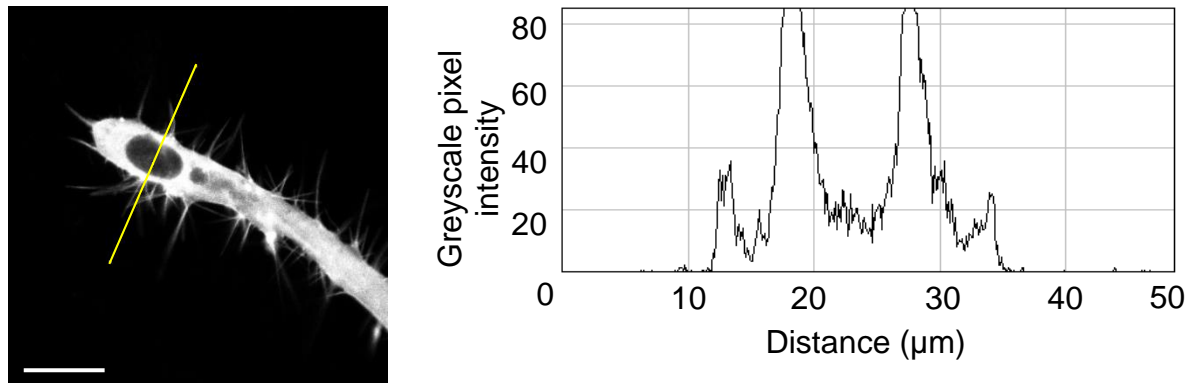


Figure 3.12 Lumen formation was confirmed by analysing the image pixel intensities and visualising 3D projections of endothelial tubules

A) An optical section of a tubule was analysed for pixel intensities and the corresponding graph was plotted which was calculated based on pixel intensities along the yellow line, scale: 20 μm. **B)** Three dimensional projectional images of the compressed confocal optical sections of a lifeact-GFP expressing tubule which was rotated to observe the endothelial tubule from different angles.

the lumen was slightly higher than the image background intensity value of zero due to the presence of the endothelial tubular surface below the lumen as the tubule is three dimensional. The intensity plot also revealed that the diameter of the lumen was approximately 6 μm . The optical image sections of the tubule were compressed and three dimensional reconstructional images of the tubule were generated using ImageJ, some examples of the different angles of the projections are shown in figure 3.12B. The three dimensional reconstructions enabled visualisation of the tubule and lumen from all different angles allowing the actin organisation and the structure of the tubule to be studied in detail. By selecting different slices to view in this way the lumen was clearly observed in the centre of the tubule which was surrounded by the endothelial tubular surface which had formed filopodia.

Expressing the lifeact peptide to visualise the F-actin fibres also proved useful for studying the presence of filopodia along with studying lumen formation, comparable images visualising endothelial tubular filopodia formation could be achieved by staining the endothelial tubules for the expression of the endothelial specific glycoprotein CD31. The image in figure 3.13A showed that CD31 was localised on the surface of endothelial cells and showed increased expression at cell-cell contacts in adhered cells. Visualising the localisation of CD31 in the co-culture assay as shown in figure 3.13B revealed that the glycoprotein was expressed on the tip and stalk cells of the tubules and provided clear visualisation of endothelial filopodia formation. However, to visualise the localisation of this protein, the tubules must be fixed and stained therefore expressing the lifeact peptide had the advantage of live cell imaging and monitoring the formation of filopodia with the development of the tubules.

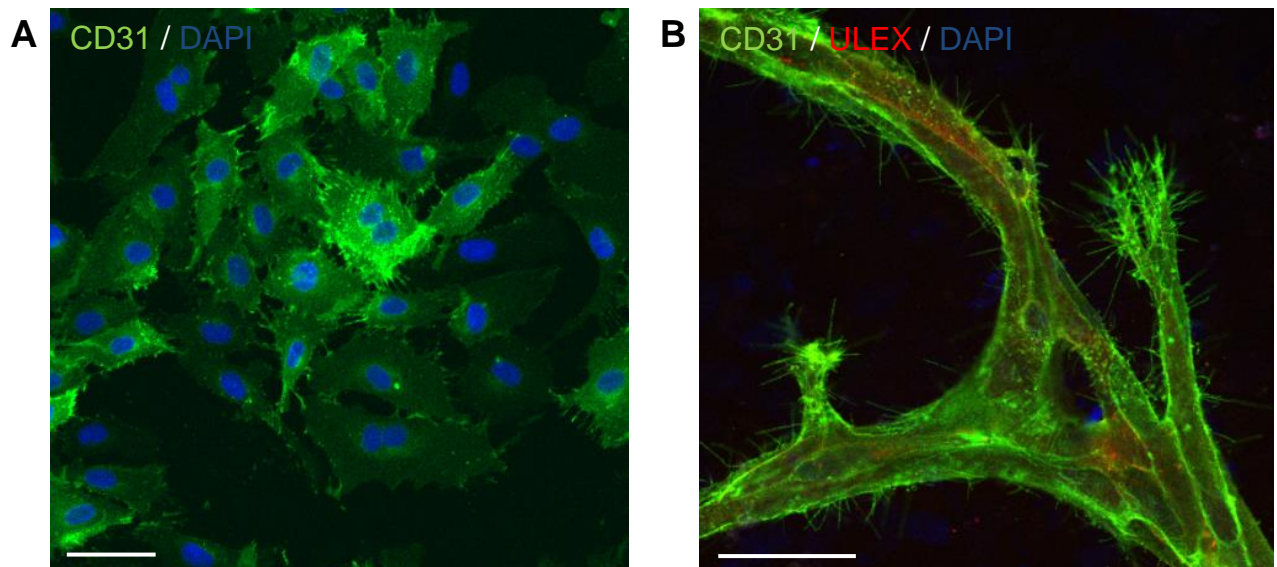


Figure 3.13 Filopodia were clearly observed on endothelial tubules by staining for the endothelial specific glycoprotein CD31

A) Endothelial cells were plated directly onto coverslips and cultured to form a confluent monolayer of cells before immunofluorescence was performed to study the localisation of the endothelial glycoprotein CD31 (green) , shown to be expressed on the surface of the endothelial cells with increased expression at cell-cell contacts. Nuclei were stained with DAPI (blue), scale: 50 μm . **B)** Endothelial cells were cultured for seven days with human dermal fibroblasts in the co-culture tube formation assay before immunofluorescence was performed. Rhodamine labelled ulex (red) was used to selectively bind to endothelial glycoproteins and glycolipids allowing the endothelial cells to be clearly distinguished from the fibroblasts in the assay, scale: 50 μm .

3.8. Visualising cellular interactions and lumen formation by using a mixture of lifeact-GFP and lifeact-RFP expressing cells

Migrating cells extend filopodia to facilitate in directed movement; these long cytoplasmic projections not only sense the micro-environment for chemotropic cues but they also play a role in aiding cell-cell interactions. To visualise the structure of the actin cytoskeleton and the interactions between the endothelial cells during the formation of tubules, endothelial cells which expressed pWPXL-lifeact-GFP or lifeact-RFP were mixed prior to plating on top of fibroblasts in the co-culture tube formation assay.

The image in figure 3.14A shows endothelial tubules consisting of lifeact-GFP and lifeact-RFP expressing cells extending filopodia from the tip cells towards the other endothelial tubule in close proximity to participate in cellular interactions. Upon studying the two coloured optical section images in figure 3.14B it was apparent that the tubule was composed of lifeact-GFP and lifeact-RFP endothelial cells undergoing lumen formation. The lifeact-GFP cell in the tubule was surrounded by the lifeact-RFP cells and there were two additional luminal areas present in the lifeact-GFP cell, the lifeact-RFP cell appeared to be underneath the lifeact-GFP cell. The two colour fluorescence images of the endothelial tubules provided greater understanding of the development of the tubules in comparison to studying one colour images. To investigate if the developing lumen within the tubule was surrounded by plasma membrane, a transverse section of the tubule spanning the luminal region was selected and a xyz plane was created. The xyz plane shown in figure 3.14C showed that the developing lumen was enclosed by plasma membrane.

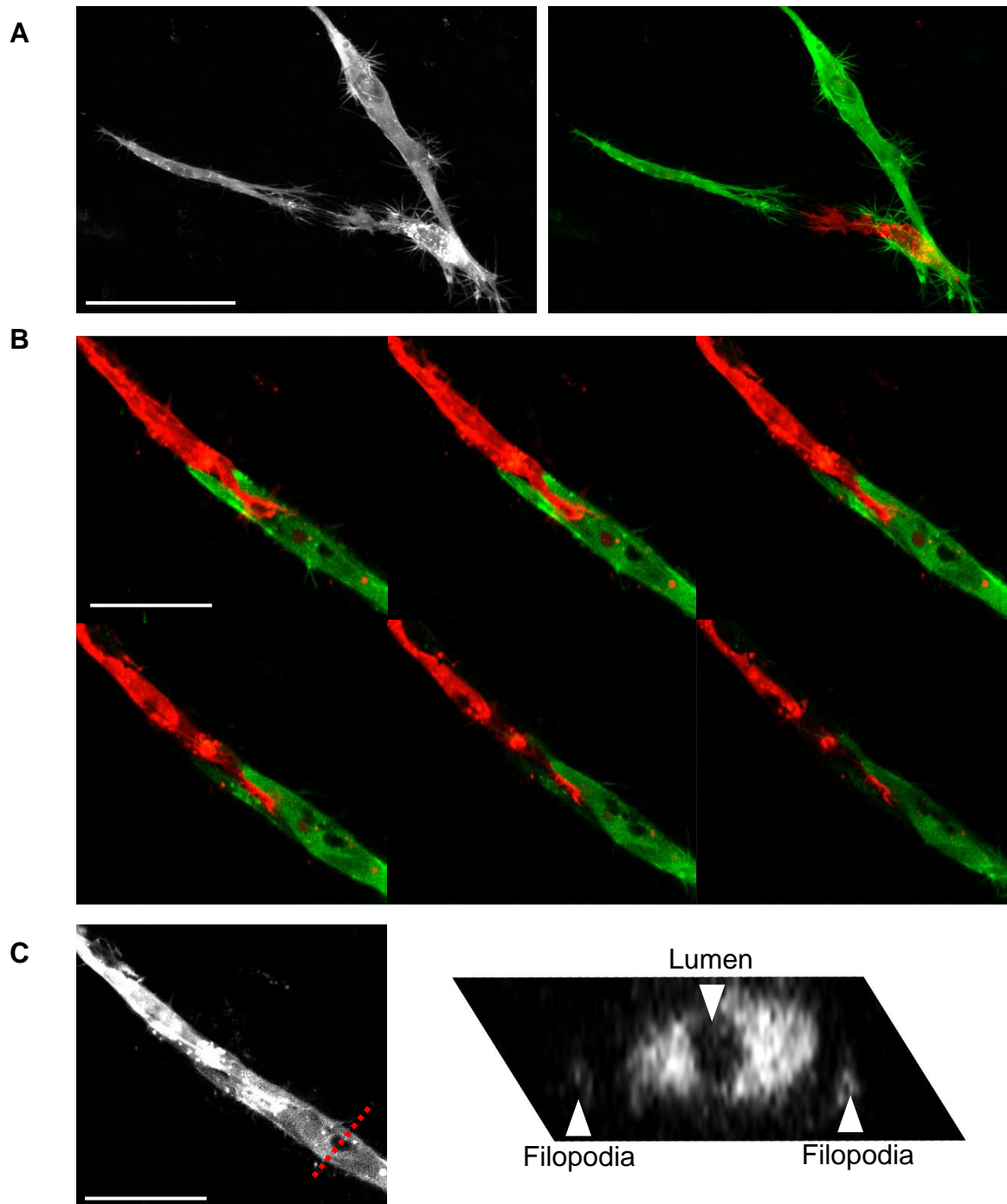


Figure 3.14 Filopodia and developing lumens formed within endothelial tubules expressing lifeact-GFP and lifeact-RFP

Endothelial cells expressing lifeact-GFP and lifeact-RFP were mixed prior to plating on top of fibroblasts in the co-culture tube formation assay, the F-actin organisation was imaged on the seventh day. **A)** Greyscale and coloured fluorescence image of filopodia extensions from lifeact-GFP and lifeact-RFP HUVECs in a tubule, **B)** Greyscale compressed confocal image of a lifeact-GFP and lifeact-RFP tubule, **C)** at the position indicated from the red dotted line on the endothelial tubule image, a xyz plane showed the developing lumen was surrounded by plasma membrane scale: 50 μm .

Using confocal microscopy alongside the expression of the lifeact peptide conjugated to the two different fluorescent proteins GFP and RFP enabled the mechanism of lumenogenesis within endothelial tubules formed in this assay to be investigated. Endothelial tubules formed using either cells expressing lifeact-GFP, lifeact-RFP or a mixture of both cell types were imaged on the seventh day of co-culture and twenty five tubules per cell type were assessed and quantified for lumen formation. The endothelial tubules were imaged using one or two colour confocal microscopy dependent on if the tubules consisted of lifeact-GFP, lifeact-RFP or a mixture of the two endothelial cell types. The imaged tubules were assessed for the presence of lumen formation by converting the coloured fluorescence images to greyscale which enabled clear visualisation of the endothelial tubules and lumens. To further study lumenogenesis in endothelial tubules formed using a mixture of lifeact-GFP and lifeact-RFP expressing cells, the corresponding coloured fluorescence image was examined, which permitted greater understanding of how the endothelial cells were arranged within the tubules. There were morphological differences of the lumens formed using the two different mechanisms, as outlined in the example images in figure 3.15. As mentioned previously in section 3.4, the presence of a curved and elongated lumen between adjacent endothelial cells showed the endothelial cell rearrangement mechanism, whereas circular luminal spaces showed the presence of vacuoles. The tubular images were manually assessed for the presence of lumen formation and the observed mechanism of lumenogenesis.

Quantification of the tubular images revealed that lumenogenesis occurred within the tubules that were formed using lifeact-GFP, lifeact-RFP and a mixture of lifeact-GFP and lifeact-RFP expressing cells. The highest percentage of lumen formation

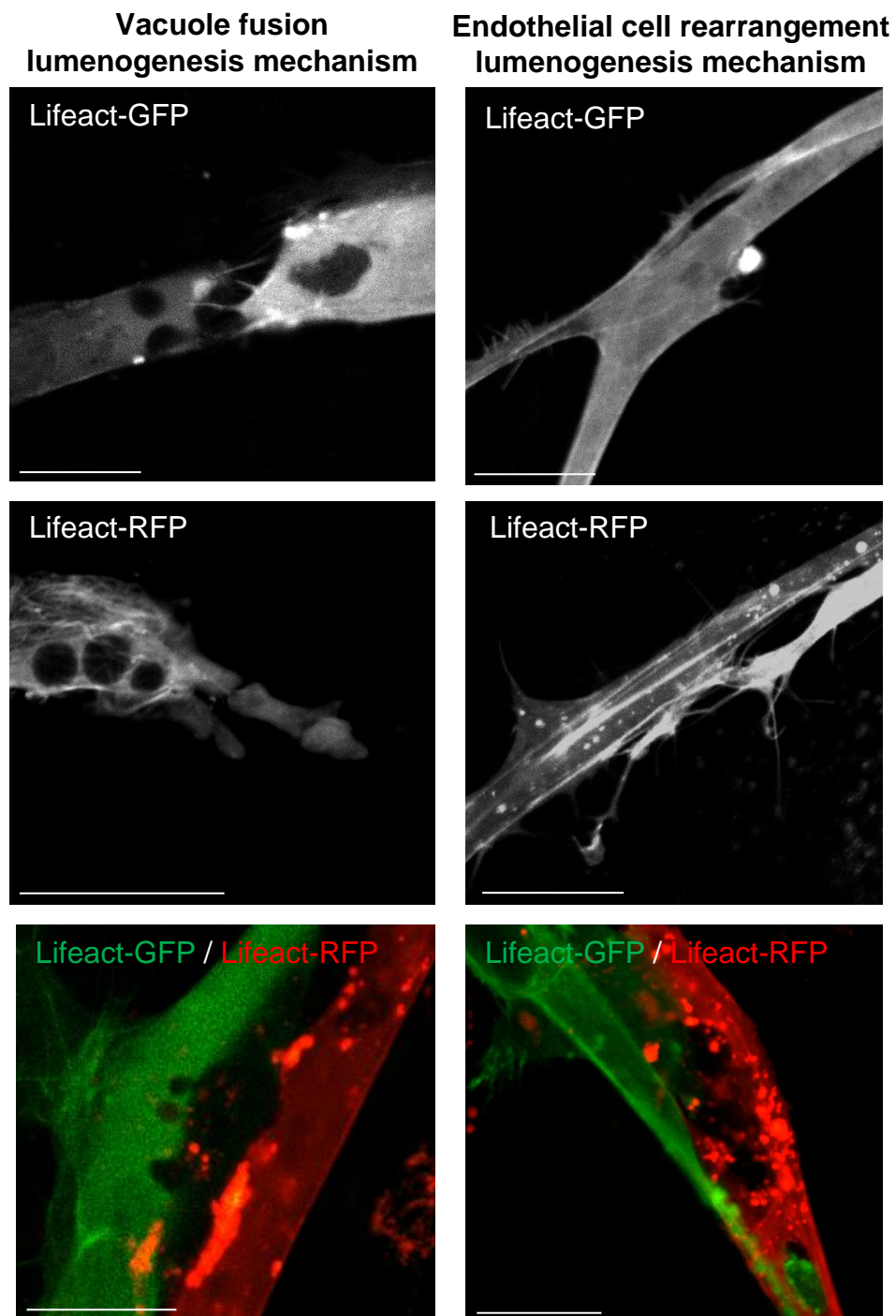


Figure 3.15 Example images of the endothelial lumenogenesis mechanisms observed in tubules which expressed the lifeact peptide conjugated to fluorescent proteins

Example confocal images of endothelial tubules which produced lumens via the vacuole fusion and the endothelial cell rearrangement mechanisms. The endothelial tubules were produced using the co-culture tube formation assay using lifeact-GFP, lifeact-RFP and a mixture of lifeact-GFP and lifeact-RFP expressing endothelial cells and imaged on the seventh day of co-culture, scale: 20 μ m.

Table 3.1 Quantification of the lumenogenesis mechanisms that were observed during endothelial tubule formation

The quantification of lumen formation and the lumenogenesis mechanisms were determined by manually assessing tubular images generated from the co-culture tube formation assay. Twenty five images for each cell type used in the co-culture assay using either lifeact-GFP, lifeact-RFP or a mixture of lifeact-GFP and lifeact-RFP expressing cells were analysed. The tubular images for each cell type used in the assay were taken from three different co-culture assays performed on different days and were pooled together to calculate percentage values of tubular lumen formation and the observed lumenogenesis mechanism.

	Lifeact-GFP expressing HUVECs	Lifeact-RFP expressing HUVECs	Lifeact-GFP and Lifeact-RFP expressing HUVECs
Tubules without lumen formation	10	13	12
Tubules with lumen formation	15	12	13
Percentage of lumen formation	60.00%	48.00%	52.00%
Vacuole fusion lumenogenesis mechanism	6	3	4
Endothelial cell rearrangement lumenogenesis mechanism	9	9	9
Percentage of lumens formed via the vacuole fusion mechanism	40.00%	25.00%	30.77%
Percentage of lumens formed via the endothelial cell rearrangement mechanism	60.00%	75.00%	69.23%

occurred in lifeact-GFP expressing tubules, 60.00% of these tubules formed lumens, followed by 52.00% for mixed lifeact-GFP and lifeact-RFP tubules and 48.00% for lifeact-RFP expressing tubules. Interestingly, both mechanisms of lumen formation were observed in tubules using all three cell types; however, as shown in table 3.1, a higher percentage of lifeact-GFP expressing tubules formed lumens via the vacuole fusion mechanism in comparison to the lifeact-RFP expressing tubules. Whereas, more lifeact-RFP expressing tubules formed lumens via the endothelial cell rearrangement mechanism compared to the lifeact-GFP expressing tubules. The endothelial tubules formed from a mixture of lifeact-GFP and lifeact-RFP expressing cells showed percentage values in between those of the individual lifeact-GFP and lifeact-RFP expressing tubules. Although overall assessment of the endothelial tubules formed using the expression of the lifeact plasmids showed that the endothelial cell rearrangement mechanism was the dominant mechanism by which lumens developed in tubules formed using the co-culture tube formation assay, with 75.00% of lifeact-RFP tubular lumens formed using this mechanism, 69.23% of lifeact-GFP and lifeact-RFP tubules and 60.00% of lifeact-GFP tubules.

3.9. Chapter discussion

The results presented in this chapter confirmed that endothelial tubules formed using the co-culture tube formation assay develop lumens during co-culture with fibroblasts. In the co-culture tube formation assay, the elongation of the endothelial cells and subsequent growth of the tubules is highly dependent on the fibroblasts depositing extracellular matrix components, which acts as a suitable scaffold to

support the extension of the endothelial cells into tubular structures¹³². Importantly, the fibroblasts must secrete pro-angiogenic factors such as VEGF to promote endothelial migration and encourage tubule formation^{134,135}. The fibroblasts secrete VEGF in response to being stimulated by bFGF, which was present in the bovine brain extract solution within the co-culture media; bFGF also stimulates the growth of the endothelial cells as well as the fibroblasts¹³⁵.

The fluorescent endothelial labelling techniques presented in this chapter, alongside confocal microscopy confirmed that lumens were formed in endothelial tubules generated using the co-culture tube formation assay, the techniques revealed clearly that lumen formation is initiated in both tip and stalk cells within tubules. The use of highly emissive fluorescent dyes and proteins to label the endothelial cells were essential for imaging the tubular structure and to distinguish between the endothelial cells and the fibroblasts in the co-cultures. Labelling of the endothelial cells prior to use in the assay with the cell proliferation dye CFSE achieved high levels of fluorescence emission from the cytoplasm of the endothelial tubules for the duration of the assay allowing the development of the tubules to be monitored effectively with confocal microscopy. CFSE was able to maintain a long cellular retention time due to becoming covalently bound to lysine residues inside the endothelial cells²²⁰. This method of CFSE labelling endothelial tubules was used in conjunction with the addition of dextran fluorescence dye into the co-culture media to confirm lumen formation via the vacuole fusion mechanism. Using a fluorescence tracer is a commonly used method to investigate lumen formation, Yang *et al.* studied lumen formation within endothelial cells on collagen gels by visualising the uptake of 6-carboxyfluorescein into endothelial luminal spaces³⁵. Similarly Kamei *et al.* used

carboxyrhodamine and showed that the fluorescence dye was endocytosed in endothelial cells cultured in collagen matrices¹⁸. The results from this study showing the internalisation of dextran fluorescence dye in CFSE labelled tubules was consistent with that observed by others that pinocytosis is responsible for the uptake of the dye. To investigate this result further, the plasma membrane could be fluorescently labelled and visualisation of membrane invaginations at the tubular edges with subsequent vesicle and vacuole formation would further support this observation.

The observation of tip cell lumens through imaging the organisation of the tubular actin cytoskeleton in this study showed that the process of lumenogenesis is not restricted to stalk cells in tubules that form in the co-culture tube formation assay. The main function of the tip cells is to sense the microenvironment to guide the direction of vascular growth, hence their presence at the front of the endothelial sprout, whereas stalk cells are located behind the tip cell to elongate the vessel through proliferation and participate in lumenogenesis¹⁵. The lumen would progressively increase in size as it expands and extend into tip cells; however the images in this study showed that lumens also initiate and develop in tip cells in tubules formed in the co-culture assay.

The most useful technique for clearly visualising the presence and morphology of endothelial lumens formed in the co-culture tube formation assay was achieved by imaging the tubular actin cytoskeleton. Imaging the organisation of the actin cytoskeleton was achieved by expressing the lifeact peptide conjugated to the fluorescent proteins GFP and RFP alongside using confocal microscopy. It is known that F-actin is a major structural component of cells, required to generate mechanical

and tensile forces which co-ordinate cellular shape and motility⁸⁷. The efficient function of the actin cytoskeleton is critical for the endothelial cells to undergo morphological changes and extend into the complex tubular structures. This new technique for imaging endothelial lumens was possible since the 17 amino acid lifeact peptide was able to bind to the actin fibres without compromising the formation of tubules⁹⁵. Using this technique enabled excellent visualisation of the actin fibres in tip and stalk cells as well as enabling studies of the cytoskeletal organisation at the tubular branching points and of the filopodia extensions along the tubular surface. Actin fibres were present in filopodia on the surface of both tip and stalk cells, to play essential roles in cellular interactions and sensing the local environment for ephrins and semaphorins to direct tubular growth¹⁴.

Interestingly, visualising the actin cytoskeleton using lifeact expression showed that there were thicker and presumably stronger cables of actin located around the developing lumen, revealing that the shape of the lumen appeared to be strengthened and supported by the actin cytoskeleton during expansion. Thicker actin fibres were also imaged at the tubular edges, which would act to distribute contractile forces throughout the endothelial cell to direct motility and extension into tubular morphologies. Since the actin fibres outlined the boundary of the luminal spaces within the endothelial cells, it was possible to clearly observe the luminal morphologies. Due to the morphological differences in the luminal appearance developed by the two lumenogenesis mechanisms of lumen formation it was possible to visually assess and quantify the lumenogenesis mechanisms observed within the tubules.

Both the vacuole fusion and endothelial cell rearrangement mechanisms of lumenogenesis were visualised in the endothelial tubules and upon assessment of the tubular images it was revealed that endothelial lumens generated using the co-culture tube formation assay formed predominantly from the endothelial cell rearrangement mechanism. However, 40.00% of lumens formed within lifeact-GFP tubules developed via the vacuole fusion mechanism, 25.00% in lifeact-RFP tubules and 30.77% in lifeact-GFP and lifeact-RFP tubules, although it is possible that the observed vacuoles were actin formations that would not contribute to the formation of a continuous lumen. Imaging the vacuole fusion mechanism of lumenogenesis was not observed using the two colour fluorescence labelling of endothelial cells using CFSE and CellTracker orange cytoplasmic dyes. Therefore it could be possible that the binding of the lifeact peptide to the individual actin fibres could disrupt the dynamic nature of the F-actin fibres and induce cellular stress due to disrupted actin cytoskeletal function. Alternatively, the lifeact peptide may alter the mechanisms of actin polymerisation and/or branching, so as to influence the mechanism of vacuole formation. Furthermore, lentiviral transduction of endothelial cells to express the lifeact peptide conjugated to fluorescent proteins could have caused adverse cellular effects due to overexpression of the peptide. However, the absence of cellular blebbing which is also a visual indication of cellular stress would suggest that lumenogenesis via vacuole formation was not simply due to cellular stress. With the caveat that the lifeact peptide may affect lumen formation, these data indicate that imaging the organisation of the actin cytoskeleton enables better visualisation of the intracellular tubular structure compared with labelling the endothelial cytoplasm with

fluorescent dyes. Therefore, allowing the intracellular process of lumen formation to be studied in greater detail.

To further investigate whether the process of lifeact binding to the actin fibres or transfecting the endothelial cells caused the formation of cellular vacuoles, fluorescently labelled phalloidin staining would be performed on the co-cultures and the tubular actin cytoskeleton would be imaged and studied for the formation of vacuoles. However, due to the presence of the fibroblasts in the co-culture it could be challenging to image the endothelial cytoskeleton this way.

Further work to continue investigating lumen formation within endothelial tubules formed using the co-culture tube formation assay, would be to use live-cell time lapse confocal microscopy to image at high resolution the process of lumen development within endothelial tubules using the established fluorescent techniques presented in this chapter. Firstly, lifeact expressing endothelial cells would be used in the co-culture assay and time lapse microscopy would permit real time visualisation of the process of lumenogenesis from the initial stages of tubule formation through to the establishment of a stable lumen that extends as an intracellular channel through many endothelial cells. Unfortunately, it was not possible to perform time-lapse imaging during this project as there was not a suitable microscope that could be used for this study. Performing time lapse imaging would provide valuable insights and aid the investigation into the mechanisms of lumen formation in endothelial tubules formed using this assay. There would however be challenging imaging requirements for this study as the same field of view would need to be imaged over the course of several weeks to study the development of the same endothelial tubules.

Chapter Four

Designing, testing and evaluating a computer based method to analyse endothelial sprouting for screening purposes

4.1. Chapter summary

The aim of this chapter was to design, test and evaluate a new computer based analysis tool for quantifying endothelial sprouting from fluorescently labelled spheroids generated using the *in vitro* hanging drop spheroid angiogenesis assay. To test the designed ImageJ Spheroid Analysis plugin, this analysis tool was applied to fluorescently labelled spheroid images which expressed a wide range of endothelial sprouting phenotypes. The different sprouting phenotypes were generated through a kinase inhibitor screen, in which a library of 80 small molecule kinase inhibitors were added into the assay and endothelial sprouting was quantified using the plugin. The resulting plugin outputs were evaluated and discussed, as well as compared to the manual process of measuring the total sprouting length of the spheroids.

A further aim of this project which is presented in this chapter was to screen kinases to identify those which have roles in endothelial sprouting, migration and tube formation and this data has been presented in analysis heat map tables to enable easy identification of kinase inhibitors which affected these processes.

The structure for this chapter is as follows: section 4.2 chapter introduction, section 4.3 presents the computer based analysis tool designed to analyse endothelial sprouting, section 4.4 testing and evaluating the computer based analysis tool, section 4.5 screening kinases to identify those with roles in sprouting angiogenesis, section 4.6 applying the computer based analysis tool to spheroids treated with p-21 activated kinase (PAK) inhibitors, section 4.7 applying the computer based analysis tool to spheroids treated with Bruton's tyrosine kinase (BTK) inhibitors, section 4.8 screening kinases to identify those with roles in endothelial migration and tube formation, section 4.9 chapter discussion.

4.2. Chapter introduction

In vitro angiogenesis assays are widely used to understand the pathways and interactions involved in the formation of new blood vessels and determine the effectiveness of pro- or anti-angiogenic agents. Angiogenesis is a complex process and at present there is not an individual assay that encompasses all aspects of angiogenesis. *In vitro* angiogenesis assays generally focus on a particular cellular process involved in angiogenesis such as endothelial migration, proliferation or tube formation; therefore there is a vital requirement to use multiple assays when screening compounds to identify and determine which parts of the angiogenic process are affected.

In the initial stages of angiogenesis, endothelial cells degrade the surrounding basement membrane and migrate towards an angiogenic stimulus; this process involves endothelial invasion, migration and proliferation which can be studied in detail using the *in vitro* hanging drop spheroid angiogenesis assay. In this assay, multicellular masses of endothelial cells are generated and embedded into an ECM component to produce a three dimensional model of angiogenesis¹¹⁰⁻¹¹³. To determine the effect of compounds or identify genes involved in endothelial sprouting the resulting lengths or numbers of the spouts can be quantified. In this chapter, the ImageJ Spheroid Analysis plugin was used to rapidly analyse these sprouting parameters automatically.

There are many widely used *in vitro* angiogenesis assays that can be employed to study the migratory response of cells; one of these is the scratch wound angiogenesis assay in which an area of cells is removed from a confluent monolayer of endothelial cells¹⁰¹. Successive images can be taken to monitor the rate of scratch

closure through cell migration and the rate or percentage of closure can be calculated to determine the effects of angiogenic agents or to identify genes that regulate cell migration^{103,109}.

The final stages of angiogenesis involve cell differentiation and the formation of three dimensional tubular structures. The ability of endothelial cells to form these structures in the presence of angiogenic compounds can be tested using the matrigel tube formation angiogenesis assay^{128,129}. The network of tubules can be easily quantified by measuring the number of complete loops formed within the endothelial network using an automated ImageJ plugin known as Angiogenesis Analyzer, which is widely and freely available and enables the effect of compounds on the angiogenic pathway to be easily assessed.

4.3. Computer based analysis tool designed to analyse endothelial sprouting

The hanging drop spheroid angiogenesis assay is an *in vitro* assay used to study the process of endothelial sprouting. Firstly in this study, time-course imaging was performed to monitor the development and formation of endothelial sprouts from the spheroids once embedded in type I collagen; this revealed that the multicellular spheroids rapidly initiated the process of sprouting angiogenesis. Extensive endothelial sprouting was visualised within two hours after the spheroid masses were embedded in collagen, as shown in figure 4.1. After the initial stage of extensive sprouting, endothelial cell remodelling was observed as shown in the images from 5.5 hrs to 12.5 hrs after embedding, where many of the highly motile and dynamic endothelial cell sprouts underwent retraction whilst other sprouts extended.

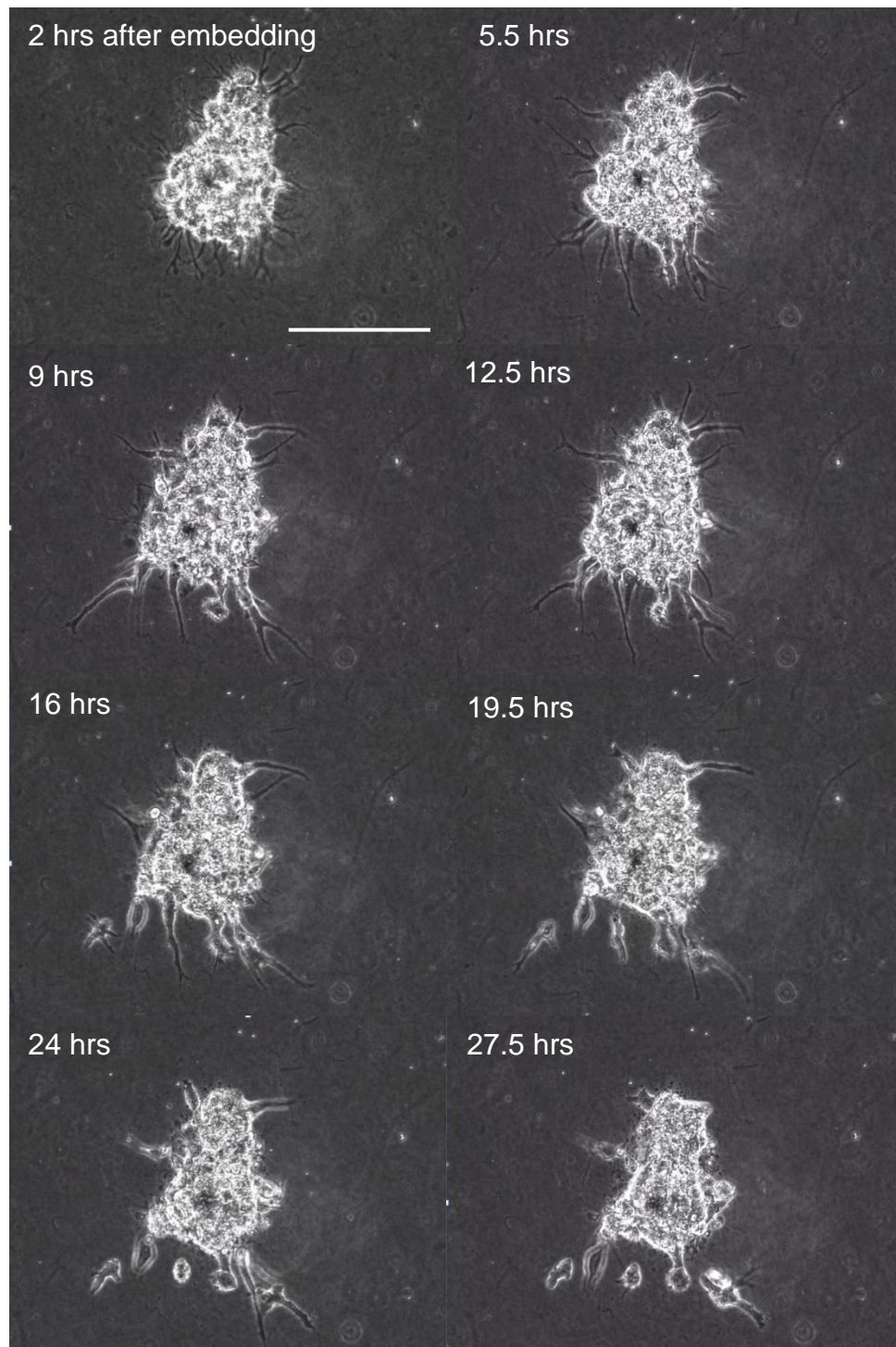


Figure 4.1 A time lapse experiment demonstrating that endothelial sprouting is a dynamic process

Phase contrast time-lapse images enabled visualisation of the process of endothelial sprouting from an endothelial cell spheroid formed using the hanging drop spheroid assay over a 27.5 hr time period, scale: 200 μm .

Imaging the spheroids 16 hrs after collagen embedding enabled visualisation of a stable network of endothelial sprouts formed from the spheroid mass as shown in figure 4.1. At this time point, the endothelial cells had formed elongated sprouts which connected to nearby sprouts through the formation of branching points. The time course study revealed that after 16 hrs, the tip cells started to migrate from the stalk cells from within the sprout, which destabilised the endothelial network and resulted in disconnected sprouts, an example image at 24 hrs has been shown in figure 4.2. Imaging the spheroids at later time points such as at 48 hrs showed that all of the tip cells as well as the stalk cells had migrated from the spheroid mass and as a result no endothelial sprouts were observed. In conclusion, time-lapse imaging of the process of endothelial sprouting revealed that 16 hrs after collagen embedding was a suitable time point for imaging the spheroids formed using the hanging drop spheroid angiogenesis assay.

In addition, the images in figure 4.1 and 4.2 revealed the challenge of analysing endothelial sprouting from phase contrast or brightfield microscopy images, these imaging modalities do not allow for the spheroids to be imaged at high resolution. The hanging drop spheroid assay generates three dimensional cellular aggregates and endothelial sprouting occurs on all sides and from angles on the spherical surface. To improve imaging resolution and enhance the visualisation of the sprouts, the endothelial cells were fluorescently labelled with a highly emissive cytoplasmic dye CFSE prior to the formation of spheroids and were subsequently imaged by taking optical sections with confocal microscopy.

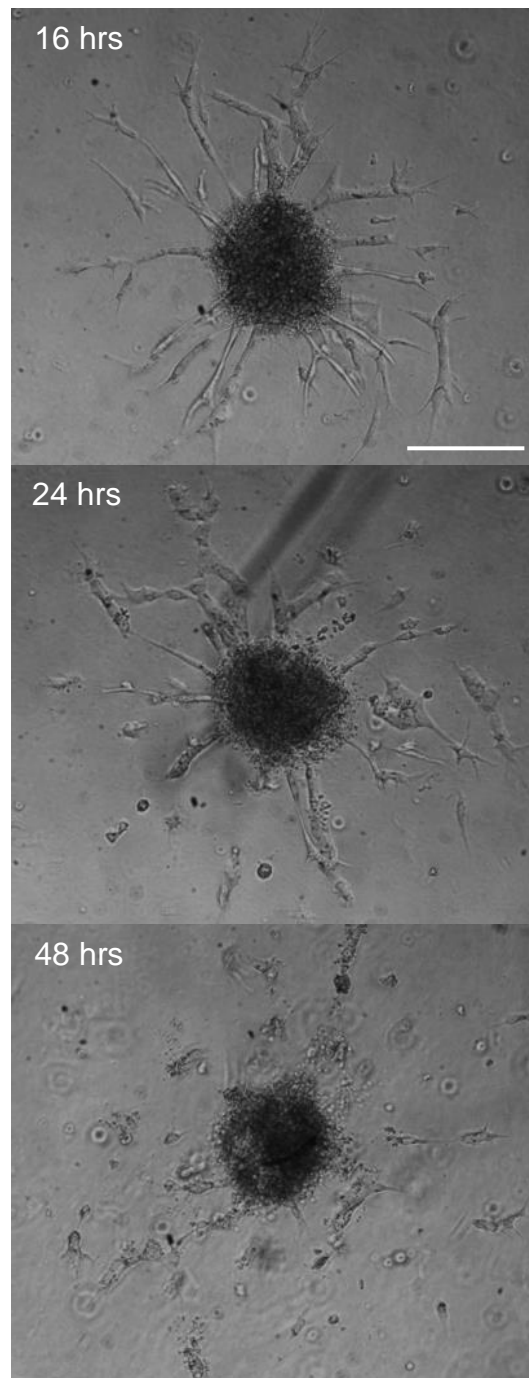


Figure 4.2 A stable endothelial sprouting network was observed sixteen hours after embedding the spheroids in collagen

Brightfield light microscopy images of endothelial spheroids formed using the hanging drop spheroid angiogenesis assay at 16, 24 and 48 hours after being embedded in a collagen I matrix, scale: 200 μm .

Initially I determined the analysis requirements and conceptual design of a computer based analysis tool that would automatically analyse endothelial sprouting from fluorescent spheroid images generated from the *in vitro* hanging drop spheroid angiogenesis assay. The computerised plugin was specifically designed to measure a range of sprouting parameters including the total length of the endothelial sprouts formed within the image, the number of endothelial sprouting segments that were produced, the number of endothelial junctions and the number of end points formed by the sprouts. The Java code for the Spheroid Analysis plugin was written by Christopher Meah (Physical Sciences of Imaging in the Biomedical Sciences Doctoral Training Centre, University of Birmingham) based on fluorescent spheroid images that exhibited a normal sprouting phenotype; an example image and the image processing steps of the plugin is shown in figure 4.3. One of the aims of this chapter was to test the capabilities of the plugin and determine if the computerised analysis tool was able to automatically process a wide range of sprouting phenotypes and to evaluate the outputs generated by the Spheroid Analysis plugin.

Figure 4.3 shows the image processing steps performed automatically by the Spheroid Analysis plugin. Initially the compressed fluorescent confocal spheroid image was loaded into ImageJ where it underwent a series of processing steps. Firstly, the fluorescent spheroid image was automatically converted into a binary image, binarisation clearly identified the endothelial cellular objects within the image and they appeared white in the image, whereas the image background appeared black, as shown in step two of figure 4.3. A mask of the binarised image data was created which was a visual representation of the endothelial sprouting network. The spheroid mass was excluded from the analysis procedure as only the endothelial

sprouts were required for analysis, therefore the mask of the spheroid mass was excluded at this stage. The remaining mask of the endothelial sprouting network was then used to generate two images, one which showed which sprouts were connected to the spheroid mass, thereby showing which endothelial cells had elongated into sprouts and a separate image showing which sprouts were disconnected from the mass, revealing which cells had migrated away from the spheroid, as shown in images 4 and 5 of figure 4.3. The mask of the sprouting network including the connected and disconnected sprouts was skeletonised using the inbuilt Skeletonize (2D/3D) plugin, which eroded the edges of the mask in a series of iterations until all of the sprouts were one pixel in diameter. Each pixel within the skeletonised network was analysed using the inbuilt Analyze Skeleton plugin (2D/3D). Each pixel was analysed according to its neighbouring pixels and was assigned as either a segment, junction or end point pixel. A segment pixel was assigned if the pixel had exactly two neighbouring pixels within the skeleton, a junction if it had more than two neighbouring pixels or an end point if it had zero or one neighbouring pixel. An endothelial segment within the skeletonised network was defined as a connected region of segment pixels. At the ends of each endothelial segment there was either a junction or an end point pixel, therefore endothelial segments were separated by two end point pixels, two junctional pixels or one end point and one junctional pixel, see figure 7.1 in section 7.1 of the appendix for further information on these parameters.

The resulting outputs of the analysis procedure by the ImageJ plugin were automatically produced in a single table upon completion of analysis. The table of analysis included quantification on the following parameters of the total number of sprouting segments, endothelial junctions, end points, total sprouting length and

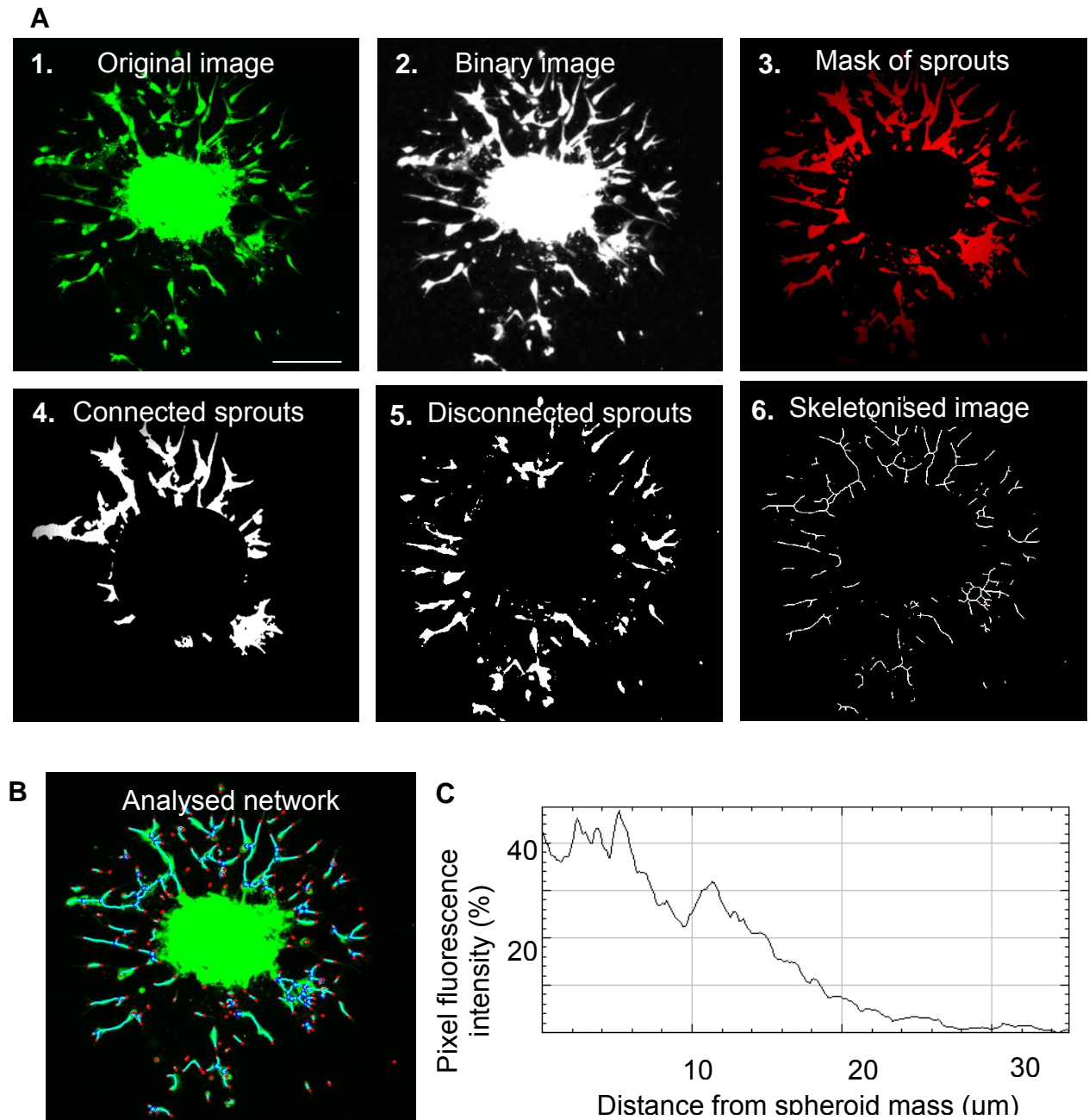


Figure 4.3 The ImageJ Spheroid Analysis plugin can be used to analyse endothelial sprouting from fluorescent spheroid images

A) The image processing steps performed by the ImageJ Spheroid Analysis plugin: 1) Original fluorescent spheroid image, 2) Binarised spheroid image, 3) Mask of the endothelial sprouts excluding the spheroid mass, 4) Mask of the sprouts connected to the spheroid mass, 5) Mask of the sprouts disconnected to the spheroid mass, 6) Skeletonised spheroid image, scale: 200 μm , **B)** An image of the analysed network of sprouts, the sprouting segments are shown in light blue, the endothelial junctions in dark blue, the end points in red, **C)** Sprouting distribution plot showing the fluorescence intensity of the pixels within the image against the distance from the spheroid mass.

average sprouting length in pixels. In addition to the table of outputs generated by the plugin, a final image was produced showing the analysed network overlaid on top of the original spheroid image, as shown in figure 4.3B. The sprouting segments were shown in the final image in a light blue colour, the pixels that were identified as junctions were shown in dark blue and the end point pixels were shown in red. The final overlaid image enabled clear visual identification of the endothelial cells that had been successfully analysed and allowed determination of how accurate the analysis process had been.

The plugin also allows the user to modify the analysis procedure if required by enabling the exact diameter of the spheroid to be inputted prior to the analysis procedure. Furthermore, the Spheroid Analysis plugin was able to generate a fluorescence intensity profile for the spheroid image shown in figure 4.3C; this intensity profile was generated by calculating the number of high fluorescence intensity pixels from within concentric ring bands from the spheroid mass until the edges of the image were reached. In this way, the fluorescence intensity profile was able to give an indication of the spouting distribution in the image.

4.4. Testing and evaluating the computer based analysis tool

A library of 80 small molecule kinase inhibitors was used in the hanging drop spheroid assay to produce a range of endothelial sprouting phenotypes which could be used to test and evaluate the capabilities of the ImageJ Spheroid Analysis plugin. The plugin was applied to five fluorescent spheroid images per inhibitor treatment and due to the large number of inhibitor molecules used in the assay, the screen was performed in 8 batches and corresponding DMSO treated control spheroids were imaged for each batch. In this way, the Spheroid Analysis plugin was tested on

spheroid images which exhibited a wide range of sprouting phenotypes including normal sprouting, hyper-sprouting, few sprouts and no sprouts, example images have been shown in figure 4.4.

For the purpose of testing the Spheroid Analysis plugin, all 80 kinase inhibitor compounds were used at their selected concentrations, it was possible that some inhibitors would induce cytotoxic effects on the endothelial cells and as a result would produce few or no endothelial sprouts during the hanging drop spheroid assay. However, it was important to test that the plugin would be able to accurately analyse these sprouting phenotypes and therefore these compounds were included during the evaluation stages of the plugin. As outlined in section 4.8, a cell viability assay was performed on a monolayer of endothelial cells and those compounds which affected cellular viability were excluded from the scratch wound and matrigel assay screen. However, it should be noted that the cell viability assay was performed by adding the inhibitor compounds to a monolayer of endothelial cells which could have induced higher cytotoxic effects compared to those in the hanging drop spheroid assay, whereby the endothelial cells were surrounded and embedded in collagen. For example, D-erythro-sphingosine at 3 μ M concentration induced hypersprouting in the spheroid assay while causing cytotoxicity in the endothelial monolayer at the same concentration.

As shown in the analysed spheroid network images in figure 4.4, the ImageJ plugin was able to accurately identify the regions of endothelial spouts within the images. The Spheroid Analysis plugin was able to quantify all sprouting phenotypes including hyper-sprouting of spheroids, which was of particular interest as such images would

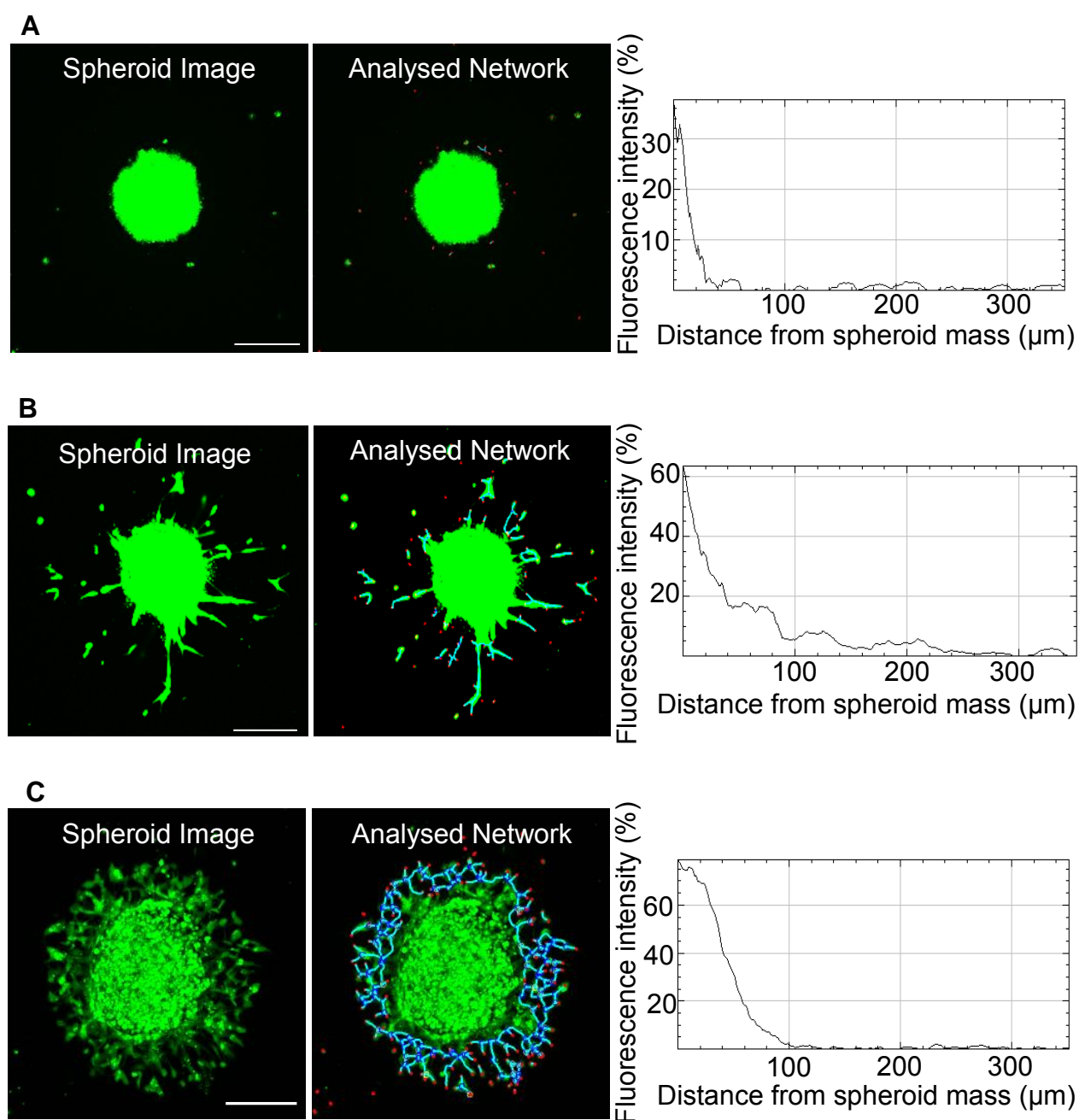


Figure 4.4 The Spheroid Analysis ImageJ plugin was capable of analysing a range of sprouting morphologies

Examples of fluorescent spheroid images captured on a confocal microscopy and analysed using the ImageJ Spheroid Analysis plugin, The capabilities of the Spheroid Analysis ImageJ plugin to analyse endothelial sprouting was tested using fluorescent images with a range of different endothelial sprouting morphologies including: **A)** no sprouts, **B)** few sprouts, **C)** many sprouts, scale: 200 μm.

be extremely difficult to analyse manually using the frequently used method of measuring the lengths of the endothelial sprouts. To determine and verify the accuracy of the results generated by the ImageJ plugin, 25 spheroid images were manually assessed for the total sprouting length and the number of sprouting junctions formed by the spheroids. To manually analyse the total sprouting length, the segmented line tool in ImageJ was used to measure the lengths of each individual endothelial sprout per spheroid and the total sprouting length was calculated using Microsoft Excel. This manual analysis process was able to calculate the total sprouting length per spheroid in approximately 3 minutes, although this depended on the number of sprouts within the image. To determine the number of endothelial junctions formed by the sprouts, the multi-point tool in ImageJ was used to count each endothelial junctional region within the image, this tool automatically numbered the selected points and the resulting output per spheroid could be generated in approximately 1 minute.

This manual analysis procedure generated results on the parameters of total sprouting length and the number of endothelial junctions in approximately 4 minutes. In comparison, the ImageJ Spheroid Analysis plugin processed an image automatically within 36 seconds, generating quantification on a number of sprouting parameters including the number of endothelial sprouting segments, the number of sprouting end points and the average sprout length, in addition to producing a fluorescence intensity plot for the image.

Twenty five spheroid images were analysed using the manual analysis procedure and the ImageJ plugin and the outputs from both methods were compared, the graphs showing the relationship between the two sets of results is shown in the plots

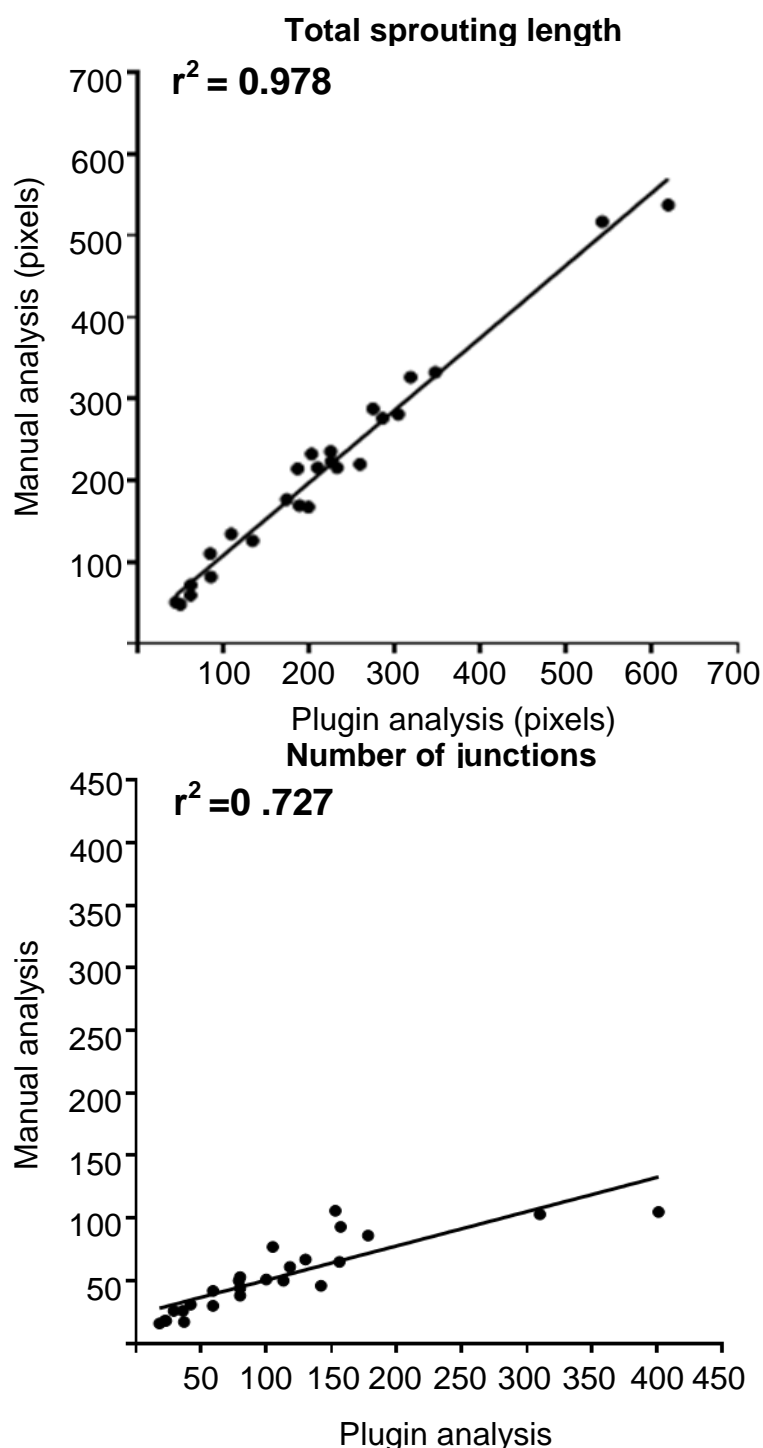


Figure 4.5 A linear relationship was calculated upon measuring the total sprouting length using the ImageJ plugin and manual analysis of spheroids

Twenty five fluorescent spheroid images from the kinase screen were analysed for the total sprouting length and number of endothelial junctions formed in the images using a manual analysis approach and the computerised ImageJ Spheroid Analysis plugin. The correlations between the two data sets were determined by calculating an r^2 value, whereby a result of 1.0 indicates an entirely linear relationship and 0.0 indicates there is no linear relationship.

in figure 4.5. The r^2 values for the parameters of total sprouting length and the number of endothelial junctions were calculated to determine if there was a linear relationship between the data generated by the two analysis methods. The plots in figure 4.5 showed that a linear relationship was determined for the total sprouting length, with an r^2 value of 0.978, where a value of 1.0 indicates an entirely linear relationship. The high r^2 value confirmed that the results generated by the ImageJ plugin for the total sprouting length were comparable to those generated by the manual analysis method. The plot showed that as the sprouting length increased; the manual analysis method calculated slightly smaller lengths than the ImageJ method; which was likely to have been due to the difficulty in manually analysing complex sprouting networks by individually outlining each endothelial sprout within the image.

The graph for the number of endothelial junctions shown in figure 4.5 revealed that the manual analysis method consistently measured fewer numbers of junctions compared with the results generated by the ImageJ method; this relationship was confirmed with an r^2 value of 0.727. The ImageJ plugin used a highly sensitive algorithm to assess each individual pixel within the image, in this way this method was able to identify single pixels as junctions; therefore junctional pixels which were very close to one another would have been classified as multiple junctional pixels by the ImageJ method, whereas the manual analysis approach would identify such regions as a single junction. The manual analysis method of counting the number of junctions became more challenging as the endothelial sprouting network became more elaborate. The higher level of detection achieved by the ImageJ plugin enabled the images to be studied in greater detail than by using the manual method.

In conclusion, it was found that the image outputs were generated 6.7 times faster by the ImageJ Spheroid Analysis plugin in comparison to the manual analysis method and that the results of the Spheroid Analysis plugin were comparable to the manual method for determining the total sprouting length. The ImageJ analysis method achieved a greater level of sensitivity and detection therefore higher numbers of junctions were also measured using the ImageJ plugin. Upon studying the images of the analysed sprouting network generated by the plugin, it was confirmed that the plugin results were accurate and that this automated analysis method could be used to rapidly quantify endothelial sprouting of fluorescently labelled spheroids.

The ImageJ Spheroid Analysis plugin was able to record quantitative information on different endothelial sprouting parameters, which included the total and average sprouting lengths, the numbers of endothelial sprouting segments, junctions and end-points. All of the parameters were measured independently; however the average sprouting length was derived from the measurements of the total sprouting length and the number of sprouting segments. To investigate how the generated outputs for each parameter measured by the plugin related to the other parameters and to identify any correlations between these measured parameters, the spheroid images from the kinase inhibitor screen were analysed using the Spheroid Analysis plugin and the Pearson product moment correlation coefficients (R) and p values from a Students t-test were calculated.

The R and p values for the parameters have been shown in table 4.1; the results revealed that all of the correlations between each parameter were highly significant, with the highest correlation calculated between the number of sprouts and the number of end points with the highest R value of 0.983 and a p value of $<1.0 \times 10^{-30}$.

Table 4.1. Significant correlations were identified between the different parameters measured using the Spheroid Analysis plugin.

The Pearson product moment correlation coefficient (R) values and p values from a Student's t-test were calculated to determine correlations between the parameters of the number of sprouting segments, number of endothelial junctions, number of end points, total and average sprout lengths measured using the ImageJ Spheroid Analysis plugin. The correlation values were calculated using the mean values for the 8 DMSO controls and 80 small molecule inhibitor compounds used in the hanging drop spheroid angiogenesis assay in the kinase screen.

<div> <div>R values</div> <div>P values</div> </div>	Number of Sprouting Segments	Number of Junctions	Number of End Points	Total Sprouting Length	Average Sprouting Length
		0.735	0.983	0.805	0.667
Number of Sprouting Segments					
Number of Junctions	3.445×10^{-16}		0.830	0.945	0.839
Number of End Points	$<1.0 \times 10^{-30}$	1.581×10^{-23}		0.893	0.771
Total Sprouting Length	3.308×10^{-21}	$<1.0 \times 10^{-30}$	$<1.0 \times 10^{-30}$		0.942
Average Sprouting Length	1.277×10^{-12}	1.702×10^{-24}	1.641×10^{-18}	$<1.0 \times 10^{-30}$	

This high correlation was closely followed by the correlation between the total sprouting length and the number of endothelial junctions as well as the average sprouting length with an R value of 0.945 and 0.942 respectively and p values of $<1.0 \times 10^{-30}$. These strong correlations suggested as expected that as the complexity of the endothelial sprouting network increased, a greater number of sprouts and sprout length, junctions and end points were detected. The lowest correlation was calculated between the number of sprouts and the average sprout length with an R value of 0.667 and p value of 1.277×10^{-12} , this result was highly significant indicating that all parameters measured by the plugin would be useful and can be used to assess endothelial sprouting. Correlation graphs were plotted using the data generated by the ImageJ Spheroid Analysis plugin for the hanging drop spheroid images studying the effect of the different kinase inhibitors, to give a visual representation of the correlation between the different parameters measured within the images. The mean value for each inhibitor and control images were plotted to study each parameter individually against the other parameters. A line of best fit was plotted onto the graphs to give an indication of the degree of correlation between the two parameters. The correlation plots in figures 4.6 and 4.7 showed that a range of sprouting phenotypes were assessed using the plugin, however there were more images which expressed a low endothelial sprouting phenotype, this result was expected since kinases play essential roles in cellular processes such as proliferation, differentiation and migration therefore inhibiting them was likely to affect endothelial sprouting.

Figure 4.6 showed the most significant correlations that were measured between the parameters, with the highest correlation observed between the number of sprouting

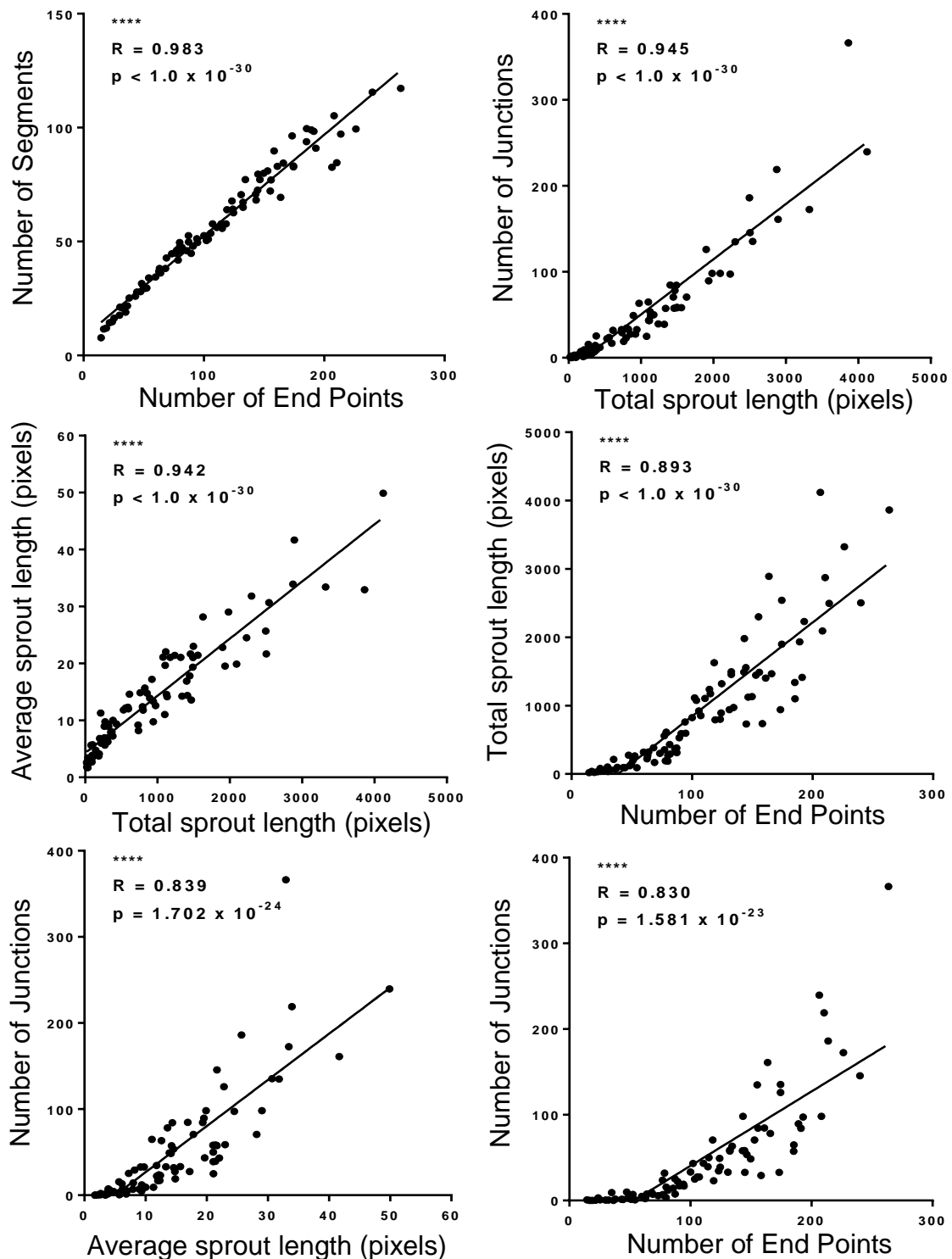


Figure 4.6 The highest correlation was calculated between the number of endothelial segments and end points

Correlation graphs were plotted using the mean values generated by the ImageJ Spheroid Analysis plugin from the kinase screen; each point represents an inhibitor from the screen performed using the hanging drop spheroid angiogenesis assay. The Pearson product moment correlation coefficient (R) values and p values from a two tailed t-test were calculated and statistical differences have been shown **** indicates $p \leq 0.0001$.

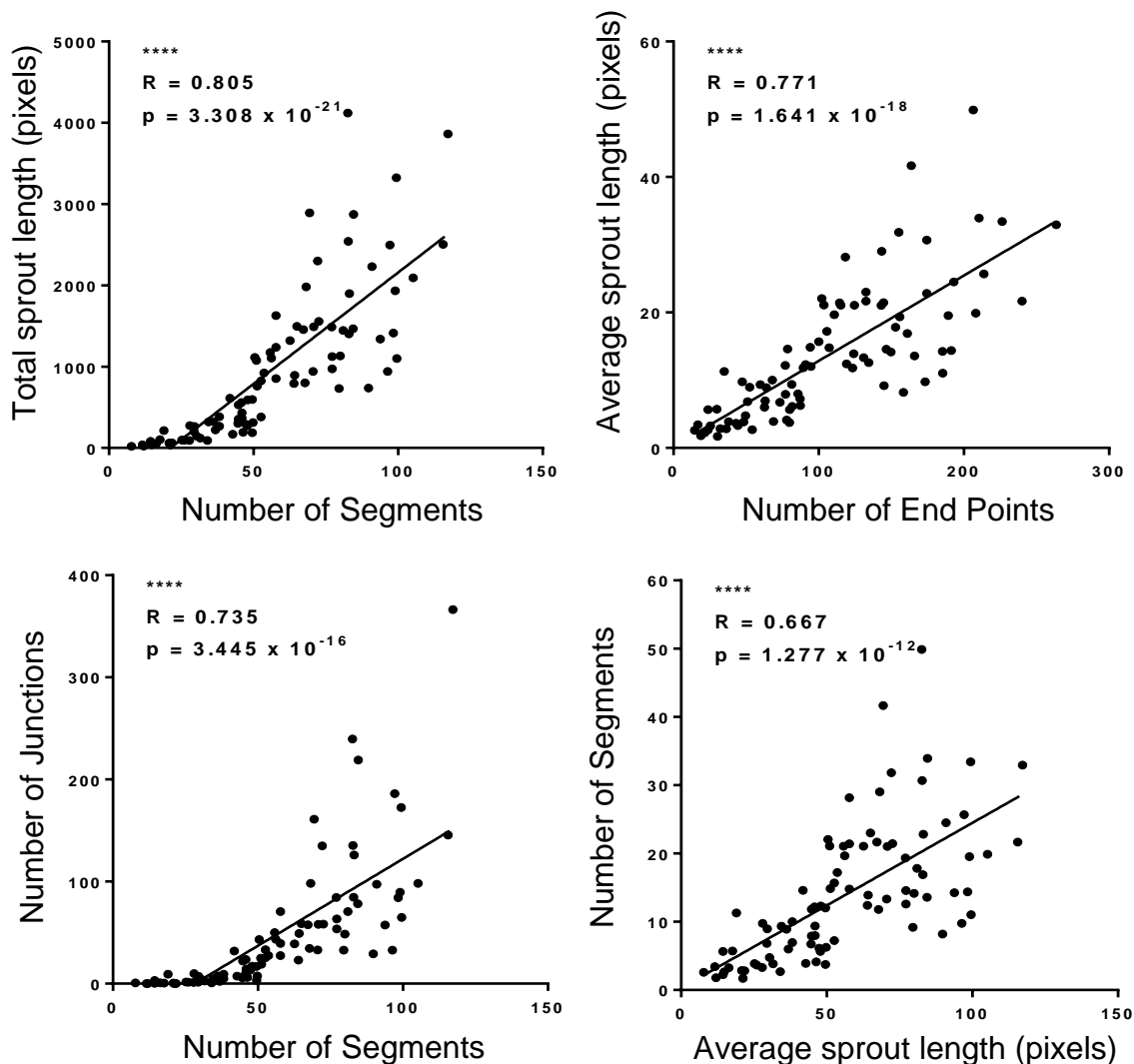


Figure 4.7 The smallest correlation was determined between the number of segments and the average sprout length

Correlation graphs were plotted using the mean values generated by the ImageJ Spheroid Analysis plugin from the kinase screen; each point represents an inhibitor from the screen performed using the hanging drop spheroid angiogenesis assay. The Pearson product moment correlation coefficient (R) values and p values from a two tailed t-test were calculated and statistical differences have been shown **** indicates $p \leq 0.0001$.

segments and the number of end points, these parameters directly correlated to each other until approximately 70 segments were measured, at higher numbers of segments there was greater variation in the numbers of end points detected. Strong correlations were also observed between the total sprouting length and the numbers of endothelial junctions, end points and average sprouting length which suggested that as the stalk cells elongated to expand the endothelial network, there was detection of the enhancement in the sprout lengths and connectivity of the sprouts.

The smallest correlation between the parameters was calculated between the average sprout length and the number of segments, as shown in figure 4.7. A high degree of variability between these parameters was observed; however the general trend for this plot was that as increased numbers of endothelial segments were detected in the images, the average sprout length also increased. The strong correlation results identified in this study revealed that the parameters of total and average sprouting length, the numbers of segments, junctions and end points would all provide informative data on the sprouting phenotype formed by the spheroids generated in the hanging drop spheroid angiogenesis assay.

4.5. Screening kinases to identify those with roles in sprouting angiogenesis

Protein kinases play essential roles in the regulation, activation and localisation of many cellular proteins involved in signalling cascades through the action of adding a phosphate group on to target substrate proteins. A library of small molecule kinase inhibitor compounds were added into the hanging drop spheroid angiogenesis assay to identify the effects the kinase inhibitors had on the processes on endothelial

sprouting. In this way, a wide range of spheroid images showing different sprouting phenotypes were generated and used to test the capabilities of the Spheroid Analysis plugin as previously described in section 4.4. Using this approach, the quantitative results generated by the Spheroid Analysis plugin on the total and average vessel length, the numbers of sprouting segments, junctions and end points could be used to identify important kinases with roles in angiogenic processes.

Example images of the spheroids have been shown in figure 4.8 and revealed that the spheroids which formed in the presence of DMSO developed elongated endothelial sprouts with various junctions that lead to further connections with other sprouts. In comparison, treatment with the various inhibitor compounds resulted in the formation of many spheroids with fewer or no endothelial sprouts produced from the spheroid mass, as previously outlined in the correlation graphs in figures 4.6 and 4.7. Example images of the spheroids generated in this assay have been shown in figure 4.8, the addition of 14 μ M LY 294002 which inhibited phosphoinositide 3-kinase (PI3K) caused complete absence of endothelial sprouting, whereas the addition of 7 μ M AG-494 or 30 μ M RG-1462 through targeting epithelial growth factor receptor kinase (EGFR) reduced endothelial sprouting compared with the DMSO treated control.

The ImageJ Spheroid Analysis plugin was used to analyse the effects of the inhibitor compounds on endothelial sprouting. Bar charts of the results generated on the parameters of total and average sprouting length and the numbers of segments, junctions and end points for eight inhibitor compounds are shown in figure 4.9, with the bar charts for all of the tested compounds shown in the appendix. The bar charts in figure 4.9 revealed that a similar and consistent pattern of results was observed

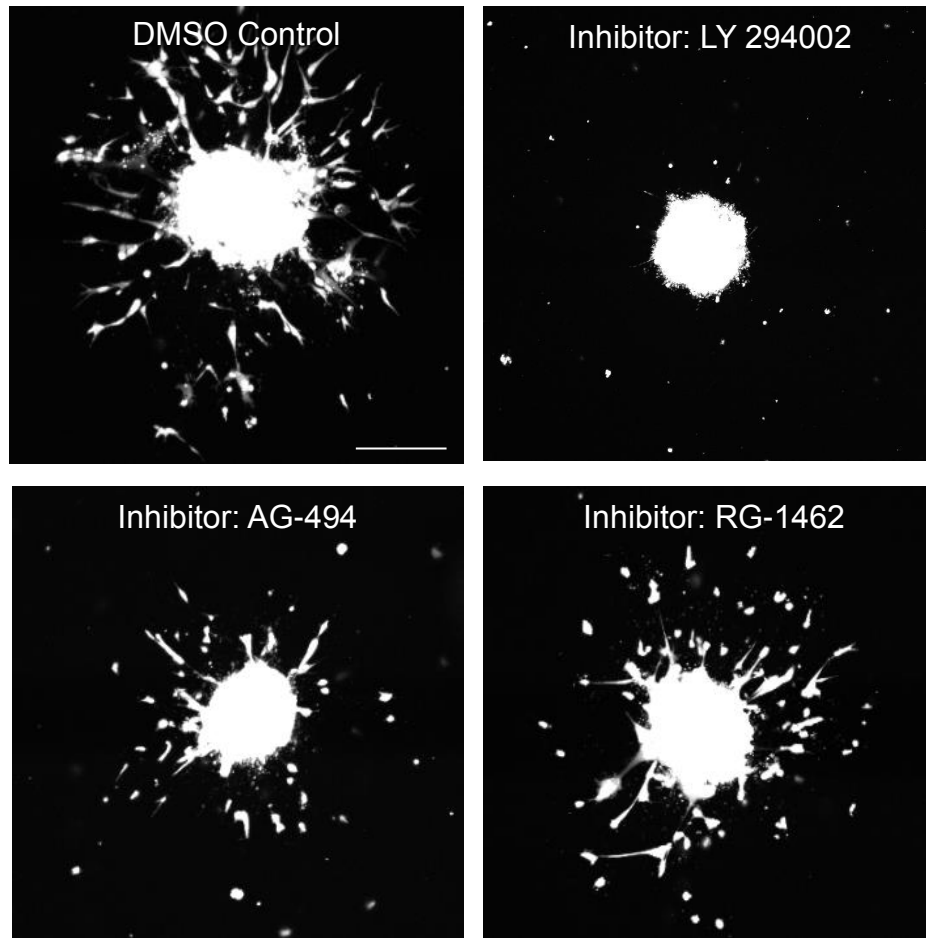


Figure 4.8 The hanging drop spheroid angiogenesis assay can be used to screen different inhibitors and determine their effects on sprouting angiogenesis

HUVECs were labelled with 5 μ M CFSE prior to use in the hanging drop spheroid angiogenesis assay, the spheroids were treated with different kinase inhibitors or DMSO as the control and confocal images were taken 16 hrs after embedding the spheroids in collagen, scale: 200 μ m.

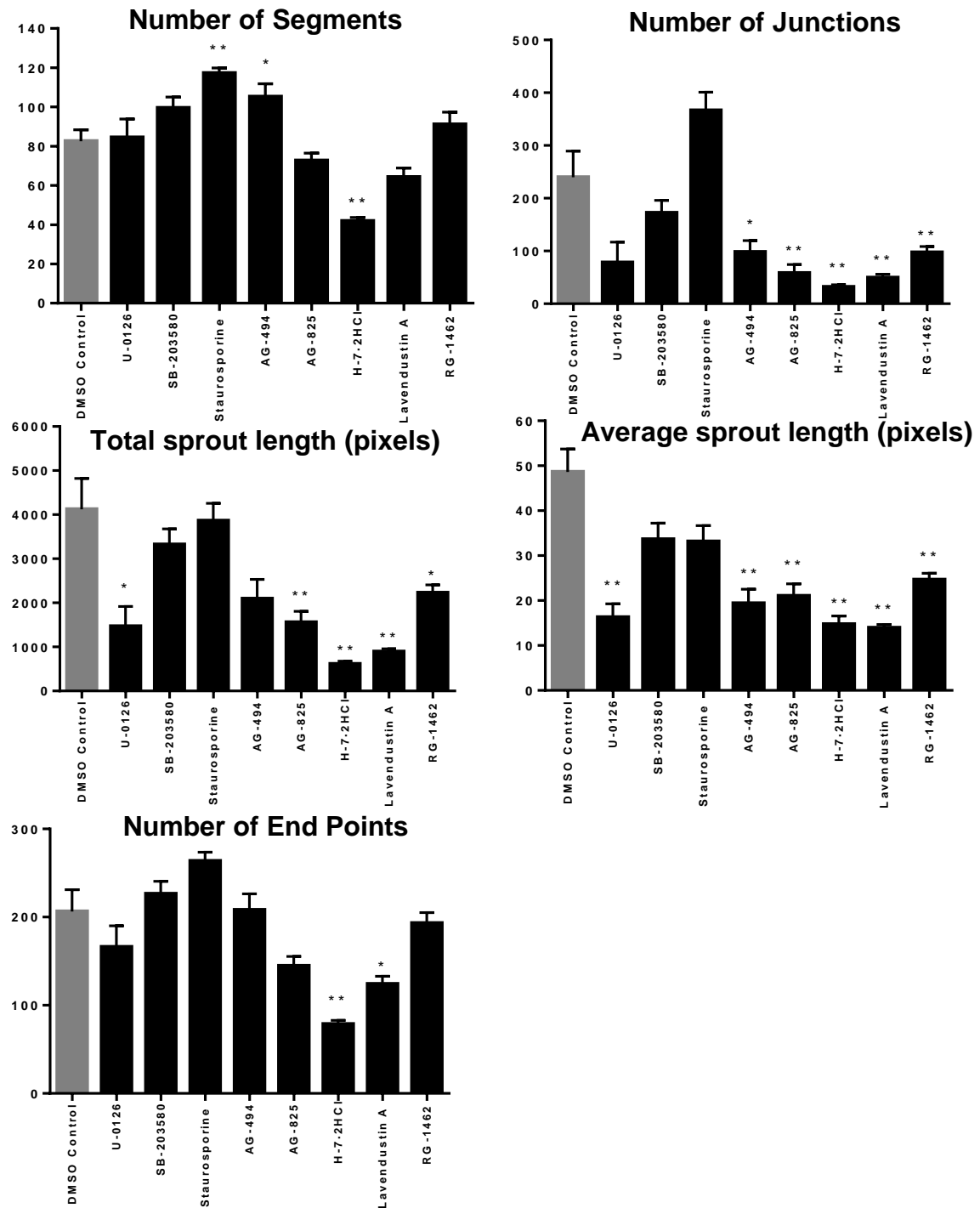


Figure 4.9 ImageJ Spheroid Analysis results for inhibiting kinases in the hanging drop spheroid angiogenesis assay

The ImageJ Spheroid Analysis plugin was used to analyse fluorescent spheroid images generated by the hanging drop spheroid angiogenesis assay with confocal imaging 16 hrs after collagen embedding. The effect of adding the kinase inhibitors U-0126, SB-203580, staurosporine, AG-494, AG-825, H-7.2HCl, lavendustin A and RG-1462 on the total and average sprouting length, the number of sprouting segments, junctions and end points was determined. Statistical analysis was performed using the Mann-Whitney test, n=5 spheroids, ** indicates $p \leq 0.01$ and * indicates $p \leq 0.05$. The error bars are the SEM.

between the different parameters measured from the fluorescent spheroid images for the various inhibitor compounds. Measuring the total sprouting length, average sprouting length and the number of junctions in the spheroid images caused the highest degree of difference between the control and inhibitor images, therefore allowing easy identification of the effect of the inhibitor on endothelial sprouting. Along with identifying a high degree of difference between the control and inhibitor images, measuring the total sprouting length would give a global understanding of the extent of endothelial sprouting. Whereas, measuring the number of junctions would provide informative information on the endothelial connectivity and complexity of the sprouting network that had developed. Therefore, these two parameters are the most useful parameters, determining the average sprouting length could also be considered, however this parameter was derived from the measurements of total sprouting length and the number of segments.

Smaller differences between the control and inhibitor images were observed upon measuring the number of sprouting segments and the number of end points. Studying these parameters could provide additional information on sprouting morphology however migrated cells were often identified as small sprouting segments with several end points, therefore studying these parameters alone would not necessarily be informative on sprouting morphology, except for extreme sprouting phenotypes such as no sprouts or hyper-sprouting, where there are large and apparent differences in the number of segments or end points.






To identify the kinase inhibitors which affected endothelial sprouting, a heat map table was generated shown in table 4.2, which enabled easy visualisation and determination of the effects on the different aspects of sprouting measured by the

plugin. The results in table 4.2 revealed that many of the inhibitor compounds reduced sprouting compared to the control spheroids, as indicated by the orange and red colours in the table. In general, if a reduced sprouting phenotype was observed due to the addition of a kinase inhibitor compound, the plugin generated results that indicated this phenotype in all of the sprouting parameters that were measured within the image.

Interestingly, the heat map table identified two compounds which caused an increase in sprouting detected by three parameters which suggested hyper-sprouting of these spheroids. A significant increase in the connectivity of the endothelial sprouts was detected by measuring the number of junctions within these images for both of the compounds, as indicated by the dark green colour in the table. The first was a pan-specific kinase inhibitor staurosporine; the plugin also identified increased numbers of segments and end points for the treatment with this compound. The second inhibitor was D-erythro-sphingosine which targeted protein kinase C (PKC), in addition to the increased number of endothelial junctions formed by the treatment of this molecule, enhanced numbers of end points and extended total sprouting length were measured, in comparison to the control images. As outlined by the previous results, measuring the number of end points within the spheroid images was useful for the identification of hyper-sprouting phenotypes.

Table 4.2 Heat map table showing the effect of kinase inhibitors on the process of sprouting angiogenesis

The ImageJ Spheroid Analysis plugin was used to quantify the total and average sprouting length, numbers of segments, junctions and end points from spheroid images to study the effect of kinase inhibitors on endothelial sprouting. The hanging drop spheroid assay was performed with the addition of each inhibitor at a concentration value ten times its IC₅₀ value. The IC₅₀ values for all inhibitors can be found in table 2.4 on page 49. Five spheroids per inhibitor were analysed and normalised to the corresponding controls. Each percentage boundary was plotted in a different colour to reflect the result, red (0-40% of control), orange (41-80%), yellow (81-120%), light green (121-160%), dark green (161-200%). The compounds in grey were used at concentrations which did not pass the cell viability assay.

			Number of segments (Segments)	Number of junctions (Junctions)	Number of end points (End Points)	Total sprouting length (TSL)	Average sprouting length (ASL)
	0-40%	Highly below control					
	41-80%	Below control					
	81-120%	Similar to control					
	121-160%	Above control					
	161-200%	Highly above control					
Compound	Target						
PD-98059	MEK						
U-0126	MEK						
SB-203580	P38 MAPK						
H-7-2HCl	PKA, PKG, MLCK, PKC						
H-9-HCl	PKA, PKG, MLCK, PKC						
Staurosporine	Pan-specific						
AG-494	EGFR, PDGFR						
AG-825	HER1-2						
Lavendustin A	EGFR						
RG-1462	EGFR						
TYRPHOSTIN 23	EGFR						
TYRPHOSTIN 25	EGFR						
TYRPHOSTIN 46	EGFR						
TYRPHOSTIN 47	EGFR						
TYRPHOSTIN 51	EGFR						
TYRPHOSTIN 1	Negative control						

Compound	Target	Segments	Junctions	End Points	TSL	ASL
TYRPHOSTIN AG 1288	Tyrosine kinases					
TYRPHOSTIN AG 1478	EGFR					
TYRPHOSTIN AG 1295	Tyrosine kinases					
TYRPHOSTIN 9	PDGFR					
Methyl-phosphonic acid	IRK					
PKC-412	PKC					
Piceatannol	Syk					
PP1	Src family					
AG-490	JAK-2					
AG-126	IRAK					
AG-370	PDGFR					
AG-879	NGFR					
LY 294002	PI 3-K					
Wortmannin	PI 3-K					
GF 109203X	PKC					
Hypericin	PKC					
Ro 31-8220 mesylate	PKC					
D-erythro-Sphingosine	PKC					
H-89·2HCl	PKA					
H-8	PKA, PKG					
HA-1004·2HCl	PKA, PKG					
HA-1077·2HCl	PKA, PKG					
Benzoic acid	EGFR, CaMK II					
KN-62	caMK II					
KN-93	caMK II					
ML-7·HCl	MLCK					
ML-9·HCl	MLCK					
2-Aminopurine	P58 PITSLRE β1					
N9-isopropyl-olomoucine	CDK					
Olomoucine	CDK					
Iso-olomoucine	Negative control					
Roscovitine	CDK					
5-Iodotubericidin	ERK2, CK1/2, adenosine kinase					
LFM-A13	BTK					

Compound	Target	Segments	Junctions	End Points	TSL	ASL
SB-202190	P38 MAPK					
PP2	Src family					
ZM 336372	cRAF					
SU 4312	Flk1					
AG-1296	PDGFR					
GW 5074	cRAF					
Palmitoyl-DL-carnitine	PKC					
Rottlerin	PKC delta					
Genistein	Tyrosine kinases					
Daidzein	Negative control					
Erbstatin analog	EGFR					
Quercetin·2H ₂ O	PI 3-K					
SU1498	Flk1					
ZM 449829	JAK-3					
BAY 11-7082	IKK pathway					
Ribofuranosylbenzimidazole	CK II					
Dimethanol dimethyl ether	PKC α, γ					
SP 600125	JNK					
Indirubin	GSK-3 β, CDK5					
Indirubin-3'-monooxime	GSK-3 β					
Y-27632·2HCl	ROCK					
Kenpaullone	GSK-3 β					
Terreic acid	BTK					
Triciribine	Akt					
BML-257	Akt					
SC-514	KK2					
BML-259	Cdk5					
Apigenin	CK-II					
BML-265	EGFR					
Rapamycin	mTOR					

4.6. Applying the computer based analysis tool to spheroids treated with p-21 activated kinase (PAK) inhibitors

P-21 activated kinases (PAKs) consist of a six membered family of enzymes which have biological roles in controlling cellular movement and motility as well as regulating the organisation of the actin cytoskeleton²²². To determine if PAKs have a role in sprouting angiogenesis, two PAK inhibitors PF-3758309 and IPA-3 were added into the culture media of the hanging drop spheroid angiogenesis assay and the spheroids were imaged 16 hours after collagen embedding. Endothelial sprouting was analysed using the ImageJ Spheroid Analysis plugin.

The quantitative results generated by the Spheroid Analysis plugin revealed that the addition of 1.25 μ M and 5.0 μ M PF-3758309 into the spheroid assay caused a significant reduction in endothelial sprouting compared with the DMSO control treated spheroids, as shown in the spheroid images and bar charts of analysis in figure 4.10. A similar pattern of results was observed for the different sprouting parameters; the most significant reductions were detected in the numbers of junctions and the total length of the endothelial sprouts with treatment using PF-3758309. PF-3758309 is a pan-specific inhibitor of PAKs and therefore inhibited all PAK isoforms. The analysis results in figure 4.10 also showed that treatment with varying concentrations of IPA-3 resulted in comparable sprouting to the DMSO controls; since IPA-3 is highly specific for PAK1, this sprouting result revealed that PAK1 is not required to produce endothelial sprouts in this assay.

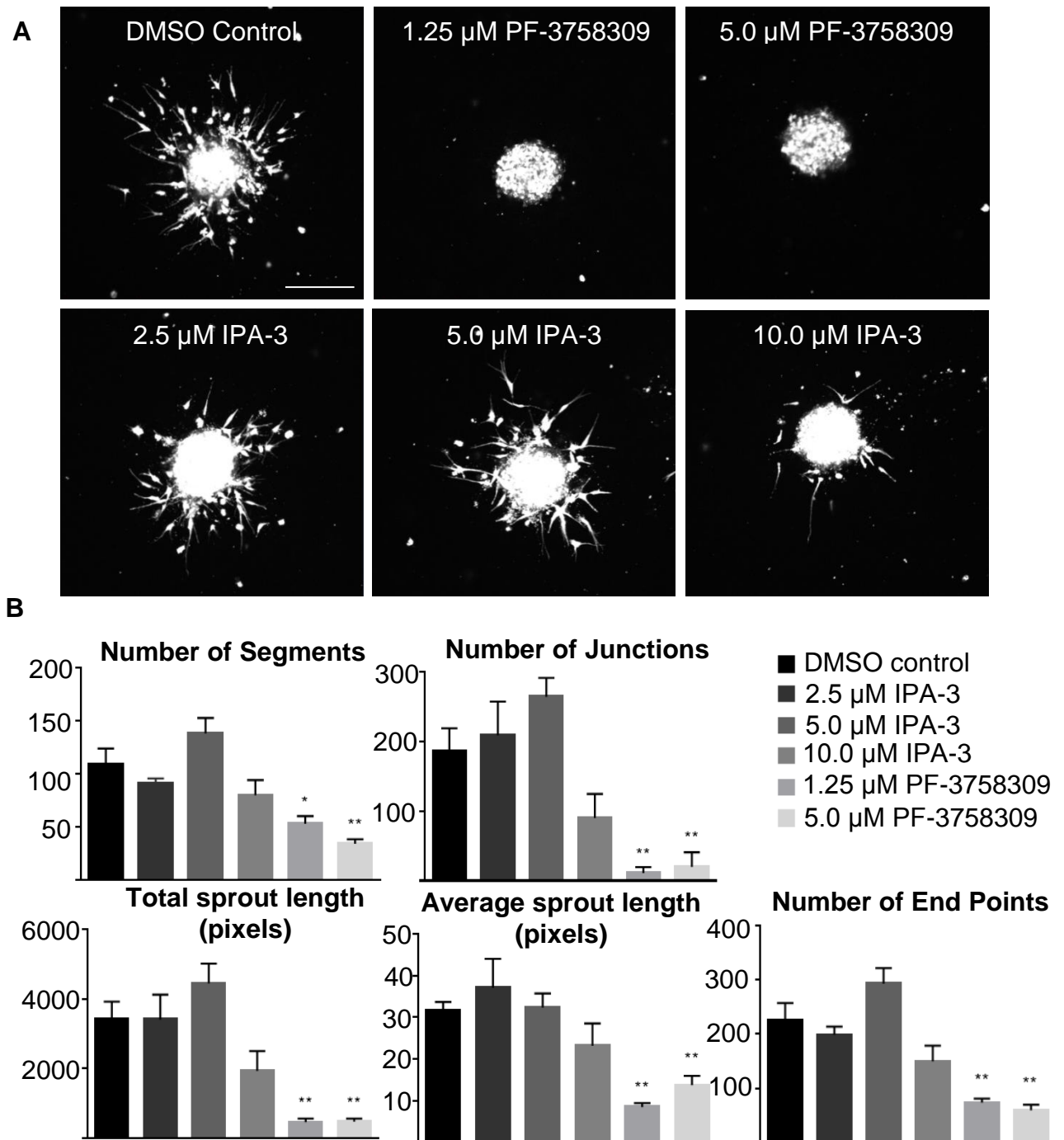


Figure 4.10 P-21 activated kinase (PAK) inhibitor PF-3758309 significantly reduced endothelial sprouting

Fluorescent endothelial spheroids were formed using the hanging drop spheroid angiogenesis assay and treated with either DMSO or a PAK inhibitor. **A)** Confocal images of the spheroids 16 hrs after collagen embedding, scale: 200 μ m, **B)** Analysis of the spheroid images performed using the Spheroid Analysis plugin. Statistical analysis was performed using the Mann-Whitney test, n=5 spheroids, ** indicates $p \leq 0.01$ and * indicates $p \leq 0.05$. The error bars are the SEM.

4.7. Applying the computer based analysis tool to spheroids treated with Bruton's tyrosine kinase (BTK) inhibitors

Bruton's tyrosine kinase (BTK) and bone marrow kinase in chromosome X (BMX) are members of the Tec family of non-receptor protein tyrosine kinases²²³. BTK plays crucial roles in many signal transduction cascades within B lineage lymphoid cells regulating cell survival, differentiation and adhesion²²⁴. Whereas, BMX is highly expressed in endothelial cells and it has been reported that in response to ischemia, BMX is activated by focal adhesion kinase (FAK) to induce angiogenesis by promoting cell migration and tube formation²²⁵.

The BTK inhibitor ibrutinib also inhibits the related Tec family kinase BMX and it was of interest to determine how inhibition of BMX, affected sprouting in this cell type²²⁶. In addition, other BTK inhibitors LFM-A13 and AVL-292 which were also highly likely to inhibit BMX were tested in this assay. The inhibitor compounds were added to the hanging drop spheroid assay and endothelial sprouting was imaged 16 hrs after collagen embedding and analysed using the ImageJ Spheroid Analysis plugin.

Ibrutinib inhibits BTK and BMX by binding covalently to its target kinase preventing the auto-phosphorylation event of the protein^{227,228}. The addition of ibrutinib in the assay significantly reduced the numbers of endothelial sprouts, junctions and end points formed by the spheroids, however no statistical differences were found between the average and total lengths of the sprouts in comparison to the DMSO controls. Images of the spheroids which were treated with the BTK inhibitors are shown in figure 4.11.

AVL-292 is a highly selective inhibitor of BTK which like ibrutinib prevents BTK auto-phosphorylation²²⁹. Figure 4.11 shows that AVL-292 treatment significantly affected endothelial sprouting with reduced numbers of endothelial sprouting segments, junctions, end points, average and total sprout lengths calculated.

LFM-A13 binds to the BTK catalytic site therefore preventing activation of its downstream targets²³⁰. The addition of LFM-A13 also significantly reduced the numbers of junctions formed by the endothelial sprouts as well as the average and total sprout lengths as shown in the images and bar charts of analysis in figure 4.11.

The quantitative analysis generated by the Spheroid Analysis plugin enabled the effect of the BTK inhibitors on the process of endothelial sprouting to be effectively studied using the different parameters. The addition of the inhibitor compounds into the assay caused a range of endothelial sprouting phenotypes due to the variations in specificity and selectivity of the compounds to their target protein. The inhibitor compounds had different modes of action and it is likely that other endothelial kinases would have been additionally inhibited with the use of these inhibitor compounds in the assay. Since it was determined that the inhibitor compounds affected endothelial sprouting, it was likely that these BTK inhibitors additionally target the endothelial expressed tyrosine kinase BMX.

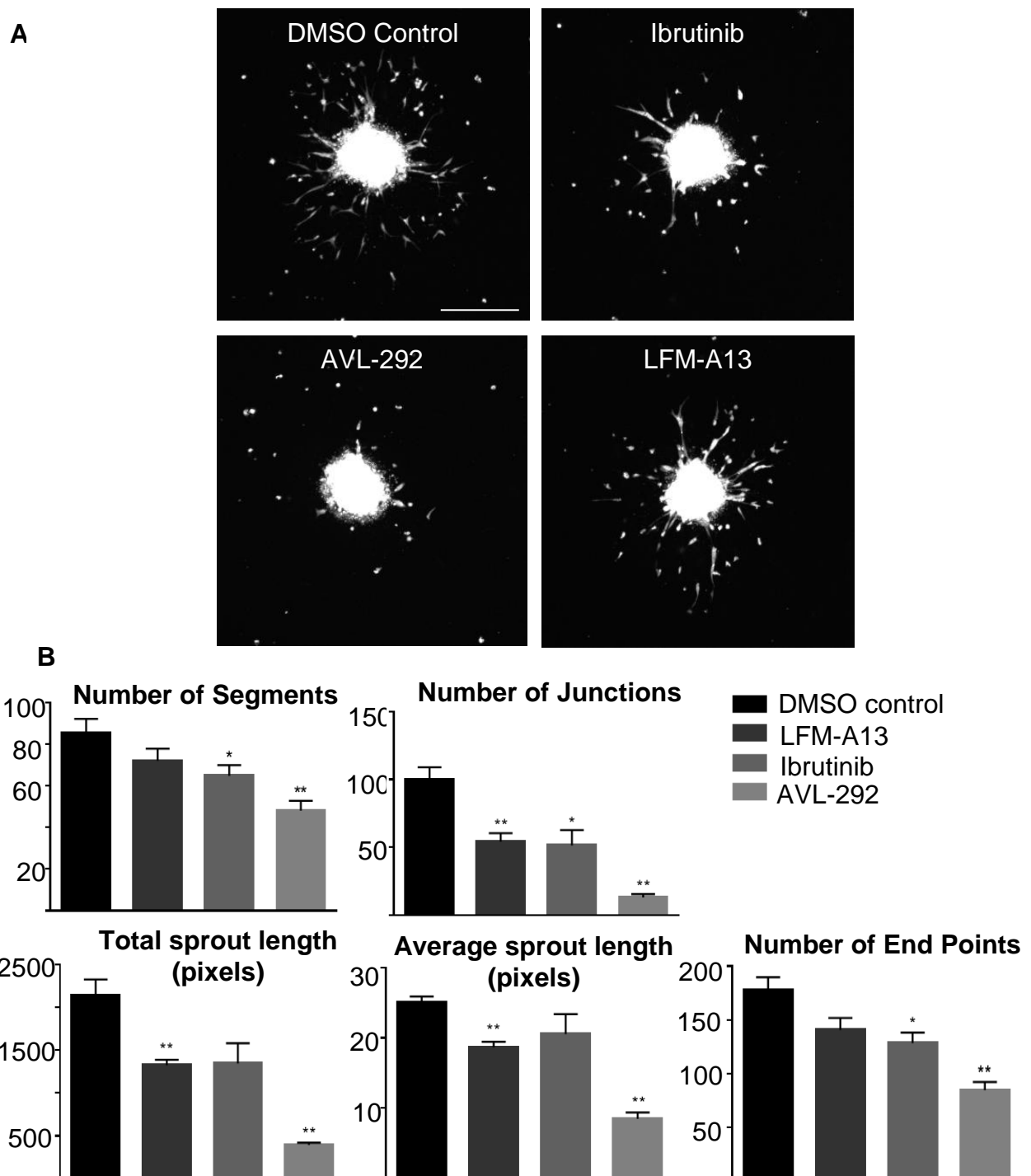


Figure 4.11 Bruton's tyrosine kinase (BTK) inhibitors significantly reduced endothelial sprouting

Fluorescent spheroids were formed using the hanging drop spheroid angiogenesis assay. Spheroids were treated with either a BTK inhibitor: 5 nM ibrutinib, 50 nM AVL-292, 25 μ M LFM-A13, or DMSO control. **A)** Confocal images 16 hrs after collagen embedding, scale: 250 μ m, **B)** Image analysis performed using the Spheroid Analysis plugin. Statistical analysis was performed using the Mann-Whitney test, n=5 spheroids, ** indicates $p \leq 0.01$, * indicates $p \leq 0.05$. The error bars are the SEM.

4.8. Screening kinases to identify those with roles in endothelial migration and tube formation

To determine whether the small molecule kinase inhibitor compounds differentially affected endothelial behaviour, the library of kinase inhibitors were added to the scratch wound angiogenesis assay and the matrigel tube formation assay, in addition to the hanging drop spheroid angiogenesis assay to identify the effects the kinase inhibitors had on the processes of endothelial cell migration and tube formation.

For the assays, the inhibitor compounds were used at a concentration of ten times their IC₅₀ values as described in chapter two section 2.4.1. Firstly, to determine the effect of the inhibitor concentrations on the viability of the endothelial cells, a cell viability assay involving the tetrazolium salt WST-1 was used to provide spectrophotometric quantification at 450 nm. The 80 small molecule inhibitor compounds were added to a monolayer of endothelial cells and the cell viability results revealed that the addition of 25 inhibitors at this concentration resulted in metabolically inactive endothelial cell populations, these inhibitors are identified by grey bars in figure 4.12. The addition of the inhibitor compounds that caused less than a 50% cell survival rate were excluded from the scratch wound and matrigel tube formation assays, this resulted in 55 inhibitor compounds that were used at their tested concentration for screening purposes within the assays and these inhibitors are shown as black bars in figure 4.12.

The scratch wound migration assay was used to specifically identify kinases that had roles in cell motility and migration. The closure of the scratch was monitored and the percentage of closure at 12 hrs was calculated and normalised to the rate of scratch

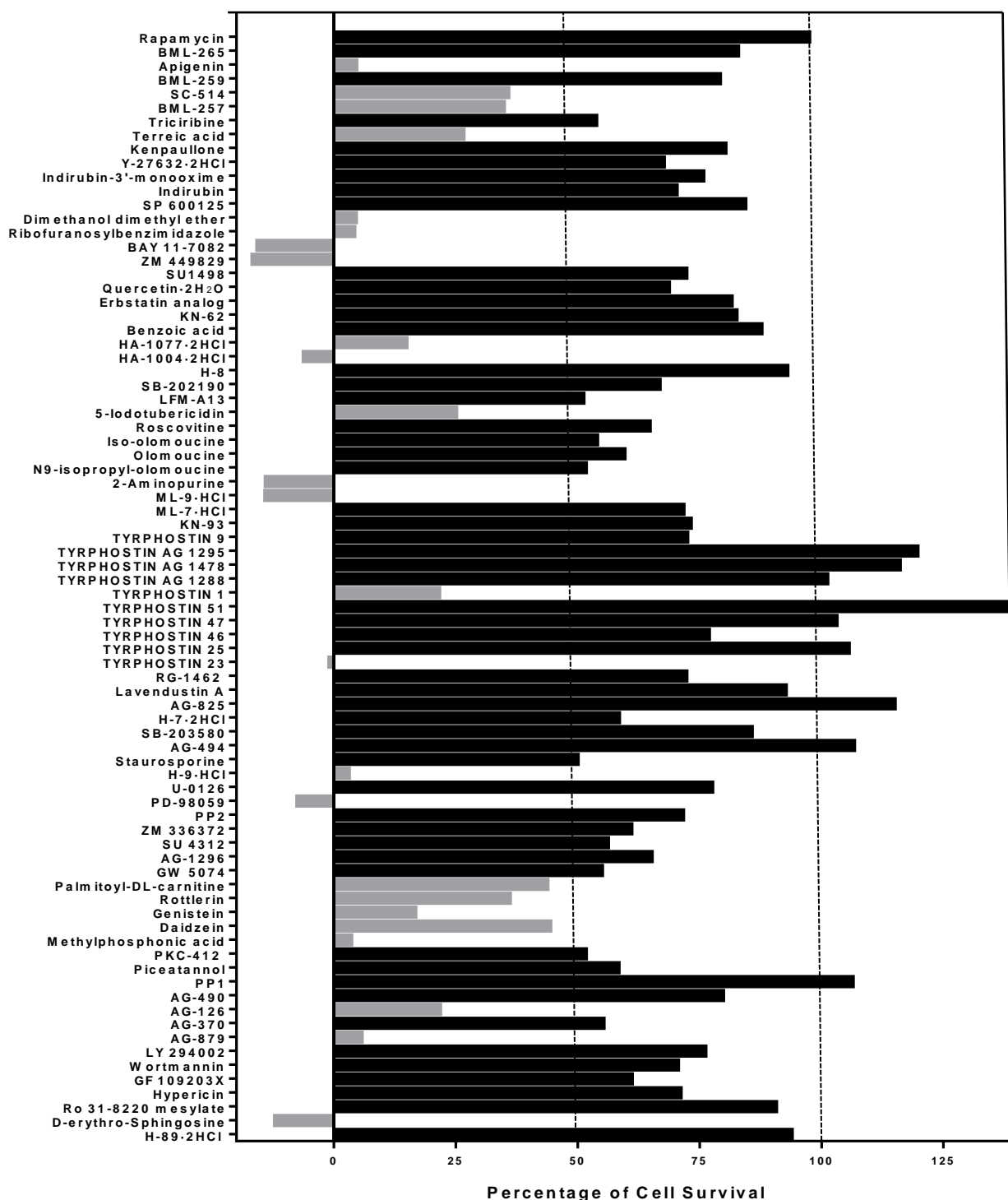


Figure 4.12 Bar charts showing the effect of the inhibitor concentrations on cell viability

HUVECs were cultured with the kinase inhibitors and cleavage of the tetrazolium salt WST-1 was measured by determining the light absorbance at 450 nm, n=4 experiments, four absorbance measurements were taken for each inhibitor and the mean percentage of cell survival rate was calculated and plotted. The inhibitor compounds identified in grey caused cell death, whereas the inhibitors identified in black were used for screening purposes.

closure of the DMSO treated controls. The images in figure 4.13 showed that the DMSO control scratch had nearly closed 12 hrs after the scratch was made due to migration of the endothelial cells into the area of the scratch. In comparison, the rate of scratch wound closure was reduced in the presence of many of the inhibitor compounds including tyrphostin 46 which targeted and inhibited EGFR. As shown in figure 4.13, a scratch was still evident within the endothelial monolayer after 12 hrs; such result implied that endothelial migration was dependent on EGF signalling.

Analysis of the scratch images to determine the percentage of scratch wound closure after 12 hrs revealed that 18 of the inhibitors caused significant reductions in the rate of scratch closure, shown in figure 4.14. Six of the inhibitors which reduced scratch closure targeted EGFR and three of the inhibitors inhibited PDGFR, both of these kinases are known to play vital roles in signalling cascades.

Interestingly, the rate of scratch wound closure was significantly enhanced upon the addition of indirubin which targeted glycogen synthase kinase-3 (GSK-3) β and cyclin-dependent kinase 5 (CDK5), this result was unexpected since treatment with indirubin has been shown to reduce tumour angiogenesis²³¹. Zhang *et al.* showed that indirubin inhibited endothelial cell proliferation using an MTS proliferation assay and additionally induced cell apoptosis²³¹.

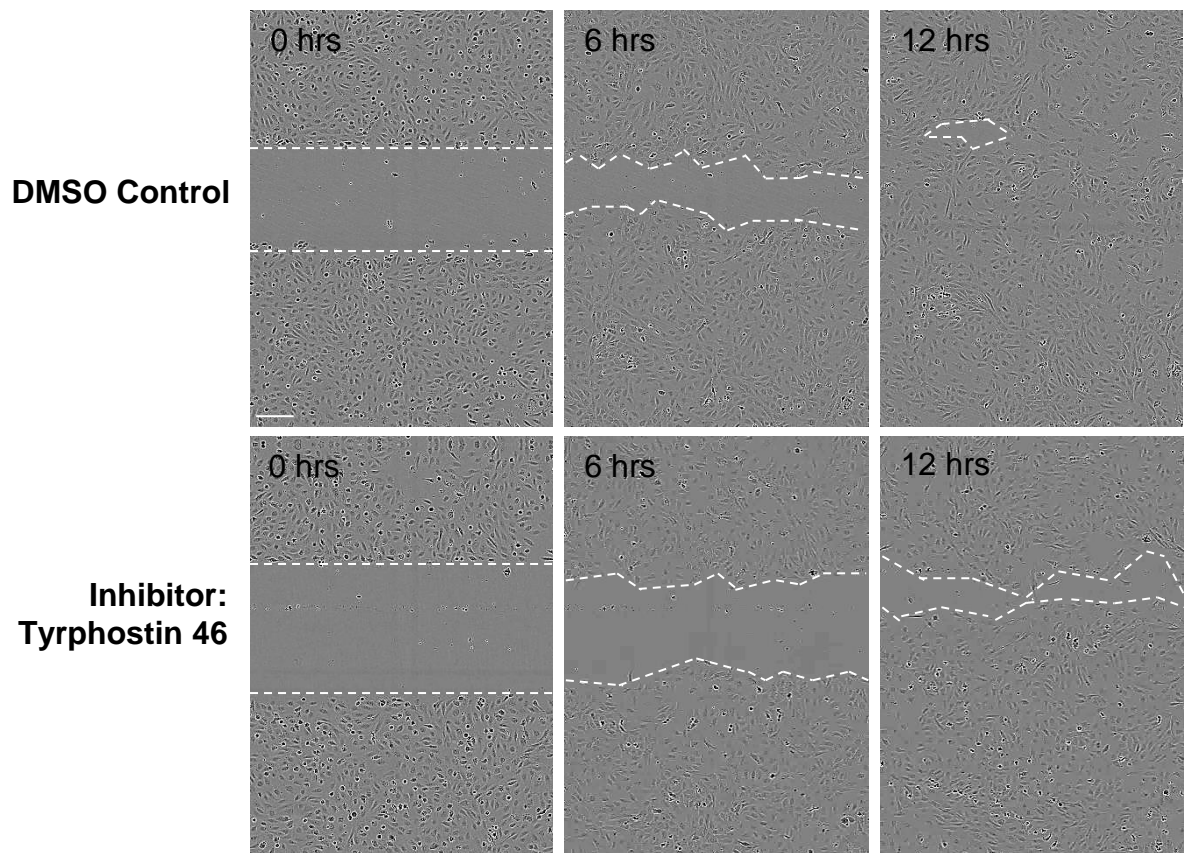


Figure 4.13 The scratch wound angiogenesis assay was used to screen kinases for those with roles in cell migration

The scratch wound assay was performed in the presence of kinase inhibitors or DMSO as the control; the images were taken 0, 6, 12 hrs after the scratch was made in a confluent monolayer of HUVECs and the rate of scratch wound closure was monitored to track cell migration, scale: 400 μm .

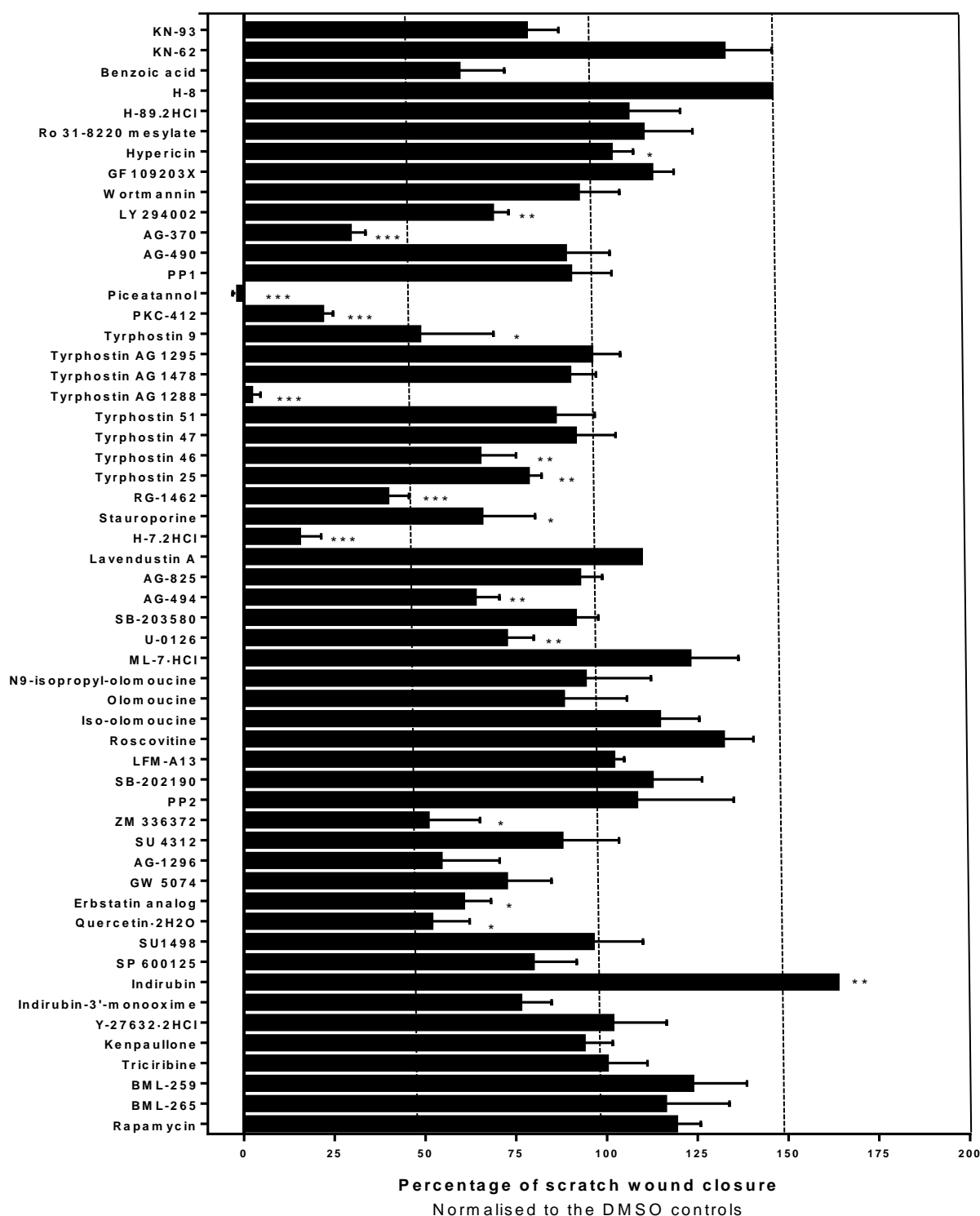


Figure 4.14 Analysis of the scratch wound angiogenesis assay identified that eighteen inhibitors significantly affected cell migration

The percentage of scratch width closure at 12 hrs was calculated and normalised to the DMSO control, n=4 experiments and an average value for scratch closure was calculated. Statistical differences were determined using a Mann-Whitney test, *** indicated $p \leq 0.001$, ** indicated $p \leq 0.01$ and * indicated $p \leq 0.05$.

The matrigel tube formation assay was used to specifically identify kinases that had roles in regulating endothelial tube formation. The numbers of endothelial loops formed by the tubular structures in the presence of the inhibitors was quantified and normalised to the number of loops formed by the endothelial cells in the presence of DMSO as the control. The example images in figure 4.15 show that a fully connected network of tubules formed in the presence of DMSO, whereas the treatment with the kinase inhibitors caused a range in the severity of defective tubular formation. The images in figure 4.15 showed that the addition of H-7·2HCl which inhibited PKA, PKG, MLCK, PKC, tyrphostin 46 which inhibited EGFR and tyrphostin 9 which inhibited PDGFR all caused abnormal tubular growth.

Upon analysis of the tubular images, 32 kinase inhibitors produced statistical differences between the numbers of loops formed by the endothelial cells compared to the number of loops formed in the presence of DMSO, as shown in figure 4.16. Ten of these inhibitors targeted EGFR which would indicate that EGFR was required for endothelial tubular formation as well as cell migration. Significant reductions were also observed upon the addition of inhibitors that targeted PDGFR. Interestingly, two inhibitor compounds Piceatannol and Y-27632·2HCl caused significant increases in the numbers of loops formed; these inhibitors targeted Syk and ROCK respectively.

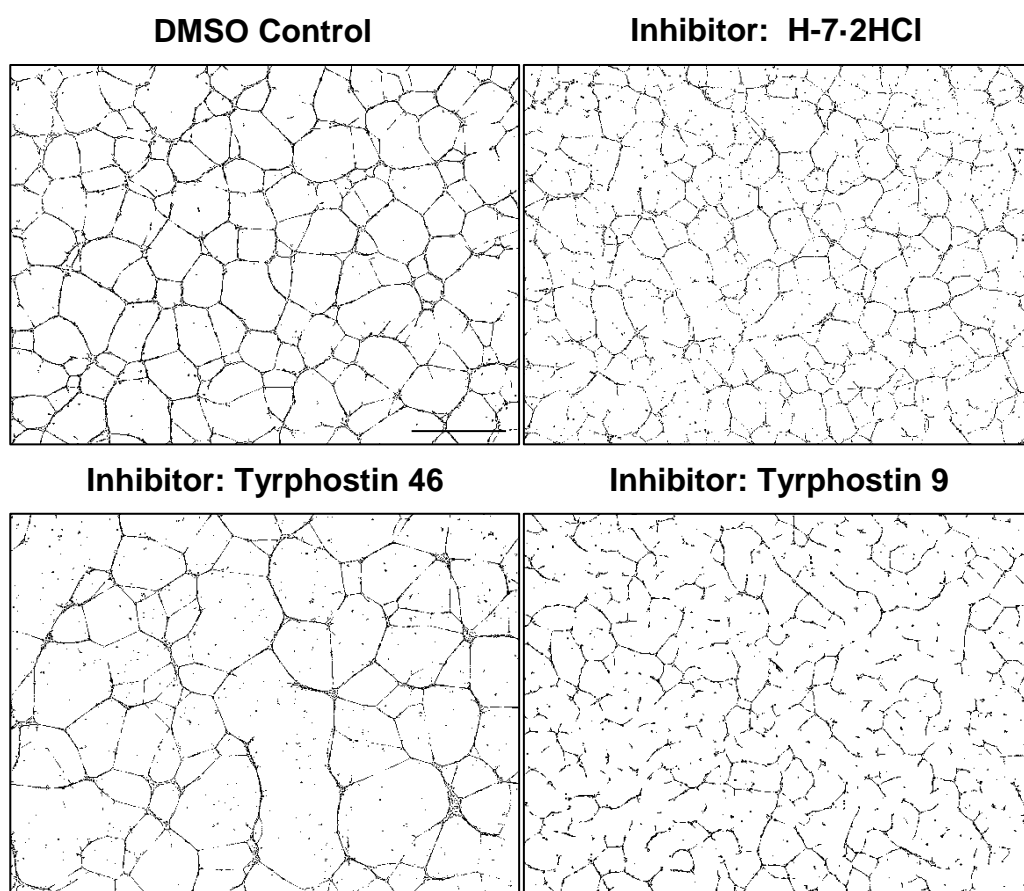


Figure 4.15 The matrigel tube formation assay was used to screen kinases with roles in endothelial tubulogenesis

The tube formation assay was carried out with the addition of the kinase inhibitors or the DMSO control and images of the tubular networks were taken after 12 hrs, scale: 800 μm .

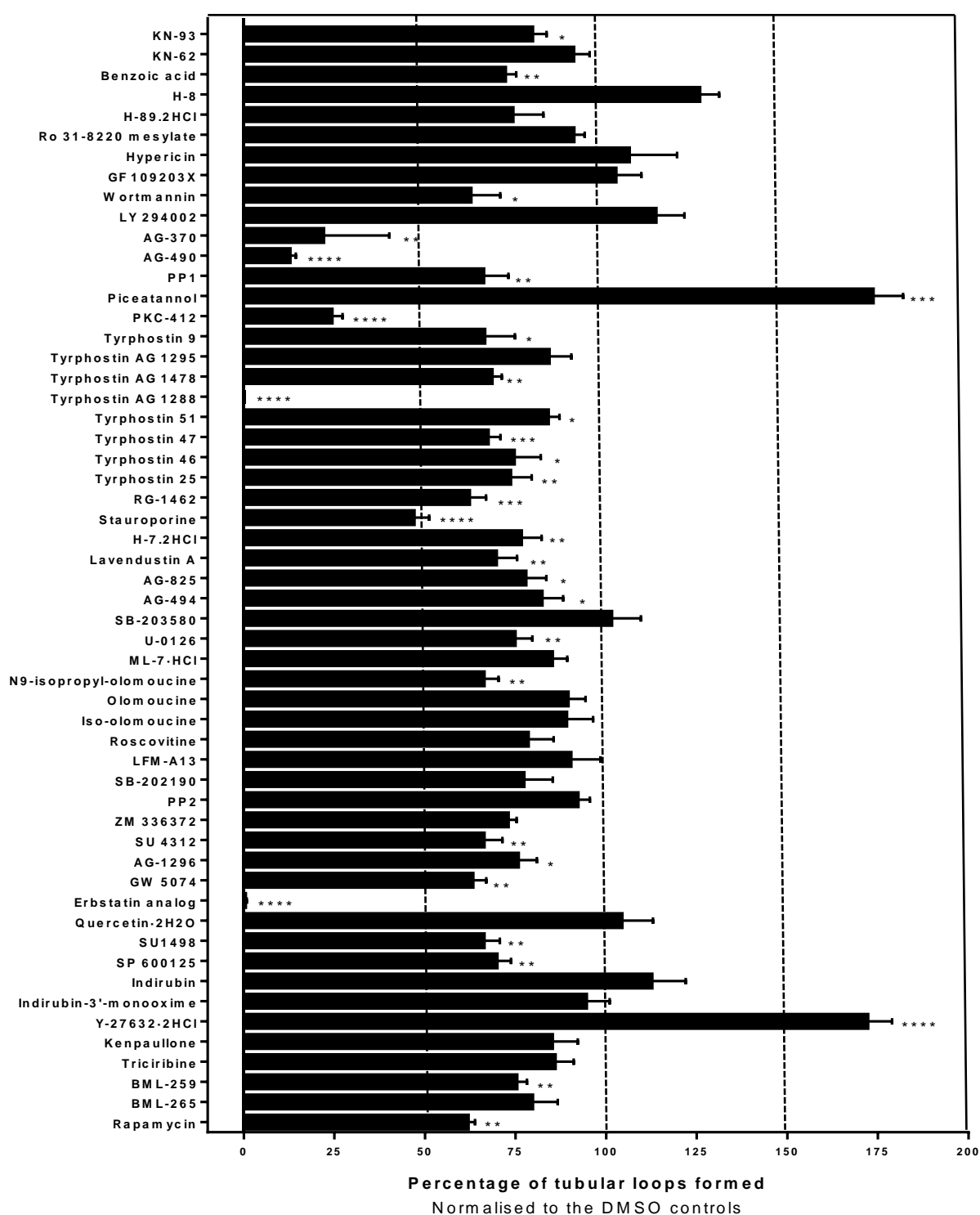


Figure 4.16 Analysis of the matrigel tubular images confirmed that 28 inhibitors significantly affected endothelial tubulogenesis






Image analysis was performed using the Angiogenesis Analyser ImageJ plugin, the number of tubular loops was calculated as a percentage and normalised to DMSO controls, n=4 images of tubule formation for each inhibitor. Statistical differences were determined using a Student's t- test, where **** indicated $p \leq 0.0001$, *** indicated $p \leq 0.001$, ** indicated $p \leq 0.01$, * indicated $p \leq 0.05$. Error bars represent the SEM.

The combined results from the hanging drop spheroid angiogenesis assay, the scratch wound assay and the matrigel tube formation assay used to assess the response to the addition of kinase inhibitors in the different assays modelling aspects of angiogenesis were normalised to their corresponding controls and percentage values were generated and displayed as a heat map in table 4.3. The total sprouting length was chosen to represent the data for endothelial sprouting as this parameter was able to give an understanding of how the overall sprouting network was affected by the addition of the inhibitor compound. The heat map table enabled easy visualisation and determination of the effects the kinase inhibitor compounds had on the processes of endothelial sprouting, migration and tube formation.

The results in table 4.3 showed that there were 14 inhibitor compounds which reduced endothelial activity in all three assays compared to the controls, as shown by the orange and red colours in the table. Six of these compounds inhibited the action of EGFR which reduced cell migration, tube formation and endothelial sprouting; these inhibitors were AG-494, RG-1462, tyrphostin 25, tyrphostin 46, benzoic acid and erbstatin analog. Four inhibitors also reduced cell migration, tube formation and endothelial sprouting by targeting PDGFR and the addition of PKC-412 reduced endothelial activity most severely by inhibiting PKC as shown by the red boxes for all three assays. The only inhibitor which was identified to increase endothelial activity in more than one assay was H-8 which acted on PKA and PKG, the addition of H-8 caused increased cell migration and tube formation but reduced endothelial sprouting length.

Table 4.3 Heat map table to show the screening results of the kinase inhibitors on endothelial migration, tube formation and sprouting.

The combined data generated from the scratch wound assay (figure 4.14), the matrigel tube formation assay (figure 4.16) and the hanging drop spheroid assay (total sprouting length from table 4.2 and figure 7.2 found in the appendix) for each inhibitor was normalised to their corresponding control data sets and the percentage was plotted in a different colour to reflect the result, red (0-40% of control), orange (41-80%), yellow (81-120%), light green (121-160%), dark green (161-200%). Each inhibitor was used at a concentration of ten times their IC₅₀ values and the IC₅₀ values for the inhibitors are stated in table 2.4 on page 49.

	0-40%	Highly below control
	41-80%	Below control
	81-120%	Similar to control
	121-160%	Above control
	161-200%	Highly above control

Compound	Target	Cell Migration	Tube Formation	Endothelial Sprouting
U-0126	MEK	Orange	Orange	Red
SB-203580	P38 MAPK	Yellow	Yellow	Yellow
H-7·2HCl	PKA, PKG, MLCK, PKC	Red	Orange	Red
Staurosporine	Pan-specific	Orange	Orange	Yellow
AG-494	EGFR, PDGFR	Orange	Orange	Orange
AG-825	HER1-2	Yellow	Orange	Red
Lavendustin A	EGFR	Yellow	Orange	Red
RG-1462	EGFR	Red	Orange	Orange
TYRPHOSTIN 25	EGFR	Orange	Orange	Orange
TYRPHOSTIN 46	EGFR	Orange	Orange	Orange
TYRPHOSTIN 47	EGFR	Yellow	Orange	Yellow
TYRPHOSTIN 51	EGFR	Yellow	Yellow	Orange
TYRPHOSTIN AG 1288	Tyrosine kinases	Red	Red	Orange
TYRPHOSTIN AG 1478	EGFR	Yellow	Orange	Orange
TYRPHOSTIN AG 1295	Tyrosine kinases	Yellow	Yellow	Orange
TYRPHOSTIN 9	PDGFR	Orange	Orange	Orange
PKC-412	PKC	Red	Red	Red
Piceatannol	Syk	Red	Dark Green	Red
PP1	Src family	Yellow	Orange	Orange
AG-490	JAK-2	Yellow	Red	Orange
AG-370	PDGFR	Red	Red	Orange

Compound	Target	Cell Migration	Tube Formation	Sprouting
LY 294002	PI 3-K			
Wortmannin	PI 3-K			
GF 109203X	PKC			
Hypericin	PKC			
Ro 31-8220 mesylate	PKC			
H-89·2HCl	PKA			
H-8	PKA, PKG			
Benzoic acid	EGFR, CaMK II			
KN-62	caMK II			
KN-93	caMK II			
ML-7·HCl	MLCK			
N9-isopropyl-olomoucine	CDK			
Olomoucine	CDK			
Iso-olomoucine	Negative control			
Roscovitine	CDK			
LFM-A13	BTK			
SB-202190	P38 MAPK			
PP2	Src family			
ZM 336372	cRAF			
SU 4312	Flk1			
AG-1296	PDGFR			
GW 5074	cRAF			
Erbstatin analog	EGFR			
Quercetin·2H ₂ O	PI3-K			
SU1498	Flk1			
SP 600125	JNK			
Indirubin	GSK-3 β , CDK5			
Indirubin-3'-monooxime	GSK-3 β			
Y-27632·2HCl	ROCK			
Kenpaullone	GSK-3 β			
Triciribine	Akt			
BML-259	Cdk5			
BML-265	EGFR			
Rapamycin	mTOR			

4.9. Chapter discussion

One of the aims of this chapter was to test and evaluate a new ImageJ plugin which had been designed to analyse endothelial sprouting. The automated computer based analysis method was tested by applying the plugin to a range of fluorescently labelled sprouting images generated by using a large library of kinase inhibitors within the hanging drop spheroid angiogenesis assay. The results presented in this chapter showed that the plugin is a useful and valuable tool for analysing endothelial spheroid images generated from the spheroid assay. The results confirmed that the plugin was able to rapidly generate quantification on a number of sprouting parameters, generating results comparable and 6.7 times faster than the manual method for calculating the total sprouting length of spheroids. Importantly, the highly sensitive plugin was able to accurately analyse a large range of sprouting phenotypes including hyper-sprouting which would be highly challenging to analyse using the manual method of measuring the lengths of the sprouts.

The brightfield and phase contrast microscopy images of the hanging drop spheroids outlined the problems faced when imaging and analysing the three dimensional structure of the sprouting spheroids. These imaging modalities did not allow for the spheroids to be imaged at high resolution as these techniques only capture one focal plane in a single image therefore many of the cellular sprouts appeared out of focus. The images presented the problem of incomplete object boundaries with minor distinctions observed between the image object of the endothelial cells and the image background of the collagen matrix. To improve the imaging resolution and to define the localisation of the endothelial cells in the sprouting process, the cells were fluorescently labelled with a high emission cytoplasmic dye CFSE prior to the

formation of spheroids. Confocal microscopy was used to generate optical sections of the sprouting spheroids which were compressed to generate a highly fluorescent, high resolution image of the spheroids which provided a clear distinction between the endothelial cells and background and as a result were easier to analyse.

A widely used approach for analysing endothelial sprouting from spheroid images is to count the number or measure the lengths of the sprouts, often computer software such as DP-Soft Olympus or ImageJ can be used to aid this manual analysis method. The user of these software tools can measure along the lengths of each individual sprout and manually record the lengths to present an average or total sprout length per condition²³³. However, such methods can be labour intensive, time consuming and subjective.

In this chapter, an ImageJ plugin known as Spheroid Analysis was used to analyse endothelial sprouting, this method of analysis enabled rapid and objective quantification of a number of different image parameters. Testing the plugin revealed that it was able to rapidly analyse a wide range of sprouting phenotypes including hyper-sprouting which would be problematic and time consuming to analyse manually. The plugin was able to analyse the images rapidly with quantitative outputs generated 6.7 times faster than the manual analysis method of measuring the total sprouting length. The plugin would be suitable for analysing both small and large imaging based studies such as for screening purposes as outlined in this study. The plugin effectively and efficiently analysed 440 spheroid images allowing the assessment and identification of kinases with roles in endothelial sprouting. As well as providing useful information on the average and total sprouting lengths, number of endothelial sprouts, junctions and end points, the plugin was able to give an

indication of the sprouting distribution represented in the image through the generation of a fluorescence intensity profile plot.

The plugin relied on a highly fluorescent spheroid image; therefore spheroids were labelled with 5 μ M CFSE to enable accurate analysis of endothelial sprouting. At present, the plugin requires a single coloured fluorescence image with one spheroid per image. Future advancements in the development of the plugin would include adaptations which would allow multiple spheroids per image to be analysed thus speeding up the imaging process and possibly providing a user selection tool which would allow the user to select which spheroids within the image to analyse. Further work would also include advancing to analysing two coloured fluorescence images, enabling the dynamics between tip and stalk cells to be studied and quantified.

The ImageJ Spheroid Analysis plugin was used to rapidly analyse spheroids treated with a range of PAK and BTK inhibitors. PAKs consist of a six membered family of enzymes which have biological roles in controlling cellular movement and motility, as well as regulating the organisation of the actin cytoskeleton²²². PAKs become activated from the binding of the Rho family of GTPases including Rac1 and Cdc42^{222,233,234}. The pan specific inhibitor PF-3758309 targets group B serine/threonine kinase PAKs as well as also inhibiting group A PAKs, although PF-3758309 is considerably less active against this PAK subfamily²³⁵. It was identified by Murray *et al.* that PF-3758309 acts through competitive binding of the ATP site within the PAKs catalytic domain to prohibit the phosphorylation event of a Rho-family guanine nucleotide exchange factor GEF-H1²³⁵. Therefore, it was unsurprising that the addition of PF-3758309 into the spheroid assay caused significant reductions in endothelial sprouting compared with the DMSO control treated spheroids. Deacon *et*

al. identified that the other PAK inhibitor IPA-3 to be a highly selective non-competitive PAK1 inhibitor²³⁶. Treatment with different concentrations of IPA-3 resulted in comparable sprouting to the DMSO controls, proving that PAKs targeted with PF-3758309 but not IPA-3 are important for endothelial sprouting.

BTK and BMX are members of the Tec family of protein tyrosine kinases which play crucial roles in many signal transduction cascades within B lineage lymphocytes and bone marrow derived cell lineages regulating cell events such as survival, differentiation and adhesion^{224,228}. BTK is not expressed in endothelial cells, however in this study it was shown that the action of the BTK inhibitors AVL-292 and LFM-A13 affected the process of endothelial sprouting as identified by analysing the spheroid images using the Spheroid Analysis plugin. The mechanisms behind the action of the BTK inhibitors has been well characterised, many inhibitors prevent activation through prevention of an auto-phosphorylation event, targeting the tyrosine residue at position 551²³⁷. Ibrutinib inhibits both BTK and BMX by covalently binding to the target protein and all BTK inhibitors used in this study were known to prevent the auto-phosphorylation event of BTK^{227-230,238}. It was likely that these inhibitor compounds were targeting BMX, a BTK related tyrosine kinase which is highly expressed in endothelial cells to reduce endothelial sprouting²²³. The results from the use of these inhibitors in the hanging drop spheroid assay therefore identified that BMX is required for endothelial sprouting.

The kinase inhibitor compounds from the small molecule inhibitor library were used to target specific kinases within endothelial cells to determine the effects of inhibiting the action of these proteins on endothelial sprouting, migration and tube formation. However, it is highly likely that each kinase inhibitor compound inhibits other protein

kinases in addition to their presumed target protein kinases. Many small molecule inhibitors have broad specificity profiles and cause inhibition of more than one protein kinase, additionally the compounds do not always only target additional kinases which have closely related or highly similar primary structures^{43,44}. Kinases play crucial roles in signal transduction pathways, therefore kinase inhibitor screens can be used as useful tools for identifying potential new roles or involvement of these proteins in cellular pathways. However, interpreting the results of kinase inhibitor screens should be approached with caution due to the low specificity these compounds have to their targets.

A particular example of the broad specificity profiles exhibited by small molecule kinase inhibitors was outlined in this study; PDGFR is not expressed in endothelial cells however the treatment with four PDGFR kinase inhibitors into the hanging drop spheroid assay, the scratch wound assay and the tube formation assay caused significant reductions in endothelial activity in all three assays. PDGFR is activated through the binding of the PDGF ligand causing an auto-phosphorylation event of the receptor and upon activation PDGFR binds to Src homology 2 (SH2) domain containing proteins to participate in downstream signalling events^{50,56}. Since PDGFR is not expressed in endothelial cells, it is likely that the inhibitor compounds used in the screen were targeting the structurally related endothelial expressed tyrosine kinase receptor VEGFR. Many commonly used therapeutic agents including sorafenib and sunitinib which are used primarily to target VEGFR to reduce vessel growth *in vivo* are known to additionally target PDGFR^{53,57-59}. PDGF signalling is also often targeted therapeutically to prevent pathological angiogenesis since there is high expression of PDGFR in pericytes, therefore blocking this receptor tyrosine kinase

causes pericytes to detach from the vessels causing destabilisation of the vasculature^{45,60-62}.

The results of the kinase inhibitor screen identified six inhibitor compounds which targeted EGFR and significantly reduced endothelial migration in the scratch wound angiogenesis assay. Additionally, ten compounds reduced tube formation in the matrigel tube formation assay by targeting EGFR, whilst nine EGFR inhibitors reduced the total sprouting length of endothelial sprouts in the hanging drop spheroid assay. The identification of EGFR having an important role in endothelial migration, sprouting and tube formation was of interest since it has been reported that EGFR is not expressed in normal endothelial cells, even though there have been many reports that have stated that EGFR is highly expressed by tumour associated endothelial cells²³⁹. The overexpression of EGFR and its ligand EGF has been associated with many different types of cancers, therefore this type I receptor tyrosine kinase has been targeted by therapeutic agents known as EGFR tyrosine kinase inhibitors (TKIs), which prevents activation of the receptor and causes an induced apoptosis of cancer cells²⁴⁰⁻²⁴⁴. Cancer cells secrete the EGFR ligand EGF in response to hypoxic conditions, subsequent binding of EGF to EGFR causes receptor dimerization followed by auto-phosphorylation and the recruitment of additional signalling and adaptor proteins which affect cellular migration, proliferation and differentiation as well as promote anti-apoptosis^{64,65,245}. The results in this study suggest that EGFR could also be expressed by normal endothelial cells and acts through EGF signalling to regulate endothelial migration, sprouting and tube formation which are critical steps within the angiogenic pathway.

Inhibiting PKC using the inhibitors H-7·2HCl and PKC-412 also impaired cell migration, endothelial sprouting and tube formation. The different isoforms of PKC become activated through signalling of intracellular calcium ions, diacylglycerol (DAG) and phospholipids such as phosphatidylserine, this activation event causes PKC to modulate transcriptional events⁶⁷. Additionally, GW 5074 reduced angiogenesis by targeting cRAF which is known to play a critical role in determining cell fate through association and regulation of the MAPK and ERK pathway²⁴⁶.

Interestingly, treatment of staurosporine in the hanging drop spheroid assay caused an enhancement of the numbers of endothelial segments, junctions and end points formed by the spheroids but caused defective cell migration and tube formation. Staurosporine is a pan-kinase specific inhibitor which is a widely used apoptotic agent for numerous cell lines²⁴⁷. Kabir *et al.* showed that staurosporine acts to induce cell death in endothelial cells through dephosphorylation of FAK causing disassembly of focal adhesion complexes²⁴⁸. It is therefore possible that staurosporine caused defective cell migration due to the high dependency of the formation of focal adhesion complexes for cell motility.

In conclusion, the kinase inhibitor screen was able to generate a range of endothelial sprouting phenotypes which proved useful for testing and evaluating the capabilities and outputs generated by the designed ImageJ Spheroid Analysis plugin. The ImageJ plugin can be applied to different morphological images of endothelial sprouting from fluorescently labelled spheroids generated using the *in vitro* hanging drop spheroid angiogenesis assay. As outlined in this chapter, the Spheroid Analysis plugin can rapidly and effectively generate quantitative results on many different sprouting parameters and is therefore suitable for large scale screening procedures

to identify compounds which affect the process of endothelial sprouting. Furthermore, the results in this chapter outlined the broad spectrum of activity exhibited by small molecule kinase inhibitors and that protein kinases particularly receptor tyrosine kinase activity was indispensable for effective endothelial migration, proliferation and tube formation.

Chapter Five

Developing, testing and evaluating computer based analysis methods for quantifying the zebrafish vasculature

5.1. Chapter summary

The aim of this chapter was to generate a computer based analysis method to quantify the development of the intersegmental blood vessels (ISVs) in embryonic *fli1-GFP* zebrafish. Two computer based analysis methods were developed using IMARIS and ImageJ software to provide quantification of the vasculature by specifically targeting the ISVs and their connectivity to the dorsal longitudinal anastomotic vessel (DLAV). The ImageJ analysis method was tested using normal and abnormal zebrafish vasculature images and compared to a frequently used manual analysis method. The advantages and disadvantages for both computer based analysis methods were considered and discussed and the results and findings of these methods are presented in this chapter.

The structure for this chapter is as follows: section 5.2 chapter introduction, section 5.3 presents the computer based analysis methods for analysing the zebrafish vasculature, section 5.4 imaging the effects of silencing vascular related genes, section 5.5 analysing and evaluating the effects of silencing vascular related genes, section 5.6 analysing the effects of inhibitor treatment on vascular development, section 5.7 evaluating the computer based analysis method, section 5.8 chapter discussion.

5.2. Chapter introduction

The zebrafish (*Danio rerio*) is a widely used *in vivo* vertebrate model used to study blood vessel formation. Imaging the cardiovascular development in this organism allows the effects of silencing genes through morpholino oligonucleotide (MO) injection to be determined and novel compounds which act on the angiogenic pathway to be identified. However, at present there are limited computer based analysis tools which are easy to use and widely available that can be applied specifically to zebrafish images to provide rapid quantification of the growth and connectivity of the developed vasculature.

Vascular analysis data presented in the literature frequently targets the development of the ISVs as these are the first angiogenic vessels to form in the zebrafish at 24 hpf¹⁴⁵. The extent of ISV disruption in response to anti-angiogenic factors such as inhibitor compounds or knocking down genes is frequently reported by manually classifying the appearance of the vasculature into categories such as 'mild', 'intermediate' or 'severe' disruption¹⁶⁴⁻¹⁶⁷ or represented by a single calculation of the number of ISVs that have connected or remain disconnected to the DLAV in the trunk and tail regions of the zebrafish embryos¹⁶⁸⁻¹⁷⁶. These analysis methods may be performed manually or assisted using imaging or microscopy software, these methods give a global view and understanding of the developed vasculature, however apart from being labour intensive, they do not provide information on the lengths of the ISVs and in the case of the manual classification system it also does not specify vascular connectivity. In this chapter, two computer based analysis methods that were developed to quantify ISV growth and development will be presented, along with the findings of testing and evaluating the analysis methods.

5.3. Computer based analysis methods for analysing the zebrafish vasculature

The ISVs are fully formed and connected to the DLAV at 48 hpf therefore the zebrafish vasculature is often imaged at this time point, when the effects of a gene knock down or the treatment with angiogenic compounds can be clearly visualised by studying the growth of the ISVs¹⁴⁵. The aim of this study was to develop computer assisted approaches to enable easy and rapid quantification of these blood vessels. To achieve accurate analysis, there was a requirement for the vascular images to have a high fluorescence intensity particularly from the ISVs and DLAV in order to assess ISV connectivity; this was achieved by compressing confocal optical sections to produce a highly fluorescent vascular image.

The first computer based approach was generated using ImageJ software, which is an open platform designed to analyse scientific images. The ImageJ analysis method consisted of a series of steps as outlined in figure 5.1. Firstly, the compressed vascular image was loaded into ImageJ, where the polygon selection tool was used to outline the DA at the positions where the ISVs sprout from during development. The line generated by the polygon selection tool was joined up around the base of the image to form a fully connected shape containing all of the vessels that were not required for the analysis process such as the DA and the PCV, shown in step 2 of figure 5.1. By clicking on the selected area with the black fill tool, these vessels were merged into the image background leaving the remaining vessels of the ISVs and DLAV within the image to be analysed. The vascular image was then binarised in step 4 to produce an 8-bit black and white image. The fill holes function shown in step 5 was used to remove loops formed by the DLAV as only the connectivity of the

ISVs was required for analysis. The despeckle function shown in step 6 was used to remove noise pixels which were acquired during the image acquisition process. The image was then skeletonised using the inbuilt Skeletonize 3D plugin, which eroded the vascular objects within the image iteratively until the vessels were visualised as a network structure 1 pixel in diameter, as shown in step 7. The skeletonised image was then analysed and quantified using the inbuilt ImageJ Analyze Skeleton (2D/3D) plugin. Each pixel from the skeletonised network was assessed according to its neighbouring pixels and assigned either as a segment, junction or end point pixel. A segment pixel was assigned if the pixel had exactly two neighbouring pixels in the skeleton, a junctional pixel was assigned if it had more than two neighbouring pixels and an end point pixel was assigned if it had zero or one neighbouring pixel. The vascular segments within the images were defined as a series of connected segment pixels which were separated either by two end point pixels, two junctional pixels or one end point and one junctional pixel, see figure 7.7 in section 7.3 of the appendix for further information on these parameters. The analysed image in step 8 of figure 5.1 shows the analysed skeleton that was generated by the ImageJ analysis method, where orange pixels represented the outline of the vessels, pink pixels indicated the presence of vascular junctions and blue pixels showed the vascular end points. The area highlighted in the red box was enlarged to show the identification of individual pixels using this approach and an overlaid image of the original zebrafish vascular image and the skeletonised vascular network was generated to determine the accuracy of the analysis procedure, as shown in step 10 of figure 5.1. The steps of the ImageJ analysis method shown in figure 5.1 from binarisation through to generating the outputs of the analysed vascular skeleton (steps 4 - 8) were recorded

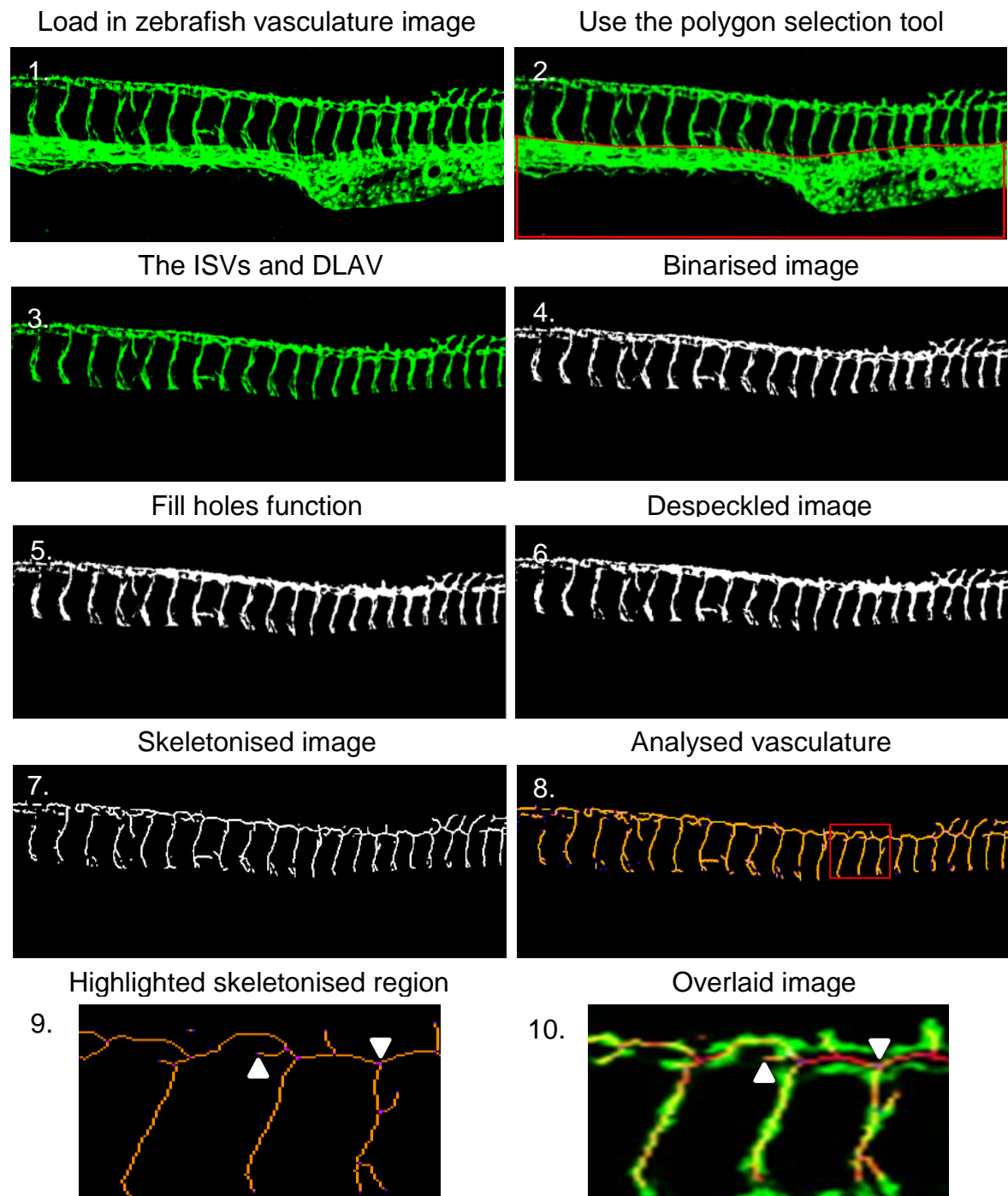


Figure 5.1 Steps of the ImageJ based approach to analyse vascular images of *fli1*-GFP zebrafish

The ISVs and DLAV were analysed by 1) loading in the vascular image, 2) removing the PCV and DA using the polygon selection tool, 3) leaving the ISVs and DLAV, 4) binarisation created a black and white image, 5) the fill holes function removed small holes in the DLAV, 6) the despeckle function removed noise pixels, 7) the vasculature was skeletonised, 8) analysis of the skeletonised vasculature, 9) the region highlighted in the red box was enlarged to show the identification of individual pixels, 10) an overlaid image of a region of the original and skeletonised images to show the accuracy of the procedure, arrows show an end point and junctional pixel.

into an ImageJ macro known as the zebrafish vasculature analysis macro this enabled semi-automated analysis of the zebrafish vascular images and reduced the processing time. See section 7.4 in the appendix for the code of the recorded zebrafish vasculature analysis macro. One limitation of this analysis method was the requirement to transfer the image data files from ImageJ to Microsoft Excel to further process the data and select the desired parameters. For this study the total and average vessel lengths were calculated in Excel as well as the total numbers of vascular junctions and end points. The semi-automated ImageJ method of analysis relied on the inbuilt plugins Skeletonize 3D and Analyze Skeleton (2D/3D) but the method was able to rapidly analyse the vascular images and the outputs of the analysed skeleton data from a single image were produced within 35 seconds.

The second analysis method was produced using the Filament Tracer module in IMARIS. In a similar way to the ImageJ method, a series of steps were produced to analyse the growth and connectivity of the ISVs, the series of steps has been shown in figure 5.2. Firstly the compressed zebrafish vascular image was loaded into IMARIS, where a three dimensional mask of the vasculature was generated using the surface function and selecting a threshold value shown in grey in step 2 of figure 5.2. The original vascular mask was created to provide a filtered version of the original image containing all of the vessels within the image; since the mask was used for all subsequent measurements of the vessels, therefore the mask must accurately represent the original vasculature. Once the mask had been created, it was possible to adapt the mask using the cutting tool by selecting the base of each ISV along the DA, in this way each ISV was disconnected from the DA, the red lines in step 4 shows where the cutting tool was positioned.

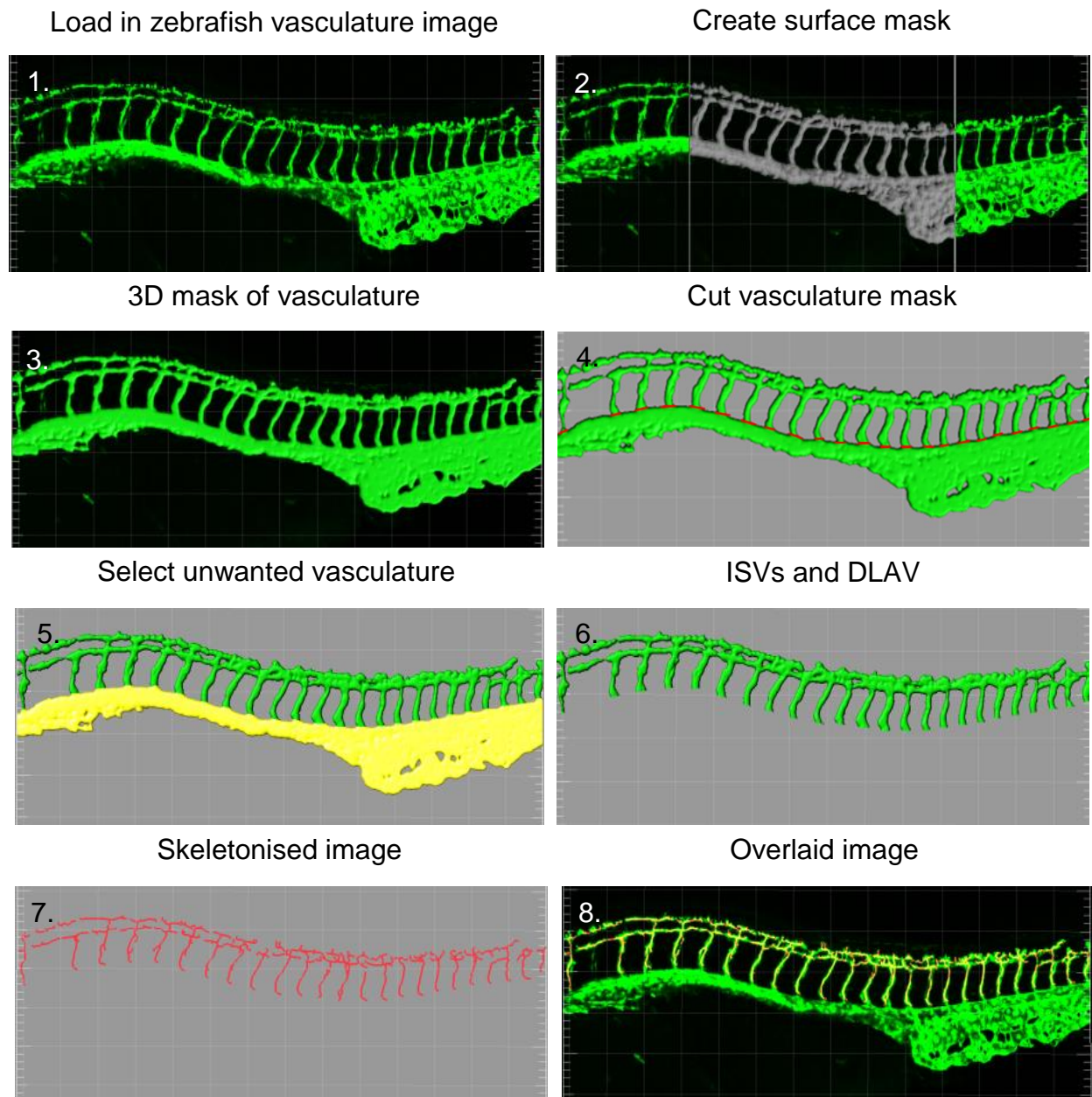


Figure 5.2 Steps of the IMARIS approach to analyse *fli1*-GFP zebrafish vascular images

The ISVs and DLAV were analysed by 1) loading in the vascular image, 2) a 3D mask of the vasculature was created in one vascular region, 3) the 3D mask was expanded to include all the vessels in the image and was rotated to allow clear visualisation and connectivity of the blood vessels, 4) the cutting tool was used to remove individual blood vessels from the image, 5) the PCV and DA was highlighted and removed, 6) leaving the ISVs and DLAV for analysis, 7) the remaining vasculature was skeletonised and analysed for a range of parameters including lengths, connectivity and end points, 8) the analysed skeleton was overlaid onto the original image to check the accuracy of the analysis procedure.

The DA and PCV were then selected and removed from the mask, leaving a mask containing the ISVs and DLAV for analysis. One limitation of this method was the requirement to rotate the image between each cut that was applied to the mask to enable the cutting tool to work; this image manipulation procedure was time consuming as approximately 24 cuts were required per image. The mask of the ISVs and DLAV was skeletonised, which reduced the vessels to a 1 pixel diameter network which was then subsequently analysed. The analysis procedure for a single image took approximately 5 minutes for images with around 24 ISVs, the time was dependent on the number of vessels within the image and the user's experience of the software. The IMARIS software presented the analysis data from the vascular skeleton as a table in the software window; this data table was exported to Microsoft Excel to calculate the total number of vessels, vascular junctions, end points and average and total vessel length. The skeletonised image was easily overlaid onto the original image to determine the accuracy of the skeletonisation step, shown in the final image of figure 5.2.

To compare the zebrafish vasculature analysis data generated by the two computer based analysis methods using ImageJ and IMARIS, images of normal zebrafish vascular development were produced by carrying out time-course imaging of *fli1*-GFP zebrafish embryos from 24 – 72 hpf. Optical image sections were compressed to produce high resolution images of the blood vessels in the trunk and tail regions of the zebrafish and the images in figure 5.3 showed the rapid growth of the ISVs.

At 24 hpf the endothelial cells of the ISVs were seen to sprout bilaterally from the DA with filopodia extending from the tip cells of the developing ISVs to direct vessel growth. From 26 hpf to 28 hpf the ISVs elongated and produced increasing numbers

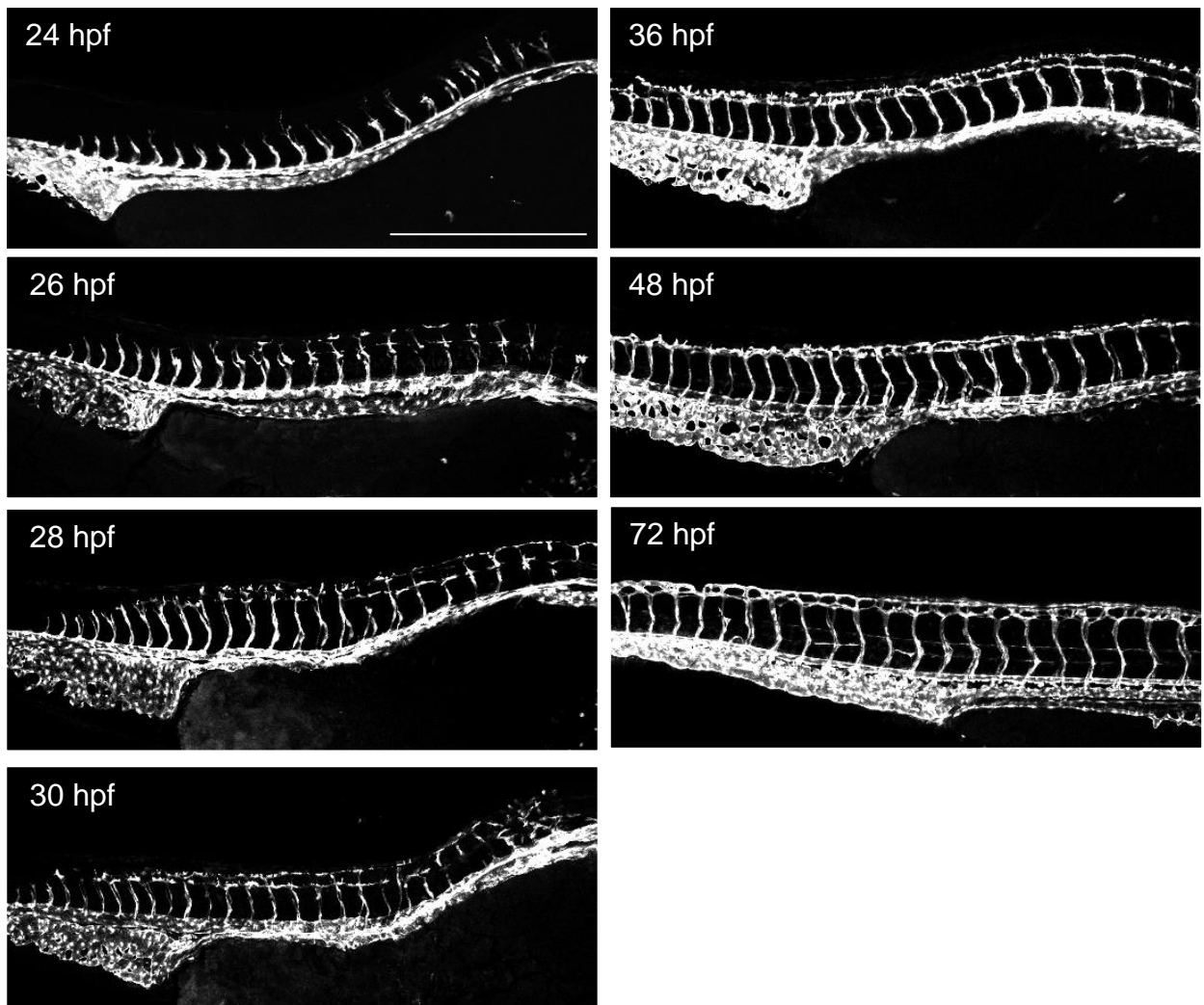


Figure 5.3 Developmental time course images of the zebrafish vasculature

Confocal microscopy images showing the development and connectivity of the ISVs with the DLAV in transgenic *fli1*-GFP zebrafish embryos from 24 hpf to 72 hpf. The ISVs sprout from the DA and fully connect with the DLAV at 48 hpf. Scale: 500 μ m.

of filopodia as they extended and began to reach the neural tube. As the vessels approached the neural tube, they separated into rostral and caudal branches which interconnected to form the DLAV¹⁵⁷. At 30 hpf and 36 hpf, the paired ISVs were clearly visible and the DLAV had almost fully formed. At 48 hpf, all of the ISVs were joined to the DLAV and the primary vessel network within the organism had been established. By 72 hpf, the entire zebrafish vascular network had fully formed to provide a functional circulatory system within the embryo that coincided with the straightening out of the tail¹⁵⁷.

The ImageJ and IMARIS methods were used to analyse the zebrafish vascular images at the following developmental time points: 24, 26, 28, 30, 36, 48 and 72 hpf; the number of blood vessel segments, vascular junctions, end points, total and average vessel lengths were measured in the images. The average values for each parameter and the standard error of the mean (SEM) at each time point were plotted and is shown in figure 5.4.

Both the ImageJ and IMARIS analysis methods provided quantification of the vasculature, studying the parameters measured in the images showed that there was a general trend in the results which indicated the rapid development and formation of the vascular system between 24 hpf and 30 hpf. The line graphs in figure 5.4 showed a rapid increase in the numbers of vessel segments, junctions, end points and total vessel length between these time points. This result correlated accordingly with the overall development of the embryo which occurs most rapidly in the first few days after fertilisation. Generally, the rate of vascular growth decreased after 30 hpf which reflected the slower rate of development in the organism.

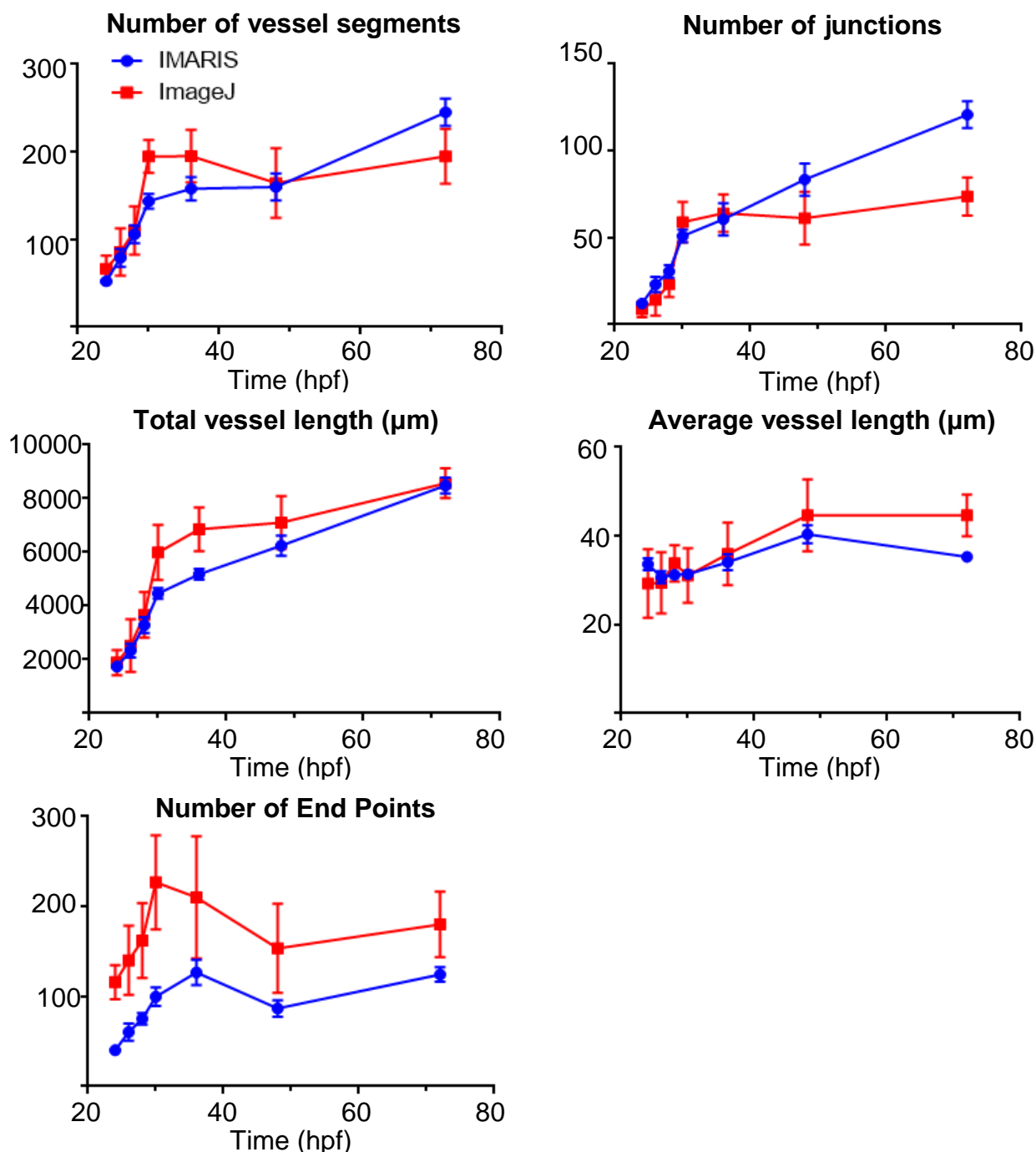


Figure 5.4 Line graphs of vascular analysis comparing the data generated by the ImageJ and IMARIS methods of analysis

The developmental time-course images of the zebrafish vascular system were analysed using the ImageJ and IMARIS analysis methods, the parameters of the total and average vessel lengths, numbers of vessel segments, junctions and end points at each time point were plotted, n=10-14 images. Error bars represent the standard error of the mean (SEM).

The graphs for the number of vessel segments and the total and average vessel lengths showed that similar results were obtained using the two analysis methods; the average vessel length remained relatively constant over the course of development, between 30-40 μm . The average vessel length was derived from the parameters of total vessel length and the number of vessel segments and since both of the analysis methods calculated an increase in total vessel length and the number of segments over time, it was expected that the average vessel length would remain relatively constant. The IMARIS method measured slightly higher numbers of segments at 72 hpf compared to the ImageJ method, but at this time point the total vessel length measured from both methods was the same, therefore a slight reduction in the average vessel length was calculated for the IMARIS method at this time point.

Similar numbers of vascular junctions were measured using the two analysis methods from 24 hpf to 36 hpf, however after 36 hpf the IMARIS analysis method continued to record increasing numbers of junctions, with a mean of 132 junctions calculated at 72 hpf compared with 74 junctions measured by the ImageJ method. The two analysis methods have different morphological post-processing steps which explain this difference; the ImageJ method used a fill holes function which is a closing operation to remove unwanted vessel loops formed in the DLAV and thereby reduced the numbers of junctions measured within the images after 36 hpf when these loops developed. The aim of the study was to specifically target the ISVs for analysis and measure the length of the ISVs and their connectivity to the DLAV; thereby the fill holes function removed the additional junctions formed by the DLAV which did not involve connectivity to the ISVs. The fill holes function could be omitted

from the analysis process if the DLAV complexity is of interest. The ImageJ method therefore continued to measure relatively constant numbers of junctions after 36 hpf, even though the complexity and connectivity of the DLAV became more elaborate. In the IMARIS method, the additional junctions and loops in the DLAV were included in the analysis as this software does not provide a function that performs this closing operation. Therefore, as the DLAV increased in complexity over time, an increased number of junctions within the vascular images was detected using the IMARIS method and this was reflected in the graph in figure 5.4.

The results for the number of end-points measured using the two analysis methods differed although a similar pattern over time was observed. The ImageJ analysis method calculated higher numbers of end points at every time point with larger error bars, compared to the results of the IMARIS analysis method which detected smaller numbers with smaller error bars. An explanation for this difference was again due to the differences in the morphological post-processing steps of the two methods. The ImageJ method uses the despeckle function to remove any unwanted noise in the image, noise are errors in the image file acquired through image acquisition and these noise pixels must be removed to improve the accuracy of analysis. The despeckle function in ImageJ used a median filter to compare each pixel to its neighbouring nine pixels and reassigned noise pixels to the image background to excluded these pixels from the analysis procedure, however if any noise pixels, image artefacts or background fluorescence remained in the image they will be identified in this analysis method as end points. Furthermore, this process could have inadvertently eroded or replaced pixels in the vascular object in the image; therefore causing minor fragmentation of the vessels upon skeletonisation, introducing higher

numbers of end points upon analysis. The IMARIS analysis method relied on the formation of a vascular mask created from the connected vascular regions within the image, the subsequent measurements and quantification were performed using only the mask rather than the original image file, thereby bypassing the requirement to remove noise or artefacts from the image.

To compare the outputs generated by the two analysis methods and determine if there was a linear relationship between the results generated by these methods, the measurements from each zebrafish image from the developmental time-course study were plotted on correlation graphs, shown in figure 5.5. The coefficient of determination values (r^2 values) for the parameters of total vessel length, number of vessel segments, junctions and end points were also calculated to determine if there was a linear relationship between the data generated by the ImageJ and IMARIS analysis methods. The plot for the average vessel length was not included as this parameter was dependent on the total vessel length and the number of segments. An r^2 value of 1.0 indicated an entirely linear relationship between the x and y coordinates, whereas an r^2 value of 0.0 indicated no linear relationship.

The highest r^2 value of 0.841 was calculated for the data generated on the parameter of total vessel length, this proved that similar and comparable results were obtained throughout zebrafish development using the two analysis methods. Measuring the number of vascular junctions within the images using the analysis methods generated an r^2 value of 0.665, the graph in figure 5.5 showed a linear relationship for the smaller numbers of junctions measured however due to IMARIS measuring the additional junctions formed in the DLAV at time points after 36 hpf, this initial linear

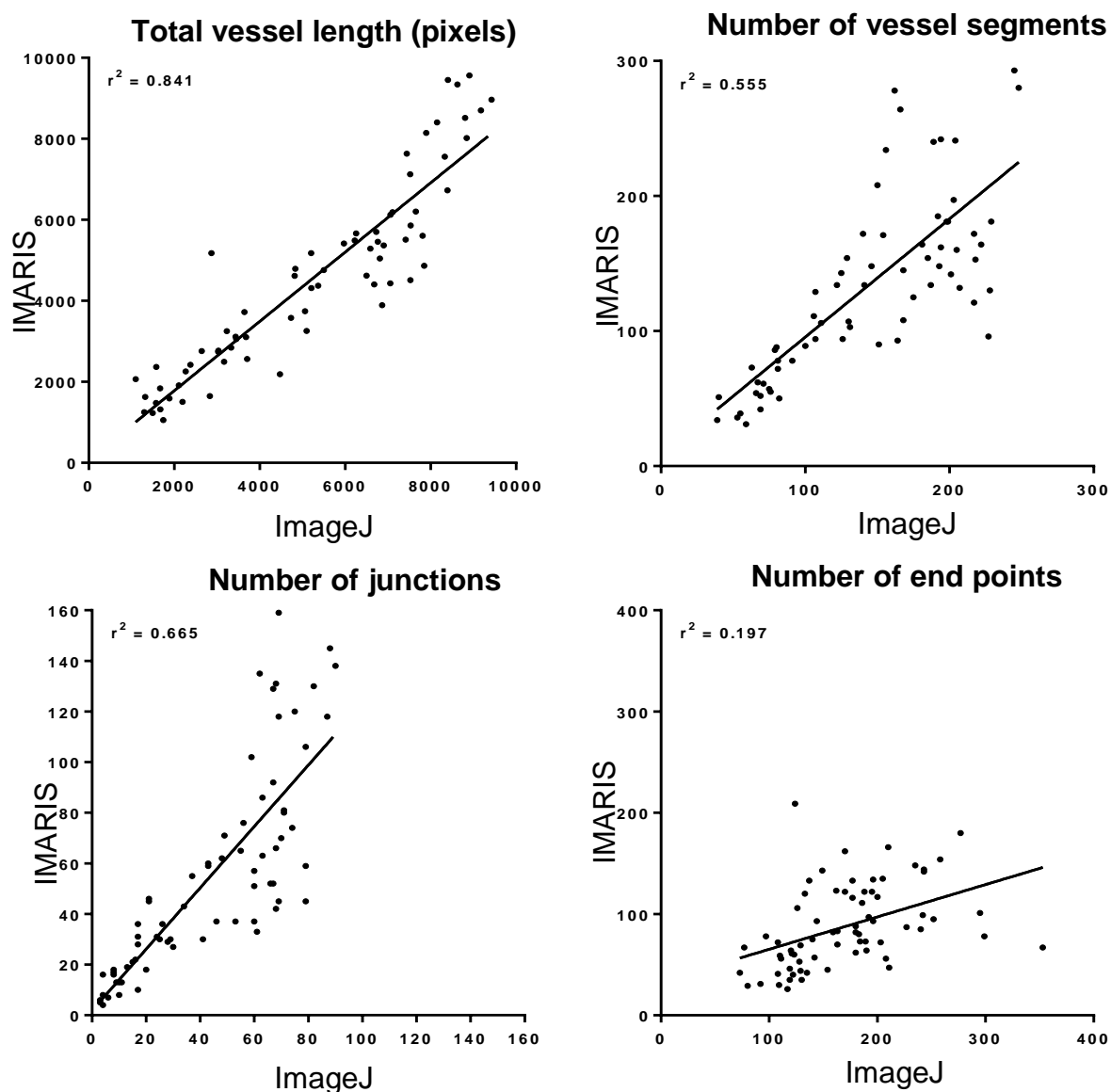


Figure 5.5 Studying linear relationships between the outputs generated from the ImageJ and IMARIS analysis methods

The measurements generated from the two analysis methods using ImageJ and IMARIS from each zebrafish vascular image from the developmental time course study were compared to identify linear relationships between the data sets. The outputs of the parameters for the total vessel length and the number of vessel segments, junctions and end points were studied. The r^2 values were calculated to give an indication of the linear relationship between the two methods and the line of best fit was plotted.

relationship was lost and the graph showed that ImageJ did not measure more than 90 junctions within the images, compared with 159 for IMARIS. An r^2 value of 0.555 was calculated for the number of vessel segments, with larger variations measured for the higher numbers of vessel segments within the images. The smallest r^2 value of 0.197 was calculated for the number of end points, proving that there was not a linear relationship between the data generated on this parameter using the two analysis methods, which was expected due to the previous results shown in figure 5.4. As previously discussed, ImageJ detected more end points within the vascular images at each time point compared with the IMARIS method and the graph in figure 5.5 showed that the highest number of end points calculated by IMARIS was 209 and for ImageJ was 353. The differences in the number of end points calculated by the ImageJ and IMARIS methods were due to the differences in the morphological post-processing operations of the two computer based analysis methods.

The ImageJ analysis method would be freely and widely available to the scientific community as the ImageJ software is in the public domain and the macro would be easy to implement and use. Additionally, this computer based analysis approach was able to rapidly and effectively analyse the zebrafish vasculature, for these reasons this analysis method was chosen for subsequent testing and evaluation by quantifying abnormal vascular development.

5.4. Imaging the effects of silencing vascular related genes

To assess the capabilities of the ImageJ analysis method to quantify abnormal vessel development, images of abnormal vasculature development were obtained by knocking down known vascular related genes using antisense morpholino oligonucleotide (MO) injections at the one cell stage of development in *fli1-GFP*

embryos. Subsequent vessel formation was imaged at either 30 hpf or 48 hpf depending on the phenotype resulting from the morpholino knock down and the ImageJ analysis method was used to analyse the growth and connectivity of the ISVs to the DLAV.

The vascular images of zebrafish embryos which had been injected with the gene targeting morpholino were compared with images obtained using a negative control mismatch morpholino. The control mismatch morpholino injected embryos showed normal vascular development, with most ISVs fully formed and connected to the DLAV at 30 hpf and all ISVs had fully connected to the DLAV at 48 hpf.

The C-type lectin CLEC14A was knocked down and the development of the zebrafish vasculature was imaged at 30 hpf and 48 hpf using confocal microscopy, the images are shown in figure 5.6A. Upon CLEC14A knock down, abnormal vessel growth was observed with stunted ISV growth and no formation of the DLAV at 30 hpf, however observing vascular development at 48 hpf revealed normal vessel development with the ISVs fully formed and connected with the DLAV.

Use of the ECSCR 5' UTR and splice targeting morpholinos caused defective and truncated ISV growth and no DLAV formation at 30 hpf when this glycosylated transmembrane protein was knocked down, shown in figure 5.6B. The mismatch control morpholinos showed normal development of the vasculature with complete formation of the ISVs with connections to the DLAV.

The knock down of the orphan adhesion G-protein coupled receptor ELTD1 shown in figure 5.7A and the predominant roundabout receptor that is expressed in the zebrafish vasculature ROBO4 caused defective growth of the ISVs when imaged at

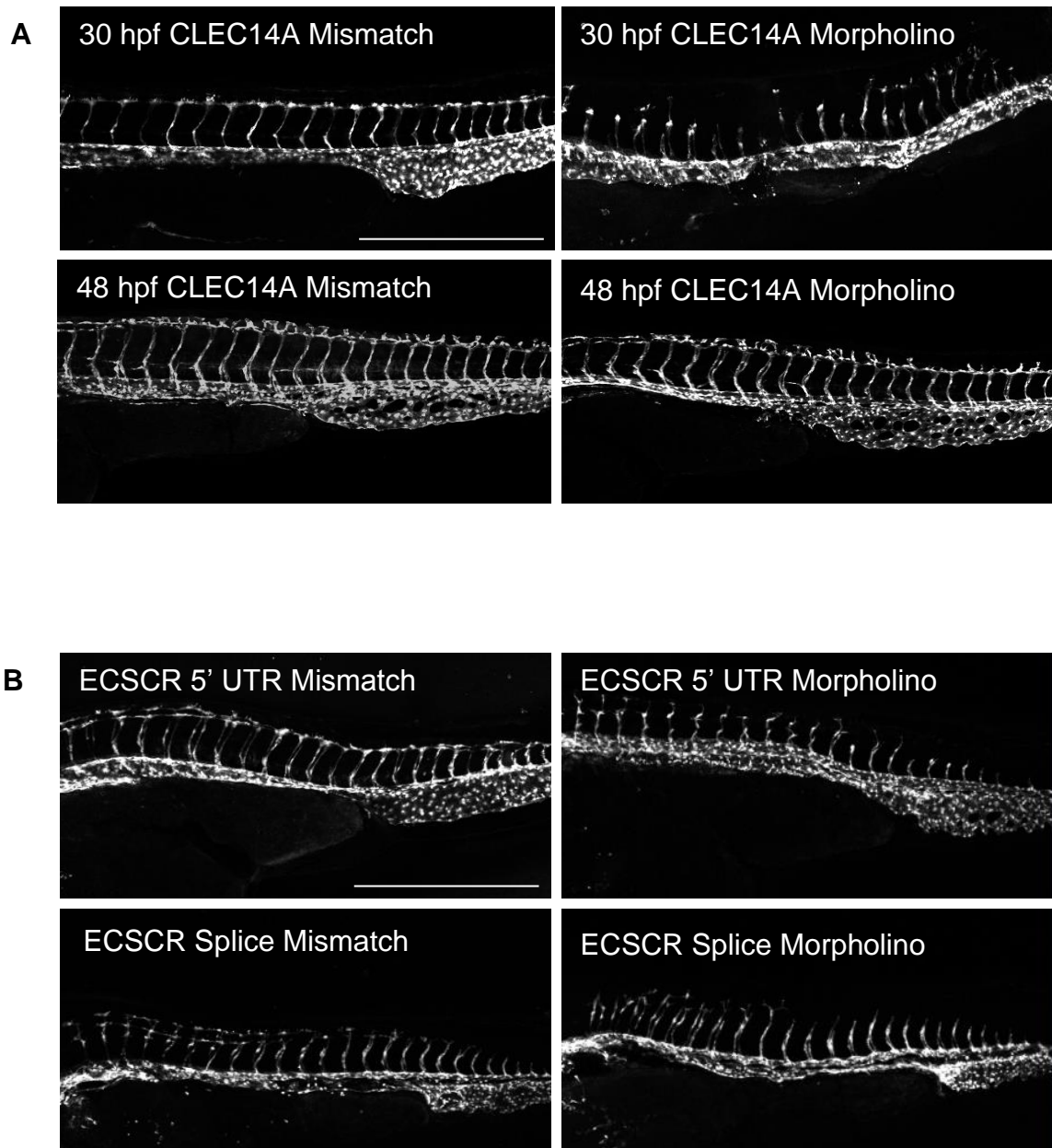


Figure 5.6 Silencing CLEC14A and ECSCR caused defective ISV development at 30 hpf in *fli1*-GFP zebrafish

Oligonucleotide morpholino injection performed at the one-cell stage of development in *fli1*-GFP zebrafish embryos silenced **A**) C-type lectin domain family 14 member a (CLEC14A) and the vasculature was imaged at 30 hpf and 48 hpf, **B**) Endothelial Cell-Specific Chemotaxis Regulator (ECSCR) using the translation-blocking (5' UTR targeting) or splice-blocking morpholino and the vasculature was imaged at 30 hpf, scale: 500 μm.

48 hpf as shown in figure 5.7B. The ISVs had misdirected growth and were truncated; the DLAV remained underdeveloped and disconnected.

VEGFA is a known potent regulator of angiogenesis and the different isoforms generated by alternative splicing regulates blood vessel development. The knock down of VEGFA in zebrafish embryos caused severe vascular defects, as shown in figure 5.7C. Upon silencing VEGFA, defective ISV sprouting from the DA was observed causing absent or severely truncated vessels with only the full length ISVs initiating the formation of the DLAV.

It was also identified in this study that RCAN1.4, which is a variant of regulator of calcineurin 1 (RCAN) and upregulated in response to VEGF signalling¹⁹⁶, was responsible for co-ordinating ISV formation in zebrafish embryos, as well as playing a global and essential role in the overall development of the organism. Silencing RCAN1.4 through morpholino injection caused disrupted vascular growth and the images in figure 5.7D showed that the RCAN1.4 targeted morpholino injected embryos remained curved around the yolk sac for a longer period of time before the straightening of the tail occurred in comparison to the control treated embryos. RCAN1.4 has been shown to be important in regulating endothelial migration and tube formation¹⁹⁷, and this result revealed an additional role for RCAN1.4 in establishing normal vascular morphology during embryonic development of zebrafish.

Members of the ETS-domain family of transcription factors play vital roles during the embryonic development of zebrafish, driving differentiation of angioblasts and enabling efficient vasculogenesis and angiogenesis²⁴⁹. Two of the transcription family

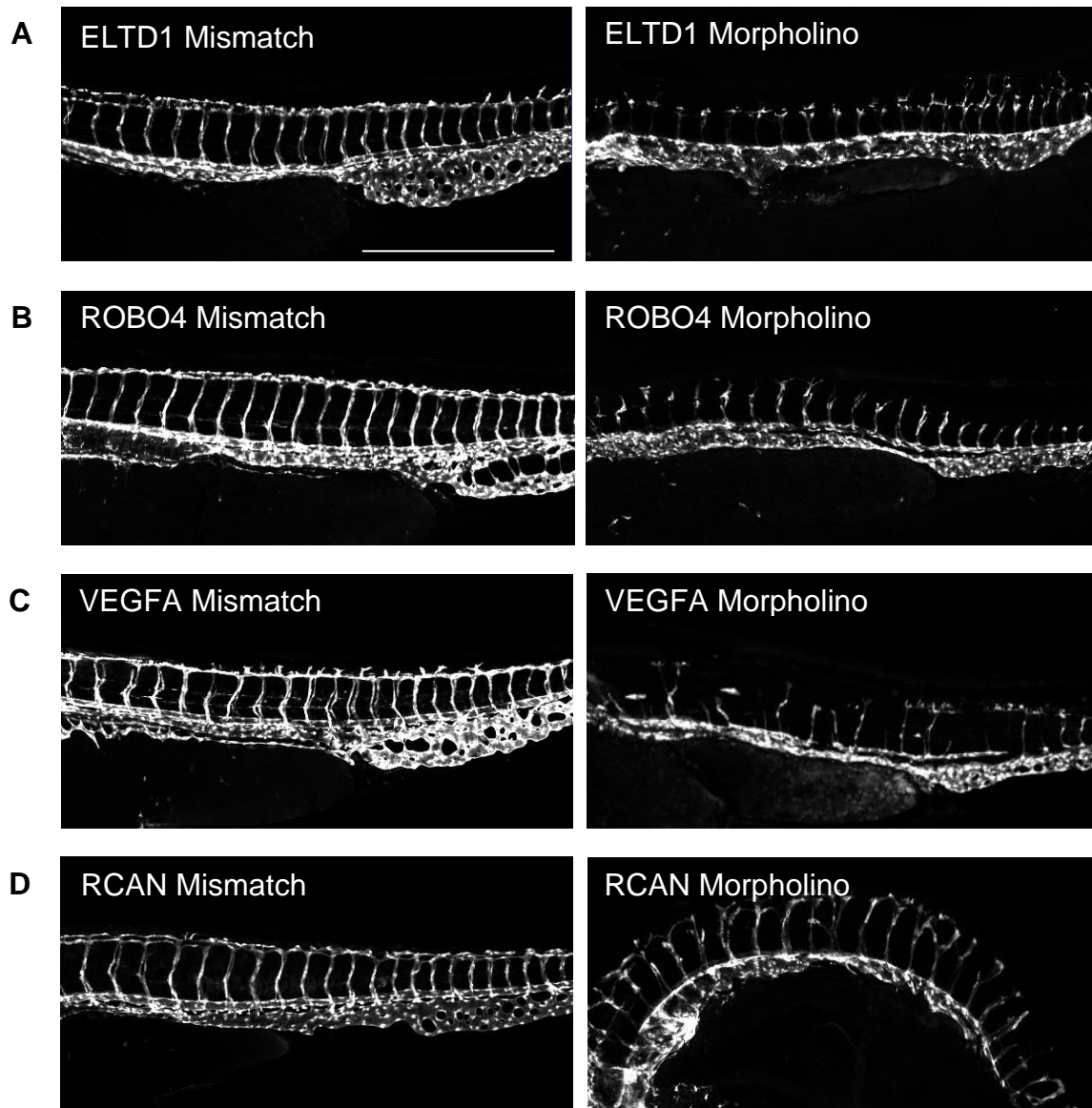


Figure 5.7 Knocking down ELTD1, ROBO4, VEGFA and RCAN disrupted ISV and DLAV growth in *fli1-GFP* zebrafish

Morpholino injection at the one-cell stage of embryonic development in *fli1-GFP* zebrafish was performed to silence **A)** EGF, Latrophilin and Seven Transmembrane Domain containing 1 (ELTD1), **B)** Roundabout 4 (ROBO4), **C)** Vascular Endothelial Growth Factor A (VEGFA), **D)** Regulator of calcineurin (RCAN), vascular imaging was performed at 48 hpf, scale: 500 μ m.

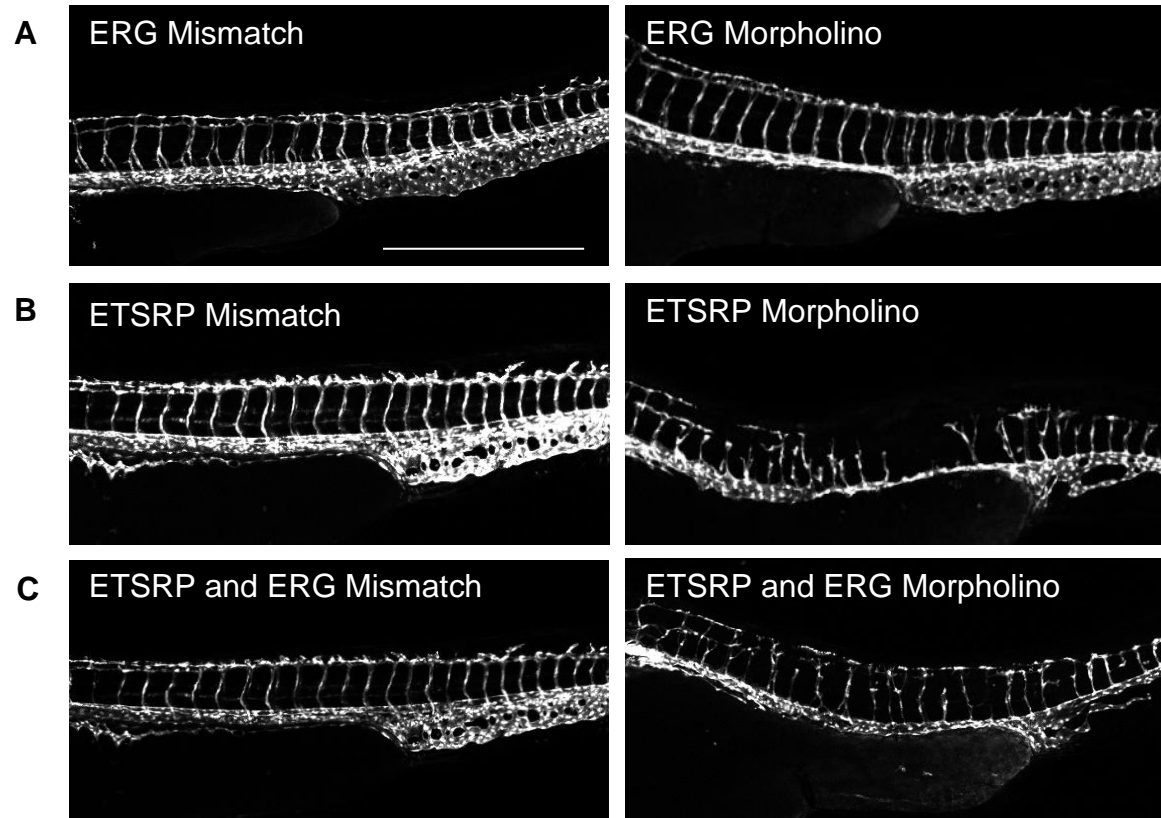


Figure 5.8 Silencing the ETS transcription factor family member ETSRP caused defective and absent ISV growth in *fli1*-GFP zebrafish

Fli1-GFP zebrafish embryos were injected at the one cell stage of development with oligonucleotide morpholino to knock down **A)** ETS Related Gene (ERG), **B)** ETS-1 Related Protein (ETSRP), **C)** ERG and ETSRP, the vasculature was imaged at 48 hpf, scale: 500 μ m.

members ERG and ETSRP were silenced and the embryos were imaged at 48 hpf. Upon ERG knock down, the vasculature developed normally as shown in figure 5.8A, the ISVs grew bilaterally and connected to the DLAV. Upon silencing ETSRP as shown in figure 5.8B there was defective ISV growth with some vessels completely absent and the DLAV failed to fully develop. Ellett *et al.* reported a synergic functional interaction between ERG and ETSRP, and therefore a double knock down to silence both transcription factors in zebrafish should have further reduced ISV growth compared to silencing ETSRP alone¹⁶⁸. However, no further vascular disruption was observed within the embryos upon knocking down both ERG and ETSRP as shown in figure 5.8C.

5.5. Analysing and evaluating the effects of silencing vascular related genes

The vascular related genes of CLEC14, VEGFA, RCAN, ROBO4, ELTD1, ECSCR, ERG and ETSRP were knocked down in zebrafish embryos to cause a range of vascular abnormalities. To test the capabilities of the ImageJ analysis method to analyse a range of vascular morphologies, the vascular images from each gene silenced were analysed using the ImageJ analysis approach. Quantitative data was collected on the vascular parameters of the number of vessel segments, junctions, end points and the average and total vessel lengths and statistical differences between the mismatch and morpholino injected embryo images were determined using the Mann-Whitney statistical test. The data generated from images captured at 30 hpf are represented in bar charts shown in figure 5.9 and at 48 hpf in figures 5.10 and 5.11.

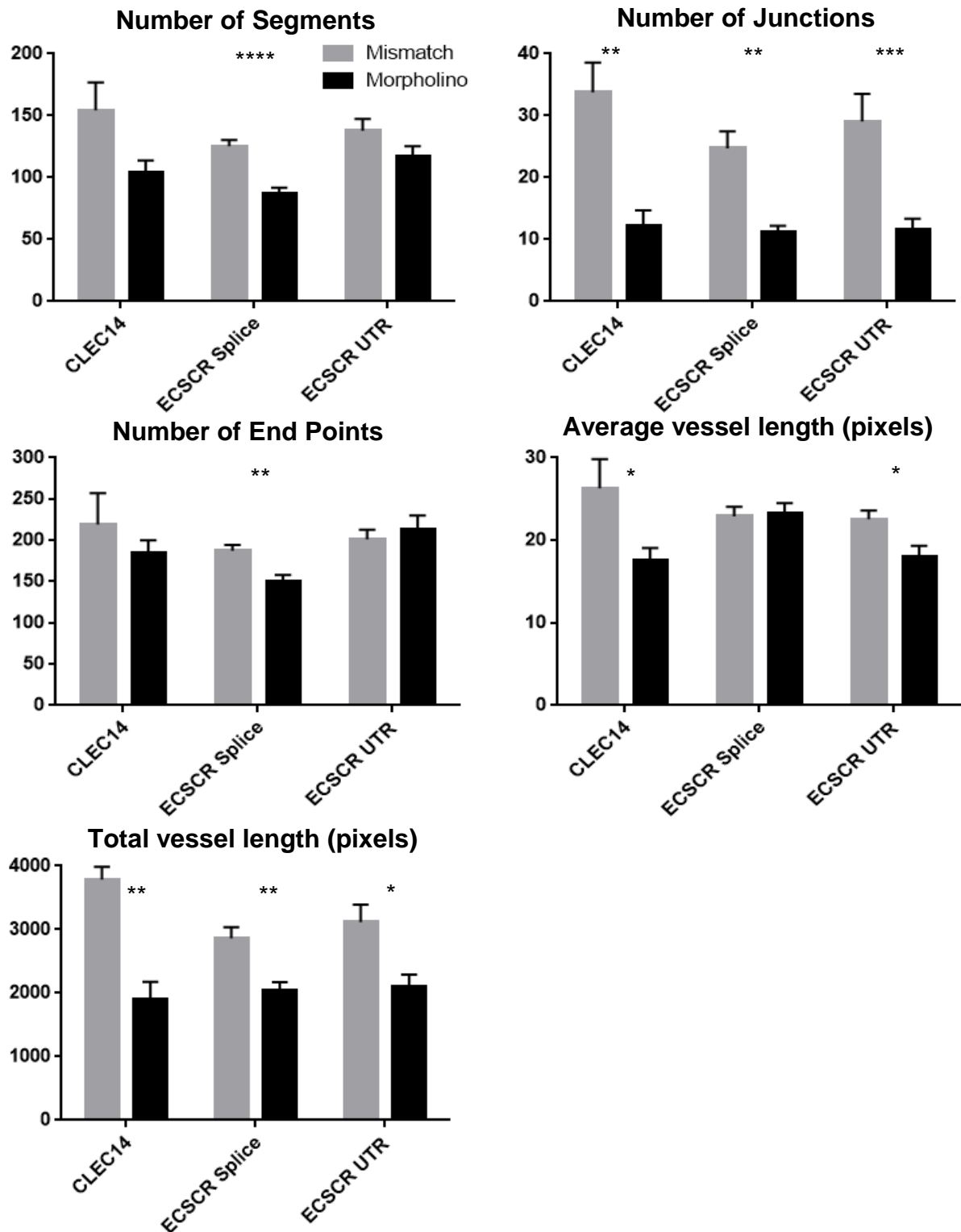


Figure 5.9 Quantitative ImageJ analysis of vascular images studying the knock down of CLEC14A and ECSCR in *fli1*-GFP zebrafish at 30 hpf

The vascular images of the mismatch (grey) and morpholino (black) injected *fli1*-GFP zebrafish targeting CLEC14A and ECSCR were analysed using the ImageJ analysis method and the data represented in bar charts. Significant differences were determined using a Mann-Whitney test, n=5-15, and error bars represent the SEM.

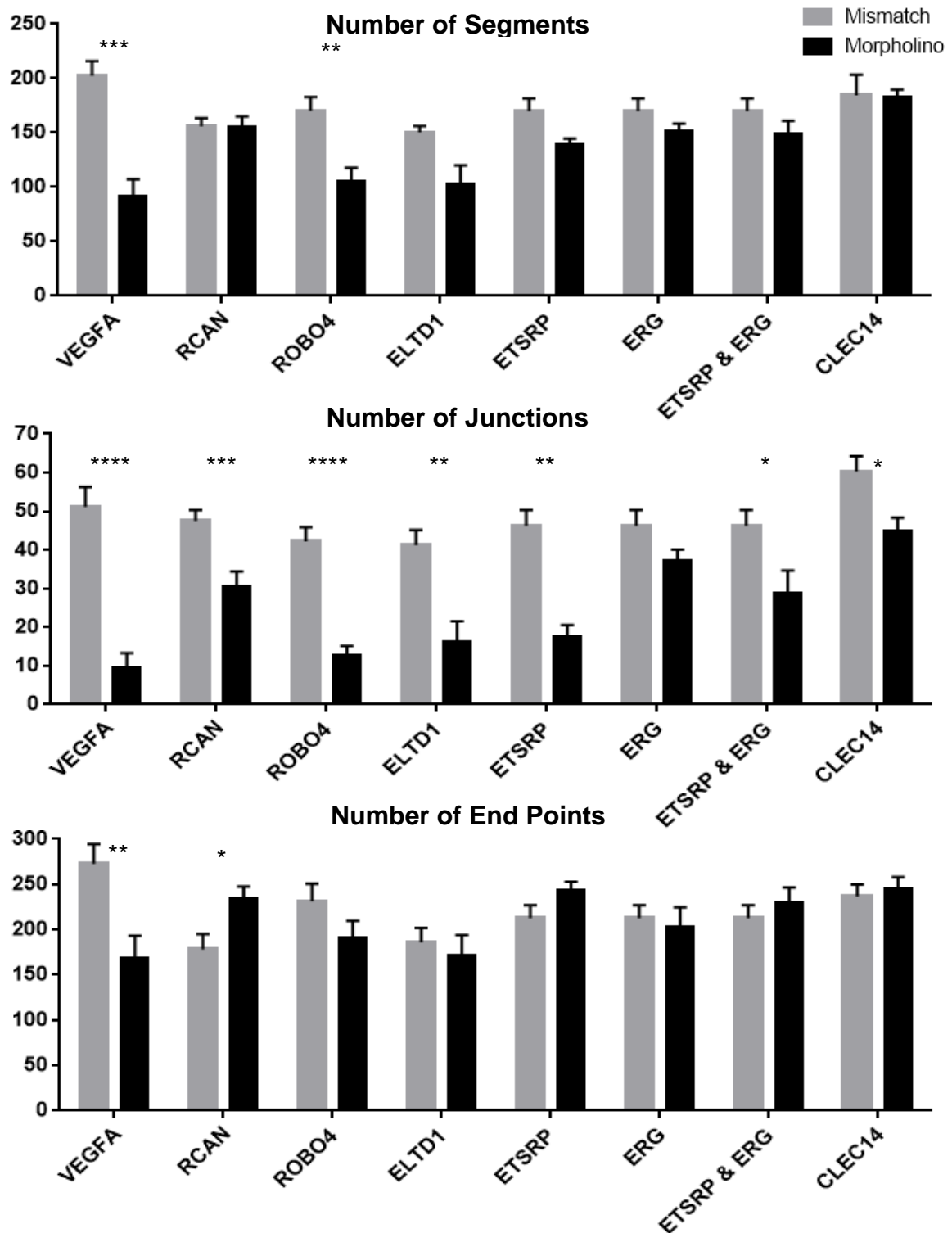


Figure 5.10 Quantitative ImageJ analysis of vascular images studying the effect of silencing vascular related genes on the number of vessel segments, junctions and end points at 48 hpf

The vascular images of the mismatch (grey) and morpholino (black) injected *fli1*-GFP zebrafish targeting VEGFA, RCAN, ROBO4, ELTD1, ETSRP, ERG, ETSRP and ERG and CLEC14A were analysed using the ImageJ analysis method and the data represented in bar charts. Significant differences were determined using a Mann-Whitney test, $n=5-15$, and error bars represent SEM.

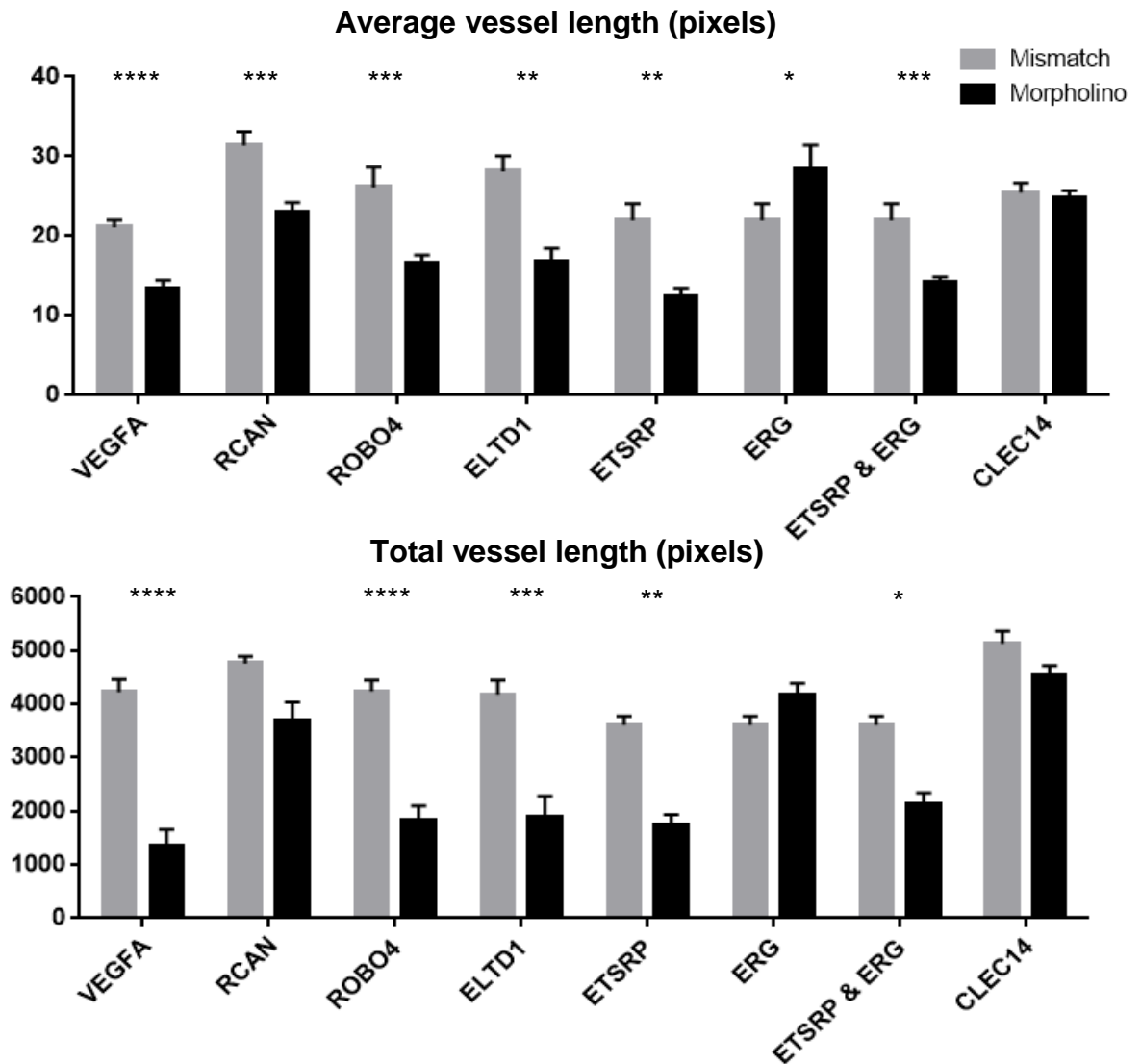


Figure 5.11 Quantitative ImageJ analysis of vascular images studying the effect of silencing vascular related genes on the average and total vessel length at 48 hpf

The vascular images of the mismatch (grey) and morpholino (black) injected *fli1*-GFP zebrafish targeting VEGFA, RCAN, ROBO4, ELTD1, ETSRP, ERG, ETSRP and ERG and CLEC14A were analysed using the ImageJ analysis method and the data represented in bar charts. Significant differences were determined using a Mann-Whitney test, n=5-15, and error bars represent the SEM.

The parameters measured in the vascular images using the ImageJ analysis approach were used to draw conclusions on the connectivity and the complexity of the vasculature formed. The bar charts in figure 5.9 showed that knocking down CLEC14 and ECSCR significantly reduced the connectivity of the vasculature and caused defective ISV growth compared to the mismatch control injected embryos at 30 hpf. The data generated from the ImageJ method revealed that using either the splice or the translation blocking morpholino to silence ECSCR caused abnormal vessel growth to similar effect. Upon studying the knock down of VEGFA, RCAN, ROBO4, ELTD1, ETSRP, ERG, ETSRP and ERG and CLEC14, a range of vascular defects and abnormalities were imaged at 48 hpf. Quantitative analysis of the vasculature revealed that there were significant reductions in the average and total lengths of the vessels when the majority of the vascular related genes were knocked down, apart from when CLEC14 and ERG were silenced, which resulted in similar vessel lengths compared to their corresponding mismatch controls. The parameters that revealed the largest differences between the mismatch and morpholino images at 48 hpf were the number of junctions, average and total vessel lengths. The number of end points between the mismatch and morpholino images remained relatively constant at 48 hpf, possibly due to the morphological post-processing steps that lead to the fragmentation of the vessels and inclusion of noise or artefact pixels, however a significant reduction in the number of end points was measured when VEGFA was silenced as shown in figure 5.10. This result suggested that measuring the numbers of end points within vascular images using this method may only be informative when there is severe vascular disruption leading to the considerable absence of ISV formation.

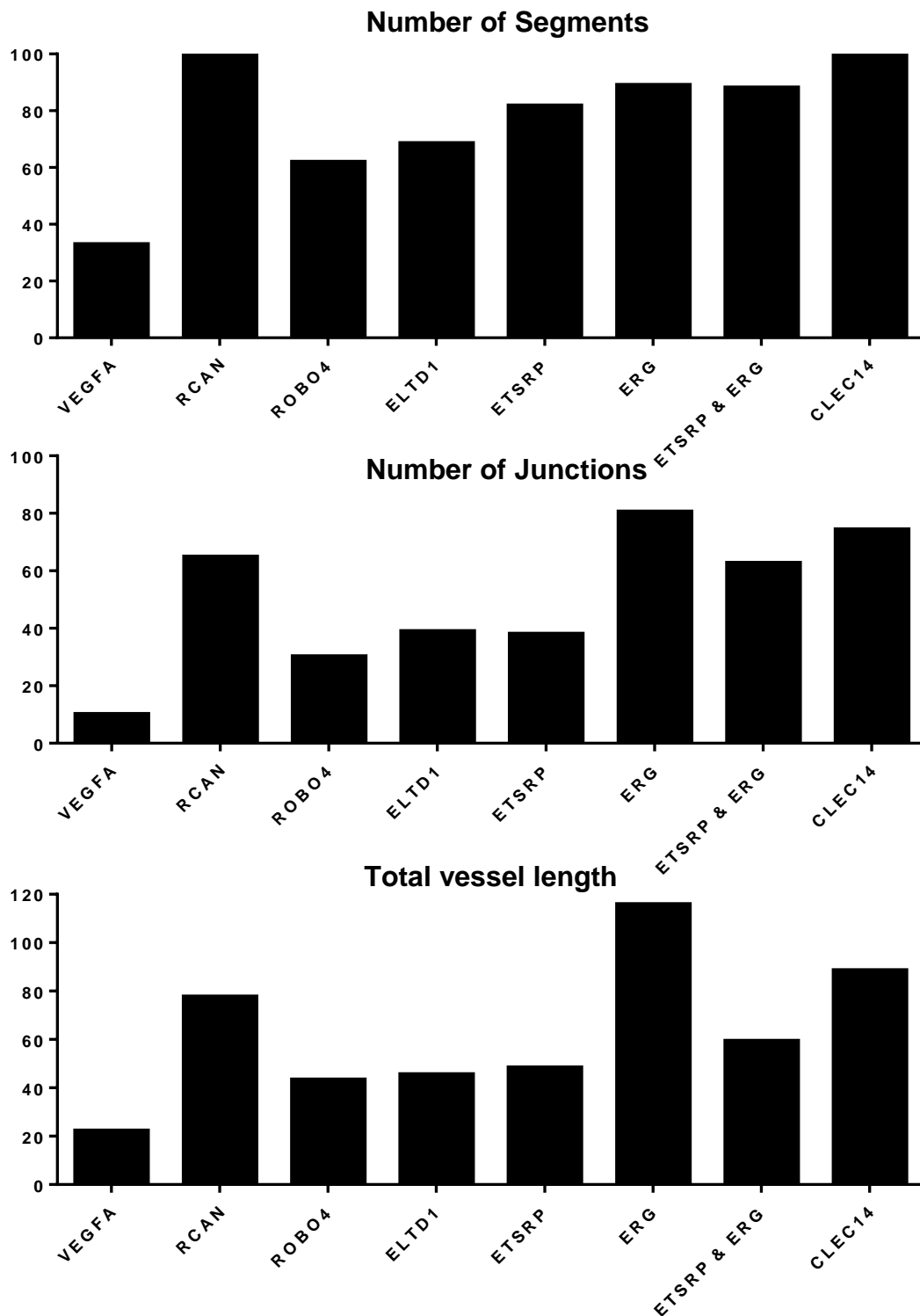


Figure 5.12 Bar charts showing the severity of vascular disruption caused by silencing vascular related genes

The parameters of the number of vessel segments, junctions and total vessel length were quantified by the ImageJ zebrafish vasculature analysis method. *Fli1-GFP* zebrafish embryos were injected with morpholino oligonucleotides to silence each vascular related gene and the developed vasculature was imaged at 48 hpf. The data generated for each gene was normalised to their corresponding control data sets to allow the severity of vascular disruption to be compared between the different silenced genes. Each bar is represented as a percentage of the control.

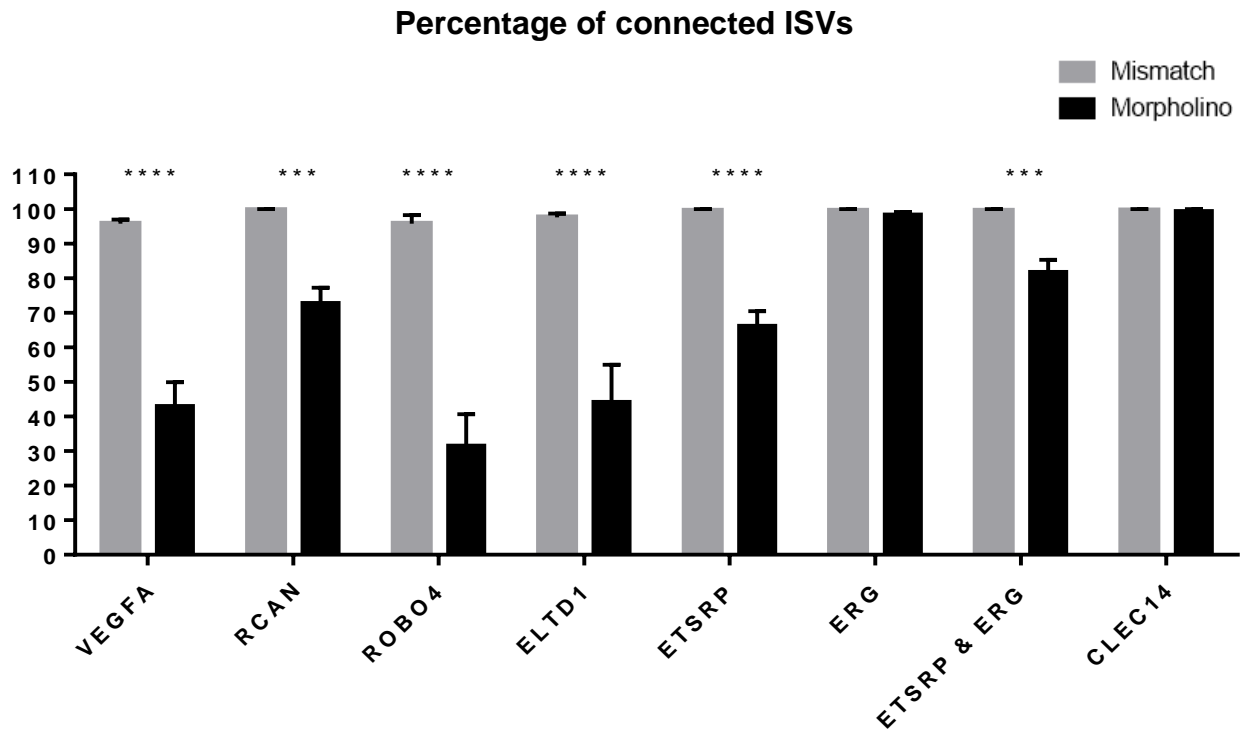


Figure 5.13 Similar patterns of results were obtained using the ImageJ and manual analysis methods

Fli1-GFP zebrafish embryos were injected with morpholino oligonucleotides to silence each vascular related gene and the developed vasculature was imaged at 48 hpf. The percentage of ISVs that connected to the DLAV in the vascular images of both the mismatch (grey) and morpholino (black) injected zebrafish were manually analysed and statistical differences were determined using a Mann-Whitney test, n=5-15, error bars represent the SEM.

The quantitative analysis of the vascular images also enabled a comparative study between the severities of vascular disruption caused by silencing the different genes; by normalising the data for each gene that was silenced and imaged at 48 hpf to their corresponding mismatch control data, the severity of the vascular disruption could be easily compared as shown in figure 5.12. The parameters that have been shown in figure 5.12 include the number of vessel segments and junctions as well as the total vessel lengths since these parameters were able to give a detailed understanding of the developed vascular morphology in the organisms, specifically identifying how many vessels developed, their connectivity and the extent of global vascular formation in the organism. The normalised graphs in figure 5.12 revealed that knocking down VEGFA caused the most severe disruption, followed by ROBO4 and ELTD1. Knocking down ERG and CLEC14 at 48 hpf caused the vessels to develop with a similar morphology to their corresponding mismatch control embryos.

To compare the results of the ImageJ analysis method against the frequently used analysis approach of manually counting the number of ISVs which connected to the DLAV, the vascular images were manually assessed for connectivity and the percentage of fully connected ISVs has been shown in figure 5.13. Comparing the severity of the vascular disruption between the different silenced genes using the manual analysis method revealed a similar pattern of results to the ImageJ analysis method, as shown by the bar charts in figures 5.12 and 5.13. The pattern of vascular disruption was studied as the total number of junctions measured by the ImageJ method was different to the number of connections counted manually. The ImageJ method measured an increased number of junctions in comparison to the manual method, as ISV outgrowths which formed in the mid region of the vessels during

vessel growth were automatically detected using ImageJ. The manual analysis method measured only the number of ISVs which formed connections with the DLAV.

The manual analysis method revealed that knocking down VEGFA, RCAN, ROBO4, ELTD1, ETSRP, ETSRP & ERG and imaging at 48 hpf caused significant reductions in the number of ISVs which grew from the DA and connected to the DLAV. A comparable result was obtained in figure 5.10 which identified that significant reductions in the numbers of junctions were measured in the vascular images using the ImageJ analysis method, with the addition of CLEC14 which was also identified by this method as causing a reduction in junction formation.

Both methods of analysis revealed that the three genes that caused severe vascular disruption when silenced were VEGFA, ROBO4 and ELTD1, with the ImageJ method identifying that silencing VEGFA caused the most severe disruption, whereas the manual method identified ROBO4. This difference was due to the different vascular phenotypes formed by knocking down these genes, silencing VEGFA lead to complete absence of ISV growth in some areas along the DA, however where the ISVs formed, they often connected to the DLAV. Whereas, in ROBO4 silenced embryos the ISVs developed through endothelial sprouting but failed to connect or form the DLAV, leading to reduced connectivity using the manual analysis method.

The ImageJ and manual analysis methods also identified that the two genes that had comparable vascular phenotypes to their corresponding control treated embryos were ERG and CLEC14 upon imaging at 48 hpf.

5.6. Analysing the effects of inhibitor treatment on vascular development

The ImageJ analysis method proved to be a useful tool for assessing the severity of vascular disruption in zebrafish when genes were silenced through MO injection; therefore the computerised approach was used to determine the effect of inhibitor concentrations on vascular development.

Inhibitor compounds are commonly added to media surrounding zebrafish embryos during development to determine the effect of the compound on vasculature formation. Sunitinib is a multi-targeted receptor tyrosine kinase inhibitor which acts on many kinases including VEGFR1-3 and PDGFR α and β thereby inhibiting angiogenesis^{58,250,251}. To study the effect of sunitinib on zebrafish vasculature development, 0.1 μ M and 1.0 μ M sunitinib treatment was given to developing zebrafish embryos at the one-cell stage. The images in figure 5.14A showed that 0.1 μ M sunitinib treatment caused no apparent vascular abnormalities compared with DMSO control treated embryos. However, severe vascular defects were observed upon 1.0 μ M sunitinib treatment, the ISVs either failed to form or remained disconnected from the DLAV.

The ImageJ analysis method was subsequently used to quantify vasculature development of sunitinib treated zebrafish embryos and revealed that the numbers of vessel segments, junctions, end points, average and total vessel lengths were all significantly reduced upon treatment with 1.0 μ M sunitinib. The total vessel length formed by embryos treated with 0.1 μ M sunitinib was also significantly reduced;

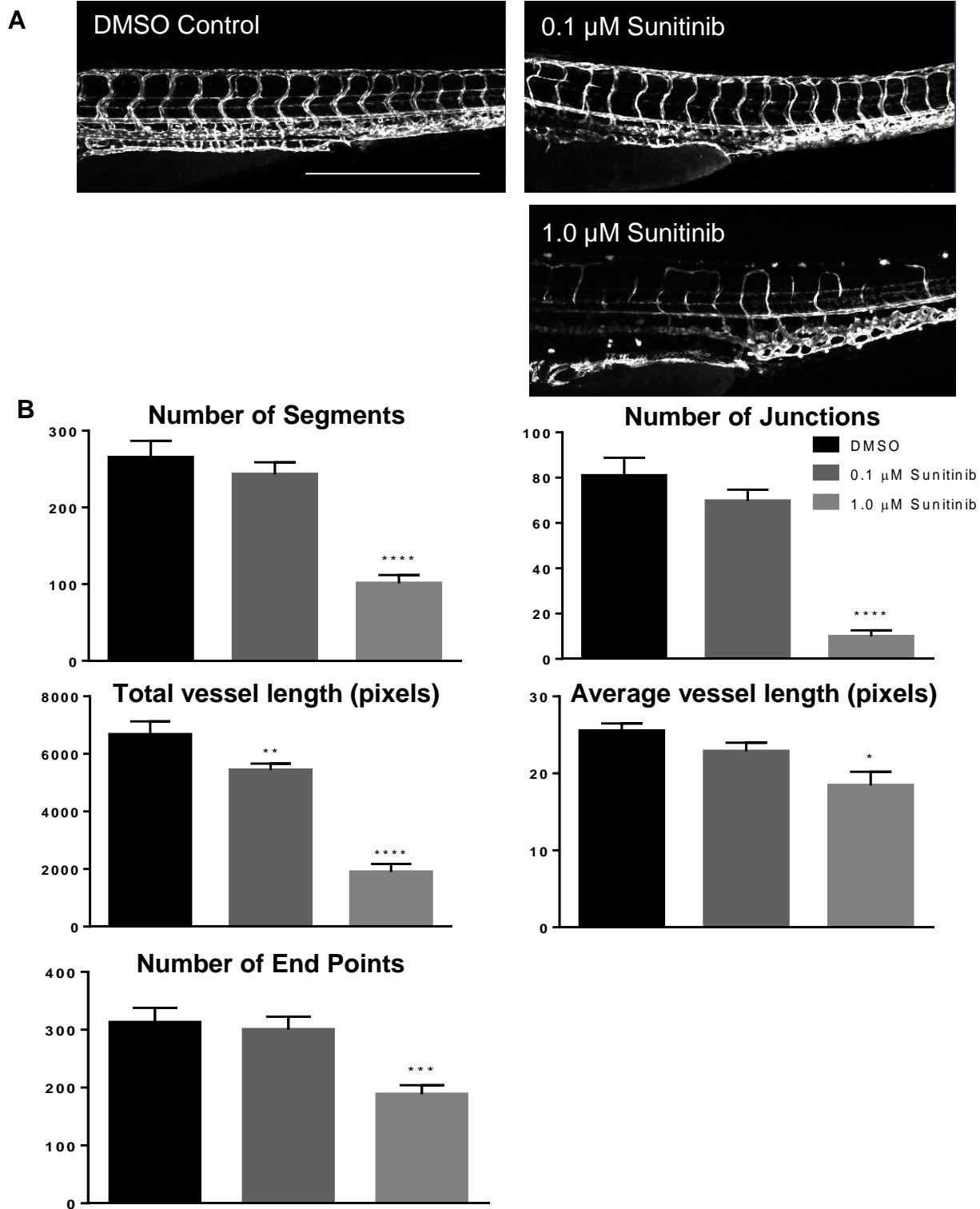


Figure 5.14 Sunitinib treatment disrupted ISV growth and DLAV connectivity

Fli1-GFP zebrafish were treated with 0.1 μ M, 1.0 μ M sunitinib treatment or DMSO in E3 media and imaged at 48 hpf. **A)** Vascular images of the DMSO or sunitinib treated embryos, scale: 500 μ m, **B)** ImageJ analysis of the vascular images, statistical differences were determined using a Mann-Whitney test, n=10. The error bars represent the SEM.

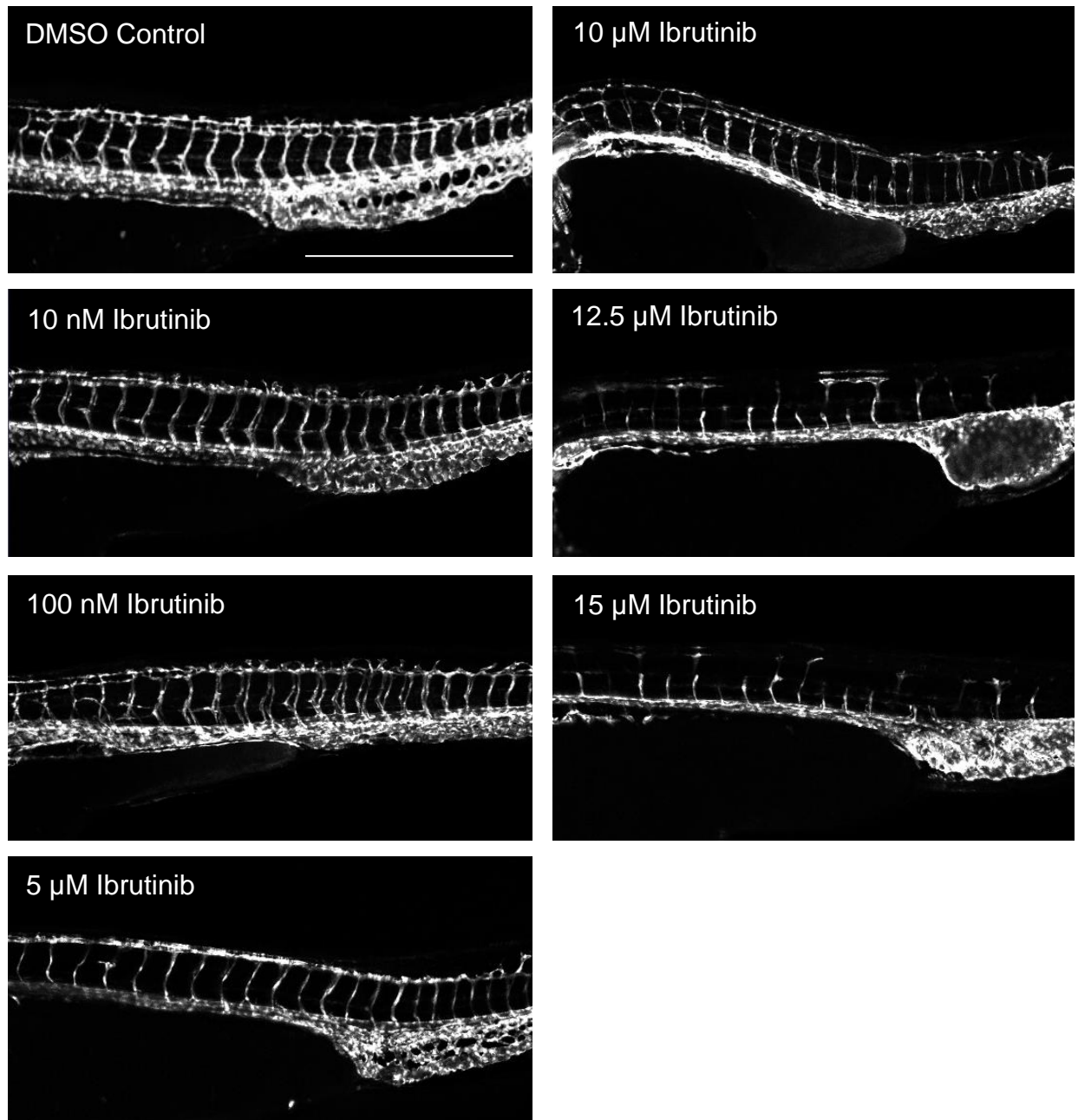


Figure 5.15 Ibrutinib treatment inhibited ISV formation in *fli1*-GFP zebrafish

Fli1-GFP embryos at the one cell stage of development were treated with 10 nM, 100 nM, 5 μ M, 10 μ M, 12.5 μ M or 15 μ M ibrutinib or 15 μ M DMSO in E3 media, the developing vasculature was imaged at 48 hpf, scale: 500 μ m.

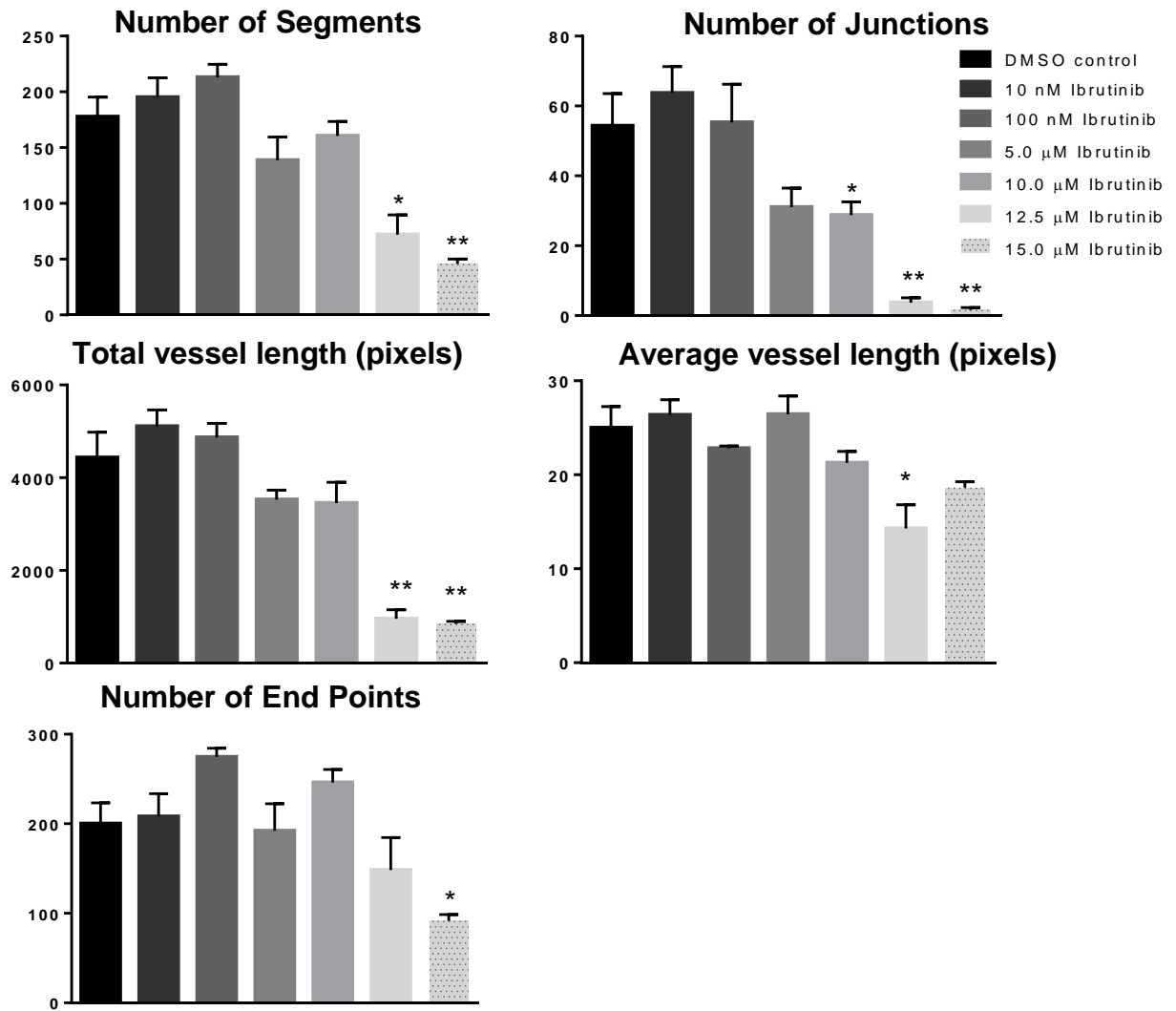


Figure 5.16 Ibrutinib treatment significantly reduced vessel growth and connectivity in *fli1*-GFP zebrafish embryos

Vascular images of embryos treated with 10 nM, 100 nM, 5 μM, 10 μM, 12.5 μM or 15 μM ibrutinib or 15 μM DMSO in E3 media were analysed using the analysis method and statistical differences were found using a Student's t test, n=3-4. Error bars represent the SEM.

however the numbers of vessel segments, junctions, end points and average vessel length remained comparable to the control treated embryos.

Another inhibitor that was used was ibrutinib which inhibits both BTK and BMX, to determine the ibrutinib concentration that affects vascular development in zebrafish, embryos were treated with a range of ibrutinib concentrations from 10 nM to 15 μ M and the vasculature was imaged at 48 hpf as shown in figure 5.15. Vascular abnormalities were observed in zebrafish embryos treated with concentrations above 5 μ M ibrutinib, these concentrations caused stunted and absent ISV sprouting as shown in figure 5.15. The DLAV failed to develop in embryos treated with 12.5 μ M and 15 μ M ibrutinib, the quantitative analysis of the vascular images using the ImageJ analysis method confirmed that embryos treated with 12.5 μ M and 15 μ M ibrutinib caused significant vascular defects shown in figure 5.16. A significant reduction in the number of vessel segments, junctions and total vessel length was calculated at these concentrations of ibrutinib treatment. The ImageJ analysis method enabled a comparative study between the different inhibitor treatments and provided quantitative analysis on the effects of using different concentrations of inhibitor compounds on vascular development.

5.7. Evaluating the computer based analysis method

The vascular images from the developmental time-course, gene knock down and inhibitor studies were analysed using the ImageJ analysis method, the average values for each developmental time point, gene silenced and each inhibitor concentration were determined. Using the combined data sets, the Pearson product moment correlation coefficient (R) and p values from a Student's t-test were calculated to study correlations between the parameters measured from the vascular

Table 5.1. Significant correlations were identified between the different parameters measured using the ImageJ analysis method.

The Pearson product moment correlation coefficient (R) values and p values from a Student's t-test were calculated to determine correlations between the parameters of the number of segments, number of junctions, number of end points, total and average vessel lengths measured using the ImageJ analysis method. The correlation values were calculated using the combined mean data sets from the time course developmental data, the inhibitor data and the gene knock down data.

<div>R values</div> <div>P values</div>	Number of Segments	Number of Junctions	Number of End Points	Total Vessel Length (pixels)	Average Vessel Length (pixels)
Number of Segments		0.899	0.726	0.879	0.533
Number of Junctions	4.475×10^{-10}		0.552	0.970	0.716
Number of End Points	2.739×10^{-5}	0.003		0.570	0.089
Total Vessel Length (pixels)	3.436×10^{-6}	3.268×10^{-16}	0.002		0.807
Average Vessel Length (pixels)	0.005	3.891×10^{-5}	0.664	6.178×10^{-7}	

images which included the number of vessel segments, junctions, end points, average and total vessel lengths.

The R and p values are shown in table 5.1; the highest correlation was calculated between the total vessel length and the number of junctions, as indicated by the smallest p value of 3.268×10^{-16} and an R value close to 1.0 of 0.970. Strong correlations were also calculated between the number of segments and the number of junctions with a p value of 4.475×10^{-10} and an R value of 0.899, as well as between the total vessel length and the number of segments with a p value of 3.436×10^{-6} and R value of 0.879. These strong correlations suggested accordingly that as the zebrafish vasculature developed, the length and the number of junctions formed by the vessels increased which reflected the complexity and connectivity of the vessels. The smallest correlations were calculated between the number of end points measured in the images and the other parameters, the highest p value of 0.664 and the lowest R value of 0.089 was calculated between the number of end points and the average vessel length. Considering the previous results in section 5.5 which outlined that the number of end points measured in the vascular images were comparatively similar between the mismatch and morpholino images for different genes that were silenced; this correlation result was unsurprising and suggested that measuring the number of end points within vascular images did not provide useful morphological information on the developed vascular network.

Correlation graphs were plotted using the data generated by the ImageJ analysis method for the developmental time course, gene knock down and inhibitor images to give a visual representation of the correlation between the different vascular parameters measured within the images, as shown in figures 5.17 and 5.18. Each

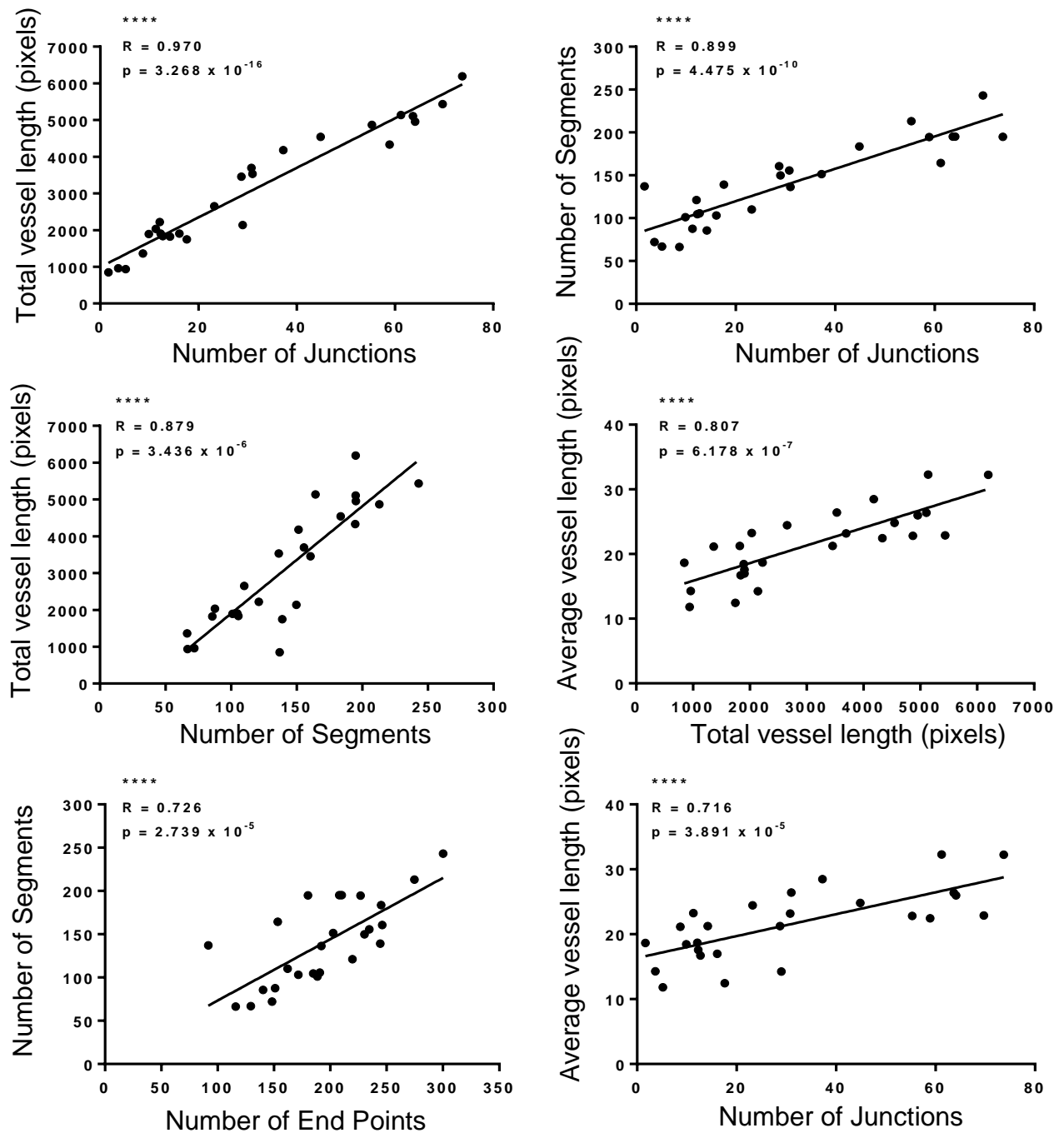


Figure 5.17 The strongest correlation was identified between the parameters of total vessel length and the number of junctions

Correlation graphs were plotted using the combined mean data sets from the ImageJ based analysis using the time course developmental data, the morpholino and inhibitor data and the inhibitor data. The Pearson Product Moment Correlation Coefficient (R) values and p values from a two tailed t-test were calculated and statistical differences have been shown **** indicates $p \leq 0.0001$.

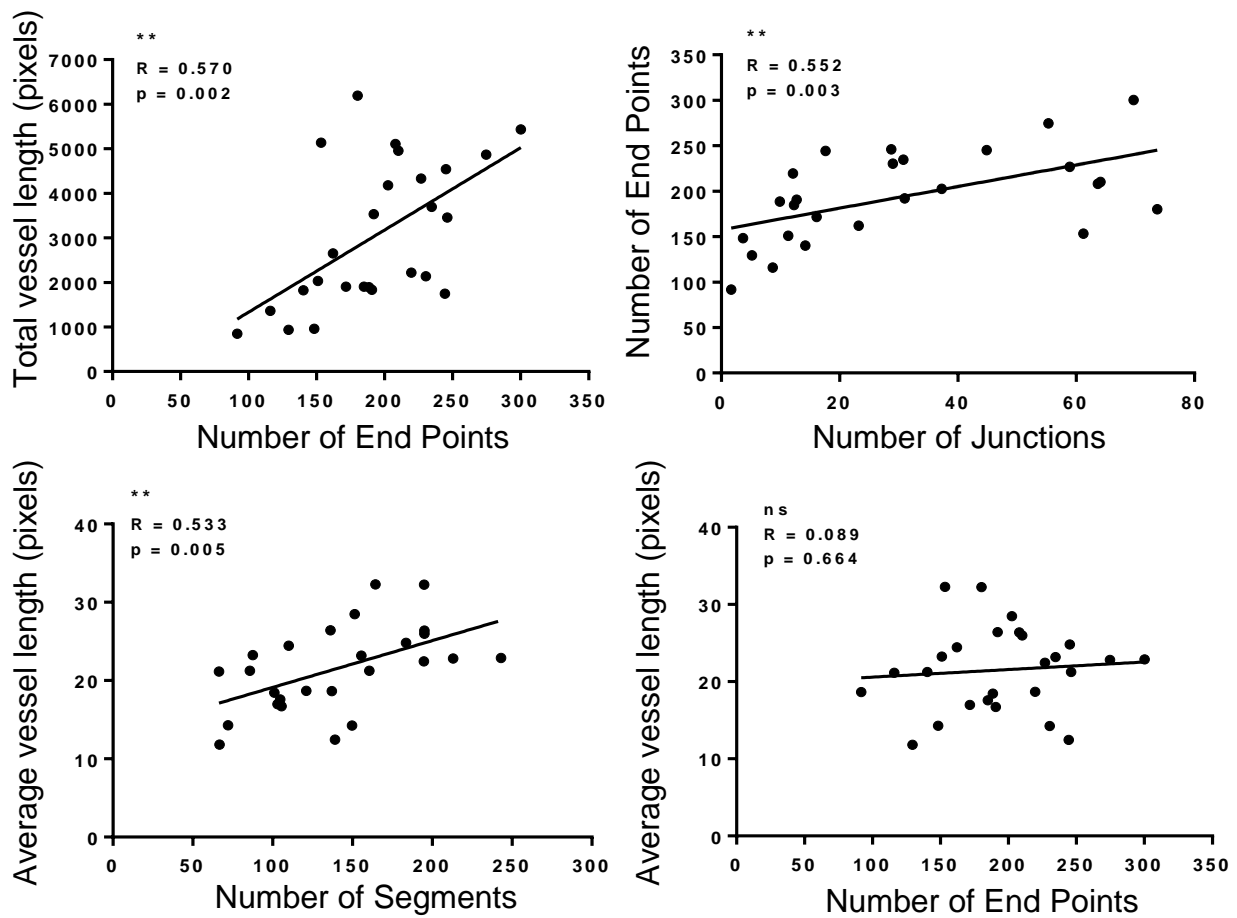


Figure 5.18 Measuring the number of end points revealed a high degree of variation in the vascular images

Correlation graphs were plotted using the combined mean data sets from the ImageJ based analysis using the time course developmental data, the morpholino and inhibitor data and the inhibitor data. The Pearson product moment correlation coefficient (R) values and p values from a two tailed t -test were calculated and statistical differences have been shown $**$ indicates $p \leq 0.01$, $*$ $p \leq 0.05$, ns $p > 0.05$.

parameter was studied individually against the other parameters and the line of best fit was plotted to give an indication of the degree of correlation between the two parameters.

The plots in figure 5.17 showed extremely significant correlations between the parameters with p values less than 0.0001. The graphs confirmed that as the vasculature developed in complexity and connectivity, an increased number of vessels and junctions were detected along with measuring longer vessel lengths confirming that the analysis results reflected accordingly with the development of the organism. The strong correlation results identified that these parameters of the total vessel length, the number of vascular junctions and the number of vessel segments would be informative when assessing zebrafish vascular morphology. The average vessel length could also be considered for use in morphological studies however due to this parameter being calculated through the dependence of the total vessel length and the number of segments, the trend for this parameter would be observed through the existing results.

The plots in figure 5.18 showed there were large variations in the number of end points measured in the vascular images. No statistical significance was found between the number of end points and the average vessel lengths. These results suggested that measuring the number of end points should not be used to draw conclusions on the vessel morphology as measuring this parameter did not give a valid indication of the complexity of the developed vasculature.

5.8. Chapter discussion

The aim of this chapter was to develop and evaluate an alternative computer based method that could be applied to fluorescent zebrafish images to generate quantification and analysis of vascular development. This aim was achieved by generating two analysis methods using ImageJ and IMARIS software which targeted the ISVs for quantitative analysis of their numbers, lengths and connectivity to the DLAV. The ISVs were specifically targeted since they are the first angiogenic vessels to form in the zebrafish¹⁴⁵. Both analysis methods can be used and applied to fluorescent vascular images to provide useful information on vessel morphology of both normal and abnormal vessel development in response to silencing vascular related genes or assessing the effect of angiogenic agents.

The computer based analysis methods were able to quantify the developing zebrafish vasculature by measuring the parameters of the total and average vessel lengths, the number of vessel segments, vascular junctions and end points formed within fluorescent zebrafish images. The two methods of analysis used different morphological post-processing steps and therefore each method offered unique advantages when compared.

The IMARIS analysis method required the production of a three dimensional vascular mask which allowed the vessels to be viewed at 360°, therefore this approach gave an excellent visual understanding of vessel connectivity. The creation of this mask by manually defining a threshold value must accurately represent the imaged vasculature as the original image file has to be discarded for analysis; however the mask production had the advantage of being able to exclude noise pixels or image artefacts. An additional limitation of this analysis method was the requirement to

detach each ISV which sprouted from the DA from the mask using the cutting tool, which only worked in a single orientation, therefore it was necessary to rotate and manipulate the position of the vascular mask in the viewer window to remove unwanted vessels from the analysis procedure. The process of cutting the individual vessels was time consuming, leading to an analysis time of approximately 5 minutes per image, dependent on the number of ISVs within the image and the user's experience of the software. The IMARIS software must be purchased from bitplane which can be expensive therefore this approach for analysing zebrafish vascular images may not be widely available to the scientific community. However, the IMARIS software has been specifically created for three dimensional rendering of two dimensional optical image sections and provides an interactive user space which enables the user to create, visualise, edit and analyse data sets within a single window within the software. The Filament Tracer module in IMARIS has been optimised to automate tracking and classification of filamentous structures such as spines and dendrites of neurons, consequently it is able to detect and analyse small vessels such as the ISVs accurately. However, the package is not specifically designed for this application; therefore the inclusion of the number of junctions formed in the DLAV after 36 hpf in the developmental time-course study caused the quantification for this parameter to increase steadily as the organism developed. The IMARIS software did not include a function which would allow for the automatic exclusion of the junctions in the DLAV such as the fill holes function used in the ImageJ analysis method. For this reason, the IMARIS analysis method would be more suitable for global vasculature analysis rather than specifically targeting the ISVs for analysis. Due to the considerable time restraints using this analysis method,

this method would be best suited for use in studies with small numbers of images, where vascular defects could be studied in detail using the 360° viewer.

In contrast, the ImageJ analysis method was not reliant on the generation of a mask thus the parameters were measured directly from the original image file. However, this revealed that the method was prone to the inclusion of noise or artefact pixels within the image and extra fragmentation of the vascular skeleton which enhanced the numbers of end points detected. The creation of the ImageJ zebrafish vasculature macro offered the significant advantage of rapid quantification of the vasculature as the image outputs were generated within 35 seconds, which was 8.6 times faster than the IMARIS analysis method. Furthermore, the fill holes function which was utilised in this method enabled the analysis method to target the ISVs specifically by removing the additional connections formed in the DLAV after 36 hpf. The ImageJ software is available free of charge and in the public domain; therefore using the macro for analysis would be easy to use and widely available. Since this analysis method was able to analyse both major and minor vascular defects in a time dependent manner, it would be suitable for analysing larger sets of zebrafish vascular images.

Both of the computer based analysis methods were able to quantify vascular images and therefore either method can be used to assess normal and abnormal vascular development. The ImageJ method was chosen in this study to analyse the vascular images from the studies of silencing genes and using inhibitor compounds since it provided rapid analysis and was therefore less time consuming. In this chapter, the studies revealed that the ImageJ analysis method can be used to quantify a range of vascular phenotypes within zebrafish embryos, therefore this analysis method could

be used as a useful tool to assess vascular development in response to knocking down genes as well as determining the effect of inhibitor compounds on vascular formation.

Significant correlations were observed between some of the parameters measured by the ImageJ analysis method; as the vascular network expanded and became more elaborate, increased numbers of vessel segments, lengths and vascular junctions were detected in the images, this result reflected accordingly with the development of the zebrafish. Measuring the parameters of the total vessel length, the number of vascular junctions and the number of vessel segments within a zebrafish image would provide an excellent overview of the vascular morphology which had developed within the organism. Measuring the total vessel length would give a global understanding of the extent of vessel formation, whereas measuring the number of junctions would be informative on the vessel connectivity. Measuring the number of vessel segments formed within the organism would suggest if endothelial sprouting had been affected. Measuring the total vessel length and the number of vessel segments would also enable a further calculation of the average vessel length, if required. Measuring the numbers of end points showed limited correlations to the other parameters and did not provide useful information on vascular morphology in this study, measuring this parameter would only be beneficial if there was severe absence of ISVs or extensive hyper-sprouting of the vasculature.

Confocal image sections can be compressed to improve image resolution and the application of post-processing image operations such as image registration, binarisation and image segmentation can be applied to fluorescent zebrafish images to aid vascular analysis; however at present there is no gold standard computer

based method that is widely used for the quantification of the zebrafish vasculature. Many of the analysis frameworks which have been reported often give excellent visual representations of the analysis but use software which is not widely available or in practice hard to implement or modify such as Visual C++ Language¹⁸³. Other methods used to analyse vascular growth include analysing ISV sprouting from the DA using primarily the process of image registration to measure increases in vessel lengths at different time points, however this method does not generate data on vessel junctions and therefore no knowledge of vessel connectivity is obtained^{181,182}.

Additional analysis methods targeting the ISVs have used microscopy software such as the Nikon Imaging Software (NIS) Elements to measure the lengths of ISVs which is neither automated nor applicable for large numbers of images¹⁷⁸. Due to the difficulties associated with implementing computer based analysis methods, many researchers continue to manually analyse the vascular disruption using scoring systems and classifying the vascular phenotypes into categories such as 'mild', 'intermediate' or 'severe' ISV disruption¹⁶⁴⁻¹⁶⁷. An alternative and frequently used approach to analyse the ISVs is to manually count the number of ISVs which connect or remain disconnected from the DLAV, this is also often represented as a percentage of the total number of ISVs^{168-170,172-177}. Both of these manual approaches to analysis are able to give a global understanding of how the vascular network has developed in the organism. The method of evaluating if the ISVs have connected to the DLAV, gives a greater understanding of ISV connectivity compared to the classification system of analysis, however the extent of ISV growth is not assessed, therefore the resulting analysis data does not provide information on whether the ISVs failed to sprout or whether they developed but were unable to form vessel

connections. The ImageJ analysis method generated in this chapter was able to provide rapid results and an understanding of the vascular morphology similar to the manual analysis methods that are currently used to assess vascular development. The ImageJ analysis method assessed vessel connectivity by calculating the number of vascular junctions within the images and additionally was able to generate informative data on vessel lengths and the number of vessels formed.

As shown in this chapter, similar results were obtained using the ImageJ analysis method compared to the results obtained using the manual method of calculating the percentage of connected ISVs in the zebrafish gene knock down study. Both methods revealed that the three genes that caused severe vascular disruption when silenced were VEGFA, ROBO4 and ELTD1 and the two genes that had comparable vascular phenotypes to their corresponding control treated embryos were ERG and CLEC14 upon imaging at 48 hpf. The manual analysis method identified that silencing ROBO4 caused fewer numbers of ISVs to connect to the DLAV in comparison to VEGFA which was identified as having the most vascular disruption using the ImageJ analysis method. Silencing VEGFA caused severe absence of ISV growth from the DA, however the ISVs that did form often connected to the DLAV. Whereas in ROBO4 knocked down embryos, widespread endothelial sprouting occurred during the formation of the ISVs however the DLAV failed to form. The ImageJ analysis method revealed that the ROBO4 silenced embryos formed twice as many vessels as VEGFA silenced embryos and also exhibited longer average and total vessel lengths. Studying a number of different parameters is useful for determining the vascular morphology which has developed in the organism.

To achieve accurate data analysis it was important to initially acquire and load a highly fluorescent vascular image particularly from the vessels of interest into the computer software. At present, both analysis methods worked most effectively when the generated analysis data was exported from ImageJ or IMARIS into Microsoft Excel, where the final calculations to obtain totalled or averaged values could be obtained. Future work, particularly on the ImageJ analysis method would be to create an extra step in the analysis process to include automation of the final calculations, eliminating the need to export the data.

In summary, two objective computerised methods using ImageJ and IMARIS software were developed which were able to quantify vascular development in zebrafish. Both computer based approaches enabled accurate analysis of the number of vessel segments, junctions, total and average vessel lengths which were unbiased and offered the potential to be used as useful analysis tools for determining the function of genes and the action of novel compounds on the angiogenic pathway.

Chapter Six

General Discussion

6.1. Overall project findings

The aim of this PhD project was to monitor, manipulate and analyse in detail the process of angiogenesis through the development of high resolution fluorescence imaging techniques and the generation of useful analysis tools to allow angiogenic images to be rapidly and effectively quantified. The quantification of images enables the comparison of the effects gene silencing or treatment with compounds which affect the angiogenic process to be effectively studied. The aims of this project were achieved by utilising the ability to fluorescently label endothelial cells and proteins prior to their use in the *in vitro* co-culture tube formation assay and the hanging drop spheroid angiogenesis assay and using transgenic *fli1*-GFP zebrafish embryos. High fluorescence emission from endothelial cells *in vitro* and *in vivo* was required to permit high resolution confocal imaging, which enabled the generation of useful computer based tools for analysing such images.

6.1.1 Summary of findings from investigating lumen formation within endothelial tubules

To investigate lumen formation in the co-culture tube formation assay various fluorescent labelling approaches were used, a new two coloured fluorescence labelling technique was established using the cytoplasmic dyes, CFSE and CellTracker orange, as well as F-actin labelling using lifeact-GFP and lifeact-RFP. The two coloured labelling approach allowed a detailed investigation into the lumenogenesis mechanisms in comparison to visualising greyscale images. Additionally, a novel technique for visualising the formation of endothelial lumens in live tubules was presented using cells which expressed the lifeact peptide conjugated to fluorescent proteins. This study revealed that F-actin fibres clearly outline luminal

boundaries and also proved useful for studying filopodia formation. Overall, the endothelial cell rearrangement mechanism was the predominant mechanism observed in the assay, the vacuole fusion mechanism was also visualised using the F-actin labelling technique although less frequently than the endothelial cell rearrangement mechanism.

6.1.2 Summary of findings from designing, testing and evaluating a computer based method to analyse endothelial sprouting for screening purposes

A new computer based analysis tool was designed which was able to rapidly and effectively quantify endothelial sprouting by measuring various sprouting parameters from fluorescent spheroid images generated from the hanging drop spheroid assay. The Spheroid Analysis plugin was able to automatically analyse a wide range of sprouting phenotypes. Upon evaluation it was determined that the analysis tool was able to generate comparable results to the frequently used manual analysis method of calculating the total sprouting length but in a time that was approximately seven times faster than the manual approach. The results from this study confirmed that the new ImageJ plugin is a useful analysis tool for screening compounds which affect the process of endothelial sprouting. The Spheroid Analysis plugin will be published online and will be freely available and widely accessible for the scientific community to use.

6.1.3 Summary of findings from developing, testing and evaluating computer based analysis methods for quantifying the zebrafish vasculature

Two computer based analysis methods were developed using IMARIS and ImageJ software, both can be used to assess and quantify the development of the zebrafish vasculature. The two analysis methods used different post-processing steps and therefore each method offered unique advantages when compared. The IMARIS analysis method enabled a detailed investigation into the developed vasculature through the use of an interactive window, whereas the ImageJ Zebrafish Analysis Vasculature Macro enabled rapid and specific analysis of ISV growth and connectivity to the DLAV. The ImageJ analysis method using established ImageJ functions will be freely available, widely accessible and produced comparable results to the frequently used manual analysis method of determining the number of connected ISVs.

6.2. Use of fluorescently labelled endothelial cells

The aims of this PhD project were achieved by utilising the ability to fluorescently label and image endothelial cells and proteins, which enabled a detailed study into the angiogenic processes of endothelial tubulogenesis and lumenogenesis in the co-culture tube formation assay, endothelial sprouting in the hanging drop spheroid assay and ISV growth and connectivity in zebrafish.

It proved essential to fluorescently label endothelial cells with highly emissive dyes prior to use in both of the *in vitro* assays of the co-culture tube formation assay and the hanging drop spheroid angiogenesis assay. It was of importance in the co-culture

tube formation assay as highly emissive fluorescence dyes and proteins proved to be critical for monitoring tubular growth and enabled the endothelial cells to be distinguished from the fibroblasts. By fluorescently labelling endothelial cells with different coloured dyes an investigation into the mechanisms of lumenogenesis was achieved.

In the hanging drop spheroid assay, the use of the highly emissive fluorescence dye CFSE proved critical for capturing high contrast images of the endothelial sprouts. The confocal image sections were compressed to produce high resolution images which showed clear endothelial cell boundaries against the collagen background, which made it possible to design and develop computer based analysis tools for the assessment and quantification of endothelial sprouting. Using confocal imaging avoided the problems of incomplete object boundaries which are often associated with non-fluorescent optical imaging techniques. The use of brightfield or phase contrast images would have been more challenging to analyse.

Similarly, imaging and studying *in vivo* blood vessel formation was possible due to the use of transgenic *fli1*-GFP zebrafish embryos which stably expressed GFP throughout their vascular endothelium. In a similar way to the spheroid images, the optical image sections were compressed to produce a high contrast image of the blood vessels against the background of the organism. These high resolution images showed clearly the growth and connectivity of the ISVs during development, which was essential for being able to generate computer based analysis tools for accurately quantifying blood vessel formation.

6.3. Comparing the computer based analysis methods

In this PhD project, three computer based analysis tools were tested and evaluated for their use of rapidly and effectively quantifying images of endothelial sprouting and blood vessel formation, these included the Spheroid Analysis plugin to analyse endothelial sprouting and the ImageJ and IMARIS analysis methods for analysing the development of the zebrafish vasculature. All three computer based analysis approaches initially required the loading of a fluorescent image with high contrast between the object of interest and the image background.

The analysis procedures used different post processing steps which were specific to the application that they were designed for; however some of the steps in the processing stages were highly similar ensuring that each pixel within the acquired image was accurately assessed. All three computer based analysis tools made use of the skeletonisation function; this is a morphological thinning function which uses an algorithm to successively erode the object in the image until a network of single pixels remains. The skeletonisation process was able to create a simple representation of the original image object. This function is performed on a binary image; binarisation was used to clearly identify the object in the image from the image background. The product of the skeletonisation function was a simplified structure of pixels which was easily and quickly assessed for the presence of end-points, junctional pixels, total number of pixels and segments. The skeletonised function worked effectively in all three analysis methods that were tested and this was shown by the overlaid images of the skeletonised and original images.

Another important process in all three analysis methods was the requirement to remove noise pixels which were acquired during image acquisition to enhance the

accuracy of the analysis procedure. Two different processes were employed to remove noise, these included the despeckle function in ImageJ and thresholding during the creation of the mask in IMARIS. The despeckle function is a highly sensitive median filtering operation; each pixel was accessed and given a reassigned intensity value based on the values of the neighbouring nine pixels. Noise was removed in the IMARIS method by selecting a threshold value during the creation of the three dimensional mask which excluded all noise pixels from the subsequent analysis steps. Both methods successfully excluded noise from the analysis process, however the despeckle function had the advantage of being an automated function, whereas manually selecting a thresholding value can cause variability between images.

It would have been useful for the IMARIS software to have an equivalent despeckle function to automate the process of noise removal as well as having an equivalent fill holes function which was used in ImageJ to remove additional vascular connections formed in the DLAV. This would have enabled the ISVs to be more specifically targeted for analysis. However, unfortunately it was not possible to alter the IMARIS platform due to the software being protected and commercially available. The ImageJ methods had the additional advantages of being freely available, widely accessible, easy to use and generated the quantitative outputs faster than the IMARIS and manual analysis methods.

6.4. Future work

6.4.1 Future work for investigating lumen formation within endothelial tubules

Using endothelial cells which expressed the lifeact peptide conjugated to fluorescent proteins proved to be a highly useful method for visualising the presence of lumen formation within endothelial tubules, however there were concerns as to whether the lifeact peptide was modifying the mechanism of lumen formation. To investigate whether the binding of the lifeact peptide to the actin fibres within the endothelial cells caused disruption to the dynamic functioning of the cytoskeleton, endothelial cells with and without lifeact expression should be used in the co-culture tube formation assay. The endothelial tubules without lifeact expression would be stained using fluorescently labelled phalloidin to compare the actin organisation in tubules formed in both co-cultures, this experiment would determine whether using lifeact expression caused any adverse effects to tubular growth or caused the formation of vacuoles.

A particular limitation in this project was that endothelial processes were imaged using confocal microscopy at single time points. In the study of investigating the formation of lumens this meant that different endothelial tubules were studied during the duration of the assay. Using live-cell time lapse confocal microscopy alongside the fluorescent imaging techniques established in this project would have enabled the same endothelial cells to be imaged throughout the tubulogenesis and lumenogenesis processes. Future work would involve ensuring access to a fluorescence microscope that was able to perform time lapse imaging, to provide valuable insights into these processes. Unfortunately, it was not possible to perform time-lapse imaging during this project due to not having access to such microscope.

Performing time lapse imaging of the co-culture assay could pose challenges due to the long duration of imaging time required as the tubules develop over a period of several weeks. Stable conditions of 37 °C in an atmosphere of 5% carbon dioxide would be required with media refreshed every other day. The microscopy system would also have to have minimal drift to enable the same field of view to be imaged during the time course, which is often a challenge associated with time lapse imaging.

6.4.2 Future work for designing, testing and evaluating a computer based method to analyse endothelial sprouting for screening purposes

The Spheroid Analysis plugin relied on a highly fluorescent spheroid image to be loaded into the analysis tool to accurately analyse endothelial sprouting, this was achieved by labelling the endothelial cells with 5 µM CFSE. The plugin also required only a single spheroid per image to be loaded into the software, if more than one spheroid was present in the image, post-processing by the user was required to remove additional spheroids from the image. Future work in the development of the plugin would enable automatic analysis of several spheroids per image, thereby reducing image acquisition time. Additionally, the ability of the plugin to be able to automatically analyse batches of images would be highly valuable as this would substantially reduce the time required to process the data generated by the plugin.

It would be interesting to further advance this analysis tool to enable processing and analysis of two coloured fluorescence images, this would enable tip and stalk cell dynamics could be studied in detail. A population of endothelial cells could be treated

and labelled with a particular fluorescence dye, and untreated cells could be labelled with a different coloured dye. The cells could be mixed and used in the hanging drop spheroid assay and the plugin could be used to assess whether the treated cells preferentially located to the tip or stalk positions of the endothelial sprouts. Another highly useful advancement of the ImageJ plugin would be to enhance the design so that it would be capable of analysing three dimensional reconstructional images of the spheroids. It would be possible to generate three dimensional reconstructional images of the spheroids using the confocal image sections and if the plugin was able to analyse these sprouting images it would provide greater knowledge on the arrangement and development of the endothelial sprouts.

6.4.3 Future work for developing, testing and evaluating computer based analysis methods for quantifying the zebrafish vasculature

Similarly to the study of investigating lumen formation, a limitation in the study of visualising ISV growth in zebrafish was that single time points of development were imaged using confocal microscopy. To further the work presented in this chapter and to gain an in depth understanding of the effects of silencing vascular related genes and the treatment with inhibitor compounds, time lapse confocal imaging would be used to study the development of the organism and vascular system from the one cell stage through to 48 hpf. Unfortunately as previously mentioned it was not possible to perform time lapse imaging during this study due to not having access to such microscope.

To achieve accurate data analysis it was important to initially acquire and load a highly fluorescent vascular image particularly from the vessels of interest into both

the IMARIS and ImageJ analysis methods. It was not possible to alter the IMARIS platform therefore the future work would involve improving the ImageJ Zebrafish Analysis Vasculature Macro. At present, the analysis method worked most effectively when the generated analysis data was exported from ImageJ into Microsoft Excel, where the final calculations to obtain totalled or averaged values could be obtained. By converting the ImageJ macro into an ImageJ plugin it would be possible to create an extra step in the analysis process to include automation of the final calculations. The addition of this step would eliminate the need to export the data from each image individually and reduce the data processing time substantially. At present, this computer based analysis method to specifically target the ISVs and DLAV for analysis is semi-automated as the PCV and DA are manually selected for removal from the analysis process, this offers a useful manipulation step whereby the user can determine which vessels to analyse. However, it may be possible to introduce a step that automatically removes the PCV and DA using shape recognition algorithms, thereby reducing the analysis time whilst specifically targeting the ISVs for analysis.

References

1. Adams, R. H. & Alitalo, K. Molecular regulation of angiogenesis and lymphangiogenesis. *Nat. Rev. Mol. Cell Biol.* **8**, 464–78 (2007).
2. Alitalo, K., Tammela, T. & Petrova, T. V. Lymphangiogenesis in development and human disease. *Nature* **438**, 946–53 (2005).
3. Aird, W. C. Endothelial cell heterogeneity. *Cold Spring Harb Perspect Med* **2**, a006429 (2012).
4. Carmeliet, P. Angiogenesis in health and disease. *Nat. Med.* **9**, 653–60 (2003).
5. Carmeliet, P. Angiogenesis in life, disease and medicine. *Nature* **438**, 932–936 (2005).
6. Lamalice, L., Le Boeuf, F. & Huot, J. Endothelial cell migration during angiogenesis. *Circ. Res.* **100**, 782–794 (2007).
7. Yang, X. & Cepko, C. L. Flk-1, a receptor for vascular endothelial growth factor (VEGF), is expressed by retinal progenitor cells. *J. Neurosci.* **16**, 6089–6099 (1996).
8. Risau, W. *et al.* Vasculogenesis and angiogenesis in embryonic-stem-cell-derived embryoid bodies. *Development* **102**, 471–478 (1988).
9. Risau, W. & Flamme, I. V asculogenesis. *Annu. Rev. Cell Dev. Biol.* **11**, 73–91 (1995).
10. Drake, C. J. Embryonic and adult vasculogenesis. *Birth Defects Res. Part C - Embryo Today Rev.* **69**, 73–82 (2003).
11. Li, J. I. E., Zhang, Y. & Kirsner, R. S. Angiogenesis in Wound Repair: Angiogenic Growth Factors and the Extracellular Matrix. **114**, 107–114 (2003).
12. Reynolds, L. P., Killilea, S. D. & Redmer, D. a. Angiogenesis in the female reproductive system. *FASEB J.* **6**, 886–892 (1992).
13. Carmeliet, P. VEGF as a key mediator of angiogenesis in cancer. *Oncology* **69**, 4–10 (2005).
14. Carmeliet, P. & Jain, R. K. Molecular mechanisms and clinical applications of angiogenesis. *Nature* **473**, 298–307 (2011).
15. De Smet, F., Segura, I., De Bock, K., Hohensinner, P. J. & Carmeliet, P. Mechanisms of vessel branching: Filopodia on endothelial tip cells lead the way. *Arterioscler. Thromb. Vasc. Biol.* **29**, 639–649 (2009).
16. Yan, M. & Plowman, G. D. Delta-like 4/notch signaling and its therapeutic implications. *Clin. Cancer Res.* **13**, 7243–7246 (2007).
17. Iruela-Arispe, M. L. & Davis, G. E. Cellular and molecular mechanisms of vascular lumen formation. *Dev. Cell* **16**, 222–31 (2009).
18. Kamei, M. *et al.* Endothelial tubes assemble from intracellular vacuoles in vivo. *Nature* **442**, 453–6 (2006).
19. Burri, P. H., Hlushchuk, R. & Djonov, V. Intussusceptive angiogenesis: Its emergence, its characteristics, and its significance. *Dev. Dyn.* **231**, 474–488 (2004).
20. Makanya, A. N., Hlushchuk, R. & Djonov, V. G. Intussusceptive angiogenesis and its role in vascular morphogenesis, patterning, and remodeling. *Angiogenesis* **12**, 113–123 (2009).
21. Korn, C. & Augustin, H. G. Mechanisms of Vessel Pruning and Regression. *Dev. Cell* **34**, 5–17 (2015).

22. Soucy, P. a & Romer, L. H. Endothelial cell adhesion, signaling, and morphogenesis in fibroblast-derived matrix. *Matrix Biol.* **28**, 273–83 (2009).
23. Herbert, S. P. & Stainier, D. Y. R. Molecular control of endothelial cell behaviour during blood vessel morphogenesis. *Nat. Rev. Mol. Cell Biol.* **12**, 551–64 (2011).
24. Lammert, E. & Axnick, J. Vascular lumen formation. *Cold Spring Harb. Perspect. Med.* **2**, 1–9 (2012).
25. Strilić, B. *et al.* The Molecular Basis of Vascular Lumen Formation in the Developing Mouse Aorta. *Dev. Cell* **17**, 505–515 (2009).
26. Abraham, S. *et al.* A Rac/Cdc42 exchange factor complex promotes formation of lateral filopodia and blood vessel lumen morphogenesis. *Nat. Commun.* **6**, 7286 (2015).
27. Xu, K. *et al.* Blood vessel tubulogenesis requires Rasip1 regulation of GTPase signaling. **20**, 526–539 (2012).
28. Jin, S., Beis, D., Mitchell, T., Chen, J. & Stainier, D. Y. R. Cellular and molecular analyses of vascular tube and lumen formation in zebrafish. 5199–5209 (2005). doi:10.1242/dev.02087
29. Blum, Y. *et al.* Complex cell rearrangements during intersegmental vessel sprouting and vessel fusion in the zebrafish embryo. *Dev. Biol.* **316**, 312–322 (2008).
30. Davis, G. E. & Bayless, K. J. An integrin and Rho GTPase-dependent pinocytic vacuole mechanism controls capillary lumen formation in collagen and fibrin matrices. *Microcirculation* **10**, 27–44 (2003).
31. Davis, G. E., Kon, W. & Stratman, A. N. Mechanisms controlling human endothelial lumen formation and tube assembly in three-dimensional extracellular matrices. *Birth Defects Res. Part C - Embryo Today Rev.* **81**, 270–285 (2007).
32. Bayless, K. J., Salazar, R. & Davis, G. E. RGD-Dependent Vacuolation and Lumen Formation Observed during Endothelial Cell Morphogenesis in Three-Dimensional Fibrin Matrices Involves the $\alpha v\beta 3$ and $\alpha 5\beta 1$ Integrins. *Am. J. Pathol.* **156**, 1673–1683 (2000).
33. Koh, W., Mahan, R. D. & Davis, G. E. Cdc42- and Rac1-mediated endothelial lumen formation requires Pak2, Pak4 and Par3, and PKC-dependent signaling. *J. Cell Sci.* **121**, 989–1001 (2008).
34. Bayless, K. J. & Davis, G. E. The Cdc42 and Rac1 GTPases are required for capillary lumen formation in three-dimensional extracellular matrices. *J. Cell Sci.* **115**, 1123–1136 (2002).
35. Yang, S., Graham, J., Kahn, J. W., Schwartz, E. a & Gerritsen, M. E. Functional roles for PECAM-1 (CD31) and VE-cadherin (CD144) in tube assembly and lumen formation in three-dimensional collagen gels. *Am. J. Pathol.* **155**, 887–895 (1999).
36. Davis, G. E. & Camarillo, C. W. An alpha 2 beta 1 integrin-dependent pinocytic mechanism involving intracellular vacuole formation and coalescence regulates capillary lumen and tube formation in three-dimensional collagen matrix. *Exp. Cell Res.* **224**, 39–51 (1996).
37. Gebala, V., Collins, R., Geudens, I., Phng, L-K., Gerhardt, H. Blood flow drives lumen formation by inverse membrane blebbing during angiogenesis in vivo. *Nature Cell Biology* **4**, 443-450 (2016).

38. Ubersax, J. a. & Ferrell Jr, J. E. Mechanisms of specificity in protein phosphorylation. *Nat. Rev. Mol. Cell Biol.* **8**, 530–541 (2007).
39. Cheng, H.-C., Qi, R. Z., Paudel, H. & Zhu, H.-J. Regulation and Function of Protein Kinases and Phosphatases. *Enzyme Res.* **2011**, 1–3 (2011).
40. Hunter, T. Protein kinases and phosphatases: The Yin and Yang of protein phosphorylation and signaling. *Cell* **80**, 225–236 (1995).
41. Hanks, S. K. & Hunter, T. Protein kinases 6. The eukaryotic protein kinase superfamily: kinase (catalytic) domain structure and classification. *FASEB J.* **9**, 576–96 (1995).
42. Fabbro, D., Cowan-Jacob, S. W. & Moebitz, H. Ten things you should know about protein kinases: IUPHAR Review 14. *Br. J. Pharmacol.* **172**, 2675–2700 (2015).
43. Davies, S. P., Reddy, H., Caivano, M. & Cohen, P. Specificity and mechanism of action of some commonly used protein kinase inhibitors. *Biochem. J.* **351**, 95–105 (2000).
44. Bain, J., McLauchlan, H., Elliott, M. & Cohen, P. The specificities of protein kinase inhibitors: an update. *Biochem. J.* **371**, 199–204 (2003).
45. Chen, H., Shen, J., Choy, E., Hornicek, F. J. & Duan, Z. Targeting protein kinases to reverse multidrug resistance in sarcoma. *Cancer Treat. Rev.* **43**, 8–18 (2016).
46. Cohen, P. Protein kinases--the major drug targets of the twenty-first century? *Nat. Rev. Drug Discov.* **1**, 309–315 (2002).
47. Wu, P., Nielsen, T. E. & Clausen, M. H. FDA-approved small-molecule kinase inhibitors. *Trends Pharmacol. Sci.* **36**, 422–439 (2015).
48. Bain, J. *et al.* The selectivity of protein kinase inhibitors: a further update. *Biochem. J.* **408**, 297–315 (2007).
49. Noble, M. E. M., Noble, M. E. M., Endicott, J. a & Johnson, L. N. Protein Kinase Inhibitors : Insights into Drug Design from Structure. **1800**, 1800–1805 (2014).
50. Shibuya, M. Vascular Endothelial Growth Factor (VEGF) and Its Receptor (VEGFR) Signaling in Angiogenesis: A Crucial Target for Anti- and Pro-Angiogenic Therapies. *Genes Cancer* **2**, 1097–1105 (2011).
51. Gotink, K. J. & Verheul, H. M. W. Anti-angiogenic tyrosine kinase inhibitors: what is their mechanism of action? *Angiogenesis* **13**, 1–14 (2010).
52. Faivre, S., Demetri, G., Sargent, W. & Raymond, E. Molecular basis for sunitinib efficacy and future clinical development. *Nat. Rev. Drug Discov.* **6**, 734–745 (2007).
53. Wilhelm, S. *et al.* Discovery and development of sorafenib: a multikinase inhibitor for treating cancer. *Nat. Rev. Drug Discov.* **5**, 835–844 (2006).
54. Podar, K. *et al.* The small-molecule VEGF receptor inhibitor pazopanib (GW786034B) targets both tumor and endothelial cells in multiple myeloma. *Proc. Natl. Acad. Sci. U. S. A.* **103**, 19478–83 (2006).
55. Dickson, M. a *et al.* Phase II Trial of Gemcitabine and Docetaxel with Bevacizumab in Soft Tissue Sarcoma. *Sarcoma* **2015**, 532478 (2015).
56. Heldin, C. H. & Lennartsson, J. Structural and functional properties of platelet-derived growth factor and stem cell factor receptors. *Cold Spring Harb. Perspect. Biol.* **5**, a009100 (2013).
57. Homsj, J. & Daud, A. I. Spectrum of activity and mechanism of action of VEGF/PDGF inhibitors. *Cancer Control* **14**, 285–294 (2007).

58. Roskoski, R. Sunitinib: A VEGF and PDGF receptor protein kinase and angiogenesis inhibitor. *Biochem. Biophys. Res. Commun.* **356**, 323–328 (2007).
59. Wilhelm, S. M. *et al.* Preclinical overview of sorafenib, a multikinase inhibitor that targets both Raf and VEGF and PDGF receptor tyrosine kinase signaling. *Mol. Cancer Ther.* **7**, 3129–3140 (2008).
60. Taeger, J. *et al.* Targeting FGFR/PDGFR/VEGFR Impairs Tumor Growth, Angiogenesis, and Metastasis by Effects on Tumor Cells, Endothelial Cells, and Pericytes in Pancreatic Cancer. *Mol. Cancer Ther.* **10**, 2157–2167 (2011).
61. Hellstrom, M., Kalen, M., Lindhal, P., Abramsson, a & Betsholtz, C. Role of PDGF-B and PDGFR-beta in recruitment of vascular smooth muscle cells and pericytes during embryonic blood vessel formation in mice. *Development* **126**, 3047 (1999).
62. Bergers, G., Song, S., Meyer-Morse, N., Bergsland, E. & Hanahan, D. Benefits of targeting both pericycles and endothelial cells in the tumour vasculature with kinase inhibitors. *J Clin Invest* **111**, 1287–1295 (2003).
63. Erber, R. *et al.* Combined inhibition of VEGF and PDGF signaling enforces tumor vessel regression by interfering with pericyte-mediated endothelial cell survival mechanisms. *FASEB J.* **18**, 338–340 (2004).
64. Amin, D. N., Hida, K., Bielenberg, D. R. & Klagsbrun, M. Tumor endothelial cells express epidermal growth factor receptor (EGFR) but not ErbB3 and are responsive to EGF and to EGFR kinase inhibitors. *Cancer Res.* **66**, 2173–2180 (2006).
65. Stern, D. F. Tyrosine kinase signalling in breast cancer: ErbB family receptor tyrosine kinases. *Breast Cancer Res.* **2**, 176–83 (2000).
66. Huang, D. *et al.* Inhibition of MAPK kinase signaling pathways suppressed renal cell carcinoma growth and angiogenesis in vivo. *Cancer Res.* **68**, 81–8 (2008).
67. Mattila, P. Protein kinase C subtypes in endothelial cells. **289**, 86–90 (1991).
68. Xu, H. *et al.* Protein kinase C alpha promotes angiogenic activity of human endothelial cells via induction of vascular endothelial growth factor. *Cardiovasc. Res.* **78**, 349–355 (2008).
69. Wickstead, B. & Gull, K. The evolution of the cytoskeleton. *J. Cell Biol.* **194**, 513–525 (2011).
70. Pollard, T. D. The cytoskeleton, cellular motility and the reductionist agenda. *Nature* **422**, 741–5 (2003).
71. Abu Taha, A. & Schnittler, H.-J. Dynamics between actin and the VE-cadherin/catenin complex: Novel aspects of the ARP2/3 complex in regulation of endothelial junctions. *Cell Adh. Migr.* **8**, 125–135 (2014).
72. Liu, T. *et al.* Regulation of vimentin intermediate filaments in endothelial cells by hypoxia. *Am. J. Physiol. Cell Physiol.* **299**, C363–C373 (2010).
73. Cooper, G. *The Cell: A Molecular Approach.* (Sinauer Associates, 2000).
74. Qin, Z. & Buehler, M. J. Structure and dynamics of human vimentin intermediate filament dimer and tetramer in explicit and implicit solvent models. *J. Mol. Model.* **17**, 37–48 (2011).
75. Bezanilla, M., Gladfelter, A. S., Kovar, D. R. & Lee, W. L. Cytoskeletal dynamics: A view from the membrane. *J. Cell Biol.* **209**, 329–337 (2015).

76. Dos Remedios, C. G. *et al.* Actin binding proteins: regulation of cytoskeletal microfilaments. *Physiol. Rev.* **83**, 433–473 (2003).
77. H. Lodish, A. Berk, S.L. Zipursky, P. Matsudaira, D. Baltimore, J. D. *Molecular Cell Biology*. (W.H. Freeman, 2000).
78. Lee, S. H. & Dominguez, R. Regulation of actin cytoskeleton dynamics in cells. *Mol. Cells* **29**, 311–325 (2010).
79. Goley, E. D. & Welch, M. D. The ARP2/3 complex: an actin nucleator comes of age. *Nat. Rev. Mol. Cell Biol.* **7**, 713–26 (2006).
80. Fritzsche, M., Erlenkämper, C., Moeendarbary, E., Charras, G. & Kruse, K. Actin kinetics shapes cortical network structure and mechanics. 1–13 (2016).
81. Prasain, N. & Stevens, T. The actin cytoskeleton in endothelial cell phenotypes. *Microvasc. Res.* **77**, 53–63 (2009).
82. Schnittler, H. *et al.* Actin filament dynamics and endothelial cell junctions: The Ying and Yang between stabilization and motion. *Cell Tissue Res.* **355**, 529–543 (2014).
83. Tzima, E. Role of small GTPases in endothelial cytoskeletal dynamics and the shear stress response. *Circ. Res.* **98**, 176–185 (2006).
84. Cramer, L. P., Siebert, M. & Mitchison, T. J. Identification of novel graded polarity actin filament bundles in locomoting heart fibroblasts: Implications for the generation of motile force. *J. Cell Biol.* **136**, 1287–1305 (1997).
85. Adams, J. C. Formation of stable microspikes containing actin and the 55 kDa actin bundling protein, fascin, is a consequence of cell adhesion to thrombospondin-1: implications for the anti-adhesive activities of thrombospondin-1. *J. Cell Sci.* **108 (Pt 5)**, 1977–1990 (1995).
86. Mattila, P. K. & Lappalainen, P. Filopodia: molecular architecture and cellular functions. *Nat. Rev. Mol. Cell Biol.* **9**, 446–454 (2008).
87. Stricker, J., Falzone, T. & Gardel, M. L. Mechanics of the F-actin cytoskeleton. *J. Biomech.* **43**, 9–14 (2010).
88. Abraham, S. *et al.* VE-Cadherin-Mediated Cell-Cell Interaction Suppresses Sprouting via Signaling to MLC2 Phosphorylation. *Curr. Biol.* **19**, 668–674 (2009).
89. Riento, K. & Ridley, A. J. Rocks: multifunctional kinases in cell behaviour. *Nat. Rev. Mol. Cell Biol.* **4**, 446–56 (2003).
90. Katoh, K. & Noda, Y. Distribution of Cytoskeletal Components in Endothelial Cells in the Guinea Pig Renal Artery. *Int. J. Cell Biol.* **2012**, 1–10 (2012).
91. Kano, Y., Katoh, K. & Fujiwara, K. Lateral zone of cell-cell adhesion as the major fluid shear stress-related signal transduction site. *Circ. Res.* **86**, 425–33 (2000).
92. Schmit, a C. & Lambert, a M. Microinjected fluorescent phalloidin in vivo reveals the F-actin dynamics and assembly in higher plant mitotic cells. *Plant Cell* **2**, 129–38 (1990).
93. Cooper, J. Effects of cytochalasin B on actin filaments. *Cold Spring Harb. Symp. Quant. Biol.* **37**, 585–593 (1987).
94. Waterman-Storer, C. M., Desai, a, Bulinski, J. C. & Salmon, E. D. Fluorescent speckle microscopy, a method to visualize the dynamics of protein assemblies in living cells. *Curr. Biol.* **8**, 1227–1230 (1998).
95. Riedl, J. *et al.* NIH Public Access. **5**, 1–8 (2010).

96. Riss, T.L., Moravec, R.A., Niles, A.L., Benink, H.A., Worzella, T.J. and Minor, L. Cell Viability Assays. *NCBI Bookshelf* (2015).
97. Filigheddu, N. *et al.* Hexarelin protects H9c2 cardiomyocytes from doxorubicin-induced cell death. *Endocrine* **14**, 113–9 (2001).
98. Goodwin, C.J., Holt, S.J., Downes, S., & Marshall N.J. Microculture tetrazolium assays: a comparison between two new tetrazolium salts, XTT and MTS. *J. Immunol. Methods* **179**, 95–103 (1995).
99. Roehm, N. W., Rodgers, G. H., Hatfield, S. M. & Glasebrook, A. L. An improved colorimetric assay for cell proliferation and viability utilizing the tetrazolium salt XTT. *J. Immunol. Methods* **142**, 257–265 (1991).
100. Ngamwongsatit, P., Banada, P. P., Panbangred, W. & Bhunia, A. K. WST-1-based cell cytotoxicity assay as a substitute for MTT-based assay for rapid detection of toxigenic *Bacillus* species using CHO cell line. *J. Microbiol. Methods* **73**, 211–215 (2008).
101. Staton, C. a., Reed, M. W. R. & Brown, N. J. A critical analysis of current in vitro and in vivo angiogenesis assays. *Int. J. Exp. Pathol.* **90**, 195–221 (2009).
102. Ammann, K. R. *et al.* Collective cell migration of smooth muscle and endothelial cells: impact of injury versus non-injury stimuli. *J. Biol. Eng.* **9**, 19 (2015).
103. Liang, C.-C. C., Park, A. Y. & Guan, J.-L. L. In vitro scratch assay: a convenient and inexpensive method for analysis of cell migration in vitro. *Nat. Protoc.* **2**, 329–333 (2007).
104. Kane, N. M. *et al.* Derivation of endothelial cells from human embryonic stem cells by directed differentiation: Analysis of microrna and angiogenesis in vitro and in vivo. *Arterioscler. Thromb. Vasc. Biol.* **30**, 1389–1397 (2010).
105. Jonkman, J. E. N. *et al.* An introduction to the wound healing assay using live-cell microscopy. *Cell Adhes. Migr.* **8**, 440–451 (2014).
106. Nobes, C. D. & Hall, A. Rho GTPases control polarity, protrusion, and adhesion during cell movement. *J. Cell Biol.* **144**, 1235–1244 (1999).
107. Etienne-Manneville, S. & Hall, A. Integrin-mediated activation of Cdc42 controls cell polarity in migrating astrocytes through PKC ζ . *Cell* **106**, 489–498 (2001).
108. Zahm, J. & Doriot, F. Cell Migration and Proliferation During the In Vitro Wound Repair of the Respiratory Epithelium. **43**, 33–43 (1997).
109. Simpson, K. J. *et al.* Identification of genes that regulate epithelial cell migration using an siRNA screening approach. *Nat. Cell Biol.* **10**, 1027–1038 (2008).
110. Del Duca, D., Werbowetski, T. & Del Maestro, R. F. Spheroid preparation from hanging drops: Characterization of a model of brain tumor invasion. *J. Neurooncol.* **67**, 295–303 (2004).
111. Kelm, J. M., Timmins, N. E., Brown, C. J., Fussenegger, M. & Nielsen, L. K. Method for generation of homogeneous multicellular tumor spheroids applicable to a wide variety of cell types. *Biotechnol. Bioeng.* **83**, 173–180 (2003).
112. Timmins, N., Dietmair, S. & Nielsen, L. Hanging-drop multicellular spheroids as a model of tumour angiogenesis. *Angiogenesis* **7**, 97–103 (2004).
113. Hillen, F. & Griffioen, A. W. Tumour vascularization: Sprouting angiogenesis and beyond. *Cancer Metastasis Rev.* **26**, 489–502 (2007).

114. Korff, T. & Augustin, H. G. Tensional forces in fibrillar extracellular matrices control directional capillary sprouting. *J. Cell Sci.* **112** (Pt 1, 3249–3258 (1999).
115. Finkenzeller, G., Stark, G. B. & Strassburg, S. Growth differentiation factor 11 supports migration and sprouting of endothelial progenitor cells. *J. Surg. Res.* **198**, 50–56 (2015).
116. Fuller, T., Korff, T., Kilian, a, Dandekar, G. & Augustin, H. G. Forward EphB4 signaling in endothelial cells controls cellular repulsion and segregation from ephrinB2 positive cells. *J Cell Sci* **116**, 2461–2470 (2003).
117. Stahl, A., Wu, X., Wenger, A., Klagsbrun, M. & Kurschat, P. Endothelial progenitor cell sprouting in spheroid cultures is resistant to inhibition by osteoblasts: A model for bone replacement grafts. *FEBS Lett.* **579**, 5338–5342 (2005).
118. Kütscher, C. *et al.* Overexpression of hypoxia-inducible factor-1 alpha improves vasculogenesis-related functions of endothelial progenitor cells. *Microvasc. Res.* **105**, 85–92 (2016).
119. Mavroeidis, L. *et al.* Metronomic vinorelbine: Anti-angiogenic activity in vitro in normoxic and severe hypoxic conditions, and severe hypoxia-induced resistance to its anti-proliferative effect with reversal by Akt inhibition. *Int. J. Oncol.* 455–464 (2015). doi:10.3892/ijo.2015.3059
120. Liu, F., Smith, J., Zhang, Z., Cole, R. & Herron, B. J. Genetic heterogeneity of skin microvasculature. *Dev. Biol.* **340**, 480–489 (2010).
121. Chung, S. W. *et al.* LHT7, a chemically modified heparin, inhibits multiple stages of angiogenesis by blocking VEGF, FGF2 and PDGF-B signaling pathways. *Biomaterials* **37**, 271–278 (2015).
122. Madri, J. a, Pratt, B. M. & Tucker, a M. Phenotypic modulation of endothelial cells by transforming growth factor beta depends upon the composition and organisation of the extracellular matrix. *J. Cell Biol.* **106**, 1375–1384 (1988).
123. Arnaoutova, I., George, J., Kleinman, H. K. & Benton, G. The endothelial cell tube formation assay on basement membrane turns 20: State of the science and the art. *Angiogenesis* **12**, 267–274 (2009).
124. Crawley, M. J. *Second Edition.* (2013).
125. Kroon, M. E., Schie, M. L. J. Van, Vecht, B. Van Der, Hinsbergh, V. W. M. Van & Koolwijk, P. Collagen type 1 retards tube formation by human microvascular endothelial cells in a fibrin matrix. 257–265 (2003).
126. Auerbach, R., Lewis, R., Shinnars, B., Kubai, L. & Akhtar, N. Angiogenesis assays: a critical overview. *Clin. Chem.* **49**, 32–40 (2003).
127. Arnaoutova, I. & Kleinman, H. K. In vitro angiogenesis: endothelial cell tube formation on gelled basement membrane extract. *Nat. Protoc.* **5**, 628–635 (2010).
128. Kureishi, Y. *et al.* The HMG-CoA reductase inhibitor simvastatin activates the protein kinase Akt and promotes angiogenesis in normocholesterolemic animals. *Nat. Med.* **6**, 1004–10 (2000).
129. Shao, R. & Guo, X. Human microvascular endothelial cells immortalized with human telomerase catalytic protein: A model for the study of in vitro angiogenesis. *Biochem. Biophys. Res. Commun.* **321**, 788–794 (2004).
130. Bishop, E. T. *et al.* An in vitro model of angiogenesis: basic features. *Angiogenesis* **3**, 335–344 (1999).

131. Heydarkhan-Hagvall, S. *et al.* Co-culture of endothelial cells and smooth muscle cells affects gene expression of angiogenic factors. *J. Cell. Biochem.* **89**, 1250–1259 (2003).
132. Tomasek, J. J., Gabbiani, G., Hinz, B., Chaponnier, C. & Brown, R. a. Myofibroblasts and mechano-regulation of connective tissue remodelling. *Nat. Rev. Mol. Cell Biol.* **3**, 349–63 (2002).
133. C.A. Staton, C. Lewis, R. B. *Angiogenesis Assays: A Critical Appraisal of Current Techniques.* (John Wiley & Sons, 2006).
134. Newman, a. C., Nakatsu, M. N., Chou, W., Gershon, P. D. & Hughes, C. C. W. The requirement for fibroblasts in angiogenesis: fibroblast-derived matrix proteins are essential for endothelial cell lumen formation. *Mol. Biol. Cell* **22**, 3791–3800 (2011).
135. Folkman, J. & Shing, Y. contrast, the FGFs are pleiotropic. They stimulate the growth of endothelial cells, smooth muscle cells, fibroblasts, and certain. **267**, 10931–10934 (1992).
136. Hetheridge, C., Mavria, G. & Mellor, H. Uses of the in vitro endothelial-fibroblast organotypic co-culture assay in angiogenesis research. *Biochem. Soc. Trans.* **39**, 1597–600 (2011).
137. Khoo, C. P., Micklem, K. & Watt, S. M. A comparison of methods for quantifying angiogenesis in the Matrigel assay in vitro. *Tissue Eng. Part C. Methods* **17**, 895–906 (2011).
138. Guidolin, D., Vacca, A., Nussdorfer, G. G. & Ribatti, D. A new image analysis method based on topological and fractal parameters to evaluate the angiostatic activity of docetaxel by using the Matrigel assay in vitro. *Microvasc. Res.* **67**, 117–24 (2004).
139. G. Carpentier, M. Martinelli, J. Courty, J. C. Angiogenesis Analyzer for ImageJ. in *4th ImageJ User and Developer Conference proceedings* 198–201 (2012).
140. Vitale, G. *et al.* Zebrafish as an innovative model for neuroendocrine tumors. *Endocr. Relat. Cancer* **21**, R67–83 (2014).
141. C. Nusslein-Volhard, R. D. *Zebrafish.* (Oxford Univeristy Press, 2002).
142. Isogai, S., Horiguchi, M. & Weinstein, B. M. The vascular anatomy of the developing zebrafish: an atlas of embryonic and early larval development. *Dev. Biol.* **230**, 278–301 (2001).
143. Nguyen, C. T., Lu, Q., Wang, Y. & Chen, J.-N. Zebrafish as a model for cardiovascular development and disease. *Drug Discov. Today Dis. Model.* **5**, 135–140 (2008).
144. Woods, I. G. *et al.* The zebrafish gene map defines ancestral vertebrate chromosomes. *Genome Res.* **15**, 1307–1314 (2005).
145. Gore, A. V, Monzo, K., Cha, Y. R., Pan, W. & Weinstein, B. M. Vascular development in the zebrafish. *Cold Spring Harb. Perspect. Med.* **2**, a006684 (2012).
146. Bill, B. R., Petzold, A. M., Clark, K. J., Schimmenti, L. a & Ekker, S. C. A primer for morpholino use in zebrafish. *Zebrafish* **6**, 69–77 (2009).
147. Summerton, J. & Weller, D. Morpholino antisense oligomers: design, preparation, and properties. *Antisense Nucleic Acid Drug Dev.* **7**, 187–195 (1997).
148. Heasman, J. Morpholino oligos: making sense of antisense? *Dev. Biol.* **243**, 209–14 (2002).

149. Klee, E. W., Shim, K. J., Pickart, M. a., Ekker, S. C. & Ellis, L. B. M. AMOD: A morpholino oligonucleotide selection tool. *Nucleic Acids Res.* **33**, 506–511 (2005).
150. Thisse, C. & Thisse, B. High-resolution in situ hybridization to whole-mount zebrafish embryos. *Nat. Protoc.* **3**, 59–69 (2008).
151. Kimmel, C. B., Ballard, W. W., Kimmel, S. R., Ullmann, B. & Schilling, T. F. Stages of embryonic development of the zebrafish. *Dev. Dyn.* **203**, 253–310 (1995).
152. Gering, M., Rodaway, a. R. F., Gottgens, B., Patient, R. K. & Green, a. R. The SCL gene specifies haemangioblast development from early mesoderm. *EMBO J.* **17**, 4029–4045 (1998).
153. Stainier, D. Y., Weinstein, B. M., Detrich, H. W., Zon, L. I. & Fishman, M. C. Cloche, an early acting zebrafish gene, is required by both the endothelial and hematopoietic lineages. *Development* **121**, 3141–3150 (1995).
154. Brown, L. a. *et al.* Insights into early vasculogenesis revealed by expression of the ETS-domain transcription factor Fli-1 in wild-type and mutant zebrafish embryos. *Mech. Dev.* **90**, 237–252 (2000).
155. Lawson, N. D. & Weinstein, B. M. In Vivo Imaging of Embryonic Vascular Development Using Transgenic Zebrafish. *Dev. Biol.* **248**, 307–318 (2002).
156. Herbert, S. P. *et al.* Selective Cell Sprouting: An Alternative. **326**, 294–299 (2009).
157. Isogai, S., Lawson, N. D., Torrealday, S., Horiguchi, M. & Weinstein, B. M. Angiogenic network formation in the developing vertebrate trunk. *Development* **130**, 5281–90 (2003).
158. Yaniv, K. *et al.* Live imaging of lymphatic development in the zebrafish. *Nat. Med.* **12**, 711–716 (2006).
159. Hogan, B. M. *et al.* Vegfc/Flt4 signalling is suppressed by Dll4 in developing zebrafish intersegmental arteries. *Development* **136**, 4001–9 (2009).
160. Leslie, J. D. *et al.* Endothelial signalling by the Notch ligand Delta-like 4 restricts angiogenesis. *Development* **134**, 839–844 (2007).
161. Karlsson, J., von Hofsten, J. & Olsson, P. E. Generating transparent zebrafish: a refined method to improve detection of gene expression during embryonic development. *Mar. Biotechnol. (NY)*. **3**, 522–7 (2001).
162. Chawla, M. S. *et al.* In vivo Magnetic Resonance Vascular Imaging Using Laser-Polarized ³He Microbubbles. *Proc. Natl. Acad. Sci. U. S. A.* **95**, 10832–10835 (1998).
163. Cheng, S. H., Chan, P. K. & Wu, R. S. S. The use of microangiography in detecting aberrant vasculature in zebrafish embryos exposed to cadmium. *Aquat. Toxicol.* **52**, 61–71 (2001).
164. Chan, J. Y.-W. *et al.* Polyphyllin D, a steroidal saponin from Paris polyphylla, inhibits endothelial cell functions in vitro and angiogenesis in zebrafish embryos in vivo. *J. Ethnopharmacol.* **137**, 64–9 (2011).
165. Schoors, S. *et al.* Partial and transient reduction of glycolysis by PFKFB3 blockade reduces pathological angiogenesis. *Cell Metab.* **19**, 37–48 (2014).
166. Verma, A. *et al.* Endothelial cell-specific chemotaxis receptor (ecscr) promotes angioblast migration during vasculogenesis and enhances VEGF receptor sensitivity. *Blood* **115**, 4614–4622 (2010).

167. Coxam, B. *et al.* carbamoyl-phosphate synthetase 2, aspartate transcarbamylase, and dihydroorotase (cad) regulates Notch signaling and vascular development in zebrafish. *Dev. Dyn.* **244**, 1–9 (2015).
168. Ellett, F., Kile, B. T. & Lieschke, G. J. The role of the ETS factor *erg* in zebrafish vasculogenesis. *Mech. Dev.* **126**, 220–9 (2008).
169. Lee, P. *et al.* Neuropilin-1 is required for vascular development and is a mediator of VEGF-dependent angiogenesis in zebrafish. *Proc. Natl. Acad. Sci. U. S. A.* **99**, 10470–10475 (2002).
170. Zeng, X.-X. I. *et al.* Phospholipase D1 is required for angiogenesis of intersegmental blood vessels in zebrafish. *Dev. Biol.* **328**, 363–76 (2009).
171. Aase, K. *et al.* Angiomotin regulates endothelial cell migration during embryonic angiogenesis. *Genes Dev.* **21**, 2055–2068 (2007).
172. Cermenati, S. *et al.* Sox18 genetically interacts With VegfC to regulate lymphangiogenesis in zebrafish. *Arterioscler. Thromb. Vasc. Biol.* **33**, 1238–1247 (2013).
173. Meadows, S. M. & Cleaver, O. Annexin A3 Regulates Early Blood Vessel Formation. *PLoS One* **10**, e0132580 (2015).
174. Quezada, M. *et al.* Antiangiogenic, antimigratory and antiinflammatory effects of 2-methoxyestradiol in zebrafish larvae. *Comp. Biochem. Physiol. C. Toxicol. Pharmacol.* **157**, 141–9 (2013).
175. Li, S. *et al.* Basal Flt1 tyrosine kinase activity is a positive regulator of endothelial survival and vascularization during zebrafish embryogenesis. *Biochim. Biophys. Acta* **1850**, 373–384 (2014).
176. Han, L. *et al.* Tracking antiangiogenic components from *Glycyrrhiza uralensis* Fisch. based on zebrafish assays using high-speed countercurrent chromatography. *J. Sep. Sci.* **35**, 1167–72 (2012).
177. Hu, G. *et al.* Polysaccharides from astragali radix restore chemical-induced blood vessel loss in zebrafish. *Vasc. Cell* **4**, 2 (2012).
178. Tal, T. L. *et al.* Immediate and long-term consequences of vascular toxicity during zebrafish development. *Reprod. Toxicol.* **48**, 51–61 (2014).
179. Vogt, a *et al.* Automated image-based phenotypic analysis in zebrafish embryos. *Dev Dyn* **238**, 656–663 (2009).
180. Tran, T. C. *et al.* Automated, quantitative screening assay for antiangiogenic compounds using transgenic zebrafish. *Cancer Res.* **67**, 11386–11392 (2007).
181. Hans, C. *et al.* 3D imaging for quantitative assessment of toxicity on vascular development in {Z}ebrafish. *Proc. IEEE Int. Conf. Eng. Med. Biol. Soc.* 5969–5972 (2011).
182. McCollum, C. W. *et al.* Embryonic exposure to sodium arsenite perturbs vascular development in zebrafish. *Aquat. Toxicol.* **152**, 152–163 (2014).
183. Feng, J., Han Cheng, S., Chan, P. K. & Ip, H. H. S. Reconstruction and representation of caudal vasculature of zebrafish embryo from confocal scanning laser fluorescence microscopic images. *Comput. Biol. Med.* **35**, 915–931 (2005).
184. Soker, S., Takashima, S., Miao, H. Q., Neufeld, G. & Klagsbrun, M. Neuropilin-1 is expressed by endothelial and tumor cells as an isoform-specific receptor for vascular endothelial growth factor. *Cell* **92**, 735–745 (1998).
185. Gluzman-Poltorak, Z. Neuropilin-2 and Neuropilin-1 Are Receptors for the 165-Amino Acid Form of Vascular Endothelial Growth Factor (VEGF) and of

- Placenta Growth Factor-2, but Only Neuropilin-2 Functions as a Receptor for the 145-Amino Acid Form of VEGF. *J. Biol. Chem.* **275**, 18040–18045 (2000).
186. Ferrara, N., Gerber, H.-P. & LeCouter, J. The biology of VEGF and its receptors. *Nat. Med.* **9**, 669–76 (2003).
 187. Carmeliet, P. *et al.* Abnormal blood vessel development and lethality in embryos lacking a single VEGF allele. *Nature* **380**, 435–439 (1996).
 188. Ferrara, N. *et al.* Heterozygous embryonic lethality induced by targeted inactivation of the VEGF gene. *Nature* **380**, 439–442 (1996).
 189. Mura, M. *et al.* Identification and angiogenic role of the novel tumor endothelial marker CLEC14A. *Oncogene* **31**, 293–305 (2012).
 190. Verissimo, A. R. *et al.* Functionally defining the endothelial transcriptome, from Robo4 to ECSCR. *Biochem. Soc. Trans.* **37**, 1214–7 (2009).
 191. Masiero, M. *et al.* A core human primary tumor angiogenesis signature identifies the endothelial orphan receptor ELTD1 as a key regulator of angiogenesis. *Cancer Cell* **24**, 229–241 (2013).
 192. London, N. R. & Li, D. Y. Robo4-dependent Slit signaling stabilizes the vasculature during pathologic angiogenesis and cytokine storm. *Curr. Opin. Hematol.* **18**, 186–90 (2011).
 193. Bedell, V. M. *et al.* roundabout4 is essential for angiogenesis in vivo. **1**, (2005).
 194. Klee, C. B., Ren, H. & Wang, X. Regulation of the calmodulin- stimulated protein phosphatase, calcineurin. *J. Biochem.* **273**, 13367–11370 (1998).
 195. Fuentes, J. J. *et al.* DSCR1, overexpressed in Down syndrome, is an inhibitor of calcineurin-mediated signaling pathways. *Hum. Mol. Genet.* **9**, 1681–1690 (2000).
 196. Hesser, B. a *et al.* Down syndrome critical region protein 1 (DSCR1), a novel VEGF target gene that regulates expression of inflammatory markers on activated endothelial cells. *Hemostasis, Thromb. Vasc. Biol.* **104**, 149–158 (2004).
 197. Holmes, K., Chapman, E., See, V. & Cross, M. J. Vegf stimulates RCAN1.4 expression in endothelial cells via a pathway requiring Ca²⁺/calcineurin and protein kinase C- δ . *PLoS One* **5**, 1–13 (2010).
 198. Sumanas, S. & Lin, S. Ets1-related protein is a key regulator of vasculogenesis in zebrafish. *PLoS Biol.* **4**, 0060–0069 (2006).
 199. Maroulakou, I. G. & Bowe, D. B. Expression and function of Ets transcription factors in mammalian development: a regulatory network. *Oncogene* **19**, 6432–6442 (2000).
 200. Cole, R. W., Liu, F. & Herron, B. J. Imaging of angiogenesis : past , present and future. *Complexity* 885–896 (2010).
 201. Stephens, D. J. & Allan, V. J. Light Microscopy Techniques for Live Cell Imaging. **82**, 82–87 (2003).
 202. Lakowicz, J. R. *Principles of Fluorescence Spectroscopy Principles of Fluorescence Spectroscopy. Principles of fluorescence spectroscopy, Springer, New York, USA, 3rd edn, 2006.* (2006). doi:10.1007/978-0-387-46312-4
 203. Sase, I., Miyata, H., Corrie, J. E., Craik, J. S. & Kinosita, K. Real time imaging of single fluorophores on moving actin with an epifluorescence microscope. *Biophys. J.* **69**, 323–8 (1995).
 204. Yuste, R. Fluorescence microscopy today. *Nat. Methods* **2**, 902–904 (2005).

205. D. Shotton, N. W. Confocal scanning microscopy : three-dimensional biological imaging. *Trends Biochem. Sci.* 435–439 (1989).
206. Shotton, D. M. Confocal scanning optical microscopy and its applications for biological specimens. *J. Cell Sci.* **94**, 175–206 (1989).
207. Hoffman, R. M. Imaging tumor angiogenesis with fluorescent proteins. *APMIS* **112**, 441–449 (2004).
208. Naumov, G. N., Akslen, L. a. & Folkman, J. Role of angiogenesis in human tumor dormancy: Animal models of the angiogenic switch. *Cell Cycle* **5**, 1779–1787 (2006).
209. Hoffman, R. M. The multiple uses of fluorescent proteins to visualize cancer in vivo. *Nat. Rev. Cancer* **5**, 796–806 (2005).
210. Murphy, P. a., Begum, S. & Hynes, R. O. Tumor angiogenesis in the absence of fibronectin or its cognate integrin receptors. *PLoS One* **10**, 1–16 (2015).
211. Inada, M. *et al.* Direct melanoma cell contact induces stromal cell autocrine prostaglandin E2-EP4 receptor signaling that drives tumor growth, angiogenesis, and metastasis. *J. Biol. Chem.* **290**, 29781–29793 (2015).
212. Rapoport, N., Gupta, R., Kim, Y. S. & O'Neill, B. E. Polymeric micelles and nanoemulsions as tumor-targeted drug carriers: Insight through intravital imaging. *J. Control. Release* **206**, 153–160 (2015).
213. Bernas, T., Zarębski, M., Cook, R. R. & Dobrucki, J. W. Minimizing photobleaching during confocal microscopy of fluorescent probes bound to chromatin: Role of anoxia and photon flux. *J. Microsc.* **215**, 281–296 (2004).
214. Hoebe, R. a *et al.* Controlled light-exposure microscopy reduces photobleaching and phototoxicity in fluorescence live-cell imaging. *Nat. Biotechnol.* **25**, 249–253 (2007).
215. Gao, X. Molecular profiling of single cells and tissue specimens with quantum dots. *Trends Biotechnol.* **21**, 371–373 (2003).
216. Dixit, R. & Cyr, R. Cell damage and reactive oxygen species production induced by fluorescence microscopy: effect on mitosis and guidelines for non-invasive fluorescence microscopy. *Plant J.* **36**, 280–290 (2003).
217. Wright, a, Bubb, W. a, Hawkins, C. L. & Davies, M. J. Singlet oxygen-mediated protein oxidation: evidence for the formation of reactive side chain peroxides on tyrosine residues. *Photochem Photobiol* **76**, 35–46 (2002).
218. Davis, G. E., Bayless, K. J. & Mavila, A. Molecular basis of endothelial cell morphogenesis in three-dimensional extracellular matrices. *Anat. Rec.* **268**, 252–275 (2002).
219. Lyons, a. B. Analysing cell division in vivo and in vitro using flow cytometric measurement of CFSE dye dilution. *J. Immunol. Methods* **243**, 147–154 (2000).
220. De Clerck, L. S., Bridts, C. H., Mertens, A. M., Moens, M. M. & Stevens, W. J. Use of fluorescent dyes in the determination of adherence of human leucocytes to endothelial cells and the effect of fluorochromes on cellular function. *J. Immunol. Methods* **172**, 115–124 (1994).
221. Sambasivarao, S. V. NIH Public Access. **18**, 1199–1216 (2013).
222. Sells, M. a *et al.* Human p21-activated kinase (Pak1) regulates actin organization in mammalian cells. *Curr. Biol.* **7**, 202–210 (1997).

223. Stoletov, K. V. & Terman, B. I. Bmx is a downstream Rap1 effector in VEGF-induced endothelial cell activation. *Biochem. Biophys. Res. Commun.* **320**, 70–75 (2004).
224. Smith, C. I. E. *et al.* The Tec family of cytoplasmic tyrosine kinases: Mammalian Btk, Bmx, Itk, Tec, Txk and homologs in other species. *BioEssays* **23**, 436–446 (2001).
225. He, Y. *et al.* Critical function of Bmx / Etk in ischemia-mediated arteriogenesis and angiogenesis. *J. Clin. Invest.* **116**, 2344–2355 (2006).
226. Honigberg, L. a *et al.* The Bruton tyrosine kinase inhibitor PCI-32765 blocks B-cell activation and is efficacious in models of autoimmune disease and B-cell malignancy. *Proc. Natl. Acad. Sci. U. S. A.* **107**, 13075–80 (2010).
227. Byrd, J. C. *et al.* Targeting BTK with ibrutinib in relapsed chronic lymphocytic leukemia. *N. Engl. J. Med.* **369**, 32 (2013).
228. Chen, X.-L., Qiu, L., Wang, F. & Liu, S. Current understanding of tyrosine kinase BMX in inflammation and its inhibitors. *Burn. Trauma* **2**, 121 (2014).
229. Evans, E. K. *et al.* Inhibition of Btk with CC-292 provides early pharmacodynamic assessment of activity in mice and humans. *J. Pharmacol. Exp. Ther.* **346**, 219–28 (2013).
230. Gilbert, C. *et al.* Chemotactic factor-induced recruitment and activation of Tec family kinases in human neutrophils. II. Effects of LFM-A13, a specific Btk inhibitor. *J. Immunol.* **170**, 5235–43 (2003).
231. Zhang, X. *et al.* Indirubin inhibits tumor growth by antitumor angiogenesis via blocking VEGFR2-mediated JAK/STAT3 signaling in endothelial cell. *Int. J. Cancer* **129**, 2502–2511 (2011).
232. Korff, T., Kimmina, S., Martiny-Baron, G. & Augustin, H. G. Blood vessel maturation in a 3-dimensional spheroidal coculture model: direct contact with smooth muscle cells regulates endothelial cell quiescence and abrogates VEGF responsiveness. *FASEB J.* **15**, 447–457 (2001).
233. Kiosses, W. B., Daniels, R. H., Otey, C., Bokoch, G. M. & Schwartz, M. a. A role for p21-activated kinase in endothelial cell migration. *J. Cell Biol.* **147**, 831–844 (1999).
234. Knaus, U. G., Wang, Y., Reilly, A. M., Warnock, D. & Jackson, J. H. Structural Requirements for PAK Activation by Rac GTPases. *J. Biol. Chem.* **273**, 21512–21518 (1998).
235. Murray, B. W. *et al.* Small-molecule p21-activated kinase inhibitor PF-3758309 is a potent inhibitor of oncogenic signaling and tumor growth. *Proc. Natl. Acad. Sci. U. S. A.* **107**, 9446–9451 (2010).
236. Deacon, S. W. *et al.* An Isoform-Selective, Small-Molecule Inhibitor Targets the Autoregulatory Mechanism of p21-Activated Kinase. *Chem. Biol.* **15**, 322–331 (2008).
237. Mahajan, S. *et al.* Src family protein tyrosine kinases induce autoactivation of Bruton's tyrosine kinase. *Mol Cell Biol* **15**, 5304–5311 (1995).
238. Kawakami, Y. *et al.* Terreic acid, a quinone epoxide inhibitor of Bruton's tyrosine kinase. *Proc Natl Acad Sci U S A* **96**, 2227–2232 (1999).
239. Hida, K. & Klagsbrun, M. A new perspective on tumor endothelial cells: Unexpected chromosome and centrosome abnormalities. *Cancer Res.* **65**, 2507–2510 (2005).

240. Kuwai, T. *et al.* Phosphorylated epidermal growth factor receptor on tumor-associated endothelial cells is a primary target for therapy with tyrosine kinase inhibitors. *Neoplasia* **10**, 489–500 (2008).
241. Pack, S. D. Simultaneous Suppression of Epidermal Growth Factor Receptor and c-erbB-2 Reverses Aneuploidy and Malignant Phenotype of a Human Ovarian Carcinoma Cell Line. *Cancer Res.* **64**, 789–794 (2004).
242. Fischer, O. M., Hart, S., Gschwind, a. & Ullrich, a. EGFR signal transactivation in cancer cells. *Biochem. Soc. Trans.* **31**, 1203–08 (2003).
243. Paez, J. . *et al.* EGFR Mutations in Lung Cancer: Correlation with Clinical Response to Gefitinib Therapy. **1497**, 1497–1501 (2006).
244. Lafky, J. M., Wilken, J. a, Baron, A. T. & Maihle, N. J. Clinical implications of the ErbB/epidermal growth factor (EGF) receptor family and its ligands in ovarian cancer. *Biochim. Biophys. Acta* **1785**, 232–265 (2008).
245. Rajput, A. *et al.* A novel mechanism of resistance to epidermal growth factor receptor antagonism in vivo. *Cancer Res.* **67**, 665–673 (2007).
246. Sheikh, A. Q. *et al.* Regulation of endothelial MAPK/ERK signalling and capillary morphogenesis by low-amplitude electric field. *J. R. Soc. Interface* **10**, 20120548 (2013).
247. Belmokhtar, C. a, Hillion, J. & Ségal-Bendirdjian, E. Staurosporine induces apoptosis through both caspase-dependent and caspase-independent mechanisms. *Oncogene* **20**, 3354–3362 (2001).
248. Kabir, J., Lobo, M. & Zachary, I. Staurosporine induces endothelial cell apoptosis via focal adhesion kinase dephosphorylation and focal adhesion disassembly independent of focal adhesion kinase proteolysis. *Biochem. J.* **367**, 145–55 (2002).
249. Sumanas, S. *et al.* Interplay among Etsrp/ER71, Scl, and Alk8 signaling controls endothelial and myeloid cell formation. *Blood* **111**, 4500–4510 (2008).
250. Abrams, T. J., Lee, L. B., Murray, L. J., Pryer, N. K. & Cherrington, J. M. SU11248 inhibits KIT and platelet-derived growth factor receptor beta in preclinical models of human small cell lung cancer. *Mol. Cancer Ther.* **2**, 471–478 (2003).
251. Farrell, A. O. *et al.* SU11248 is a novel FLT3 tyrosine kinase inhibitor with potent activity in vitro and in vivo. **101**, 3597–3605 (2003).

Appendices

7.1 Identification of the different parameters measured by the ImageJ Spheroid Analysis plugin for spheroid quantification

The ImageJ Spheroid Analysis plugin was used to quantify endothelial sprouting from fluorescently labelled spheroid images generated using the *in vitro* hanging drop spheroid angiogenesis assay. As shown by figure 7.1A, the Spheroid Analysis ImageJ plugin was able to process the spheroid images by skeletonising the network of endothelial cells surrounding the spheroid mass. After the skeletonisation process, the endothelial sprouts appeared as a network of single pixels within the image, each pixel was assessed according to its neighbouring eight pixel values and subsequently categorised as either an end point, junction or segment pixel.

A segment pixel was assigned if the pixel being assessed had exactly two neighbouring pixels that were also part of the skeletonised network, whereas an end point pixel was assigned if there was only one or zero neighbouring pixels. A junctional pixel was assigned if the pixel being assessed had more than two neighbouring pixels. In this way, all pixels within the skeletonised network were analysed and each pixel was colour coded accordingly. All end point pixels were identified in red and junctional pixels in dark blue as shown in figures 7.1B and 7.1C. Endothelial segments within the spheroid images were therefore separated by either two end point pixels, two junctional pixels or one end point and one junctional pixel, and all segmental pixels were identified in light blue, as shown in figure 7.1D. Following the pixel analysis, the ImageJ plugin automatically calculated the total segment length by summing the number of pixels assigned as a segment pixel and the average segment length was calculated by dividing the total segment length by the number of endothelial segments from within an image.

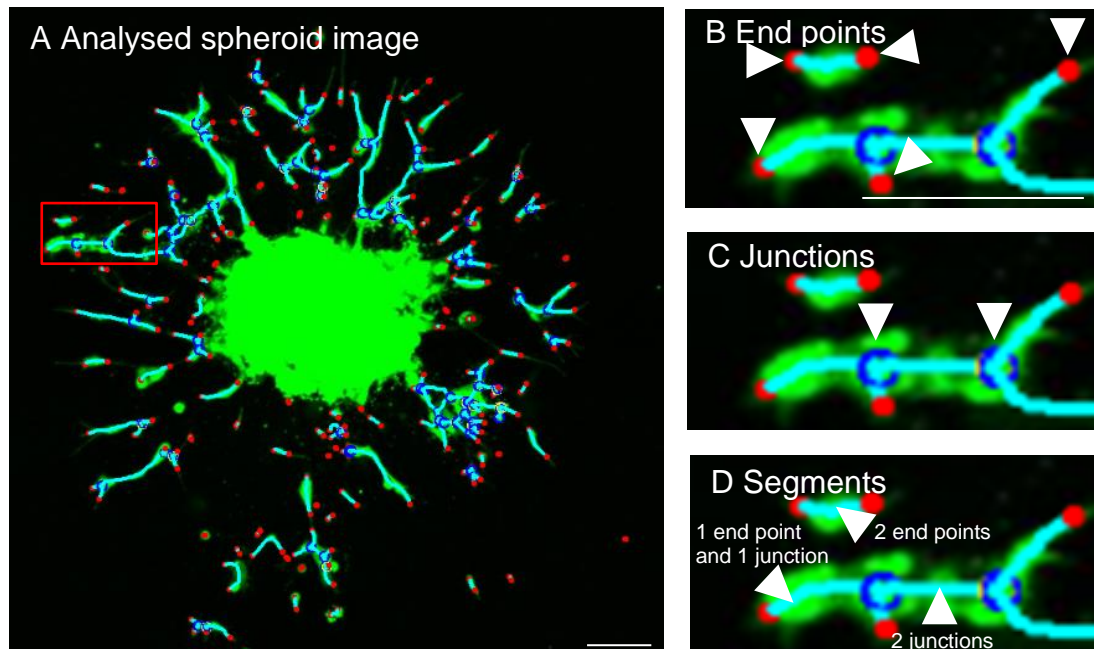


Figure 7.1 Identification of the parameters measured by the Spheroid Analysis plugin for the quantification of endothelial sprouting

The ImageJ Spheroid Analysis plugin was used to analyse fluorescent spheroid images generated using the hanging drop spheroid angiogenesis assay. **A)** An image of the analysed network of endothelial sprouts produced by the ImageJ plugin from a fluorescently labelled spheroid image. The sprouting segments are shown in light blue, the endothelial junctions in dark blue and the end points in red. The red box highlights a selected region which was magnified to show in detail the identification of the different parameters that were measured by the plugin. **B)** A magnified image of an endothelial sprout analysed by the Spheroid Analysis ImageJ plugin, the arrows show the identification of five end points, shown in red, scale: 100 μm . **C)** The arrows show the identification of two endothelial junctions shown in dark blue. **D)** The endothelial segments are shown in light blue, an endothelial segment was defined as a region of connected segmental pixels separated either by two end points, two junctional points or one junction and one end point, an example of each of these has been shown and identified with arrows in the image, scale: 100 μm .

7.2 Screening kinases to identify those with roles in endothelial sprouting

A library of 80 small molecule kinase inhibitor compounds were added into the *in vitro* hanging drop spheroid angiogenesis assay to identify the effects the kinase inhibitors had on the processes on endothelial sprouting. In this way, a wide range of spheroid images showing different sprouting morphologies were generated and used to test the capabilities of the Spheroid Analysis plugin as described in this thesis in section 4.4.

The ImageJ Spheroid Analysis plugin was used to analyse the effects of the kinase inhibitor compounds on endothelial sprouting by applying the plugin to images of fluorescently labelled spheroids which were treated in the hanging drop spheroid assay with the inhibitor compounds. Five spheroids were imaged and analysed per inhibitor condition and bar charts of the results generated on the parameters of total and average endothelial sprouting length and the numbers of endothelial segments, junctions and end points have been shown in figures 7.2 – 7.6. Statistical analysis was performed using the Mann-Whitney test.

The sprouting results for this study as presented in figures 7.2 – 7.6 were normalised to their corresponding controls and converted to percentages and were represented in heat map tables, as shown in tables 11 and 12 in chapter four.

Total sprouting length - Percentage of control (%)

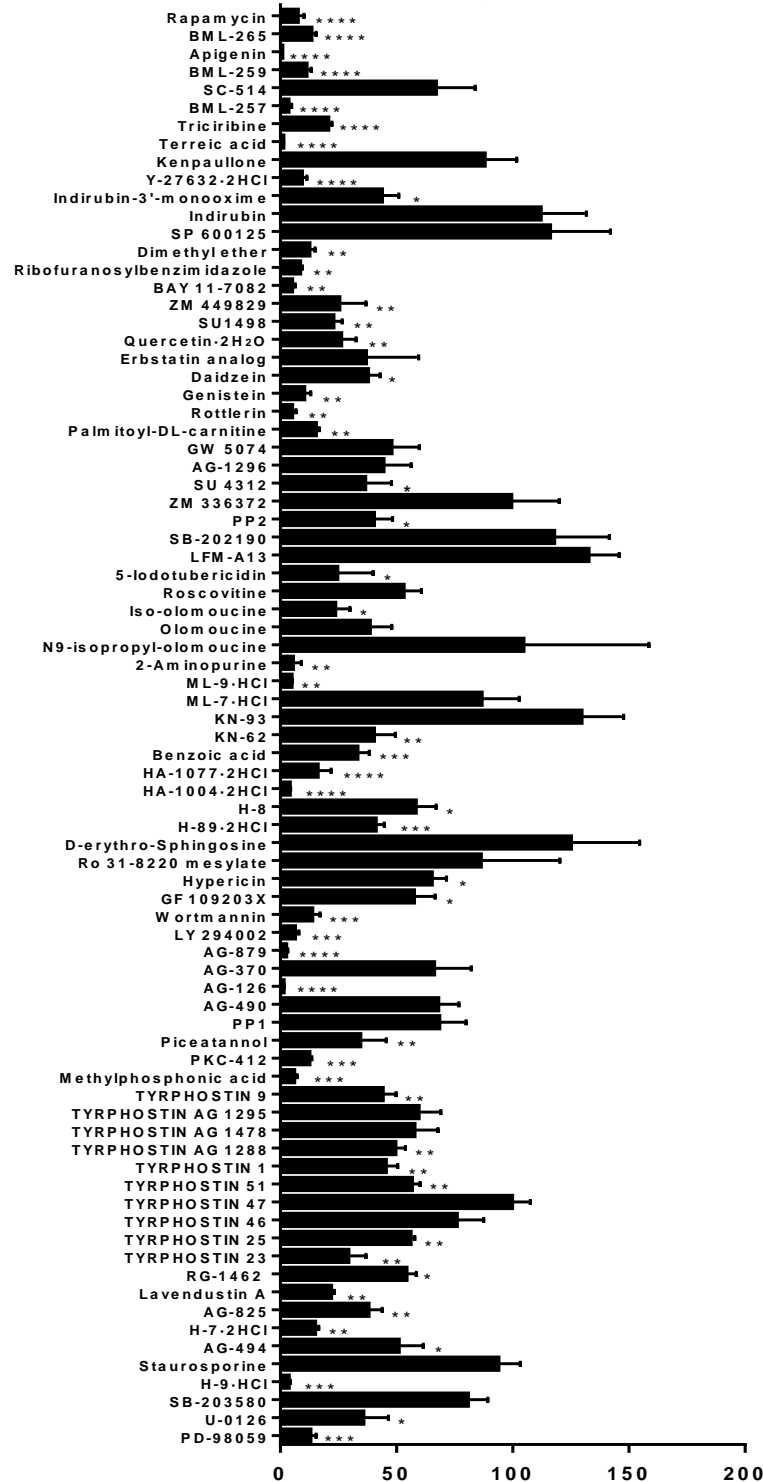


Figure 7.2 The effect on the total sprouting length when kinase inhibitors were added to the hanging drop spheroid assay

The ImageJ Spheroid Analysis plugin was used to analyse the total sprouting length of fluorescently labelled spheroids generated using the hanging drop spheroid angiogenesis assay with confocal imaging 16 hrs after collagen embedding. Statistical analysis was performed using the Mann-Whitney test, n=5 images per condition, **** indicates $p \leq 0.0001$, *** indicates $p \leq 0.001$, ** indicates $p \leq 0.01$ and * indicates $p \leq 0.05$. The error bars are the SEM.

Average sprouting length - Percentage of control (%)

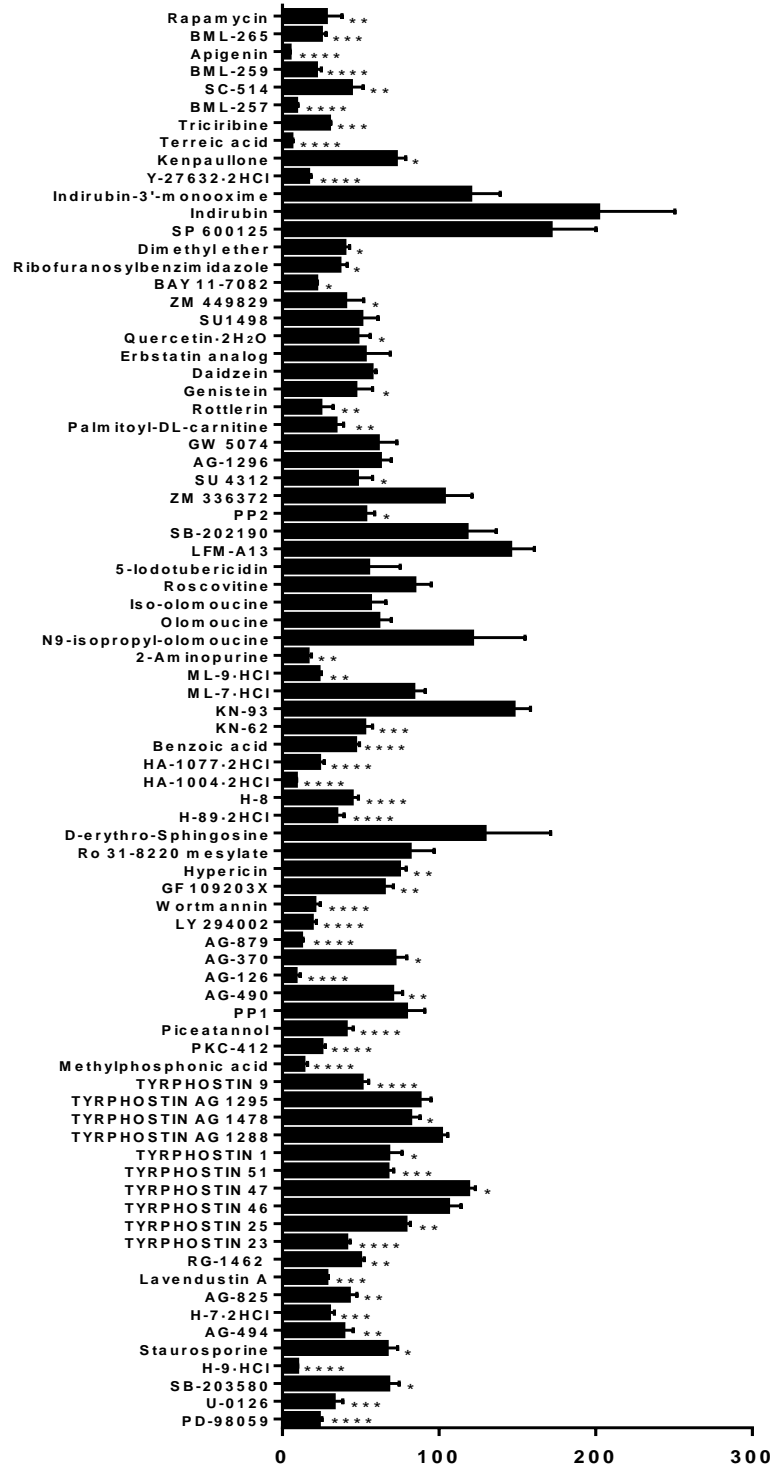


Figure 7.3 The effect on the average sprouting length when kinase inhibitors were added to the hanging drop spheroid assay

The ImageJ Spheroid Analysis plugin was used to analyse the average sprouting length of fluorescently labelled spheroids generated using the hanging drop spheroid angiogenesis assay with confocal imaging 16 hrs after collagen embedding. Statistical analysis was performed using the Mann-Whitney test, n=5 images per condition, **** indicates $p \leq 0.0001$, *** indicates $p \leq 0.001$, ** indicates $p \leq 0.01$ and * indicates $p \leq 0.05$. The error bars are the SEM.

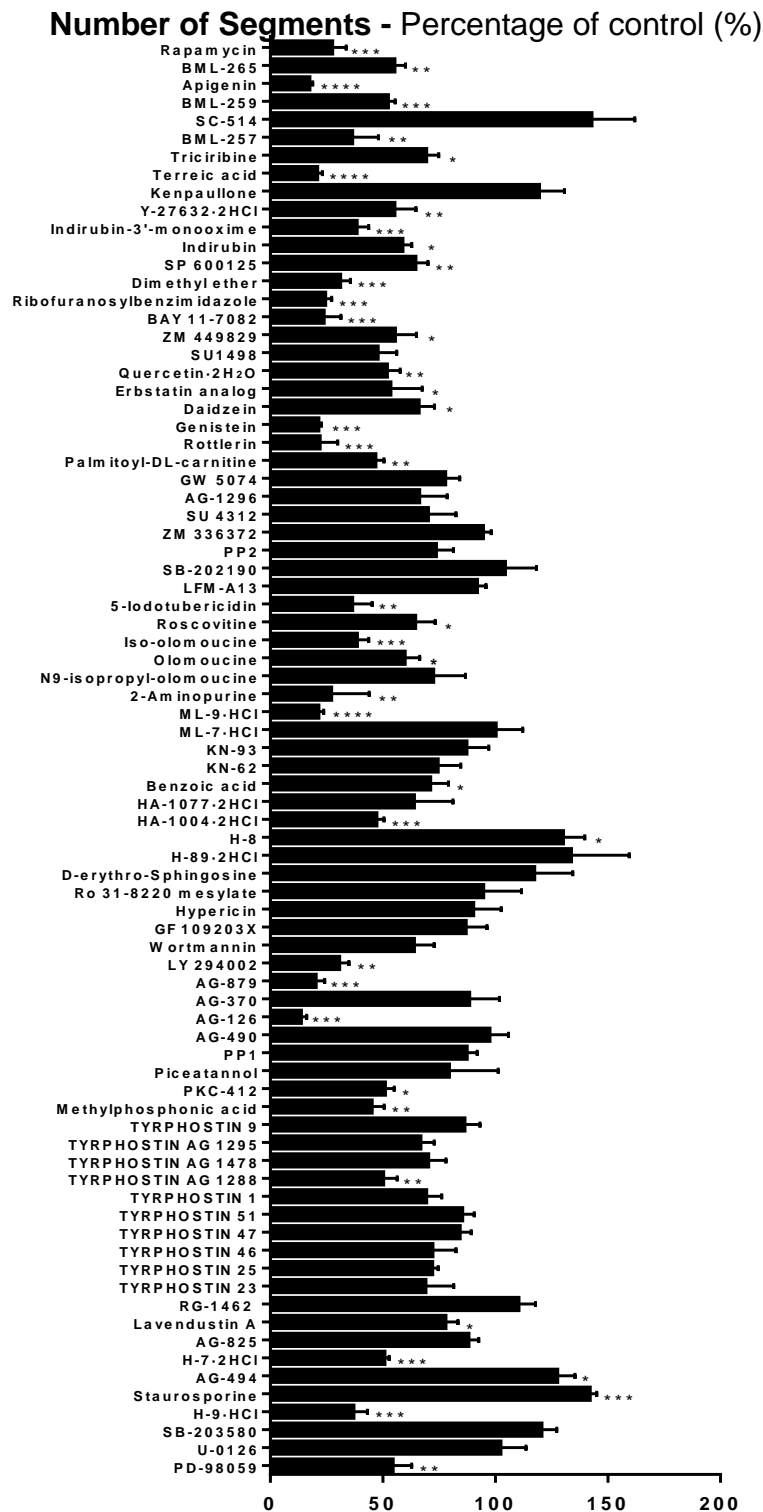


Figure 7.4 The effect on the number of segments when kinase inhibitors were added to the hanging drop spheroid assay

The ImageJ Spheroid Analysis plugin was used to analyse the number of segments of fluorescently labelled spheroids generated using the hanging drop spheroid angiogenesis assay with confocal imaging 16 hrs after collagen embedding. Statistical analysis was performed using the Mann-Whitney test, n=5 images per condition, **** indicates $p \leq 0.0001$, *** indicates $p \leq 0.001$, ** indicates $p \leq 0.01$ and * indicates $p \leq 0.05$. The error bars are the SEM.

Number of Junctions - Percentage of control (%)

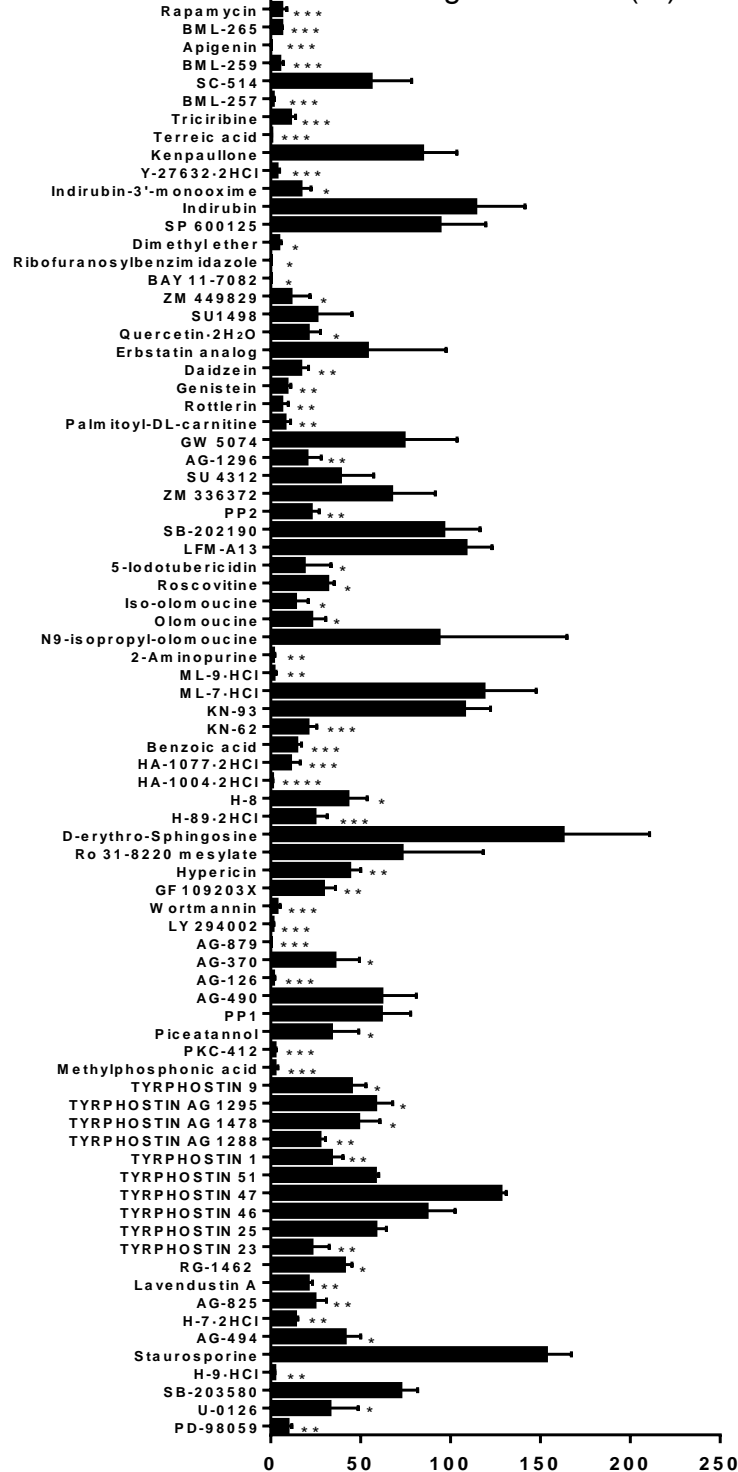


Figure 7.5 The effect on the number of junctions when kinase inhibitors were added to the hanging drop spheroid assay

The ImageJ Spheroid Analysis plugin was used to analyse the number of junctions of fluorescently labelled spheroids generated using the hanging drop spheroid angiogenesis assay with confocal imaging 16 hrs after collagen embedding. Statistical analysis was performed using the Mann-Whitney test, n=5 images per condition, **** indicates $p \leq 0.0001$, *** indicates $p \leq 0.001$, ** indicates $p \leq 0.01$ and * indicates $p \leq 0.05$. The error bars are the SEM.

Number of End points - Percentage of control (%)

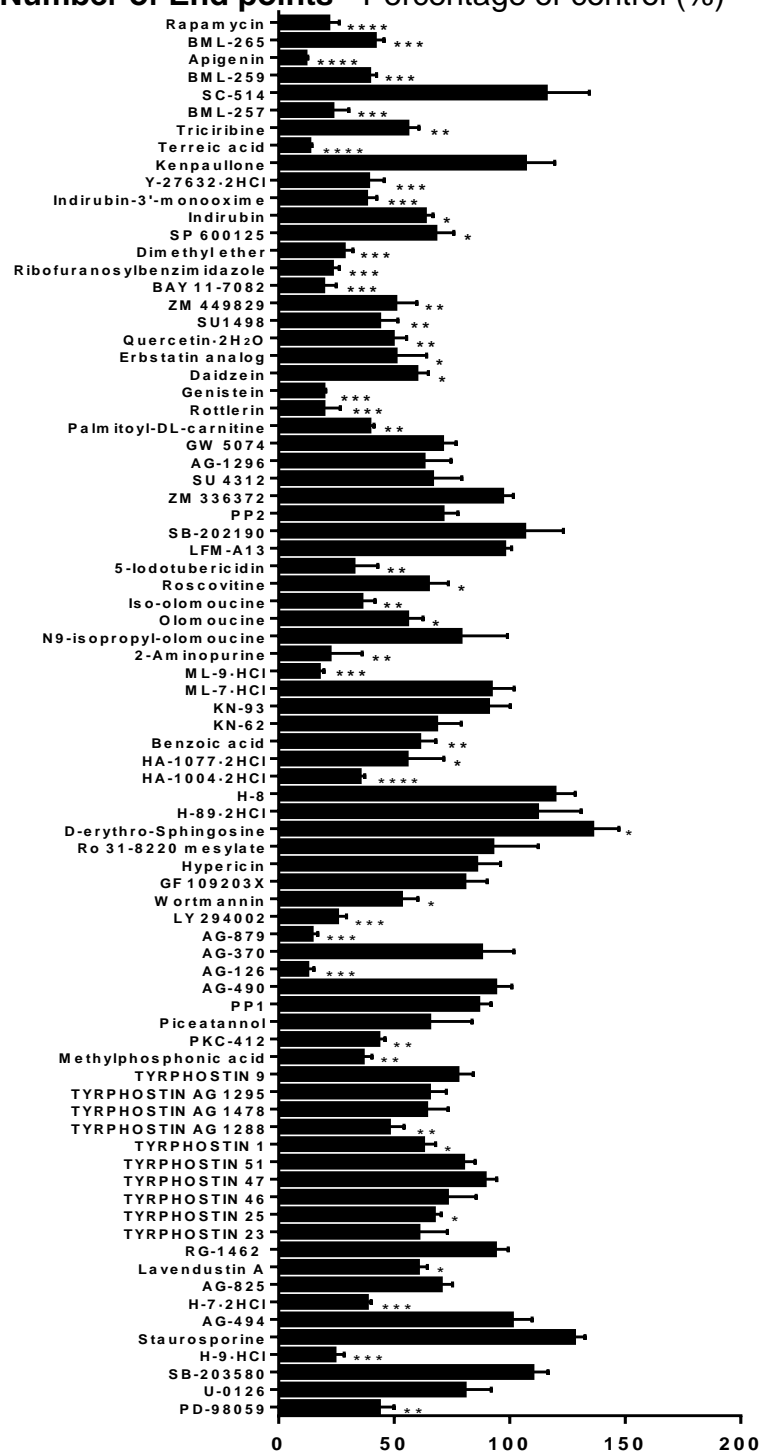


Figure 7.6 The effect on the number of end points when kinase inhibitors were added to the hanging drop spheroid assay

The ImageJ Spheroid Analysis plugin was used to analyse the number of end points of fluorescently labelled spheroids generated using the hanging drop spheroid angiogenesis assay with confocal imaging 16 hrs after collagen embedding. Statistical analysis was performed using the Mann-Whitney test, n=5 images per condition, **** indicates $p \leq 0.0001$, *** indicates $p \leq 0.001$, ** indicates $p \leq 0.01$ and * indicates $p \leq 0.05$. The error bars are the SEM.

7.3 Identification of the different parameters measured by the computer analysis tools for quantifying intersegmental blood vessel growth and connectivity

The ImageJ and IMARIS computer based analysis methods were developed to analyse and quantify the growth of the ISVs within zebrafish and the connectivity of these vessels to the DLAV. Both of the computer based methods used a skeletonisation function to simplify the vascular network to a series of single pixels, which were individually assessed according to their neighbouring pixel values. Each pixel within the vascular skeleton was categorised as an end point, junctional or segmental pixel and colour coded accordingly, as shown in figure 7.7A.

A segment pixel was assigned if the pixel being assessed had exactly two neighbouring pixels, whereas an end point pixel was assigned if the pixel had zero or one neighbouring pixel. A junctional pixel was assigned if the pixel being assessed had more than two neighbouring pixels. All end point pixels were labelled blue in colour and junctional pixels were labelled in pink, as shown in figures 7.7B and 7.7C respectively. A vascular segment was defined as a connected region of segment pixels between two end point pixels, two junctional pixels or one end point and one junctional pixel. All vascular segment pixels were shown in orange within the analysed image, as shown in figure 7.7D. After the pixels within the vasculature image had been analysed, the calculations of the total and average vessel lengths were determined.

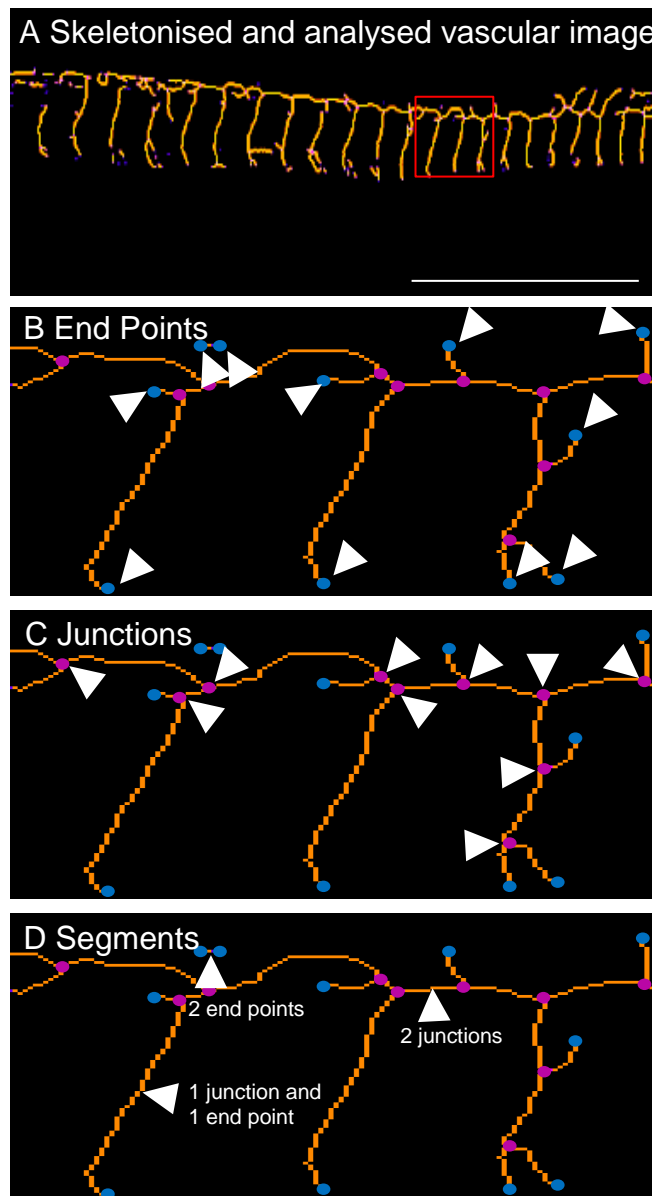


Figure 7.7 Identification of the parameters measured by the computer analysis methods for the quantification of intersegmental blood vessel growth and connectivity

The computer analysis methods using ImageJ and IMARIS analysed the skeletonised zebrafish vascular network in a similar way to produce outputs on the numbers of end points, junctions and vessel segments. The images shown in this figure were generated using the ImageJ analysis method. **A)** An image of the analysed and skeletonised network of ISVs and DLAV, vessel segments are shown in orange, junctions in pink and end points in blue. The red box highlights a selected region which was enlarged to show the identification of the different parameters that were measured, scale: 500 μm . **B)** An enlarged image of a region of skeletonised vasculature, arrows show the identification of end points. **C)** The arrows show the identification of junctions. **D)** A vascular segment was defined as a connected region of segment pixels between two end points, two junctional points or between one junction and one end point, an example of each has been identified with arrows.

7.4 ImageJ zebrafish vasculature analysis macro

The zebrafish vasculature analysis macro was generated as part of the ImageJ analysis method for the quantification of the intersegmental blood vessels (ISVs) and their connectivity to the dorsal longitudinal anastomotic vessel (DLAV) in *fli1*-GFP embryonic zebrafish. The ImageJ analysis method for quantifying fluorescent images of the zebrafish vasculature is presented in this thesis in section 5.3. The image processing steps of binarisation through to generating the outputs of the analysed vascular skeleton which correlate to steps four through to eight in the method were generated as a macro. The macro can be transferred and saved to ImageJ to allow for semi-automated analysis of zebrafish vasculature images.

```
run("8-bit");  
setOption("BlackBackground", true);  
run("Make Binary");  
run("Fill Holes");  
run("Despeckle");  
run("Skeletonize (2D/3D)");  
run("Analyze Skeleton (2D/3D)", "prune=none show");
```

Figure 7.8 ImageJ zebrafish vasculature analysis macro code

The ImageJ macro was generated to allow for the semi-automated analysis of the ISVs in vascular images of *fli1*-GFP zebrafish embryos. The code for the macro can be transferred and saved to ImageJ.